# Molecular Modeling of Gas Adsorption, Phase Behaviors, and Surface Area Characterization in Shale Organic Nanoporous Media

by

Yingnan Wang

A thesis submitted in partial fulfillment of the requirements for the degree of

Doctor of Philosophy

in

Petroleum Engineering

Department of Civil and Environmental Engineering

University of Alberta

**ABSTRACT**

Shale gas plays an increasingly important role in meeting the growing global energy demand and reducing carbon emissions. Unlike conventional reservoirs, shale, including both organic and inorganic matter, can have an extensive amount of pores ranging from a few to hundreds of nanometers. Kerogen, as the main constituent of shale organic matter, has exceptionally high surface area due to extensive nanoscale pores, in which hydrocarbons behave very differently from the bulk, and surface adsorption becomes significant due to the strong fluid–surface interactions. This thesis investigates gas adsorption, phase behaviors, and surface area characterization in shale organic (kerogen) nanoporous media.

Due to extensive nanoscale pores in kerogen, the nanoconfined hydrocarbon adsorption and phase behaviors can be largely altered from that of the bulk, which can further affect shale gas production processes. Contributions are made to the following questions: (1) What is the phase behavior of hydrocarbon in kerogen nanopores? (2) How does the pore size distribution (volume partitioning) affect shale gas adsorption and production processes in kerogen? (3) How can $CO_2$ injection help enhance gas recovery in organic shale media? Considering the first question, engineering density functional theory is applied to predict the phase behavior of a pure component in nanopores, and the applicability of widely used traditional methods, like various versions of the Kelvin equation and equation-of-state-with-capillary-pressure models, in shale organic mesopores and micropores has been investigated. In pursuing the second question, the effect of pore size distribution/volume partitioning on the hydrocarbon recovery from shale organic nanoporous media has been studied. Interplays between bundle-of-capillary nanopores and bulk are considered. By adopting the actual shale pore size distributions, the constant volume depletion method is used to simulate shale gas recovery. For the third question, the $CO_2$ 'huff-n-puff' process is applied in nanopore–bulk multiscale models with varying pore size distributions to study the $CO_2$ injection effect coupling the volume partitioning effect on gas adsorption and recovery.

On the other hand, the surface area is an important parameter for methane adsorption estimation in shale nanoporous media. Methane adsorption behaviors can vary drastically in micropores and mesopores, and rock surface type may also greatly affect its adsorption. The Brunauer–Emmett–Teller (BET) method has been extensively used to characterize the surface area of various porous materials. However, its applicability for the surface area characterization

of kerogen mesopores has not been investigated yet. Contributions are made to the following questions: (4) Which surface area measurement method is suitable for kerogen? (5) How do the kerogen characteristics affect surface area measurements and the applicability of the BET method in kerogen? To pursue the fourth and fifth questions, we provide a systematic discussion on measurements of shale rock properties including rock compositions, specific surface area, and pore size distributions, which are important parameters for methane adsorption in shale nanoporous media. Particular attention is paid to the assumptions and working mechanisms proposed in various interpretation methods which are embedded in shale rock properties and adsorption characterizations. The effect of geometrical and energetical heterogeneity on $N_2$ adsorption isotherms and the subsequent BET surface area characterization is studied by using grand canonical Monte Carlo simulations.

As a whole, this thesis investigates gas adsorption and phase behaviors in kerogen nanopores. The effect of pore size distribution and $CO_2$ injection effect on gas adsorption and recovery in kerogen are also studied. Additionally, we also investigate surface area characterizations of kerogen by gas adsorption. This thesis provides some crucially important insights into the optimization of shale gas recovery, geological $CO_2$ sequestration, $CH_4$ adsorption capacity prediction, and shale gas-in-place (GIP) estimation in kerogen nanoporous media.

**PREFACE**

CHAPTER 1 (Introduction Chapter) outlines the research background, problem statement, research objectives, and structure of the thesis.

A version of CHAPTER 2 has been published by Yingnan Wang, Nadia Shardt, Chang Lu, Huazhou Li, Janet A.W. Elliott, and Zhehui Jin (2020). Validity of the Kelvin Equation and the Equation-of-state-with-capillary-pressure Model for the Phase Behavior of a Pure Component under Nanoconfinement. Chemical Engineering Science 226 (2020) 115839. https://www.sciencedirect.com/science/article/pii/S0009250920303717?via%3Dihub. Yingnan Wang performed all research and composed the first draft of this chapter under the direction and supervision of Zhehui Jin. Nadia Shardt and Janet A.W. Elliott provided motivation for this work. Chang Lu and Huazhou Li gave assistance to calibrate the Peng–Robinson equation of state phase equilibrium calculations. All authors contributed to the version of the chapter presented in this thesis.

A version of CHAPTER 3 has been published by Yingnan Wang and Zhehui Jin (2019). Effect of Pore Size Distribution on Hydrocarbon Mixtures Adsorption in Shale Nanoporous Media from Engineering Density Functional Theory. Fuel 254 (2019) 115650. https://www.sciencedirect.com/science/article/abs/pii/S0016236119310026. Yingnan Wang performed all research and composed the first draft of this chapter under the direction and supervision of Zhehui Jin.

A version of CHAPTER 4 has been published by Yingnan Wang and Zhehui Jin (2021). Hydrocarbon Mixture and $CO_2$ Adsorptions in A nanopore–bulk Multiscale System in Relation to $CO_2$ Enhanced Shale Gas Recovery. Chemical Engineering Journal 415 (2021) 128398. https://www.sciencedirect.com/science/article/abs/pii/S1385894720345101. Yingnan Wang performed all research and composed the first draft of this chapter under the direction and supervision of Zhehui Jin.

A version of CHAPTER 5 has been published by Yingnan Wang, Wanying Pang, and Zhehui Jin (2022). Effect of Energetical and Geometrical Heterogeneity of Kerogen on BET Surface Area Characterization and Methane Adsorption. Energy Fuels 2022, DOI: 10.1021/acs.energyfuels.2c01603. https://pubs.acs.org/doi/abs/10.1021/acs.energyfuels.2c01603. Yingnan Wang Yingnan Wang performed all research and composed the first draft of this

chapter under the direction and supervision of Zhehui Jin. Wanying Pang provided motivation for this work.

CHAPTER 6 (Conclusion Chapter) summarizes the conclusions reached in this thesis as well as the recommendations for future research.

**ACKNOWLEDGMENTS**

To Dr. Zhehui Jin, thank you for your generous guidance in my academics. Your commitment to mentoring, supervising, and teaching is inspiring, and I have greatly benefited from it during my Ph.D. study.

To Drs. Janet A.W. Elliott, Juliana Leung, Arvind Rajendran, and Joachim Moortgat, thank you for your willingness and time being my examination committee, and for your valuable comments on my thesis.

To Drs. Janet A.W. Elliott and Nadia Shardt, thank you for your boundless enthusiasm, our interfacial-tension-related discussions, and our collaborations.

To Drs. Huazhou Li and Chang Lu, thank you for your boundless enthusiasm, our equations of state related discussions, and our collaborations.

To all past and present members of the Jin, Li, and Elliott research groups I have been lucky to get to know; thank you for sharing your knowledge, advice, and passion.

To all faculty, administrative staff, postdoctoral researchers, and undergraduate and graduate students, I have had the pleasure of meeting or working with, thank you for enriching my graduate study experience.

To the Natural Sciences and Engineering Research Council of Canada (NSERC) and the University of Alberta, thank you for your financial support of this thesis.

To my family, thank you for your nonstop support and encouragement.

To Ms. Zhao, thank you for your accompaniment and continuous support throughout my Ph.D. period. Deeply appreciated.

## Table of Contents

## List of Tables

## List of Figures

公式章 (下一章) 节 1

# CHAPTER 1 Introduction

## 1.1. Research Background

Natural gas plays a consistently progressively significant role to fulfill the global energy demand as a transition fuel. According to the U.S. Energy Information Administration (EIA) prediction, the global demand for natural gas will grow up to more than 20% in the next three decades [1]. On the other hand, due to the continuous depletion of conventional natural gas reservoirs, shale gas has become an important natural gas source. Unlike conventional reservoirs, surface adsorption plays a dominant role in shale gas due to the strong fluid–surface interaction in nanosized pores in shale media [2-4]. Shale rocks are heterogeneous complex structural and mineralogical systems consisting of inorganic matters and organic matters [5, 6]. As the main constituent of organic matter, kerogen consists of a significant amount of nanoscale pores and it generates hydrocarbons via chemical decomposition [7], which is also the main methane storage site [6, 8, 9]. Due to the significant fluid–surface interactions and inhomogeneous fluid distributions in nanoscale pores, the properties and phase behavior of nanoconfined fluids are very different from bulk [10-12]. Therefore, thoroughly investigating gas adsorption, phase behaviors, and surface area characterization in shale organic (kerogen) nanoporous media becomes utterly important in the optimization of shale gas recovery, geological $CO_2$ sequestration, $CH_4$ adsorption capacity prediction, and shale GIP estimation in kerogen media.

To predict the phase behavior of hydrocarbon in nanopores, various versions of the Kelvin equation and equation-of-state-with-capillary-pressure (EOS–$P_{cap}$) models have been widely used though controversies surrounding their validities exist. Assuming that the vapor phase behaves as an ideal gas and the liquid phase is incompressible, one can derive the Kelvin equation [13]. Thus, due to the fluid distribution inhomogeneity in nanopores [14], the applicability of the Kelvin equation is under debate. For capillary evaporation, most studies claimed that the Kelvin equations largely overestimate evaporation pressure in sub-10-nm pores [15-17]. For capillary condensation, disagreement also exists in sub-10-nm pores. Some researchers claimed that the simplified Kelvin equation (SKE) becomes invalid in sub-10-nm pores and the deviation becomes more significant as pore size decreases [17-20], while, on the other hand, some researchers

otherwise indicated the validity of the SKE and the complete Kelvin equation (CKE) in sub-10-nm pores [21-25]. In contrast to the Kelvin equations, several extended equation-of-state (EOS) methods have been developed to describe the phase behavior of fluid in a nanopore. One popular method is using a cubic EOS to describe vapor- and liquid-phase properties combined with capillary pressure (EOS–$P_{cap}$) [26-31]. Various EOS–$P_{cap}$ models [15, 30-34] have been widely used to obtain the properties of hydrocarbon mixtures in nanopores for shale oil recovery. To obtain the vapor–liquid equilibria (VLE), EOS–$P_{cap}$ models always need to implement successive substitutions and numerical iterations to satisfy the chemical and mechanical equilibrium [33]. Though EOS–$P_{cap}$ models can consider fluid compressibility, they cannot fully consider the fluid inhomogeneous distribution caused by the fluid–surface interaction in nanopores. A few studies have incorporated adsorption layer thickness into the EOS–$P_{cap}$ model to improve their performance in nanopores [32, 35, 36]. However, so far, neither the Kelvin equation nor the EOS–$P_{cap}$ models can fully account for fluid distribution inhomogeneity [14] in nanopores due to fluid–surface interactions. Another defect of the Kelvin equation and EOS–$P_{cap}$ models is their prediction of the bulk critical point (CP). Due to the interfacial tension (IFT) vanishing at the bulk CP, both Kelvin equation and EOS–$P_{cap}$ models generally predict the critical point of confined fluids to be unshifted [29, 31, 33]. While the existence of a hysteresis critical point (HCP) [37] under nanoconfinement, which is different from the bulk CP has been well documented from experiments, molecular modeling, and simulation studies [37, 38]. Thus, their validities in predicting phase behaviors in shale nanopores have been much debated, especially in sub-10-nm pores.

Besides, due to numerous nanoscale pores in shale organic media, the effect of pore size distribution can be an important factor in gas adsorption. In the past, a number of works using molecular simulations and theoretical calculations have been applied to study the properties and phase behaviors of nanoconfined hydrocarbons mainly based on a single-pore model [10-12, 39-44], while ignoring pore size distribution (PSD), *i.e.*, the volume partitioning in various pores. For example, Didar *et al.* [12], Jin and Firoozabadi [11], and Bui *et al.* [44] used grand canonical Monte Carlo (GCMC) to study the fluid properties of hydrocarbon mixtures in various nanoscale pores. Although the nanoconfinement effect on fluid adsorption has been studied in various computational and theoretical

works, most of the works were performed based on a single-pore model. However, unlike monodispersed porous materials, such as carbon nanotubes, shale has various pores ranging from a few nanometers to micrometers. The pore size distribution (PSD), *i.e.*, the volume partitioning in different pores and their interplay, may play an important role in shale gas recovery. In addition, in these works, while the bulk pressure has been varied, the bulk composition usually remains the same [11, 44]. However, based on the field observation, the produced fluid composition has been changing throughout production [45]., which is another limitation for a single-pore model to describe gas adsorption and recovery in shale nanoporous media. Recently, a few works have been reported on the study of the effect of PSD on the confined pure or hydrocarbon mixtures by the pore-size-dependent equation of state (PR-C EOS). [46, 47] or the gauge-GCMC method [48]. Although these works provided some insights into the effect of PSD on the phase behavior of confined hydrocarbons, models that can explicitly consider the effect of PSD on hydrocarbon mixtures, fluid–fluid interactions, and fluid–surface interactions have not yet been developed.

Furthermore, these plentiful nanopores further result in ultra-low permeability and porosity [49-51] which causes difficulties in gas production. Based on field data [52], shale gas production rates generally plummet rapidly which greatly hampers its exploration and development activities. In fact, the average recovery efficiency of shale gas can be surprisingly low, less than 10% even, with the horizontal and hydraulic fracturing methods implemented [53]. As one of the most promising enhanced gas recovery (EGR) methods, $CO_2$ injection has been proven to be an effective method to drive up shale gas production rate and enhance its recovery [52]. On the other hand, considering abundant storage capacity and the readily-available underground as well as surface infrastructure, $CO_2$ injection into shale gas reservoirs can be a viable option to alleviate carbon emissions through geological $CO_2$ sequestrations [54, 55]. The $CO_2$ 'huff-n-puff' is one of the most widely used $CO_2$-EGR methods in shale gas exploitation [52, 56-58], which can be generally separated into $CO_2$ injection ('huff'), well shut-in ('soak'), and production ('puff') periods [59, 60]. There have been a few experiments that implemented the $CO_2$ 'huff-n-puff' process to investigate its effect on shale gas recovery [61-64], in which the powdered shale samples are always chosen as the object. Researchers found that the

desorption efficiency of adsorbed methane is enhanced by $CO_2$ injection, *i.e.*, the $CO_2$ 'huff-n-puff' process can increase the gas recovery for shale gas reservoirs. Apart from the experiments, molecular simulations and other theoretical modeling have also been applied to study the $CO_2$ 'huff-n-puff' performance in shale gas recovery and geological $CO_2$ sequestration from molecular perspectives [5, 65-74]. Though different modelling/simulations are used to study the performance of $CO_2$ 'huff-n-puff' process, these researchers found that $CO_2$ injection can enhance methane recovery to different degrees. Although these numerical modelling studies are helpful to understand the effect of $CO_2$ injection on shale gas recovery and geological $CO_2$ sequestration, the underlying mechanisms governing these phenomena occurring in nanosized pores, like the composition change, the interplay between bulk and nanopores, mixtures competitive adsorption/desorption during $CO_2$ injection/sequestration, *etc.*, are largely ambiguous. For these molecular simulations, while they studied $CO_2$-EGR and $CO_2$ sequestration from molecular perspectives, they generally assume that the bulk phase volume is much larger than that of nanopores so that the fluid injection into and release from the nanopores do not alter the fluid compositions in bulk. However, as we mentioned above, the pore volume in nanopores can be comparable to that of macropores/fractures in shale reservoirs [8, 75]. Due to the comparable pore volume, adsorbed/released fluids in/from nanopores could influence bulk fluid properties, which in turn could further affect fluid density distributions in nanopores through chemical equilibrium [70, 71, 76, 77]. Therefore, the volume partitioning among nanopores and macropores/fractures (bulk) can play an important role in fluid properties and phase behaviors [48, 78-81]. Recently, a few works incorporated such a nanopore–bulk multiscale system to study the properties of pure and hydrocarbon mixtures [48, 78, 80-84]. They generally show that hydrocarbon mixture phase behaviors in the nanopore–bulk multiscale system are different from those in the systems with infinitely large bulk reservoirs. However, to the best of our knowledge, the effect of volume partitioning on $CO_2$-EGR and $CO_2$ sequestration during the $CO_2$ 'huff-n-puff' process has not been revealed yet.

Additionally, the surface area of kerogen is another important parameter for gas adsorption and recovery in shale reservoirs. Due to extensive nanoscale pores, the surface area can be exceptionally high in kerogen so an accurate surface area is indispensable for

methane ($CH_4$) adsorption estimation in shale nanoporous media. To measure the surface area, low-pressure gas adsorption isotherms coupled with the Brunauer–Emmett–Teller (BET) theory have been widely used to characterize the surface area of various porous media, including activated carbon [85], metal organic frameworks (MOFs) [86-88], silica [89-91], zeolite [92], and shale samples/isolated kerogens, [93, 94] *etc*. However, the BET theory might not be suitable for gas adsorption in the kerogen system. The BET theory assumes that the multilayer adsorption of ideal gas takes place on a perfectly-smooth ideal homogeneous surface [7]. On the other hand, in contrast to the basic assumptions in BET theory, the kerogen surface may not be perfectly smooth [6] (*i.e.*, geometrical heterogeneity), and it carries energetical heterogeneity [95] with a number of heteroatoms such as N, S, and O. Thus, the applicability of the BET theory for the surface area characterization of kerogen mesopores is questionable and has not been investigated yet. There have been a number of previous studies on the effect of energetical and geometrical heterogeneity on the BET surface area ($S_{BET}$) in porous media [86, 96-104]. For example, Gómez-Gualdrón *et al.* [86], Tian and Wu [105], Gelb and Gubbins [106], and Coasne *et al.* [91] compared $S_{BET}$ in micro- and mesoporous MOFs with the $N_2$-accessible surface area (NASA). While these studies have provided important insights into the effect of energetical and geometrical heterogeneity on $S_{BET}$, a careful analysis of their effect on kerogen $S_{BET}$ is still lacking. In addition, whether $S_{BET}$ can be a good indicator for methane ($CH_4$) adsorption capacity in kerogen nanopores remains unanswered.

As a whole, this thesis investigates gas adsorption and phase behaviors in kerogen nanopores. The effect of pore size distribution and $CO_2$ injection effect on gas adsorption and recovery in kerogen are also studied. Additionally, we also investigate surface area characterizations of kerogen by gas adsorption. This thesis provides some crucially important insights into the optimization of shale gas recovery, geological $CO_2$ sequestration, $CH_4$ adsorption capacity prediction, and shale gas-in-place (GIP) estimation in kerogen nanoporous media.

### 1.2. Problem Statement

While a number of theoretical works have been devoted to investigating gas adsorption, phase behaviors, and surface area characterization of kerogen, there are still

some unsolved problems that are essential for shale gas exploration, shale GIP estimation, $CO_2$ geological sequestration, *etc*. The main issues are addressed as follows:

- A fluid confined in a nanopore behaves very differently from its bulk form as a result of strong fluid–surface interactions. To predict the phase behavior of a pure component in nanopores, various versions of the Kelvin equation and equation-of-state-with-capillary-pressure (EOS–$P_{cap}$) models have been widely used. However, there has been much debate on the validity of the classical Kelvin equation, especially in sub-10-nm pores.
- Shale has an extensive number of pores ranging from a few to hundreds of nanometers, in which hydrocarbons behave very differently from the bulk, and surface adsorption becomes significant due to the strong fluid–surface interactions. In the past, a number of works using molecular simulations and theoretical calculations have been applied to study the properties and phase behaviors of nanoconfined hydrocarbons mainly based on a single-pore model, while ignoring pore size distribution (PSD), *i.e.*, the volume partitioning in various pores. Thus, the effect of PSD on gas adsorption and recovery in kerogen is unclear.
- Plentiful nanopores result in ultra-low permeability and porosity, causing difficulties in gas production. As an enhanced gas recovery (EGR) method, $CO_2$ injection has been proven to be an effective method to drive up shale gas production. The $CO_2$ injection effect coupled with the PSD effect on kerogen gas adsorption is unknown.
- Kerogen, as the main constituent of shale organic matters, has exceptionally high surface areas due to extensive nanoscale pores. The Brunauer–Emmett–Teller (BET) method has been extensively used to characterize the surface area of various porous materials. It assumes that the multilayer adsorption of ideal gas takes place on a perfectly-smooth ideal homogeneous surface, while the kerogen surface may not be perfectly smooth (*i.e.*, geometrical heterogeneity), and it carries energetical heterogeneity with a number of heteroatoms such as N, S, and O. Thus, its applicability for the surface area characterization of kerogen mesopores has not been investigated yet.

## 1.3. Objectives

The objectives of this thesis can be divided into two parts: I) gas adsorption and phase behaviors in shale organic nanoporous media; II) surface area characterization of shale organic media. The detailed objectives are listed below.

I. Gas adsorption and phase behaviors in shale organic nanoporous media:

- To investigate pure hydrocarbon adsorption and phase behaviors in shale organic nanopores by using a single-pore model and the validity of the Kelvin equation and the EOS–$P_{cap}$ method in kerogen small nanopores.
- To investigate the effect of PSD/volume partitioning on gas adsorption and recovery by using a multi-scale bulk–nanopore model.
- To investigate the effect of $CO_2$ injection coupled with the PSD effect on gas adsorption, gas recovery, and $CO_2$ geological sequestration by using a multi-scale bulk–nanopore model.

II. Surface area characterization of shale organic media:

- To investigate the effect of geometrical and energetical heterogeneity on $N_2$ adsorption isotherms and the subsequent BET surface area ( $S_{BET}$ ) characterization. To investigate the applicability of the BET method for the surface area characterization of kerogen mesopores. To investigate the correlation between $S_{BET}$ and methane adsorption.

## 1.4. Thesis Scope

The focus of this thesis is on investigating the mechanisms of hydrocarbons in shale organic nanoporous media (kerogen) and surface area characterization of kerogen that can predict the gas adsorption, phase behaviors, and gas recovery. This thesis provides some crucially important insights into the optimization of shale gas recovery, geological $CO_2$ sequestration, $CH_4$ adsorption capacity prediction, and shale GIP estimation in kerogen media. It is divided into two parts.

Part I investigates the mechanisms of gas adsorption and its phase behaviors in shale organic nanoporous media, including three chapters (*i.e.*, CHAPTER 2, CHAPTER 3, and CHAPTER 4). CHAPTER 2 outlines a single-pore model to predict gas adsorption and phase behaviors of confined hydrocarbon pure component in organic nanopores. The

engineering density functional theory (DFT) is applied to predict gas adsorption and phase behavior of propane in nanopores. The validity of some traditional methods (*i.e.*, various versions of the Kelvin equation and equation-of-state-with-capillary-pressure models) for pure hydrocarbon phase behaviors in nanopores with various pore sizes has been investigated. A simple graphical method is introduced to study the vapor–liquid equilibrium by using bulk pressure–volume, chemical-potential–density, and chemical potential–pressure relations. CHAPTER 3 extended the single-pore model to a multiscale nanopore–bulk model to investigate the pore size distribution (PSD)/volume partitioning effect on gas adsorption by the engineering DFT. The constant volume depletion (CVD) method is intended to simulate the hydrocarbon recovery from the nanopores in the shale matrix through the natural and hydraulic fractures. We can explicitly calculate density distributions and average densities of fluids in nanopores and the bulk region at given pressure conditions and provide important insights into the effect of PSD on shale gas recovery. CHAPTER 4 proposes the $CO_2$ injection effect coupled with the PSD effect on shale gas and its recovery. The $CO_2$ injection effect is studied by the $CO_2$ 'huff-n-puff' process with a CVD setting in nanopore–bulk multiscale models. Part I of this thesis thus provides some insights into the mechanisms of shale gas adsorption, phase behaviors, its exploitations, and geological $CO_2$ sequestrations in kerogen nanoporous media.

Part II investigates the surface area characterizations of shale organic nanoporous media, including CHAPTER 5. In CHAPTER 5, the effect of geometrical and energetical heterogeneity on $N_2$ adsorption isotherms and the subsequent BET surface area characterization is studied by gas adsorption using grand canonical Monte Carlo (GCMC) simulations. Additionally, the applicability of the Brunauer–Emmett–Teller (BET) method of kerogen surface area characterization is investigated. Part II of this thesis thus provides surface area characterization methods for kerogen and its important application on methane adsorption in shale organic nanopores.

The last chapter of this thesis, CHAPTER 6, highlights the main outcomes of this work.

公式章 (下一章) 节 1

## CHAPTER 2 Validity of the Kelvin Equation and the Equation-of-State-with-Capillary-Pressure Model for the Phase Behavior of a Pure Component under Nanoconfinement

(A version of this chapter has been published in Chemical Engineering Science 226 (2020) 115839 by Yingnan Wang, Nadia Shardt, Chang Lu, Huazhou Li, Janet A.W. Elliott, and Zhehui Jin)

**Abstract**

A fluid confined in a nanopore behaves very differently from its bulk form as a result of strong fluid–surface interactions. To predict the phase behavior of a pure component in nanopores, various versions of the Kelvin equation and equation-of-state-with-capillary-pressure (EOS–$P_{cap}$) models have been widely used. There has been much debate on the validity of the classical Kelvin equation, especially in sub-10-nm pores. Within the framework of the EOS–$P_{cap}$ models, numerical iterations have been widely used to obtain the vapor–liquid equilibrium (VLE). Herein, we summarize the controversies surrounding the validity of the Kelvin equation. In slit pores with widths larger than 8 nm, we find that the Kelvin equation agrees with (within 10%) the equilibrium vapor-phase pressures of nano-confined propane as calculated by engineering density functional theory for temperatures between 310 K and 360 K. In addition, we introduce a simple graphical method using bulk pressure–volume, chemical-potential–density, and chemical potential–pressure relations to obtain the VLE using the EOS–$P_{cap}$ model. While the classical Kelvin equation takes only surface tension as an input and returns a solution for VLE up until the surface tension vanishes at the bulk CP, the EOS–$P_{cap}$ model predicts a limiting temperature that is different from the bulk critical (CP). The predictions from the Kelvin equations and EOS–$P_{cap}$ models can be improved by considering adsorption layer thickness.

## 2.1. Introduction

Fluids confined in nanopores have attracted extensive interest among scientists and engineers, owing to their broad applications in unconventional oil/gas production [107], fuel cells [108], heterogeneous catalysts [109], adsorption [16], drying processes [110, 111], water purification [112], and climate engineering [113-115]. Due to strong fluid–pore wall interactions, fluid density distributions are inhomogeneous in nanopores and fluid behavior is very different from the bulk [14, 116, 117]. It is well known from experimental and modeling studies that fluids confined in nanopores can undergo capillary condensation or evaporation at different vapor-phase pressures than the bulk-phase saturation pressure [15, 23, 118]. In addition, nanoconfinement can induce a limiting point where vapor–liquid equilibrium (VLE) vanishes, and this limiting point is shifted from the critical point of the bulk phase. As a result, the properties of fluids confined in nanopores cannot be simply predicted by the conventional equation of state (EOS) modeling [23, 25].

To predict the phase behavior of a pure component in a nanopore, the capillary pressure difference between liquid and vapor phases, $P_{cap}$, arising from the highly curved liquid–vapor interfaces must be combined with the equality of liquid and vapor chemical potentials for phase equilibrium. Assuming that the vapor phase behaves as an ideal gas and the liquid phase is incompressible, one can derive the Kelvin equation [13]. On the other hand, using an EOS [119] to describe the vapor and liquid phases, one can obtain an EOS–$P_{cap}$ model [120]. Neither the Kelvin equation nor the EOS–$P_{cap}$ models account for fluid distribution inhomogeneity [14] in nanopores due to fluid–surface interactions.

The complete Kelvin equation [25] (CKE) has been widely used to predict the vapor-phase pressure $P^V$ of a pure component at a given temperature $T$ in a nanopore down to a few nanometers,

$$RT\ln\left(\frac{P^V}{P_0}\right) = -\frac{2\gamma V_m^L}{r_m} + V_m^L\left(P^V - P_0\right) \tag{2-1}$$

where $P_0$ is the bulk saturation pressure; $\gamma$ is the bulk vapor–liquid interfacial tension (IFT) at $T$; $V_m^L$ is the bulk liquid molar volume at $T$ and $P_0$; $R$ is the universal gas

constant; and $r_m$ is the radius of the mean curvature, *i.e.*, $\frac{1}{r_m}=\frac{1}{2}\left(\frac{1}{r_1}+\frac{1}{r_2}\right)$, where $r_1$ and $r_2$ are the principal radii of curvature. The radius of mean curvature $r_m$ has various relationships with different geometries and phase transition types as listed in **Appendix A.1**.

The second term on the right-hand side of Eq. (2-1) is often considered to be negligible compared to the first term [121], *i.e.*,

$$\frac{2\gamma}{r_m} >> P_0 - P^V . \tag{2-2}$$

Thus, the simplified Kelvin equation (SKE) is given as [17, 21, 121-124],

$$RT\ln\left(\frac{P^V}{P_0}\right)=-\frac{2\gamma V_m^L}{r_m} . \tag{2-3}$$

While these Kelvin equations can accurately predict fluid condensation and evaporation pressures in sub-100-nm pores [24, 25, 125-127], there has been much debate on their validity in sub-10-nm pores [23] as depicted in **Figure 2-1 (a).** The data points in **Figure 2-1 (a)** show deviations between the vapor-phase pressures from the Kelvin equations and those from experimental/modeling studies, given as:

$$\Delta P^V\,\% = \frac{P_{Kel}^V - P_{\exp/\mathrm{mod}}^V}{P_{Kel}^V}, \tag{2-4}$$

in which $P_{Kel}^V$ and $P_{\exp/\mathrm{mod}}^V$ are the vapor-phase pressures from the Kelvin equations and experimental/molecular modeling studies, respectively. (The literature references for **Figure 2-1** are listed in **Appendix A.2**). In most of the research summarized in **Figure 2-1 (a)**, the contact angles of the fluids on the substrates are either measured [15, 23, 125] or assumed [15-22, 24, 25, 118, 126-129] to be zero in the Kelvin equations and experiments, simulations, and theoretical calculations, while in a few studies the contact angle was assumed to be a small finite value [126, 128, 130] (details given in **Table A-2 (c)**). A lack of rigorous determination of the correct contact angles might be responsible for some of the discrepancies shown in **Figure 2-1 (a)**.

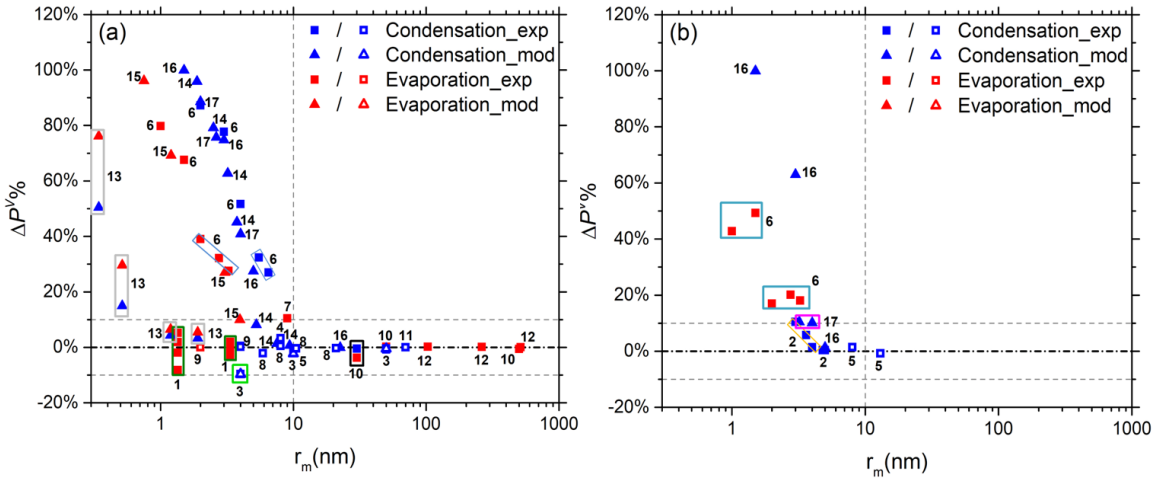


**Figure 2-1** The relative deviations of measured or modeled vapor-phase pressures from the Kelvin equations, $\Delta P\%$. Panel (a) depicts $\Delta P\%$ of the Kelvin equations without taking into account an adsorption layer thickness; Panel (b) represents $\Delta P\%$ of the Kelvin equations where adsorption layer thickness was taken into account. Filled and open symbols represent the deviations from the SKE and CKE, respectively; blue and red symbols depict the deviations of condensation and evaporation pressures from Kelvin equations, respectively; squares and triangles represent experimental and modeling studies, respectively. These data points are numbered to indicate their sources, and the numbering can be found in **Table A-2**. Data points in the same colored boxes are from the same source. The vertical dashed line indicates $r_m$ = 10 nm below which controversy about the validity of Kelvin equations arises. The horizontal dashed lines represent $\left|\Delta P^{V}\%\right| < 10\%$.

In terms of capillary evaporation in sub-10-nm pores, most studies claimed that the Kelvin equations largely overestimate evaporation pressure [15-17]. For example, by using nanofluidic devices, Jatukaran *et al.* [15] directly observed propane evaporation in 9-nm-deep two-dimensional silica nanochannels and found that evaporation takes place at pressures significantly lower than the predictions from the SKE. By using non-local density functional theory (NLDFT), Ravikovitch *et al.* [16] compared nitrogen capillary evaporation pressures in open cylindrical pores of diameters between 1 and 8 nm with those from the Kelvin equation and found that the SKE predicts much higher evaporation pressures.

Disagreement also exists in capillary condensation predictions. A number of studies [17-20] claimed that the SKE becomes invalid in sub-10-nm pores and as pore size decreases, the deviation becomes more significant. For example, Walton *et al.* [19] used NLDFT and grand canonical Monte Carlo (GCMC) simulations to study the nitrogen adsorption isotherm in 5- to 10-nm graphitic slit pores. They found that the SKE

predictions of condensation pressure had large deviations from the GCMC simulation results when the pore width was less than 7 nm.

On the other hand, several studies otherwise indicated the validity of the SKE and CKE in sub-10-nm pores [21-25]. Zhong *et al.* [23] studied the condensation of propane in a nanofluidic system. They reported that the measured propane condensation pressures in 8-nm silica nanochannels agree excellently with the CKE predictions. Shardt and Elliott [118] used an activity-coefficient-with-capillary-pressure model to predict vapor–liquid phase diagrams of nitrogen/argon mixtures in 4-nm (diameter) cylindrical pores and compared their predictions to measurements by Alam *et al.* [131]. For pure nitrogen or argon, Shardt and Elliott's model reduces to the CKE. They considered the liquid–vapor curvature difference between adsorption and desorption in cylindrical pores and found that the CKE is valid in 4-nm (diameter) cylindrical pores for condensation of pure nitrogen and both condensation and evaporation of pure argon. Factorovich *et al.* [132] studied the vapor-phase pressures of water nanodroplets (evaporation) by using grand canonical molecular dynamics (GCMD) simulation. They claimed that the SKE can accurately predict the evaporation vapor–phase pressures for water droplets with diameters as small as 1.2 nm. It should be noted that, for nanodroplets, there is no fluid interaction with a substrate that may be the source of some discrepancies with the Kelvin equation in the other studies.

To better describe confined fluid properties, a few studies considered adsorption film thickness in the Kelvin equations as shown in **Figure 2-1 (b)** (the literature references for **Figure 2-1** are listed in **Appendix A.2**). The effective pore radii for Kelvin equations are adjusted according to the adsorption film thickness, which could be a constant or determined by experimental or simulated adsorption isotherms. The Barrett–Joyner–Halenda (BJH) method [133] involves introducing adsorption layer thickness into the Kelvin equations by fitting a statistical thickness equation to the measured nitrogen adsorption data. Broekhoff *et al.* [134, 135] modified the Kelvin equation by adding a function of adsorption thickness and pressure, which was fitted to experimental adsorption data. Compared with predictions from the Kelvin equations without correction as depicted in **Figure 2-1 (a)**, considering adsorption layer thickness significantly improves the performance of the Kelvin equations, predicting vapor-phase pressures

accurately ( $\left|\Delta P^{V}\,\%\right| < 10\ \%$ ) down to a 5-nm mean radius. Note that all data points shown in **Figure 2-1 (b)** are predictions from the SKE or CKE considering adsorption layer thickness. Kruk *et al.* [17] studied nitrogen adsorption/desorption using a siliceous molecular sieve nanochip with parallel cylindrical pores of diameters ranging from 2 to 7 nm. They compared their experimental results with predictions from the SKE for both adsorption and desorption. They also investigated the SKE with adsorption layer thickness. While the SKE predictions for both condensation and evaporation pressures show large deviations compared to experimental results, those considering an adsorption layer have much better agreement with experiments. Miyahara *et al.* [18] proposed a model by considering pore-wall potential and curvature-dependent surface tension in the SKE. They compared the condensation pressures in 2- to 4-nm silicate-like cylindrical pores from molecular dynamics (MD) simulations with those from their model and the SKE. They reported that the predictions from the SKE of the nitrogen condensation pressure are much higher than those from MD simulations, while their proposed model has an excellent agreement with MD simulations.

In contrast to the Kelvin equations which treat the vapor phase as an ideal gas and the liquid phase as an incompressible fluid, several extended equation-of-state (EOS) methods have been developed to describe the phase behavior of fluid in a nanopore. For example, an EOS with shifted critical parameters model [29, 43] is widely used to describe confined fluid properties and phase behaviors. Recently, scaled particle theory has been extended to study the properties and phase behaviors of confined Lennard Jones and square-well fluids [136-138]. Another popular method is using a cubic EOS to describe vapor- and liquid-phase properties combined with capillary pressure (EOS–$P_{cap}$) [26-31]. Melrose [119] introduced several corrections into the Kelvin equation, treating the vapor as a non-ideal gas, and treating the liquid as a compressible liquid. While some authors use the term "Kelvin equation" to include these advanced models, in this paper we use the term "Kelvin equation" to apply strictly to the SKE and CKE which assume ideal gas and incompressible liquid, and use the term "EOS–$P_{cap}$ model" when a cubic equation of state is used for fluid properties. Various EOS–$P_{cap}$ models [15, 30-34] have been widely used to obtain the properties of hydrocarbon mixtures in nanopores for shale oil recovery and have been implemented in reservoir simulators [34] to predict the well productivity and

ultimate recovery. Successive substitutions and numerical iterations are generally used to obtain the vapor–liquid equilibria (VLE) by satisfying the chemical and mechanical equilibrium [33]. To take into account surface adsorption, a few studies have incorporated adsorption layer thickness into the EOS–$P_{cap}$ model [32, 35, 36]. Similar to the Kelvin equations, because IFT vanishes at the bulk CP, the critical point of confined fluids using EOS–$P_{cap}$ models is generally predicted to be unshifted [29, 31, 33]. Tan *et al.* [139] claimed that the "critical" temperature in nanopores is lower than the bulk CP by using the EOS–$P_{cap}$ model with numerical iteration, while they did not unravel the cause. On the other hand, the existence of a hysteresis critical point (HCP) [37] under nanoconfinement, which is different from the bulk CP has been well documented from experiments, molecular modeling, and simulation studies [37, 38].

In this paper, we first summarize the controversies surrounding the validity of the Kelvin equations for fluids in nanopores. We evaluate the applicability of the CKE and the SKE for propane in carbon slit nanopores by comparing condensation/evaporation pressures [15, 23] from the Kelvin equations to those predicted by engineering density functional theory (engineering DFT) [140]. The validity of the CKE-with-adsorption-film (CKE–A) model is also tested. Engineering DFT has been widely used to predict the properties of pure hydrocarbons and their mixtures under nanoconfinement, showing excellent agreement with experiments [15] and molecular simulations [39]. In this work, within the framework of the EOS–$P_{cap}$ model, we introduce a graphical method to illustrate the underlying physics of vapor–liquid equilibrium with the same predictions as using numerical iterations. The pressure–volume ($P$–$V$), pressure–density ($P$–$\rho$), and chemical-potential–density ($\mu$–$\rho$) relations from the Peng–Robinson EOS (PR–EOS) [141] combined with capillary pressure are used to obtain the chemical and mechanical equilibrium between vapor and liquid phases. We deduce the vapor-phase properties from the bulk stable vapor-phase branch, while those of the liquid phase is obtained from the bulk metastable liquid-phase branch. By using such a graphical approach, we find that there exists a limiting temperature for a pure component in a nanopore, above which vapor–liquid coexistence cannot occur. In addition, we also compare the performance of the PR–EOS with the capillary pressure (PR–$P_{cap}$) model without considering adsorption layer thickness to the performance of the PR–$P_{cap}$ model corrected for adsorption layer

thickness (PR–$P_{cap}$–A). By doing so, we illustrate the effect of considering adsorption layer thickness on the predictions of the EOS–$P_{cap}$ model.

The remainder of this chapter is organized as follows. In **Section 2**, we present the governing equations and graphical methods for the CKE, the SKE, the PR–$P_{cap}$ model, engineering DFT, and adsorption layer thickness for use in the CKE–A and PR–$P_{cap}$–A models. In **Section 3**, we first compare vapor-phase pressures at VLE in nanopores from various approaches with engineering DFT. We observe the limiting points from PR–$P_{cap}$ and PR–$P_{cap}$–A models and use graphical methods to explain the underlying mechanism. In **Section 4**, we summarize the key findings and conclusions.

## 2.2. Governing Equations and Methodology

### 2.2.1. The Complete Kelvin Equation (CKE)

The Kelvin equation is based on macroscopic thermodynamics for the vapor and liquid phase equilibrium, assuming that the vapor phase behaves as an ideal gas and the liquid phase is incompressible. Within the framework of the Kelvin equation, the strong fluid–surface interactions within nanopores are not taken into account directly, but rather indirectly by the capillary pressure, which is the pressure difference between vapor and liquid phases. The Young–Laplace (YL) equation is used to account for capillary pressure $P_{cap}$. For a slit pore, the YL equation has the following form [142]

$$P^V - P^L = P_{cap} = \frac{2\gamma\cos\theta}{W}, \tag{2-5}$$

where $P^V$ and $P^L$ are the pressures of the vapor and liquid phases, respectively, $\gamma$ is the bulk vapor–liquid IFT at the given temperature $T$, $\theta$ is the contact angle measured through the liquid, and $W$ is the slit pore width. In this paper, all IFTs used are from the NIST Chemistry WebBook. Assuming that the liquid phase completely wets the surface, $\theta$ = 0°. For VLE in slit nanopores, vapor and liquid phases reach both chemical and mechanical equilibrium at the given temperature $T$ [119, 143],

$$\mu^V\left(T, P^V\right) = \mu^L\left(T, P^L\right), \tag{2-6}$$

$$P^V - P^L = \frac{2\gamma}{W}, \tag{2-7}$$

in which $\mu^V$ and $\mu^L$ are pure component vapor- and liquid-phase chemical potentials, respectively. Assuming that the vapor phase behaves as an ideal gas and that the liquid phase which can exist below the bulk saturation pressure $P_0$ is incompressible, the chemical potentials of vapor and liquid phases can be expressed as,

$$\mu^V\left(T,P^V\right)=\mu^V\left(T,P_0\right)+RT\ln\left(\frac{P^V}{P_0}\right), \tag{2-8}$$

$$\mu^L\left(T,P^L\right)=\mu^L\left(T,P_0\right)+V_m^L\left(P^L-P_0\right). \tag{2-9}$$

where $V_m^L$ is the bulk liquid molar volume at $T$ and $P_0$; $R$ is the universal gas constant. Combining Eqs. (2-6) – (2-9),

$$RT\ln\left(\frac{P^V}{P_0}\right)=V_m^L\left(P^L-P_0\right). \tag{2-10}$$

Substituting Eq. (2-7) into Eq. (2-10) yields the CKE equation [13, 25, 119, 144],

$$RT\ln\left(\frac{P^V}{P_0}\right)=-\frac{2\gamma V_m^L}{W}+V_m^L\left(P^V-P_0\right). \tag{2-11}$$

### 2.2.2. The Simplified Kelvin Equation (SKE)

In Eq. (2-11), the capillary pressure is often considered to be much larger than the difference between the vapor-phase pressure and bulk saturation pressure [13], *i.e.*,

$$\frac{2\gamma}{W}>>P_0-P^V. \tag{2-12}$$

Then, Eq. (2-11) can be simplified to the SKE [122, 145],

$$RT\ln\left(\frac{P^V}{P_0}\right)=-\frac{2\gamma V_m^L}{W}. \tag{2-13}$$

### 2.2.3. Peng–Robinson Equation of State with Capillary Pressure (PR–Pcap) Model

Unlike the Kelvin equations, the PR–$P_{cap}$ model uses the PR–EOS which is a van der Waals type EOS to describe the liquid and vapor phases. The capillary pressure in the PR–$P_{cap}$ model comes from the YL equation as shown in Eq. (2-5). Again, for VLE, the chemical potentials of each phase are equal at the given $T$, *i.e.*,

$$\mu^V\left(T,P^V\right)=\mu^L\left(T,P^L\right), \tag{2-14}$$

where $P^V - P^L = P_{cap} = \frac{2\gamma}{W}$. $\mu^V$ and $\mu^L$ can be obtained from the PR–EOS [141] (see **Appendix A.3**).

While previous works applied successive substitutions and numerical iterations to obtain the VLE by solving Eq. (2-14) [29, 31, 33], in this work, we illustrate the underlying physics of VLE by introducing a graphical method. The bulk *P*–*V* isotherm, *P*–*ρ*, and *μ*–*ρ* relations from the PR–EOS [141] at the given *T* are shown in **Figure 2-2**. Here, we describe how to obtain the chemical and mechanical equilibrium between vapor and liquid phases (PR–EOS parameters are provided in **Appendix A.4**). On the *P*–*V* and *P*–*ρ* curves, **Point A** represents the liquid phase at $P > P_0$ and **Point G** represents the vapor phase at $P < P_0$. **Points B** and **E** depict the bulk saturation points, respectively; **Points C** and **D** indicate the mechanical stability limits of superheated liquid and supersaturated vapor phases, respectively. At $P_0$, bulk vapor and liquid phases have equal pressures and chemical potentials (*i.e.*, the intersection between **Lines AC** and **DG**) as shown in **Figure 2-3 (a)**.

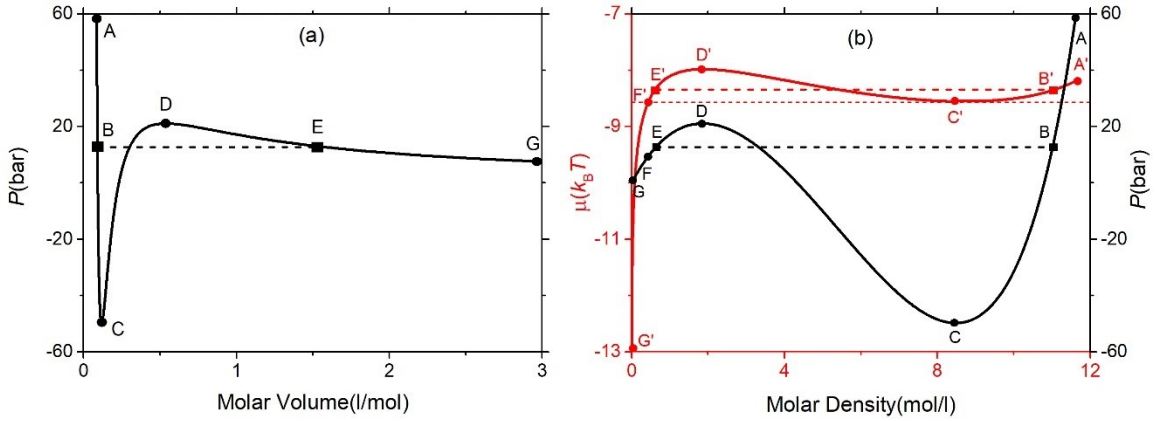


**Figure 2-2** (a) *P*–*V*; (b) *P*–*ρ* and *μ*–*ρ* relations for propane at *T* = 310 K from the PR–EOS. In the *P*–*V* and *P*–*ρ* diagrams, **Point A** represents the liquid phase at a pressure higher than $P_0$; **Point G** represents the vapor phase at a pressure lower than $P_0$. **Points B** and **E** depict the bulk saturation points; **Points C** and **D** depict the mechanical stability limits of superheated liquid and supersaturated vapor phases, respectively; **Points A'** to **G'** are the corresponding points from **A** to **G** in the *μ*–*ρ* diagram. **Point F'** represents the lower limit of chemical potential based on the chemical potential equality given in Eq. (2-14) and **Point F** is the corresponding point on the *P*–*ρ* curve at the same molar density.

Under nanoconfinement, due to liquid wetting the solid surfaces, the liquid–vapor interface is curved toward the vapor and, due to the liquid–vapor interfacial tension, the

liquid has a lower pressure than the vapor. We deduce the vapor-phase properties from the stable vapor-phase branch (**Line EG**), while those of the liquid phase is obtained from the bulk metastable liquid-phase branch (**Line BC**). Therefore, the chemical potential ranges of the metastable liquid phase and the stable vapor phase are **B'C'** and **E'G'**, respectively, as shown in **Figure 2-2 (b)**. To ensure chemical potential equality between vapor and liquid phases, the lower limit of vapor-phase pressure is dictated by **Point F'** on the $\mu$–$\rho$ curve and **Point F** on the $P$–$\rho$ curve in **Figure 2-2 (b)**. VLE under confinement can be obtained by shifting the liquid-phase $\mu - P$ curve to the right-hand side by a distance of $P_{cap}$ as shown in **Figure 2-3 (b)**. Then, the new intersection dictates the pressures under confinement, $P_0^*$, the vapor-phase pressure when read from the bottom axis in **Figure 2-3 (b),** and the liquid phase pressure when read from the top axis of **Figure 2-3 (b)**.

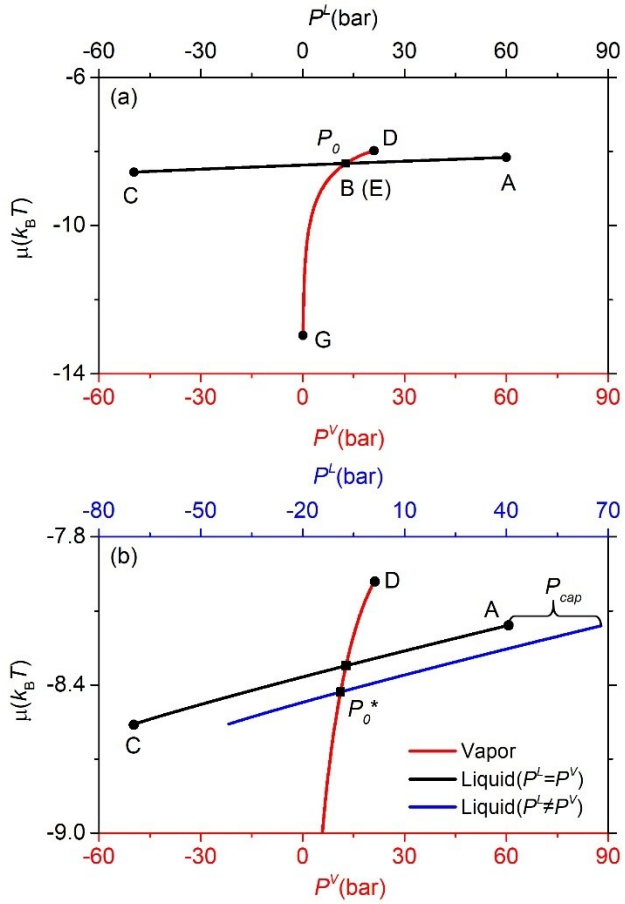


**Figure 2-3** Illustration of chemical potential equality between vapor and liquid phases for (a) bulk propane and (b) propane in a confined space at $T$ = 310 K. Red and black lines

represent bulk vapor and liquid phase $\mu$–$P$ relations, respectively; the blue line represents the confined liquid phase $\mu$–$P$ relation. **Points A, B (E), C, D,** and **G** correspond to the points shown in **Figure 2-2**. In (a) $P_0$ represents the bulk vapor–liquid equilibrium pressure which is the same for the vapor and liquid phases as shown by alignment of the bottom and top axes. In (b) $P_0^*$ represents the confined equilibrium pressures, to be read from the bottom axis for vapor-phase pressure and from the top axis for liquid pressure.

### 2.2.4. Engineering Density Functional (DFT) Theory

Based on the heterogeneous molecular distributions in nanopores, engineering DFT constructs the grand potential $\Omega\left[\rho(\mathbf{r})\right]$ in an open system, which is the functional of density distribution $\rho(\mathbf{r})$. The grand potential functional $\Omega\left[\rho(\mathbf{r})\right]$ of the system is the thermodynamic function of choice and is related to the Helmholtz free energy functional $F\left[\rho(\mathbf{r})\right]$ via the Euler–Lagrange transformation [146],

$$\Omega\left[\rho(\mathbf{r})\right] = F\left[\rho(\mathbf{r})\right] + \int \rho(\mathbf{r})\left[\Psi(\mathbf{r}) - \mu\right] d\mathbf{r}, \tag{2-15}$$

where $d\mathbf{r}$ is differential volume, and $\rho(\mathbf{r})$ is the number density distribution at position $\mathbf{r}$; $\Psi(\mathbf{r})$ is the solid surface external potential at the position $\mathbf{r}$; and $\mu$ is the bulk chemical potential [147].

The Helmholtz free energy $F\left[\rho(\mathbf{r})\right]$ is further decomposed into two parts: an ideal gas term $F^{id}\left[\rho(\mathbf{r})\right]$ and the excess term arising from the intermolecular interactions $F^{ex}\left[\rho(\mathbf{r})\right]$,

$$F\left[\rho(\mathbf{r})\right] = F^{id}\left[\rho(\mathbf{r})\right] + F^{ex}\left[\rho(\mathbf{r})\right], \tag{2-16}$$

where the $F^{id}\left[\rho(\mathbf{r})\right]$ term is known exactly. The $F^{ex}\left[\rho(\mathbf{r})\right]$ term consists of two parts: one part is obtained by extending the PR–EOS with a weighted density approximation (WDA) [148] to inhomogeneous conditions to account for the physical interactions; the other part accounts for the long-range intermolecular attractions by using a quadratic density expansion (QDE) [149, 150]. (see **Appendix A.5**)

At equilibrium, the grand potential functional reaches a minimum [140]. Therefore, the equilibrium density distributions of species can be obtained by minimization of the grand potential functional [151],

$$\rho(\mathbf{r}) = \exp\left[\beta\mu - \beta\Psi(\mathbf{r}) - \frac{\delta\beta F^{ex}\left[\rho(\mathbf{r})\right]}{\delta\rho(\mathbf{r})}\right], \tag{2-17}$$

where $\beta = 1/(k_B T)$, with $k_B$ and $T$ being the Boltzmann constant and absolute temperature, respectively. The density distribution in Eq. (2-17) is solved by Picard iteration [152]. In fact, under nanoconfinement, due to inhomogeneous fluid distributions and fluid–surface interactions, pressure is anisotropic and position-dependent [143]. Within the framework of DFT, we use the pressure of the bulk vapor phase which is in chemical equilibrium with the fluids under nanoconfinement to denote the pressure. On the other hand, the Kelvin equations and EOS-based methods cannot take into account such a pressure tensor in nanopores [143], but use a uniform value to describe the pressure in nanopores. The bulk density is used as the initialization to calculate density distribution at the first pressure. The initial guesses for other pressures are from the density distributions at the preceding pressures. The PR–EOS uses the critical temperature and critical pressure as input parameters, thus can reproduce the pure-component vapor pressures well [143]. On the other hand, its predictions of densities and molar volumes are relatively poor [153]. Therefore, a volume shift parameter (VSP) is often used to correct the predicted molar volume and density [153, 154], while it does not alter the saturation points. The dimensionless VSP [155] used in this work is given as,

$$\tilde{\rho}(\mathbf{r}) = \frac{\rho(\mathbf{r})}{1 + \rho(\mathbf{r})C}, \tag{2-18}$$

where $C = VSP \times b$, $b$ is the volume parameter for component $i$ from the PR–EOS, and $\tilde{\rho}(\mathbf{r})$ is the corrected equilibrium density distribution. The same VSP is also used to correct the density calculated by PR–EOS. The parameters used in engineering DFT are provided in **Table A-3** in the **SI**. More details about engineering DFT can be found in [140]

For simplicity, we simulate a carbon-slit pore that is described by two planar structureless graphite surfaces to represent nanopores in the system [140, 156, 157], which has been applied to the study of gas adsorption in shale and shown excellent agreement with GCMC simulation results and experimental data [14]. In a carbon-slit pore, the density distributions only vary in the $z$ direction perpendicular to the solid surfaces, *i.e.*,

$\tilde{\rho}(\mathbf{r}) = \tilde{\rho}(z)$. We use the 10-4-3 Steele potentials to describe the fluid–surface interactions $\varphi_{sf}$ [158],

$$\varphi_{sf}(z) = 2\pi\rho_s\varepsilon_{sf}\sigma_{sf}^2\Delta\left[\frac{2}{5}\left(\frac{\sigma_{sf}}{z}\right)^{10} - \left(\frac{\sigma_{sf}}{z}\right)^4 - \frac{\sigma_{sf}^4}{3\Delta(0.61\Delta + z)^3}\right], \tag{2-19}$$

where $z$ represents the position in the perpendicular direction relative to the pore surface; $\rho_s = 114\ \text{nm}^{-3}$ is the density of graphite and $\Delta = 0.335\ \text{nm}$ represents the interlayer spacing of graphite; $\varepsilon_{sf}$ and $\sigma_{sf}$ are potential expansion parameters and follow the simple mixing rule: $\varepsilon_{sf} = \sqrt{\varepsilon_s\varepsilon_f}$, and $\sigma_{sf} = (\sigma_s + \sigma_f)/2$. Here, we set the energy and size parameters of graphite surface to $\sigma_s = 0.3345\ \text{nm}$, $\varepsilon_s / k_B = 28\ \text{K}$ and the fluid energy $\varepsilon_f$ and size parameters $\sigma_f$ for hydrocarbon species are from the modified Buckingham exponential-6 intermolecular potentials for the $CH_3$- group, the -$CH_2$- group, and $CH_4$ as in our previous work [31]. In slit nanopores, the external potential $\Psi(\mathbf{r})$ in Eq. (2-17) is given as,

$$\Psi(z) = \varphi_{sf}(z) + \varphi_{sf}(W - z). \tag{2-20}$$

**Figure 2-4** depicts the metastable and equilibrium branches from DFT calculations. Though the phase transition hysteresis observed in capillary phenomena could also be caused by a difference in liquid–vapor interface curvature between pore filling and emptying [118] or by dynamic contact angle effects [159], the hysteresis loops calculated in our slit pore DFT calculations are closely related to the existence of metastable states [16, 160]. In slit pores, condensation (vapor to liquid transition) is hindered (compared with equilibrium) due to the existence of metastable adsorption films, while evaporation (liquid to vapor transition) is not affected by such metastability according to previous experimental data [16]. As in Ravikovitch *et al.* [16], we use the metastable condensation and the equilibrium transition points to dictate capillary condensation and evaporation in nanopores as depicted in **Figure 2-4**. In addition, as *T* increases, the hysteresis loops in nanopores shrink and eventually reach hysteresis critical points (HCP) [37] beyond which there is no hysteresis observed [161].

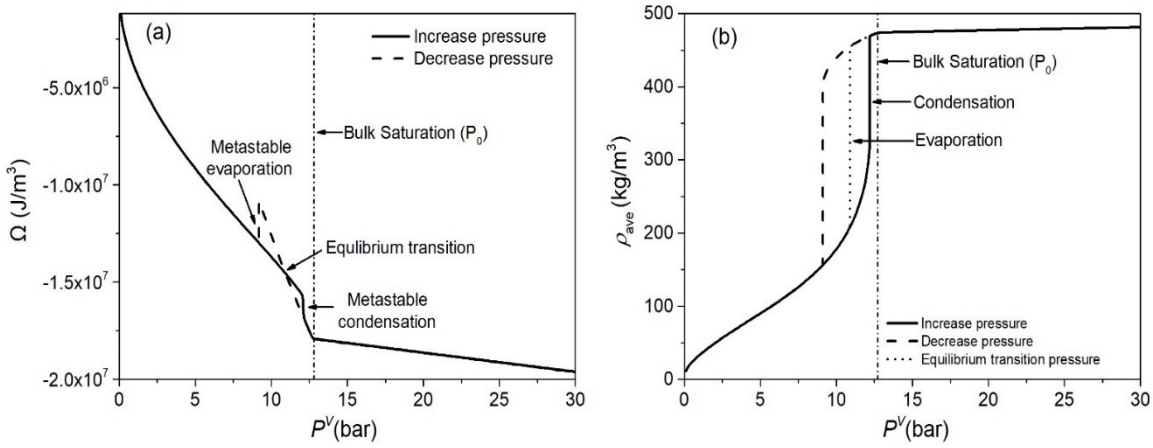


**Figure 2-4** Illustration of condensation and evaporation pressures of propane in 8-nm slit pores at $T$ = 310 K calculated using engineering density functional theory (engineering DFT). Panel (a) and (b) present minimum grand potential and average density, respectively. The solid line represents the adsorption branch, the dashed line represents the desorption branch, and the dotted line in (b) represents the equilibrium transition branch. For comparison, the bulk saturation pressure $P_0$ is shown with a dash-dotted line.

According to some previous experimental measurements [162, 163], methane always completely wets graphite surfaces, and thus the methane–graphite contact angle would be zero. Considering that propane has a stronger attraction to the surface than methane in graphite pores [79, 140], we assume that the contact angle between propane and graphite is zero for use in the Kelvin equations.

### 2.2.5. Adsorption Layer Thickness

DFT can also provide adsorption layer thicknesses for use in the CKE–A and PR–$P_{cap}$–A models. As in the Barrett–Joyner–Halenda (BJH) adsorption model [17, 133], we assume that the density of the adsorption layer is the same as the bulk liquid phase density $\rho_{b,0}^{L}$ at $P_0$. The adsorption layer thickness $L_{ads}$ can be obtained from $\rho(z)$ calculated by engineering DFT as,

$$L_{ads}(P,T,W)=\frac{\int_0^W \rho(z)-\rho_b(P,T)\,dz}{2\left[\rho_{b,0}^{L}(T)-\rho_b(P,T)\right]}, \tag{2-21}$$

where $\rho_b(P,T)$ represents the bulk density at $P$ and $T$, $\rho_{b,0}^{L}$ represents the bulk liquid density at $P_0$, and $\rho(z)$ is the equilibrium branch in engineering DFT [41]. An illustration of the adsorption layer is shown in **Figure 2-5**. As pressure increases, $L_{ads}$ from Eq.

(2-21) increases and can be larger than $W$, when propane in nanopores becomes liquid-like. Thus, we set the upper limit of $L_{ads}$ to be $W/2$. Then, the effective pore size $W_{eff}$ in the CKE–A and PR–$P_{cap}$–A models is denoted as,

$$W_{eff} = W - 2L_{ads}, \tag{2-22}$$

and $P_{cap}$ in the PR–$P_{cap}$–A model is,

$$P^V - P^L = P_{cap} = \frac{2\gamma}{W_{eff}}. \tag{2-23}$$

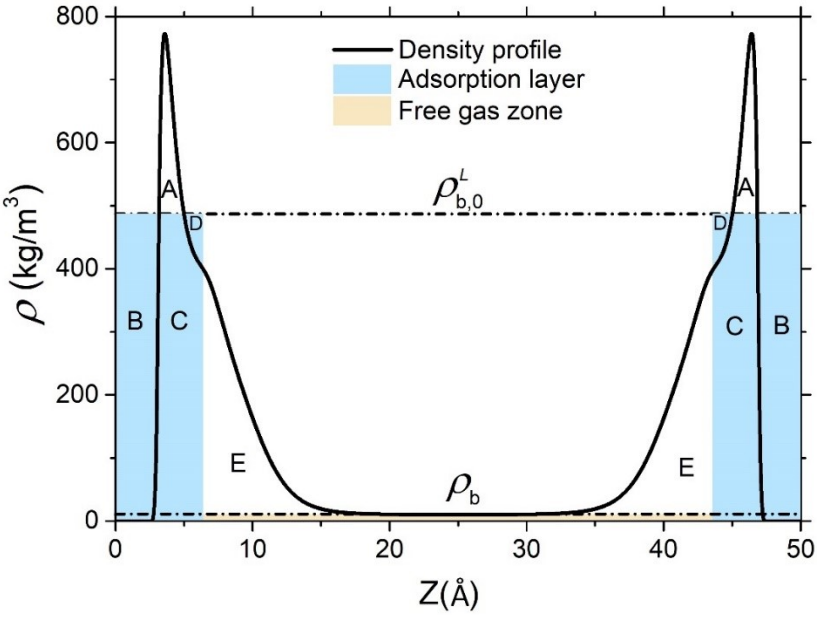


**Figure 2-5** Propane density distribution at 5 bar and 310 K in a 5-nm slit pore. The black solid line represents the density profile from engineering DFT, the light blue zone represents the adsorption layer, and the yellow zone depicts the free gas zone. The bulk density ($\rho_b$) and the bulk liquid density at $P_0$ ($\rho^L_{b,0}$) are also shown. According to Eq. (2-21), the area of Zone (A+C+E) is equal to that of Zone (B+C+D).

### 2.3. Results and Discussions

We present propane vapor-phase pressures at VLE in nanopores at various $T$ from the engineering DFT, CKE, SKE, PR–$P_{cap}$, and PR–$P_{cap}$–A models in **Figure 2-6**. The hysteresis in the DFT calculations can be seen as a difference in the vapor-phase pressures for condensation versus evaporation, while no such hysteresis exists with the thermodynamic models. In general, due to density inhomogeneity caused by fluid–surface interactions, which becomes less significant for confined fluids as $W$ increases,

propane vapor-phase pressures at VLE in nanopores approach $P_0$, and the deviations between predictions from DFT and other macroscopic thermodynamic equations become smaller. We also present nanofluidic measurements from Zhong *et al.* [23] and Jatukaran *et al.* [15], showing that engineering DFT is in excellent agreement with these experiments. In large nanopores ($W \geq 20$ nm), the confinement effect on propane vapor-phase pressures at VLE is insignificant. While various thermodynamic methods underestimate the condensation pressures, they overestimate the evaporation pressures. However, in small nanopores ($W \leq 10$ nm), both condensation and evaporation pressures are drastically reduced. The CKE, SKE, and PR–$P_{cap}$ models largely overestimate propane condensation and evaporation pressures. Note that because these thermodynamic approaches describe a state of vapor–liquid equilibrium, the comparison should be made with the evaporation pressures from the engineering DFT [16]. We present a summary of comparison results in **Table 2-1**. $\Delta P^V\%$ is defined as $\Delta P^V\% = \frac{P_{eq}^V - P_{DFT}^V}{P_{DFT}^V} \times 100\%$, where $P_{eq}^V$ is vapor-phase pressure at VLE from thermodynamic equations (*i.e.*, CKE, SKE, CKE–A, PR–$P_{cap}$, and PR–$P_{cap}$–A), $P_{DFT}^V$ represents the evaporation pressure at VLE from DFT. The deviations between these macroscopic thermodynamic approaches and engineering DFT are temperature-dependent. We also notice that the difference between the SKE and CKE predictions for propane in slit nanopores is negligible.

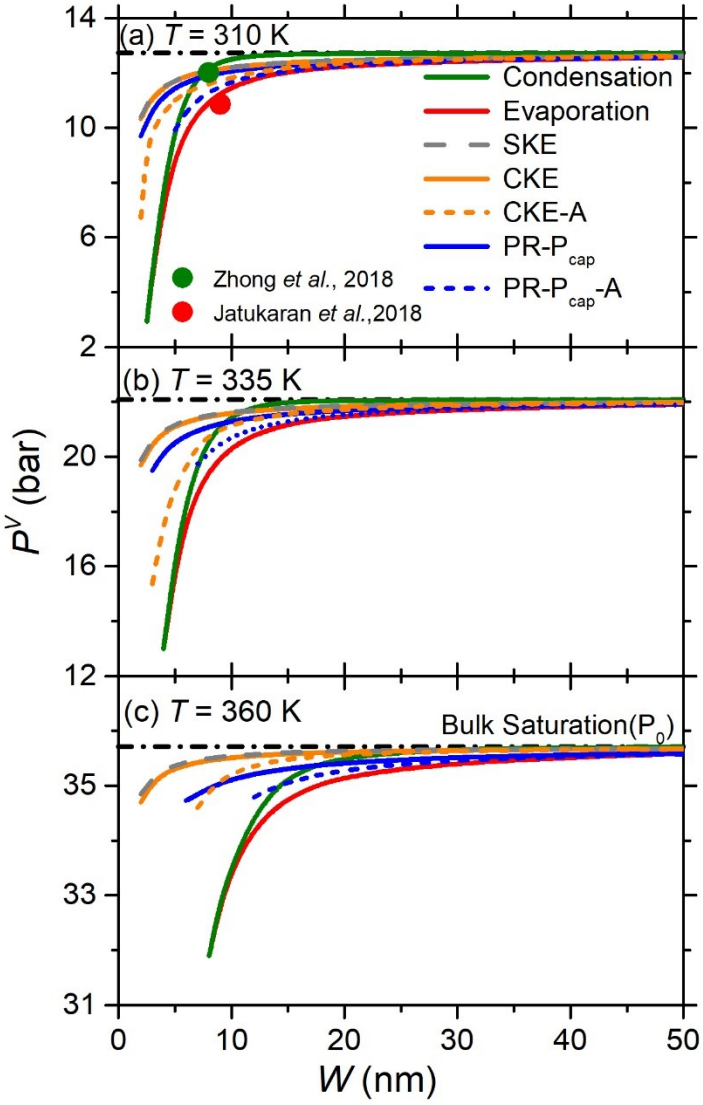


**Figure 2-6** Propane vapor-phase pressures at VLE in nanopores at (a) $T$ = 310 K; (b) $T$ = 335 K; and (c) $T$ = 360 K. Green and red solid lines represent condensation and evaporation pressures from engineering DFT, respectively. Dashed gray lines, solid orange, and short dashed orange lines represent vapor-phase pressures at VLE from SKE, CKE, and CKE–A models, respectively. Solid and dashed blue lines represent vapor-phase pressures at VLE from PR–$P_{cap}$ and PR–$P_{cap}$–A models, respectively. Green and red circles represent experimental data of condensation from Zhong *et al.* [23] and evaporation from Jatukaran *et al.* [15], respectively. For comparison, the bulk saturation pressures $P_0$ are shown with black dash-dotted lines.

**Table 2-1** The vapor-phase saturation pressure difference percentage ($\Delta P^V\% = \frac{P_{eq}^V - P_{DFT}^V}{P_{DFT}^V} \times 100\%$) in slit nanopores for different widths of various methods. Note that N/A indicates no data because of hysteresis critical points, and/or limiting points.

| | 310K | | | | 335K | | | | 360K | | | |
|---|---|---|---|---|---|---|---|---|---|---|---|---|
| | 5nm | 8nm | 10nm | 20nm | 5nm | 8nm | 10nm | 20nm | 5nm | 8nm | 10nm | 20nm |
| SKE | 32.7% | 10.7% | 6.6% | 1.7% | 34.3% | 10.8% | 6.6% | 1.7% | N/A | 11.3% | 6.4% | 1.3% |
| CKE | 32.3% | 10.5% | 6.5% | 1.7% | 33.8% | 10.5% | 6.4% | 1.6% | N/A | 11.2% | 6.3% | 1.3% |
| CKE–A | 24.5% | 6.2% | 3.3% | 0.8% | 19.7% | 6.8% | 4.2% | 1.1% | N/A | 9.4% | 5.4% | 1.1% |
| PR–$P_{cap}$ | 29.4% | 9.0% | 5.3% | 1.1% | 30.1% | 8.6% | 4.9% | 0.9% | N/A | 9.6% | 5.1% | 0.7% |
| PR–$P_{cap}$–A | 12.1% | 3.3% | 1.7% | 0.1% | N/A | 3.8% | 2.0% | 0.2% | N/A | N/A | N/A | 0.3% |

Compared to other methods, the CKE–A and PR–$P_{cap}$–A models that take into account adsorption layer thickness perform better. As $W$ decreases, hysteresis CPs [38, 164], above which hysteresis vanishes, are observed in the results of engineering DFT calculations, and these hysteresis critical points occur at larger $W$ when $T$ increases. Meanwhile, the limiting pore size $W_{lim}$ is also observed in the CKE–A, PR–$P_{cap}$, and PR–$P_{cap}$–A models. While $W_{lim}$ is the smallest pore size for which adsorption layers do not fill the nanopores before condensation occurs in the CKE–A model, it represents the smallest pore, where vapor–liquid coexistence can occur in the PR–$P_{cap}$ and PR–$P_{cap}$–A models. Similar to engineering DFT, as $T$ increases, $W_{lim}$ increases in both the PR–$P_{cap}$ and PR–$P_{cap}$–A models. In general, these macroscopic thermodynamic equations show a good agreement with engineering DFT for propane in carbon slit pores for $W \geq 8$ nm, while disagreement becomes significant for $W \leq 5$ nm.

To better illustrate the limiting points at which VLE disappears, we present the $P$–$T$ diagrams for various nanopores in **Figures 2-7** and **2-8**. In nanopores, vapor-phase pressures at VLE decrease and approach $P_0$ as $W$ increases. However, because the Kelvin equations and PR–$P_{cap}$ model do not take into account the inhomogeneous density distributions, they underestimate the nanoconfinement effect and pore vapor-phase pressures at VLE are higher than the evaporation/condensation pressures from engineering DFT. The CKE–A and the PR–$P_{cap}$–A models show better agreement with engineering DFT. The difference between the predicted vapor-phase pressures at VLE from the CKE and the SKE is negligible. As $W$ increases, the predicted vapor-phase pressure at equilibrium from the PR–$P_{cap}$–A model approaches the evaporation pressure from engineering DFT. In addition, while the CKE and SKE show that the CP is not shifted due to zero IFT at the bulk CP, the PR–$P_{cap}$ and PR–$P_{cap}$–A models present the limiting temperature $T_{lim}$, beyond which there is no vapor–liquid phase coexistence. For

the CKE–A model, the limiting temperature $T_{lim\_fill}$ occurs because the adsorption layer thickness is larger than the pore size. For the PR–$P_{cap}$–A model, both kinds of limiting temperatures (*i.e.*, $T_{lim}$ and $T_{lim\_fill}$) exist, while only $T_{lim}$ is shown in figures because $T_{lim} < T_{lim\_fill}$ in our cases. On the other hand, engineering DFT shows the hysteresis critical temperature $T_{ch}$, which is the threshold temperature for the existence of hysteresis in adsorption and desorption isotherms and is different from the bulk CP [37]. Above $T_{ch}$, adsorption and desorption isotherms overlap and the hysteresis zone vanishes. As $W$ decreases, both $T_{ch}$ from engineering DFT and $T_{lim\_fill}$ from the CKE–A as well as $T_{lim}$ from the PR–$P_{cap}$ and PR–$P_{cap}$–A models decrease.

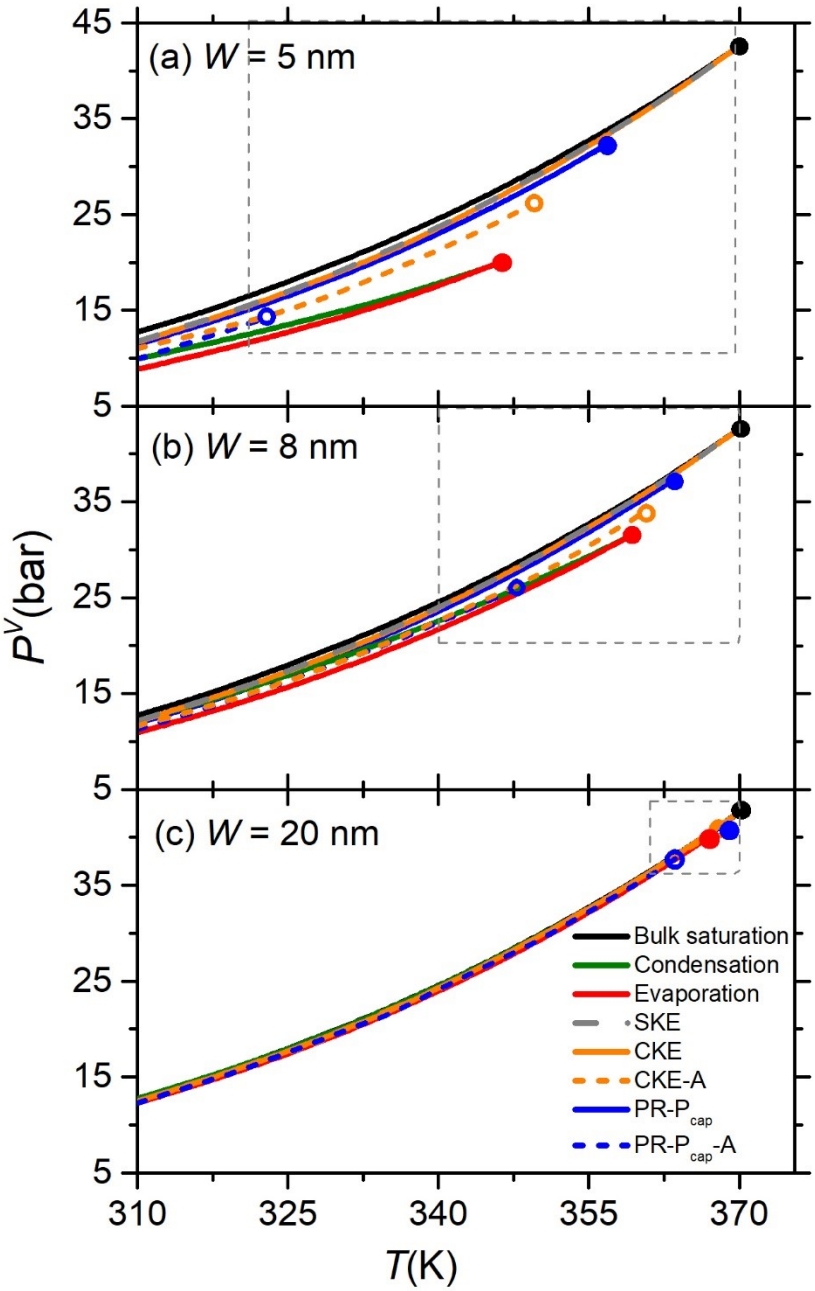


**Figure 2-7** Propane *P*–*T* diagrams in slit nanopores of different widths: (a) $W = 5$ nm; (b) $W = 8$ nm; and (c) $W = 20$ nm. The black solid lines represent the bulk saturation pressures and the black circle represents the bulk critical point. The red circles represent the hysteresis critical temperatures $T_{ch}$ obtained from engineering DFT calculations of vapor-phase pressures for condensation (green lines) and evaporation (red lines). Dashed gray lines, solid orange, and short dashed orange lines represent vapor-phase pressures at VLE from the CKE, CKE–A, and SKE, respectively. Filled and open blue circles represent the limiting temperatures $T_{lim}$ from the PR–$P_{cap}$ and PR–$P_{cap}$–A models, respectively, and open orange circles represent the limiting temperatures due to complete

pore filling $T_{lim\_fill}$ from the CKE–A model.

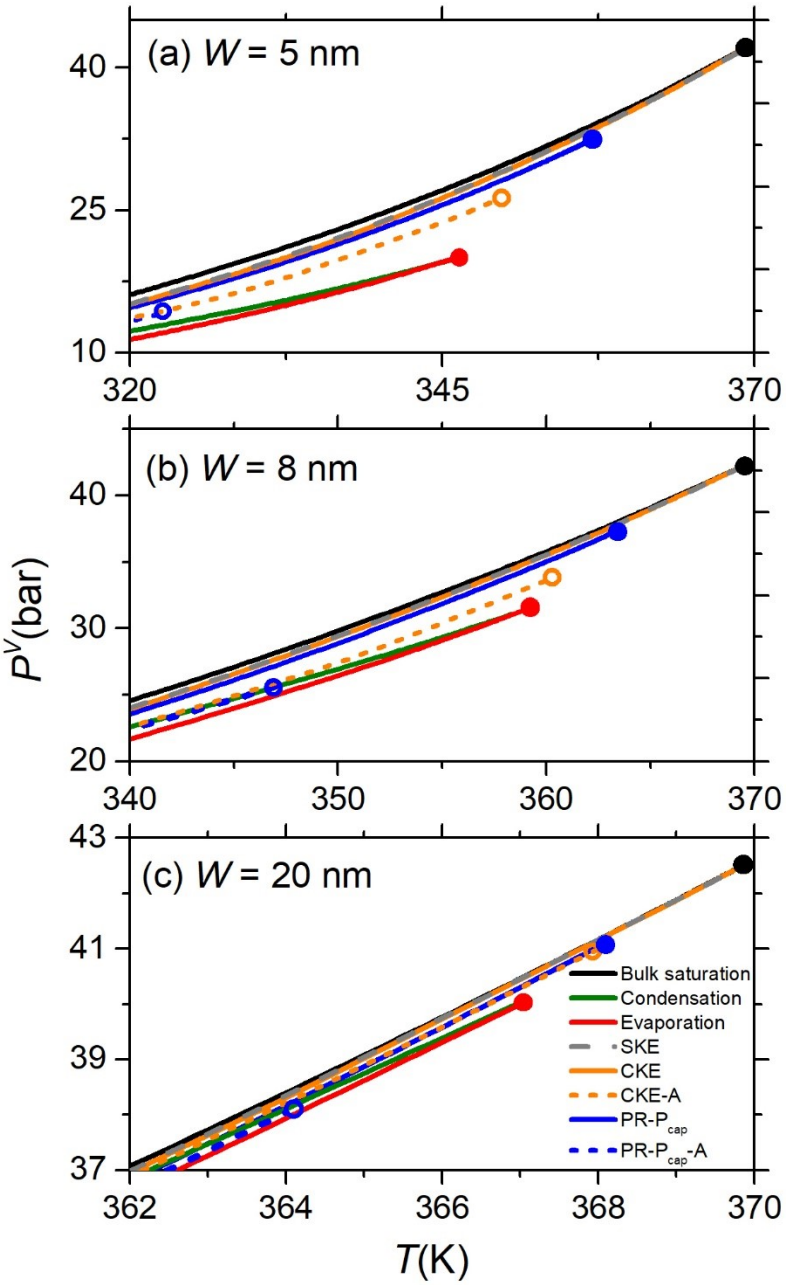


**Figure 2-8** The corresponding highlighted parts shown in **Figure 2-7** for propane *P*–*T* diagrams in slit nanopores of different widths: (a) $W$ = 5 nm; (b) $W$ = 8 nm; and (c) $W$ = 20 nm. The black solid lines represent the bulk saturation pressures and the black circle represents the bulk critical point. The red circles represent the hysteresis critical temperatures $T_{ch}$ obtained from engineering DFT calculations of vapor-phase pressures for condensation (green lines) and evaporation (red lines). Dashed gray lines, solid orange, and short dashed orange lines represent vapor-phase pressures at VLE from the CKE, CKE–A, and SKE, respectively. Filled and open blue circles represent the limiting temperatures $T_{lim}$ from the PR–$P_{cap}$ and PR–$P_{cap}$–A models, respectively, and open

orange circles represent the limiting temperatures due to complete pore filling $T_{lim\_fill}$ from the CKE–A model.

To better understand $T_{lim}$ in the PR–$P_{cap}$ and PR–$P_{cap}$–A models, we present the $\mu$–$P$ relations in bulk and under nanoconfinement at various $T$ from the PR–$P_{cap}$ model in **Figure 2-9**. We define $P_{cap\_max}$ as the pressure difference between **Points C** and **F**. $P_{cap\_max}$ dictates the maximum $P_{cap}$ for chemical potential equilibrium, such that if $P_{cap} > P_{cap\_max}$, there is no vapor–liquid coexistence. In a given nanopore, as $T$ increases, $P_{cap\_max}$ decreases. As a result, there is no chemical potential equality in small nanopores at high $T$, when $P_{cap} > P_{cap\_max}$. Such behavior results in the emergence of $T_{lim}$ in the PR–$P_{cap}$ and PR–$P_{cap}$–A models.

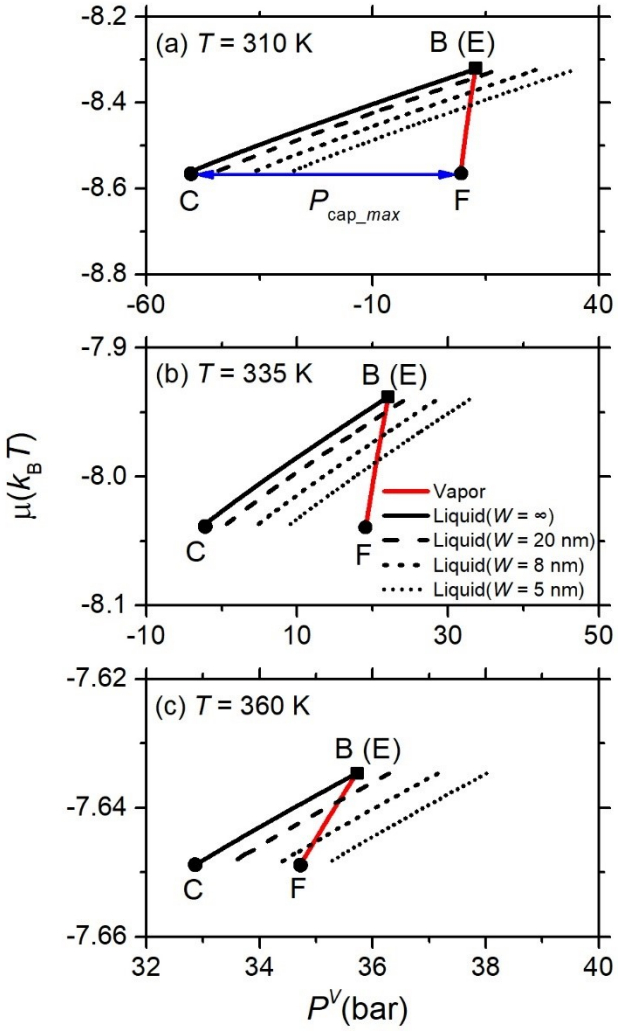

**Figure 2-9** $\mu$–$P$ relations from the PR–P$_{cap}$ model for bulk propane and propane under nanoconfinement at various $T$: (a) $T$ = 310 K; (b) $T$ = 335 K; and (c) $T$ = 360 K. Red solid lines represent vapor-phase $\mu$–$P$ relations; black solid, dashed, short dashed, dotted lines represent $\mu$–$P$ relations of the bulk liquid ($W = \infty$) and liquid confined in $W$ = 20 nm, $W$ = 8 nm, and $W$ = 5 nm pores, respectively. **Points B (E), C,** and **F** correspond to the points shown in **Figure 2-2**

In **Figure 2-10**, we present the dependence of $P_{cap\_max}$ and $P_{cap}$ on $T$ in various nanopores from the PR–P$_{cap}$ model. For clarity, we also depict $T_{lim}$ at different conditions in **Figure 2-7**. The intersections between $P_{cap\_max}$–$T$ and $P_{cap}$–$T$ curves are the same as $T_{lim}$ from the numerical calculation. Therefore, based on $P_{cap\_max}$–$T$ and $P_{cap}$–$T$ curves, $T_{lim}$ at various conditions can be easily obtained without extensive trial-and-error calculations as in numerical iteration methods [33].

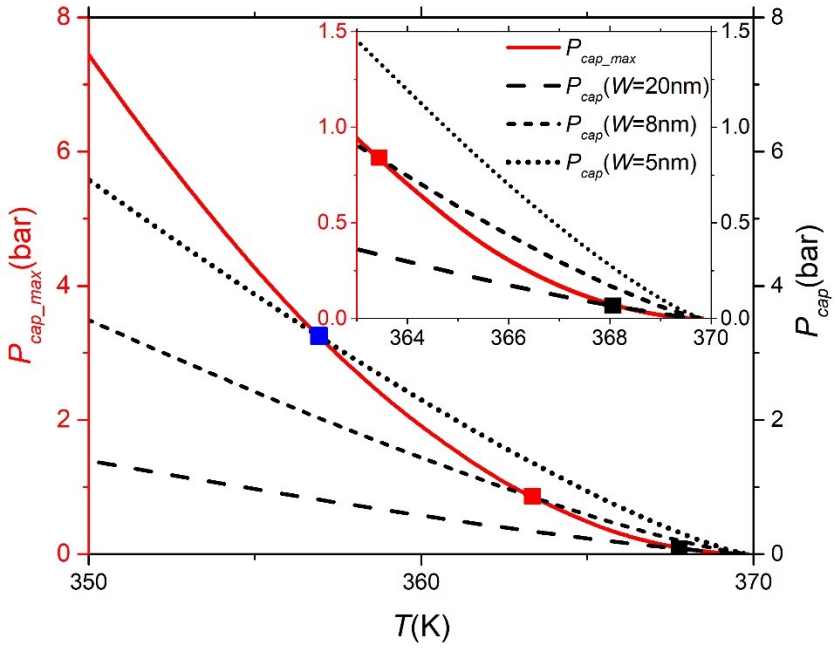


**Figure 2-10** The dependence of maximum capillary pressure $P_{cap\_max}$ and capillary pressure $P_{cap}$ on $T$ calculated using the PR–P$_{cap}$ model for propane in slit nanopores of different widths. The red line represents $P_{cap\_max}$ at various $T$. Dashed, short dashed, and dotted lines depict $P_{cap}$ in nanopores of $W$ = 20 nm, $W$ = 8 nm, and $W$ = 5 nm, respectively. Black, red, and blue squares represent the limiting temperatures $T_{lim}$ in nanopores of $W$ = 20 nm, $W$ = 8 nm, and $W$ = 5 nm, respectively, from **Figure 2-7**. If $P_{cap} > P_{cap\_max}$, then vapor–liquid coexistence in that size of pore at that temperature is not possible.

We also depict the $\mu$–$P$ relations in bulk and under nanoconfinement at various temperatures from the CKE and the SKE in **Figures 2-11** and **2-12**, respectively. Unlike the PR–$P_{cap}$ and PR–$P_{cap}$–A models, there is always an intersection between the vapor- and liquid-phase $\mu$–$P$ curves, because the metastable limit (*i.e.*, the unstable state) of the liquid phase is not considered as in the CKE and SKE.

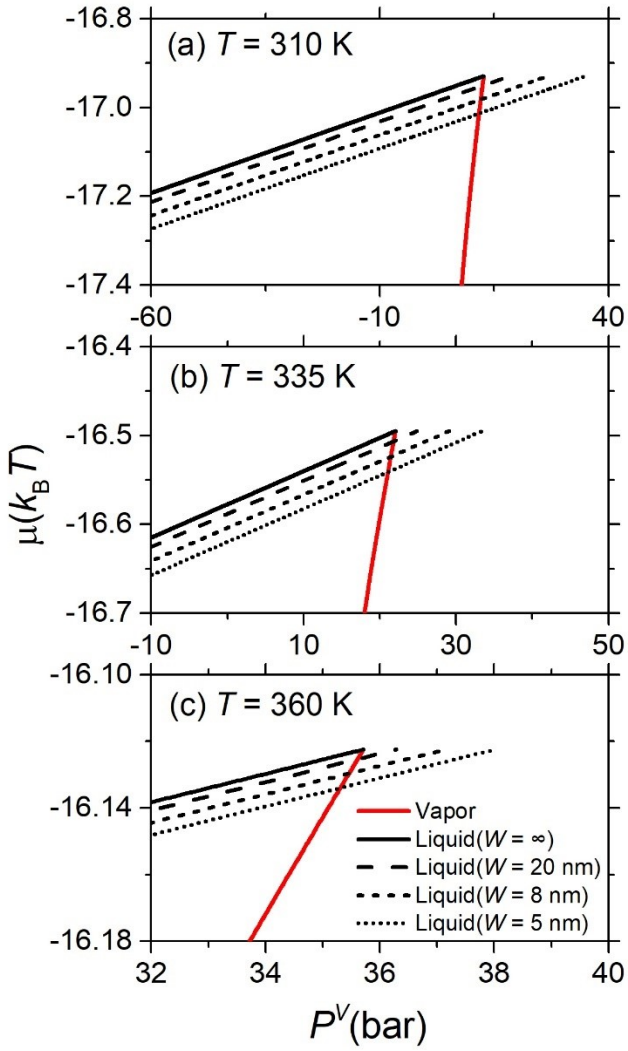


**Figure 2-11** $\mu$–$P$ relations from the CKE for bulk propane and propane under nanoconfinement at various $T$: (a) $T$ = 310 K; (b) $T$ = 335 K; and (c) $T$ = 360 K. Red solid lines represent vapor-phase $\mu$–$P$ relations; black solid, dashed, short dashed, and dotted lines represent $\mu$–$P$ relations of the bulk liquid ($W = \infty$) and the liquid in nanopores of $W$ = 20 nm, $W$ = 8 nm, and $W$ = 5 nm, respectively.

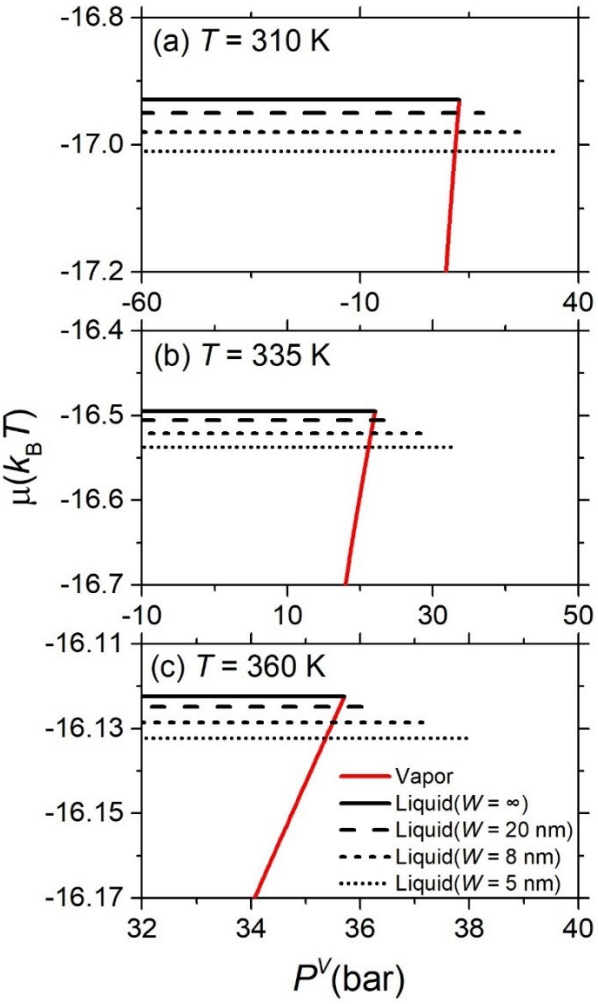


**Figure 2-12** $\mu$–$P$ relations from the SKE for bulk propane and propane under nanoconfinement at various $T$: (a) $T$ = 310 K; (b) $T$ = 335 K; and (c) $T$ = 360 K. Red solid lines represent vapor-phase $\mu$–$P$ relations; black solid, dashed, short dashed, and dotted lines represent $\mu$–$P$ relations of the bulk liquid ($W = \infty$) and of the liquid in nanopores of $W$ = 20 nm, $W$ = 8 nm, and $W$ = 5 nm, respectively.

## 2.4. Conclusions

In this work, by using engineering DFT for propane in graphite nanopores, we investigate the controversy surrounding the validity of the Kelvin equations in nanopores. A lack of correct contact angles might be a possibility for the observed discrepancies in comparisons of the Kelvin equations. We also tested the performance of the PR–$P_{cap}$ and PR–$P_{cap}$–A models. Unlike previous work using numerical iterations to get the vapor–liquid coexistence in EOS–$P_{cap}$ models, we use $P$–$V$ and $\mu$–$\rho$ relations to solve the

chemical and mechanical equilibrium by deducing the liquid-phase properties from the bulk metastable branch and the vapor-phase properties from the bulk stable branch.

For propane in graphite slit nanopores in the grand canonical ensemble, we find that the Kelvin equations and EOS–$P_{cap}$ models all overestimate the evaporation pressure while underestimating the condensation pressure in small nanopores. Based on our calculations, in large slit nanopores ($W \geq 8$ nm), compared with engineering DFT predictions, these thermodynamic equations can accurately predict the vapor-phase pressures at VLE ($\left|\Delta P^{V}\,\%\right| < 10\,\%$) in nanopores. However, in sub-5-nm slit pores, these approaches may become inapplicable ($\left|\Delta P^{V}\,\%\right| > 10\,\%$). From comparisons of Kelvin equations with other thermodynamic equations, we found that the performance of these thermodynamic models improves by incorporating more accurate cubic EOS descriptions for the vapor and liquid phases and by considering the thickness of the adsorption layer. We also found that the differences in the predicted vapor-phase pressures at VLE in nanopores between the CKE and SKE are negligible. More interestingly, we also observed limiting temperatures in the PR–$P_{cap}$ and PR–$P_{cap}$–A models, beyond which there is no vapor–liquid phase coexistence, because for the required $P_{cap}$, the liquid phase would be unstable according to the cubic EOS. In other words, both DFT and PR–$P_{cap}$ models predict limiting temperatures, which are different from the bulk phase CP. As pore size increases, the limiting temperature increases and approaches the bulk critical point. These findings may provide important insights into the prediction of phase behaviors of confined fluids which are at the heart of many engineering applications, such as shale/tight oil production [165].

公式章 (下一章) 节 1

## CHAPTER 3 Effect of Pore Size Distribution on Hydrocarbon Mixtures Adsorption in Shale Nanoporous Media from Engineering Density Functional Theory

(A version of this chapter has been published in Fuel 254 (2019) 115650 by Yingnan Wang and Zhehui Jin)

### Abstract

Unlike the conventional reservoir, shale can have an extensive amount of pores ranging from a few to hundreds of nanometers, in which hydrocarbons behave very differently from the bulk, and surface adsorption becomes significant due to the strong fluid–surface interactions. In the past, a number of works using molecular simulations and theoretical calculations have been applied to study the properties and phase behaviors of nanoconfined hydrocarbons mainly based on a single-pore model, while ignoring pore size distribution (PSD), *i.e.*, volume partitioning in various pores. In this work, we use engineering density functional theory (DFT) to study the effect of PSD and volume partitioning on the hydrocarbon recovery from shale nanoporous media. Interplays between bundle-of-capillary nanopores and bulk are considered. By adopting the actual shale PSDs, we use the constant volume depletion (CVD) method to simulate shale gas recovery. The equilibrium properties at given pressure conditions are determined by the chemical equilibrium between nanopores and the bulk region as well as materials balance. We find that as pressure drops, while the average densities of the lighter components (*i.e.*, $C_1$ and $C_2$) in nanopores decrease, those of $C_3$ and $nC_4$ first increase, then decrease. It also shows that with more larger pores, while the residual ratios of hydrocarbons in nanopores are higher, the overall recovery factors are higher due to more significant volume expansions in the bulk region. Overall, PSD has non-negligible effects on hydrocarbon mixture adsorption in shale nanoporous media, especially for heavier components. Our work should provide a fundamental understanding about the effect of PSD on hydrocarbon mixture adsorption in shale nanoporous media and important insights into the optimization of shale gas recovery.

## 3.1. Introduction

Nowadays, shale gas plays an important role in the global energy supply due to the continuous depletion of conventional oil/gas reservoirs in recent years [140, 166]. Unlike the conventional reservoirs, where pores are generally large, in the range of several micrometers, shale consists of a significant amount of nanoscale pores, ranging from a few to hundreds of nanometers [167]. In nanoscale pores, fluid–surface interactions become significant and fluid distributions are inhomogeneous. The strong surface adsorption in shale nanopores can significantly enhance the fluid-in-place [44, 140]. As a result, the properties and phase behavior of nanoconfined fluids are very different from bulk [10-12] and one cannot use the conventional equation of state (EOS) modeling which is widely used in conventional reservoirs to describe shale gas recovery [10, 48]. Understanding the adsorption and properties of nano-confined hydrocarbons is key to the accurate estimation of fluid-in-place in shale and prediction of well productivity.

A number of experimental works have been reported on the behavior of hydrocarbons under nanoconfinement [23, 24, 168-172]. Among them, Zhong *et al*. [23] and Yang *et al*. [24] found that in sub-10 nm pores, the hydrocarbon condensation pressure decreases significantly from the bulk. Luo *et al*. [173, 174] used nano-scale capillaries to study the bubble point temperature of confined pure and hydrocarbon mixtures. They found that the effect of nanoconfinement is insignificant in large pores (38.1 nm), but strong in small pores (4.3 nm).

On the other hand, a number of theoretical and simulation works have been reported on the phase behaviors of nanoconfined fluids[10-12, 39-44]. Didar *et al.* [12] used grand canonical Monte Carlo (GCMC) simulations to investigate the phase behavior of pure and hydrocarbon mixtures in nanopores. They found that, due to nanoconfinement, the critical temperature and pressure decrease, and the pore-size-dependent phase envelope further influences cumulative gas production. Jin and Firoozabadi [11] used GCMC simulations to study hydrocarbon mixture adsorption in nanopores and found that while the lighter component adsorption decreases, the heavier component adsorption increases as pressure decreases. Bui *et al.* [44] used both GCMC and molecular dynamics (MD) simulations to study the fluid properties of hydrocarbon mixtures in nanoconfinement. They found that due to strong fluid–surface interactions, the recovery of the heavier hydrocarbons from nanopores is limited, which becomes more obvious as pore size decreases.

While molecular simulations can explicitly consider intermolecular and fluid–surface interactions, they can be computationally expensive for heavier hydrocarbons and high-pressure conditions [175, 176]. Engineering density functional theory (DFT) which extends the PR-EOS to the inhomogeneous conditions has been used to study bubble/dew points of confined hydrocarbon fluids [39], and adsorption in shale nanoporous media [10, 140], showing excellent agreement with experimental data and molecular simulations. In contrast to molecular simulations, while engineering DFT can significantly reduce the calculation time, it cannot provide details about molecular configurations. Although the effect of nanoconfinement has been studied in various computational and theoretical works, most of the works were performed based on a single-pore model. However, unlike the monodispersed porous materials, such as carbon nanotubes, shale has various pores ranging from a few nanometers to micrometers. The pore size distribution (PSD), *i.e.*, the volume partitioning in different pores and their interplay, may play an important role in shale gas recovery.

Recently, a few works have been reported on the study of the effect of PSD on the confined pure or hydrocarbon mixtures. Luo *et al*. [46, 47] used a pore-size-dependent equation of state (PR-C EOS) to extend the PR-EOS by van der Waals equations [177, 178]. The PR-C EOS considers the fluid–surface interaction and relates the fluid phase behavior to the fourth dimension of confining pore diameter [46, 47]. They found that bubble points in both bulk and nanopores will be suppressed and a sharp rise in the gas–oil ratio (GOR) occurs at pressures below the bubble point in a liquid-rich shale. Jin *et al*. [48] studied the phase behavior of confined pure methane by using the gauge-GCMC method [41, 179], considering the interplay between the bulk and nanopores. They found that the pore filling occurs in smaller pores first, then in larger pores. The phase behaviors of methane in the multi-pore model could be estimated from the related fluid characteristics in the single-pore model, only if they have similar temperature–density diagrams. Wang *et al*. [81] used PR-EOS with capillary pressure model to study the phase behavior of various reservoir fluids with the effect of PSD. They assumed that liquid-phase hydrocarbons have the same composition in nanopores of different pore sizes. As pressure drops, evaporation always occurs in the larger nanopores first; only after the larger nanopores completely vaporize, does the evaporation process start in the smaller nanopores. Although these works provided some insights into the effect of PSD on phase behavior of confined hydrocarbons,

the model which can explicitly consider the effect of PSD on hydrocarbon mixtures, fluid–fluid interactions, and fluid–surface interactions has not yet been developed.

In this work, we use engineering DFT to study the adsorption and properties of hydrocarbon mixtures in nanopores with the PSD effect. We separate the shale nanoporous media into two distinct parts: bulk region and nanopores. Due to the interplay between bulk and bundle-of-capillary nanopores, although there is no direct interaction among fluids in different nanopores, they influence each other via volume partitioning and materials balance. Due to fluid–surface interaction in nanopores, as pressure drops, the composition of released fluids from nanopores is different from the bulk, which in turn affects the bulk composition. At a given pressure, the fluids in nanopores and the bulk region are in chemical equilibrium, which is also constrained by materials balance. In other words, fluids in nanopores and bulk regions are correlated. Therefore, different PSD and volume partitioning would result in varying hydrocarbon adsorption behavior in shale nanoporous media. Very recently, we have shown that such volume partitioning can strongly affect the bubble/dew point of hydrocarbon mixtures in connected nanopores and bulk region [180]. The PSD in our calculation is constructed based on the actual Eagle Ford [167], Middle Bakken [181], and Horn River [182] shale sub-formation characterizations. We simulate shale gas recovery by using the constant volume depletion (CVD) method as depicted in **Figure 3-1**. During the CVD process, the bulk region volume is expanded to lower bulk pressure. The fluids in the excess volume in the bulk region are removed to maintain the original bulk volume [81]. This process intends to simulate the hydrocarbon recovery from the nanopores in shale matrix through the natural and hydraulic fractures [183]. By using engineering DFT, we can explicitly calculate density distributions, average densities of fluids in nanopores and bulk region at given pressure conditions and provide important insights into the effect of PSD on shale gas recovery. While we illustrated the effect of PSD, we should note that the presence of brine and heterogeneity of shale nanoporous media are not considered in this work.

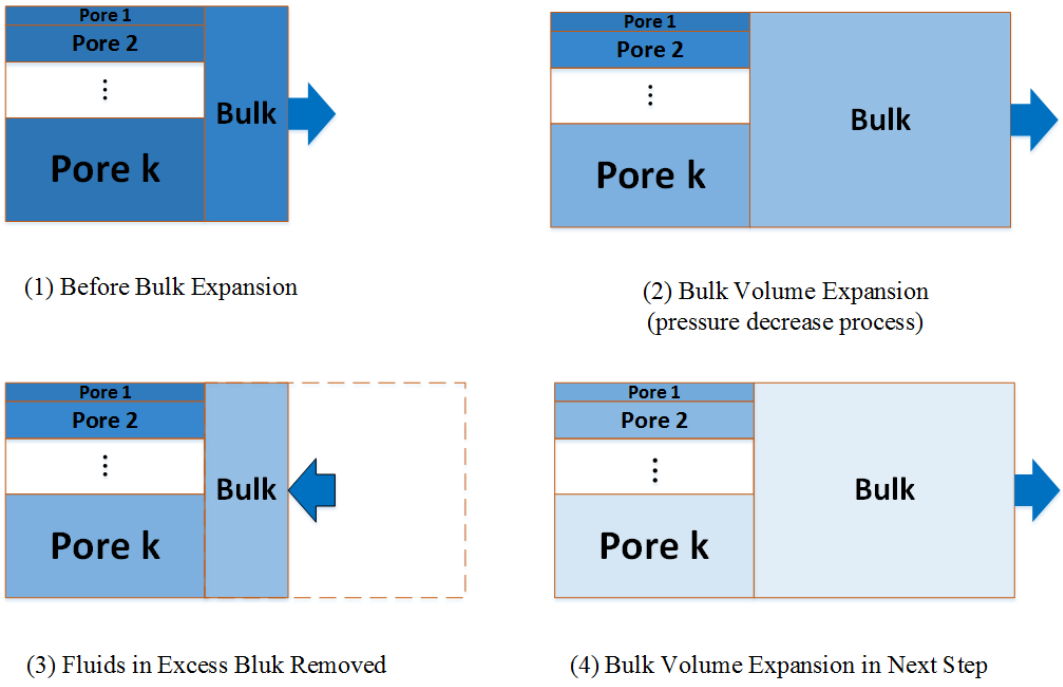


**Figure 3-1** Schematic of constant volume depletion in nanopore–bulk model for hydrocarbon mixtures. The darker color presents higher hydrocarbon densities.

The remainder of this chapter is organized as follows. In section 2, we introduce the nanopores–bulk region model. In section 3, we describe the molecular model and engineering DFT calculations. In section 4, we investigate the effect of PSD on the shale gas adsorption and recovery process by using the CVD method. In section 5, we summarize key conclusions and discuss potential implications.

## 3.2. Model and Methodology

### 3.2.1. Nanopore–Bulk Model

DFT is based on the framework of an open system with the equivalence of chemical potentials of species to that in a fictitious bulk reservoir [146]. We separate the shale nanoporous media into two distinct parts: bulk region and nanopores. The bulk region may refer to hydraulic and natural fractures as well as macropores in the shale matrix, where fluids behave as bulk. It is observed that in large pores ($\geq$ 50 nm), the phase behavior is similar to bulk [125, 170]. Akkutlu *et al.* [184] claimed that pore size cut-off varies depending on the hydrocarbon compositions, as it increases as hydrocarbon mixtures become leaner, *i.e.*, with more than 98 mol% of $C_1$ it is close to 40 nm. A number of works used 50 nm as the limit of bulk [46, 170, 185]. Thus, in this work, by using 50 nm as the cut-off size, we ensure the hydrocarbons in these regions behave as bulk. On

the other hand, pores of sizes less than 50 nm are treated as nanopores and we explicitly consider fluid–surface interactions. Based on the PSDs from Eagle Ford [167], Horn River [182], and Middle Bakken [181] shale sub-formation characterizations, four distinct pore widths and bulk are used to represent micropores and mesopores in shale: 2 nm (< 2 nm), 5 nm (2~10 nm), 15 nm (10~20 nm), and 30 nm (20~50 nm), and bulk (>50 nm). In this work, we study the effect of PSD at a temperature much higher than the cricondentherm of hydrocarbon mixtures so that capillary condensation/evaporation and hysteresis, as reported in previous works [39], are not considered. The pore volumes in each nanopore and bulk region are presented in **Table 3-1**. In our model, pressure $P$ is dictated by the fluid pressure in the bulk region. While the chemical potentials of fluids in nanopores are the same as that in bulk at equilibrium, we do not consider the interfaces between nanopores and the bulk region. It has been shown that the mechanical equilibrium between nanopores and bulk is always automatically satisfied by the equality of chemical potentials [186].

**Table 3-1** Nanopore–bulk volume fractions based on the Eagle Ford [167], Middle Bakken [181], and Horn River [182] shale PSD characterization.

| | Nanopores | | | | Bulk |
|---|---|---|---|---|---|
| | 2 nm | 5 nm | 15 nm | 30 nm | |
| Eagle Ford | 11.50% | 27.50% | 12.00% | 18.00% | 31.00% |
| Middle Bakken | 2.87% | 15.00% | 33.38% | 34.53% | 14.22% |
| Horn River | 0.48% | 2.59% | 4.61% | 20.73% | 71.59% |

### 3.2.2. Molecular Model and Theory

We use the engineering DFT to consider the chemical equilibrium between hydrocarbon fluids in the bulk region and nanopores. The temperatures in nanopores and bulk regions are the same. We apply the engineering DFT calculations to nanopores only, for given bulk pressure and temperature conditions. The equilibrium hydrocarbon densities in the bulk region and density distributions in nanopores are determined by mass conservation and equivalence of chemical potentials of species in nanopores and bulk.

Within the framework of DFT, for a given nanopore, the grand potential $\Omega\left[\left\{\rho_i(\mathbf{r})\right\}\right]$, which is a function of density distribution $\left\{\rho_i(\mathbf{r})\right\}$, is the thermodynamic function of choice and is related to the Helmholtz free energy functional $F\left[\left\{\rho_i(\mathbf{r})\right\}\right]$ via the Euler–Lagrange transformation [146],

$$\Omega\left[\left\{\rho_i(\mathbf{r})\right\}\right] = F\left[\left\{\rho_i(\mathbf{r})\right\}\right] + \sum_i \int \rho_i(\mathbf{r})\left[\Psi_i(\mathbf{r}) - \mu_i\right] d\mathbf{r}, \tag{3-1}$$

where $d\mathbf{r}$ is differential volume, and $\rho_i(\mathbf{r})$ is the number density distribution of component $i$ at position $\mathbf{r}$; $\Psi_i(\mathbf{r})$ is the solid surface external potential of the component $i$ at the position $\mathbf{r}$; $\mu_i$ is the chemical potential of component $i$ in bulk [147].

The Helmholtz free energy $F\left[\left\{\rho_i(\mathbf{r})\right\}\right]$ is further decomposed into two parts: the ideal-gas term $F^{id}\left[\left\{\rho_i(\mathbf{r})\right\}\right]$ and the excess term arising from the intermolecular interactions $F^{ex}\left[\left\{\rho_i(\mathbf{r})\right\}\right]$,

$$F\left[\left\{\rho_i(\mathbf{r})\right\}\right] = F^{id}\left[\left\{\rho_i(\mathbf{r})\right\}\right] + F^{ex}\left[\left\{\rho_i(\mathbf{r})\right\}\right]. \tag{3-2}$$

The functional of the ideal-gas term is given as [147],

$$\beta F^{id}\left[\left\{\rho_i(\mathbf{r})\right\}\right] = \sum_i \int d\mathbf{r}\rho_i(\mathbf{r})\left[\ln \rho_i(\mathbf{r}) - 1\right], \tag{3-3}$$

where $\beta = 1/(k_B T)$; $k_B$ and $T$ represent Boltzmann constant and the absolute temperature, respectively.

In Eq. (2-16), the excess Helmholtz free energy functional includes two parts. One part is obtained by extending the PR-EOS with weighted density approximation (WDA) [148] to inhomogeneous conditions to account for the physical interactions,

$$F_{ph}^{ex}\left[\left\{\rho_i(\mathbf{r})\right\}\right] = \int d\mathbf{r}\phi_{ph}\left[\rho_i(\mathbf{r})\right], \tag{3-4}$$

where $\phi_{ph}\left[\rho_i(\mathbf{r})\right]$ is the reduced excess Helmholtz energy density functional. We use $n_{0i}(\mathbf{r})$ and $n_{3i}(\mathbf{r})$ functions in Rosenfeld's fundamental measure theory [148] to mathematically represent the "geometrical properties" of molecules and account for interactions in inhomogeneous conditions,

$$\begin{cases} n_{0i}(\mathbf{r}) = \dfrac{1}{\pi\sigma_i^2}\displaystyle\int d\mathbf{r}'\rho_i(\mathbf{r}')\delta\left(\frac{\sigma_i}{2} - |\mathbf{r}-\mathbf{r}'|\right) \\ n_{3i}(\mathbf{r}) = \displaystyle\int d\mathbf{r}'\rho_k(\mathbf{r}')\theta\left(\frac{\sigma_i}{2} - |\mathbf{r}-\mathbf{r}'|\right) \end{cases}, \tag{3-5}$$

where $\delta(\mathbf{r})$ is the Dirac delta function and $\theta(\mathbf{r})$ is the Heaviside step function, and $\sigma_i$ is the "effective diameter" of component $i$. As a result, the reduced excess Helmholtz $\phi_{ph}\left[\{\rho_i(\mathbf{r})\}\right]$ extended by WDA is expressed as,

$$\begin{aligned}\phi_{ph}\left[\{\rho_i(\mathbf{r})\}\right] &= \phi_{ph}\left[\{n_{\alpha i}(\mathbf{r})\}\right] \\ &= -n_0\ln(1-4n_3) - \frac{\sum_{j,k} n_{0j} n_{0k} a_{jk}}{8\sqrt{2}n_3 k_B T}\ln\left[\frac{1+4\left(1+\sqrt{2}\right)n_3}{1+4\left(1-\sqrt{2}\right)n_3}\right],\end{aligned} \tag{3-6}$$

where $n_0 = \sum_i n_{0i}$, $n_3 = \sum_i n_{3i}$; $a_{jk} = \sqrt{a_j a_k}\left(1-k_{jk}\right)$ and $a_i$ represents the energy parameter of component $i$; $k_{jk}$ is the binary interaction coefficient (BIC) between components $j$ and $k$ as given in **Table B-1**.

The other part of excess Helmholtz free energy $F_{pe}^{ex}\left[\{\rho_i(\mathbf{r})\}\right]$ accounts for the long-range intermolecular attractions by using quadratic density expansion (QDE) [149, 150].

$$\beta F_{pe}^{ex} = -\frac{1}{4}\sum_{i,j}\iint d\mathbf{r}d\mathbf{r}'\beta u_{ij}^{pe}\left(|\mathbf{r}-\mathbf{r}'|\right)\left[\rho_i(\mathbf{r})-\rho_i(\mathbf{r}')\right]\left[\rho_j(\mathbf{r})-\rho_j(\mathbf{r}')\right], \tag{3-7}$$

in which the pair potential $u_{ij}^{pe}(r)$ is modeled by the attractive part of the Lennard-Jones potential,

$$u_{ij}^{pe}(r) = \begin{cases} 0, & r < \sigma_{ij} \\ -\varepsilon_{ij}^{pe}\left(\dfrac{\sigma_{ij}}{r}\right)^6, & r \geq \sigma_{ij} \end{cases}, \tag{3-8}$$

where $\varepsilon_{ij}^{pe}$ and $\sigma_{ij}$ are the potential expansion parameter and cross molecular diameter between components $i$ and $j$. In this work, we use the simple combing rules to calculate $\varepsilon_{ij}^{pe}$ and $\sigma_{ij}$, *i.e.*,

$$\begin{cases} \varepsilon_{ij}^{pe} = \sqrt{\varepsilon_i^{pe}\varepsilon_j^{pe}} \\ \sigma_{ij} = \left(\sigma_i + \sigma_j\right)/2 \end{cases}. \tag{3-9}$$

where $\varepsilon_i^{pe}$ and $\sigma_i$ of different hydrocarbon component $i$ as well as other PR-EOS parameters are shown in **Table B-2**.

At equilibrium, the grand potential functional reaches the minimum [140],

$$\frac{\delta\Omega\left[\left\{\rho_i(\mathbf{r})\right\}\right]}{\delta\rho_i(\mathbf{r})}=0, \tag{3-10}$$

where the symbol $\delta$ represents the functional derivative. The equilibrium density distributions of species are obtained by the minimization of the grand potential functional [151],

$$\rho_i(\mathbf{r})=\exp\left[\beta\mu_i-\beta\Psi_i(\mathbf{r})-\frac{\delta\beta F^{ex}\left[\left\{\rho_i(\mathbf{r})\right\}\right]}{\delta\rho_i(\mathbf{r})}\right]. \tag{3-11}$$

The density distribution in Eq. (2-17) is solved by the Picard iteration method [152]. The bulk density is used as the initialization for the calculation of the first pressure. The initial guess for other pressures is from the density distributions at the preceding pressure. The dimensionless volume shift parameter (VSP) [155], which is obtained by fitting the equilibrium density distribution at $T=0.7T_c$, is used to correct the equilibrium density distributions obtained from Eq. (2-17),

$$\tilde{\rho}_i(\mathbf{r})=\frac{\rho_i(\mathbf{r})}{1+\rho_i(\mathbf{r})\sum_i X_i C_i} \tag{3-12}$$

where $C_i=VSP\times b_i$, $b_i$ is the volume parameter for component $i$ from PR-EOS, and $\tilde{\rho}_i(\mathbf{r})$ is the corrected equilibrium density distribution.

For simplicity, we use carbon-slit pores which are described by two planar structureless graphite surfaces to represent nanopores in the system [140, 156, 157]. Such carbon nanopore structures have been applied to the study of gas adsorption in shale and shown excellent agreement with GCMC simulation results and experimental data [10]. In a carbon-slit pore, the density distributions only vary in the $z$ direction perpendicular to the solid surfaces, *i.e.*, $\tilde{\rho}_i(\mathbf{r})=\tilde{\rho}_i(z)$. We use the 10-4-3 Steele potentials to describe the fluid–surface interactions $\varphi_{si}$ [158],

$$\varphi_{si}(z)=2\pi\rho_s\varepsilon_{si}\sigma_{si}^2\Delta\left[\frac{2}{5}\left(\frac{\sigma_{si}}{z}\right)^{10}-\left(\frac{\sigma_{si}}{z}\right)^{4}-\frac{\sigma_{si}^4}{3\Delta(0.61\Delta+z)^3}\right], \tag{3-13}$$

where $z$ represents the position in the perpendicular direction relative to the pore surface; $\rho_s=114$ nm$^{-3}$ is the density of graphite and $\Delta=0.335$ nm represents the interlayer spacing of graphite; $\varepsilon_{si}$ and $\sigma_{si}$ are potential expansion parameters and follow the simple mixing rule. Here, we set $\sigma_s=0.3345$ nm, $\varepsilon_s/k_B=28$ K and the energy and size parameters for hydrocarbon species are from the modified Buckingham exponential-6 intermolecular potentials for $CH_3$-group, -$CH_2$- group, and $CH_4$ as in our previous work [31]. In slit-nanopores, the external potential $\Psi_i(\mathbf{r})$ for component $i$ in Eq. (2-17) is given as,

$$\Psi_i(z)=\varphi_{si}(z)+\varphi_{si}(W-z). \tag{3-14}$$

The average density of component $i$ in nanopores $\rho_{ave,i}$ is given as,

$$\rho_{ave,i}=\frac{\int_0^{W_{ef}}\tilde{\rho}_i(z)\,dz}{W_{ef}}, \tag{3-15}$$

where $W_{ef}=W-\sigma_s$ is the effective pore size; $W$ is the pore size [187].

In our engineering DFT calculations, the system temperature is fixed at 363.15 K and the initial pressure $P^{init}$ is 300 bar. The $C_1$-$C_2$-$C_3$-n$C_4$ quaternary mixture is studied and the initial overall mole fractions $X_i^{init}$ at $P^{init}$ are given as

$$X_i^{init}=\frac{m_i^{init}}{\sum_j m_j^{init}}, \tag{3-16}$$

with

$$m_i^{init}=\rho_{i,b}^{init}V_b+\sum_W\rho_{i,W}^{init}V_{p,W}, \tag{3-17}$$

where $V_{p,W}$ is pore volume of nanopores of $W$, $V_b$ is bulk volume, $\rho_{i,b}^{init}$ and $\rho_{i,W}^{init}$ are average densities of component $i$ in bulk and nanopores of $W$ at $P^{init}$, respectively, $m_i^{init}$ is the total

mass of component $i$ at $P^{init}$. While $\rho_{i,b}^{init}$ is obtained from the PR-EOS for given mole fraction of hydrocarbon mixture in bulk at $P^{init}$, $\rho_{i,W}^{init}$ are obtained from engineering DFT as shown in Eq. (3-15).

As $P$ decreases, $V_{p,W}$ does not change but $V_b$ expands and fluids in the excess bulk volume are then removed during the CVD process. We first apply materials balance for each component $i$ to calculate the expanded bulk volume $V_{i,b}^o$ before fluid removal at the given $P$,

$$V_{i,b}^o = \frac{m_i^o - \sum_W \rho_{i,W} V_{p,W}}{X_{i,b}\rho_b}, \tag{3-18}$$

where $m_i^o$ is the total mass of component $i$ at $P$ before removal, $\rho_{i,W}$ and $X_{i,b}$ is average density in nanopores of $W$ and bulk mole fraction of component $i$ at $P$, respectively. We use the iterative method to find the bulk mole fraction $\{X_{i,b}\}$, which gives the convergent $V_{i,b}^o$ from each component $i$ as $V_b^o$. In general, $V_b^o$ is larger than $V_b$, and the removed fluids $m_i^{re}$ in the excess bulk volume are given as,

$$m_i^{re} = \left(V_b^o - V_b\right)\rho_{i,b}. \tag{3-19}$$

As a result, the remaining fluids in the system $m_i^n$ at $P$ are given as

$$m_i^n = m_i^o - m_i^{re}. \tag{3-20}$$

Then, $m_i^n$ serve as $m_i^o$ in Eq. (3-18) at the subsequent pressure. In each step, we lower the bulk pressure by 1 bar until the end pressure $P^{end} = 10$ bar.

### 3.3. Results and Discussions

In this section, we use three simplified PSD from Eagle Ford [167], Middle Bakken [181], and Horn River [182] shale sub-formations to study the effect of PSD on shale gas adsorption and recovery of $C_1$-$C_2$-$C_3$-$nC_4$ quaternary mixtures. The initial mole fractions in the bulk region are given in **Table 3-2** and the corresponding phase diagrams of bulk hydrocarbon mixtures are

shown in **Figure B-1**. The mole fraction of quaternary mixtures is obtained from experimental data [188].

**Table 3-2** Initial bulk mole fractions for $C_1$-$C_2$-$C_3$-$nC_4$ mixtures [188].

| | $C_1$ | $C_2$ | $C_3$ | $nC_4$ | Sum |
|---|---|---|---|---|---|
| C1-$C_2$-$C_3$-$nC_4$ mixture | 0.7152 | 0.1639 | 0.095 | 0.0259 | 1 |

In **Figure 3-2**, the average mass densities of each component and their mixtures of $C_1$-$C_2$-$C_3$-$nC_4$ mixtures in varying nanopores and bulk are depicted. For $C_1$ and $C_2$, both average mass densities decrease as pressure decreases. Due to strong competitive adsorption in nanoconfinement, $C_1$ average mass density is lowered in small nanopores and even lower than that in bulk. Compared to $C_1$ and $C_2$, $C_3$ and $nC_4$ average mass densities increase in small pores (*i.e.*, $W = 2$ nm) as pressure decreases. Especially for $nC_4$, even at $P^{end}$, the average mass density in 2 nm pores is higher than that at $P^{init}$ due to strong $nC_4$–surface interactions. Thus, as pressure drops, while the lighter components can be released from nanopores, a large portion of $C_3$ and $nC_4$ may remain in nanopores. The mass density of mixtures in all nanopores decreases as pressure drops. The effect of PSD is more significant on the heavier components and the fluids in smaller pores. Interestingly, with more larger nanopores in PSD (*i.e.*, Horn River), the increase in $nC_4$ average densities in nanopores is more significant, while the opposite is true for $C_1$ and $C_2$.

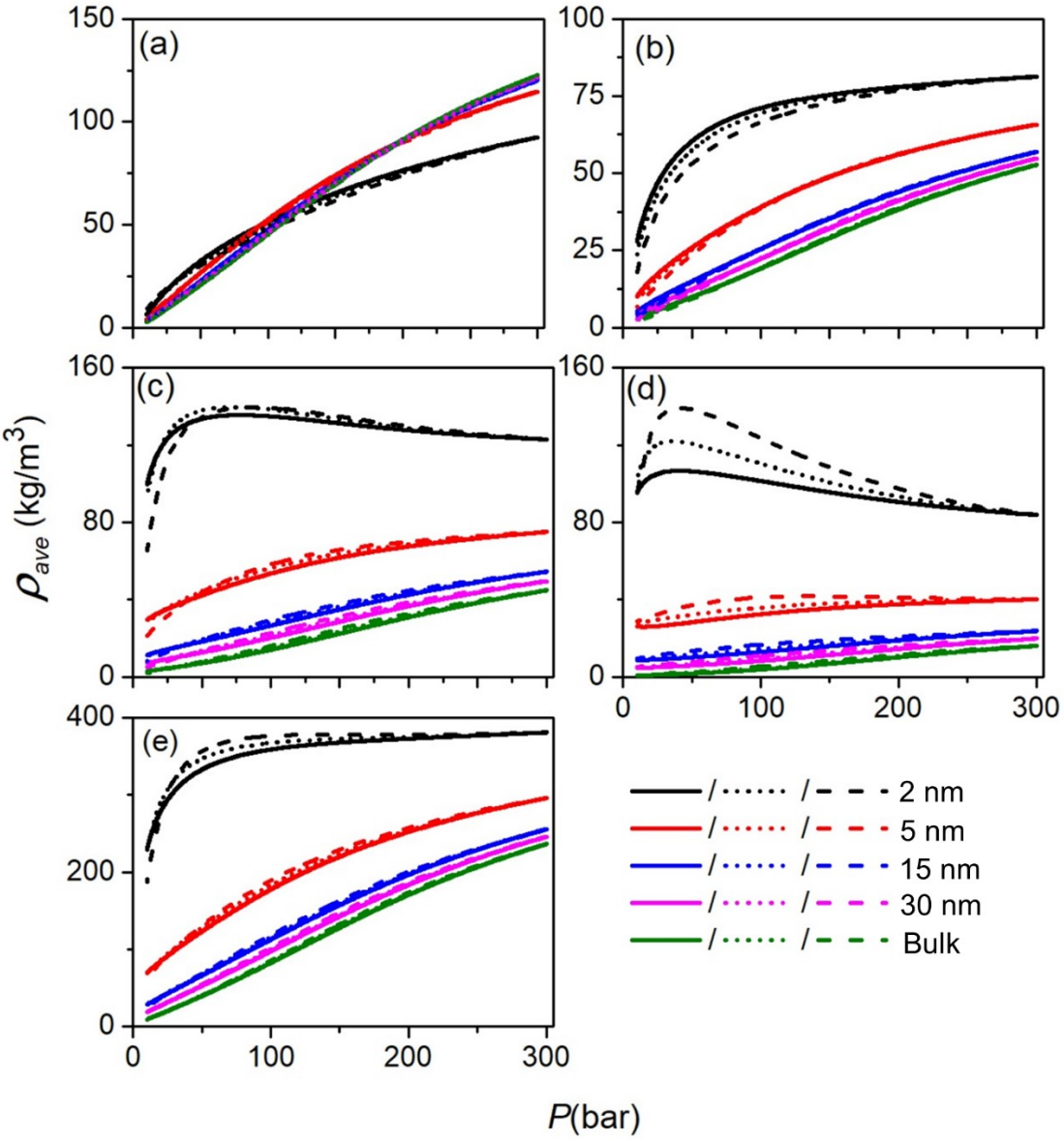


**Figure 3-2** The average mass densities of (a) $C_1$, (b) $C_2$, (c) $C_3$, (d) $nC_4$, and (e) their mixtures in nanopores of 2 nm (black), 5 nm (red), 15 nm (blue), 30 nm (magenta) and bulk (olive) at $T$ = 363.15 K. Solid, dotted, and dashed lines represent Eagle Ford, Middle Bakken, and Horn River, respectively.

To investigate the PSD effect, we present the bulk mole fraction of each component in **Figure 3-3**. The fraction is influenced by the interplay between nanopores and the bulk region. In general, PSD has a stronger effect on the bulk mole fraction of the heavier components. With more smaller nanopores (*i.e.*, Eagle Ford), the variation in the bulk composition is more significant. For the lighter components, the effect of PSD is insignificant until pressure is lower than 50 bar. However, for the heavier components, the deviation among various PSD cases is

non-negligible. For example, the bulk $C_3$ composition deviation between Eagle Ford and Horn River cases can reach around 10 % at 150 bar, while that of $nC_4$ can be around 25 %. At 60 bar, the deviation in bulk $nC_4$ composition can be around 50 %, which significantly influences $nC_4$ recovery. Because the hydrocarbon mixtures in the excess volume of the bulk region are removed during each pressure drop, the variation in the bulk compositions dictates the effect of PSD on the recovered fluids.

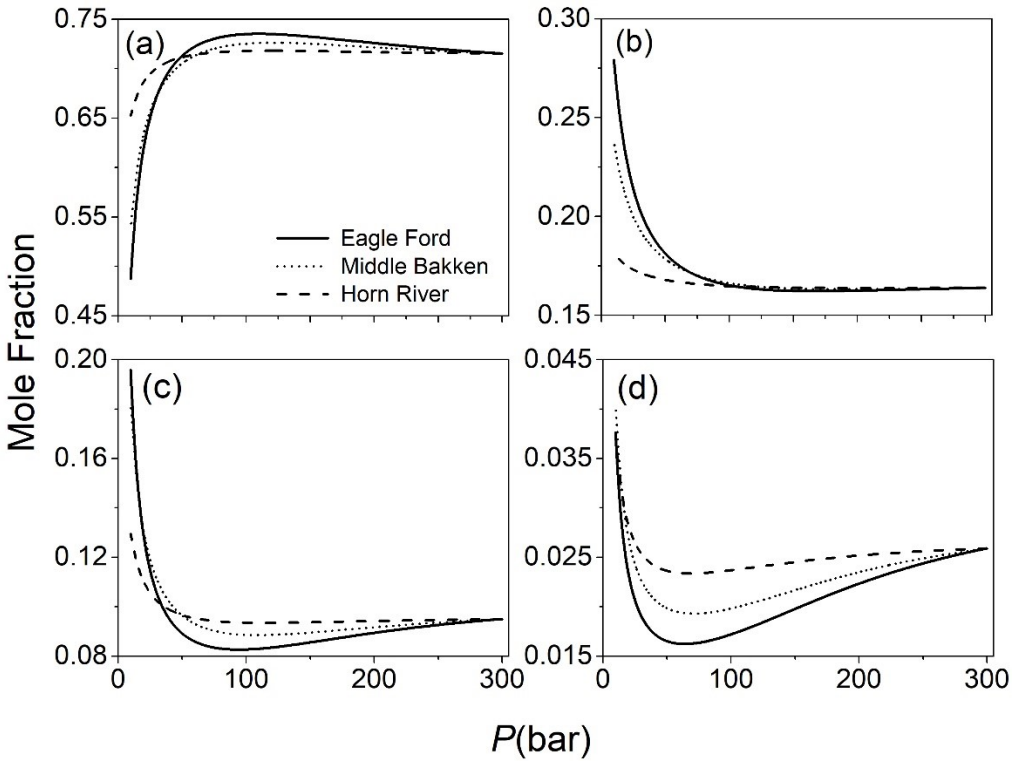


**Figure 3-3** Bulk mole fractions of (a) $C_1$, (b) $C_2$, (c) $C_3$, and (d) $nC_4$ of $C_1$-$C_2$-$C_3$-$nC_4$ mixtures in different PSDs at $T$ = 363.15 K. Solid, dotted, and dashed lines represent Eagle Ford, Middle Bakken, and Horn River, respectively.

We present the enhancement factor of each component and their mixtures in various nanopores over bulk in **Figure 3-4**. The enhancement factor for a single component and mixture is given as,

$$\begin{cases} f_{i,W}^{enh} = \rho_{i,W} / \rho_{i,b} \\ f_{mix,W}^{enh} = \sum_i \rho_{i,W} / \sum_i \rho_{i,b} \end{cases}, \tag{3-21}$$

where $\rho_{i,W}$, $\rho_{i,b}$ are average mass densities of component $i$ at given $P$ in nanopores of $W$ and bulk, respectively. Wu *et al*. found that due to the stronger fluid–surface interaction in smaller nanopores, both components show higher enhancement factors in smaller nanopores [189]. The enhancement factors of the heavier components are larger due to the stronger fluid–surface interactions. For $nC_4$, the enhancement factor can be more than two orders of magnitude in small nanopores (*i.e.*, $W = 2$ nm). As pore size decreases, the enhancement factor of component $i$ increases. For $C_1$, its enhancement factor is less than 1 at high pressures due to competitive adsorption. The enhancement factors increase as pressure decreases. Overall, the effect of PSD is insignificant on the enhancement factor for the quaternary hydrocarbon mixtures.

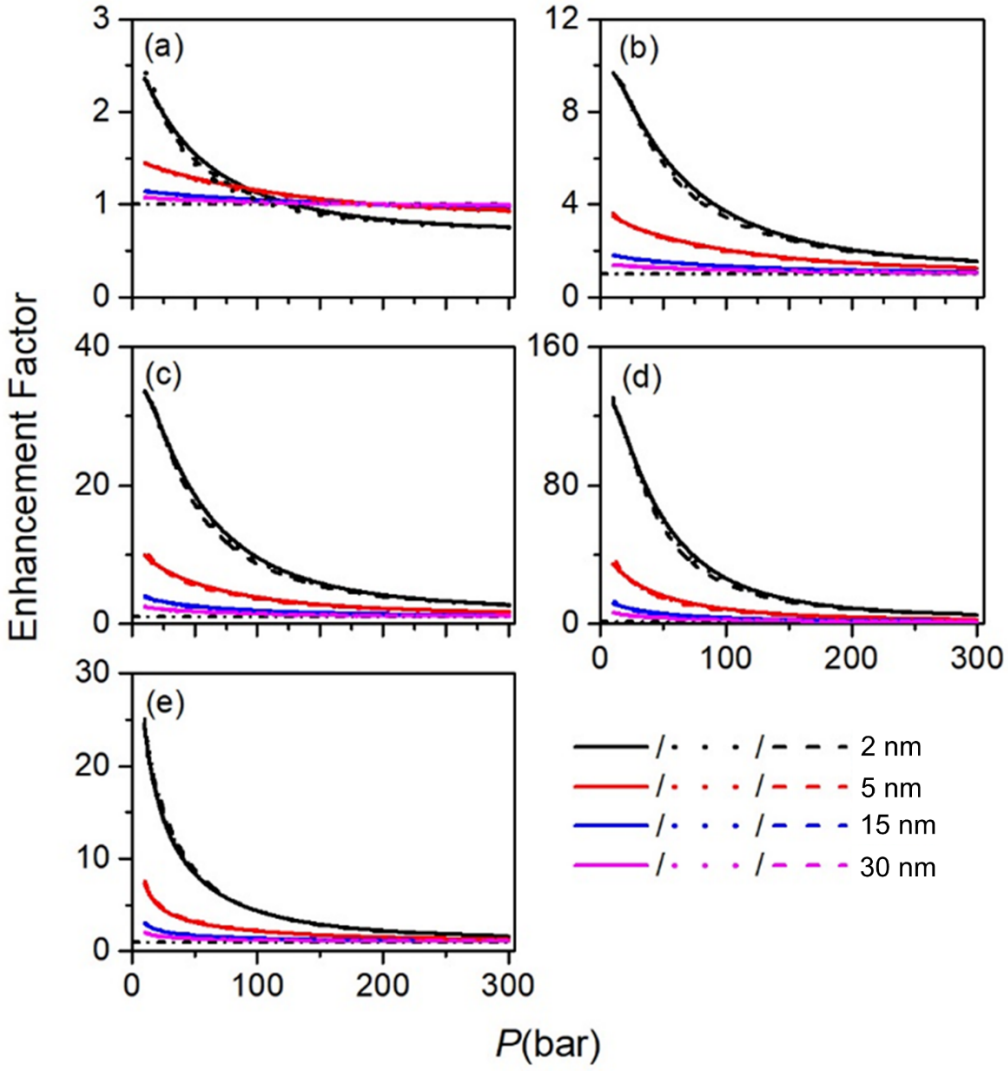


**Figure 3-4** The enhancement factors of (a) $C_1$, (b) $C_2$, (c) $C_3$, (d) $nC_4$, and (e) their mixtures in

nanopores of 2 nm (black), 5 nm (red), 15 nm (blue), 30 nm (magenta) at $T$ = 363.15 K. Solid, dotted, and dashed lines represent Eagle Ford, Middle Bakken, and Horn River, respectively. For clarity, we also present the unity enhancement factor as black dash-dotted lines.

The effect of PSD on the released fluids from nanopores and bulk regions during each pressure drop is shown in **Figure 3-5**. The released fluid densities of component $i$ from nanopores $\Delta\rho_{i,W}$ and bulk region $\Delta\rho_{i,b}$ during each pressure drop are given as,

$$\begin{cases} \Delta\rho_{i,W} = \rho_{i,W}^{old} - \rho_{i,W}^{new} \\ \Delta\rho_{i,b} = \rho_{i,b}^{old} - \rho_{i,b}^{new} \end{cases}, \tag{3-22}$$

where the superscript *new* and *old* represent the present and previous pressures, respectively. Due to strong surface absorption in small nanopores (*i.e.*, $W = 2$ nm), $C_3$ and $nC_4$ are not released. Compared to the lighter components, the effect of PSD on the heavier components is more significant, especially in small nanopores. In contrast to the nanopores, the effect of PSD on released fluids during each pressure drop is less significant in the bulk region. The interplay between the nanopores and bulk region results in the different bulk compositions (as shown in **Figure 3-3**) and adsorption behavior in nanopores (as shown in **Figure 3-2**). Such correlated behavior in turn affects the compositions of cumulative released fluids from the entire nanopore–bulk system as shown in **Figure 3-6**. Similar to **Figure 3-3**, the effect of PSD on cumulative released fluids compositions is significant, especially in small nanopores and the heavier components.

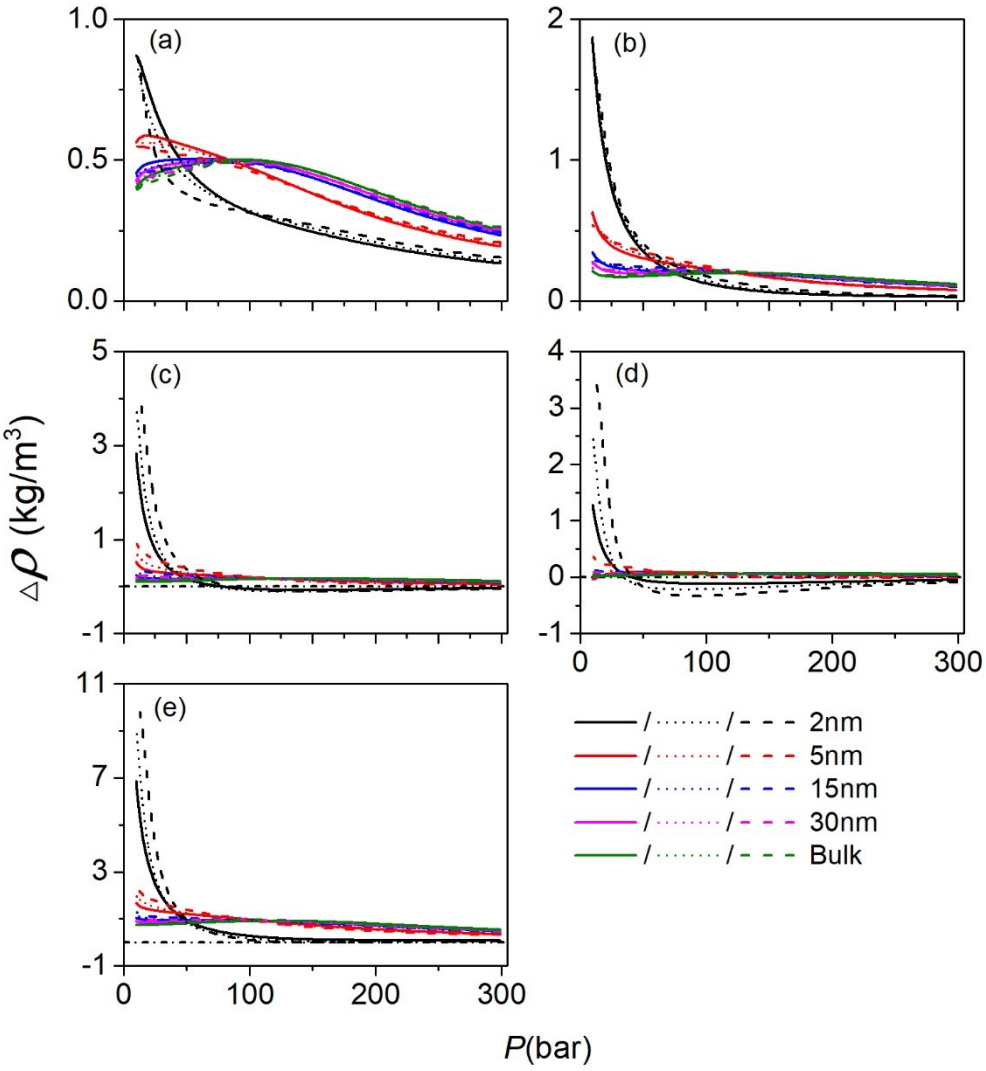


**Figure 3-5** The released (a) $C_1$, (b) $C_2$, (c) $C_3$, and (d) $nC_4$ and (e) their mixtures from nanopores of 2 nm (black), 5 nm (red), 15 nm (blue), 30 nm (magenta) and the bulk region (olive) during each pressure drop at $T$ = 363.15 K. Solid, dotted, and dashed lines represent Eagle Ford, Middle Bakken, and Horn River, respectively. For clarity, we also present the boundary of releasing and adsorbing as black dash-dotted lines.

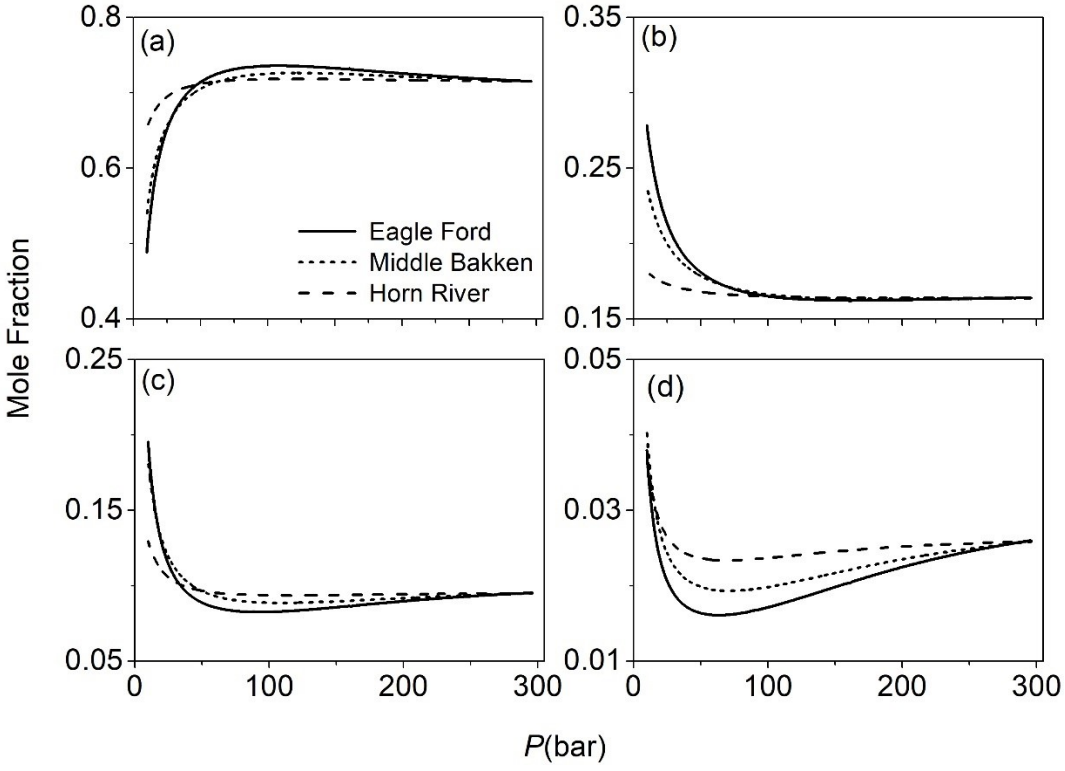


**Figure 3-6** Mole fractions of cumulative released fluids from the entire nanopore–bulk system of (a) $C_1$, (b) $C_2$, (c) $C_3$, and (d) $nC_4$ in different PSD at $T$ = 363.15 K. Solid, dotted, and dashed lines represent Eagle Ford, Middle Bakken, and Horn River, respectively.

Based on the average mass densities, we can obtain the residual ratios $R_{i,W}^{res}$ of different components in nanopores and the bulk region in **Figure 3-7**. The residual ratios of each component $i$ in nanopores $R_{i,W}^{res}$ and bulk region $R_{i,b}^{res}$ and their mixtures in nanopores $R_{mix,W}^{res}$ and the bulk region $R_{mix,b}^{res}$ at given $P$ are given as,

$$\begin{cases} R_{i,W}^{res} = n_{i,W}^{res} / n_{i,W}^{init} \\ R_{i,b}^{res} = n_{i,b}^{res} / n_{i,b}^{init} \\ R_{mix,W}^{res} = \sum_i n_{i,W}^{res} / \sum_i n_{i,W}^{init} \\ R_{mix,b}^{res} = \sum_i n_{i,b}^{res} / \sum_i n_{i,b}^{init} \end{cases}, \tag{3-23}$$

where $n_{i,W}^{res}$ is the remaining amount of component $i$ at given $P$ in nanopores of $W$ and $n_{i,W}^{init}$ is the initial amount of component $i$ at $P^{init}$ in nanopores of $W$. For both $C_1$ and $C_2$, $R_{i,W}^{res}$

decreases as pressure decreases. However, for $C_3$ and $nC_4$, in small nanopores (*i.e.*, $W = 2$ nm), $R_{i,W}^{res}$ can be higher than 1, indicating that as pressure drops, these hydrocarbon fluids in these nanopores may not be recovered. The effect of PSD on the heavier components and the fluids in smaller pores is more significant, resulting in the $nC_4$ residual ratio higher for PSD with more larger pores (*i.e.*, Horn River).

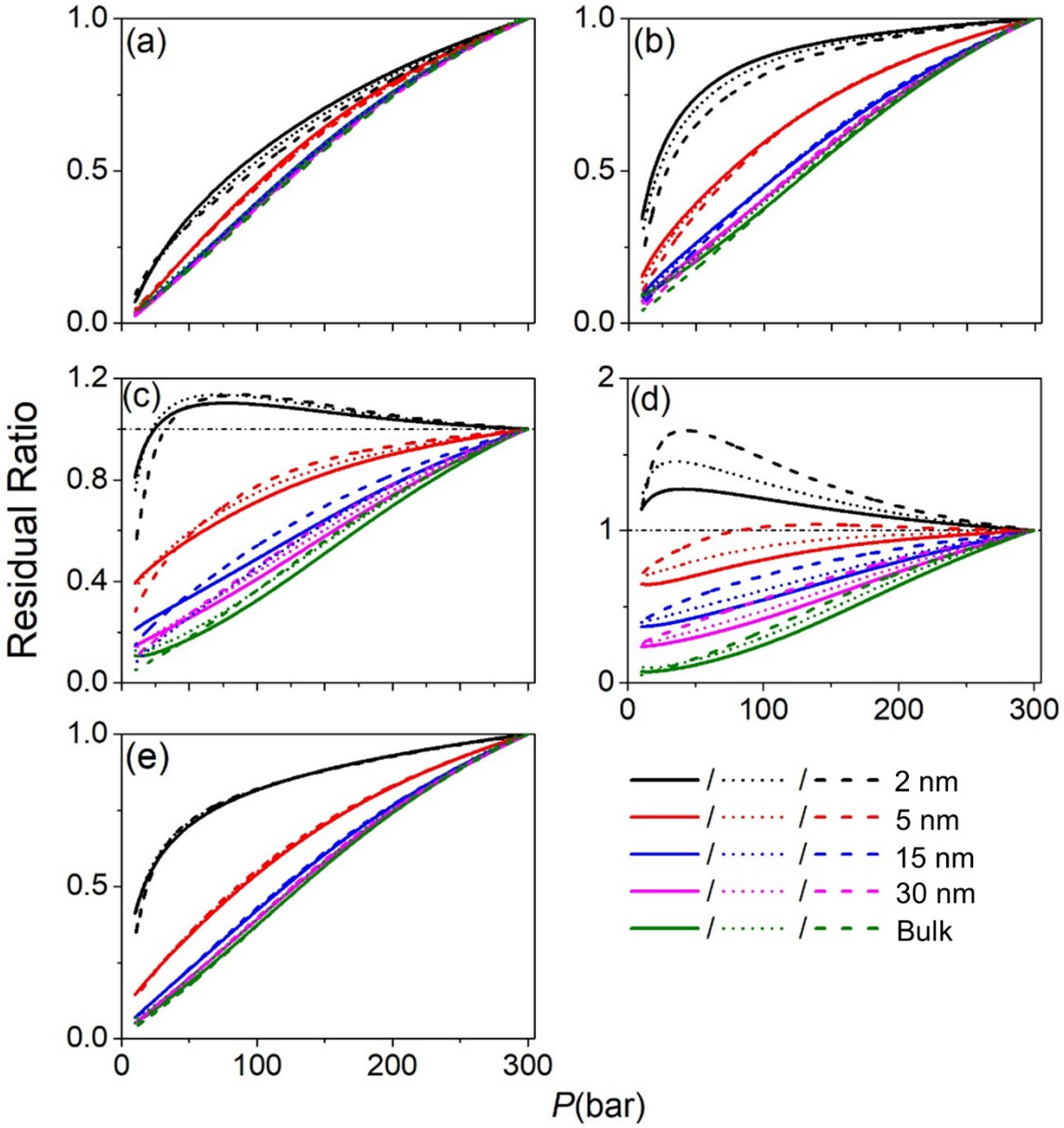


**Figure 3-7** The residual ratios of (a) $C_1$, (b) $C_2$, (c) $C_3$, (d) $nC_4$, and (e) their mixtures in nanopores of 2 nm (black), 5 nm (red), 15 nm (blue) 30 nm (magenta), and bulk region (olive) at $T$ = 363.15 K. Solid, dotted, and dashed lines represent Eagle Ford, Middle Bakken, and Horn River, respectively. For clarity, we also present the unity residual ratio as black dash-dotted lines.

To better understand the effect of PSD on the overall recovery factors of each component and their mixture from the whole system in **Figure 3-8**. we present the overall recovery factor $Re_i$ of component $i$ and their mixtures given as,

$$\begin{cases} Re_i = 1 - \dfrac{\sum\limits_W \rho_{i,W} V_{p,W} + \rho_{i,b} V_b}{\sum\limits_W \rho_{i,W}^{init} V_{p,W} + \rho_{i,b}^{init} V_b} \\ Re_{mix} = 1 - \dfrac{\sum\limits_i \left( \sum\limits_W \rho_{i,W} V_{p,W} + \rho_{i,b} V_b \right)}{\sum\limits_i \left( \sum\limits_W \rho_{i,W}^{init} V_{p,W} + \rho_{i,b}^{init} V_b \right)} \end{cases} \tag{3-24}$$

where $\rho_{i,W}^{init}$, $\rho_{i,W}$ are average mass densities of component $i$ in a pore of given $W$ at $P^{init}$ and $P$, respectively; $\rho_{i,b}^{init}$, $\rho_{i,b}$ are mass densities of component $i$ in bulk at $P^{init}$ and $P$, respectively. It shows that the overall recovery factors for all hydrocarbon components are higher when PSD has more larger pores (*i.e.*, Horn River). Especially for $nC_4$, this phenomenon seems contradictory to that shown in **Figure 3-7**. It is because Horn River has a larger portion of the bulk region than Eagle Ford and Middle Bakken cases, in which the volume expansion in the bulk region is significant. The effect of PSD on hydrocarbon recovery is more pronounced on the heavier components.

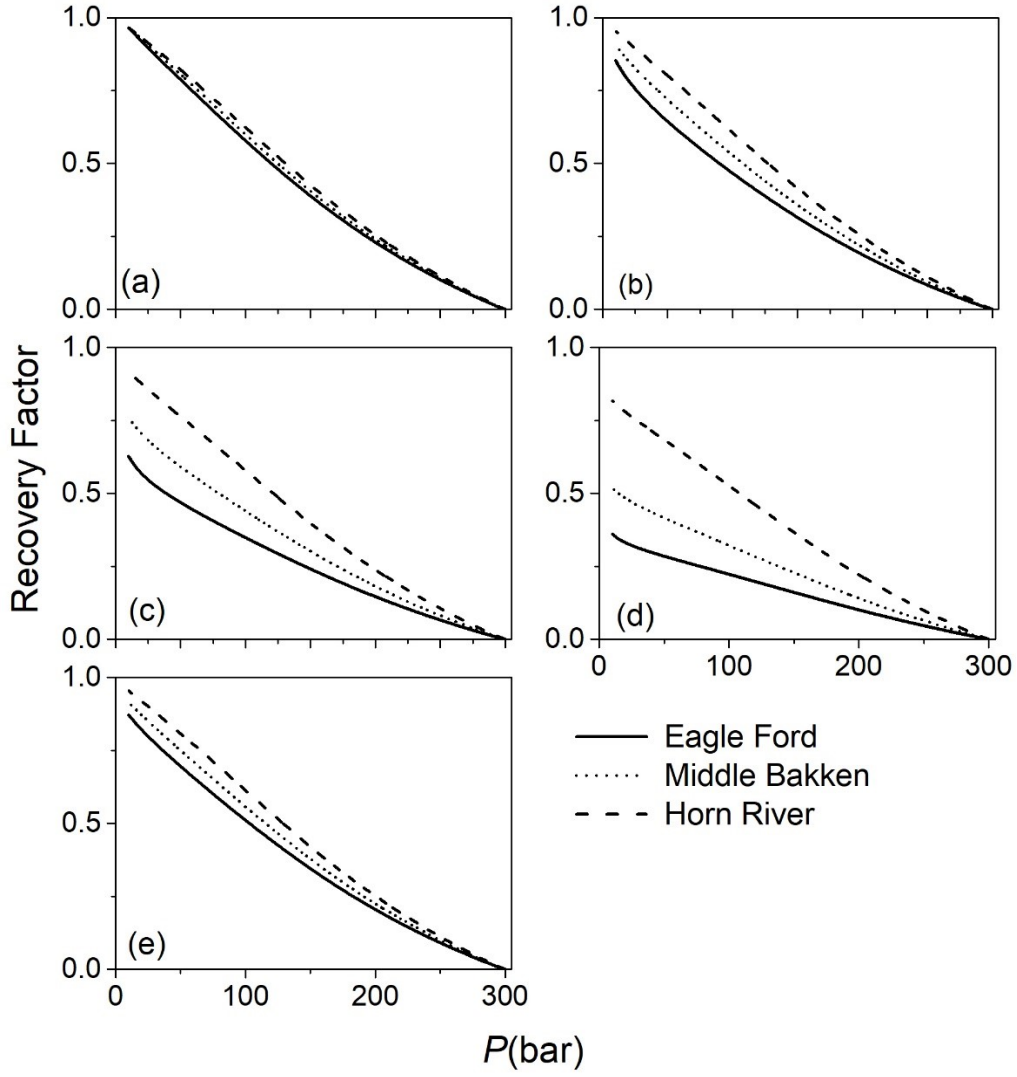


**Figure 3-8** The overall recovery factors of (a) $C_1$, (b) $C_2$, (c) $C_3$, (d) $nC_4$, and (e) their mixtures at $T$ = 363.15 K. Solid, dotted, and dashed lines represent Eagle Ford, Middle Bakken, and Horn River, respectively.

### 3.4. Conclusions

In this work, we used engineering DFT to investigate the effect of PSD on the adsorption and properties of confined hydrocarbon mixtures employing PSDs from Eagle Ford [167], Middle Bakken [181], and Horn River [182] sub-formation characterization. We considered $C_1$-$C_2$ mixtures and $C_1$-$C_2$-$C_3$-$nC_4$ quaternary mixtures.

In the $C_1$-$C_2$-$C_3$-$nC_4$ quaternary mixture case, average mass densities of heavier hydrocarbons in small nanopores, *i.e.*, $C_3$ and $nC_4$, first increase, then decrease as pressure decreases. For $C_1$ and $C_2$, as pressure drops, the average mass densities in all nanopores decrease. $C_1$ average mass density in small nanopores is even lower than bulk, due to competitive

adsorption. Unlike $C_1$ and $C_2$, $C_3$ and $nC_4$ in micropores (*i.e.*, $W \leq 2$ nm) might not be recoverable during the pressure drop process. The effect of PSD is pronounced in quaternary mixtures. Due to the interplay between the nanopores and bulk region, bulk fluid compositions are strongly influenced, especially for the heavier components. The deviation in the $nC_4$ bulk mole fraction can be up to 50%. PSD also affects the residual ratio of hydrocarbon fluids in nanopores and the bulk region. The effect of PSD is more pronounced for the heavier components and the fluids in smaller nanopores. The overall recovery factor is strongly affected by PSD, as it increases as the portion of larger pores increases.

Collectively, PSD strongly influences the released fluids, bulk fluid compositions, and hydrocarbon mixture adsorption in nanopores, especially for the heavier components. It also influences residual ratios, compositions of produced fluids, and recovery factors. Our work should provide a fundamental understanding about the effect of PSD on hydrocarbon mixture behavior in shale porous media and important insights into the optimization of shale gas recovery. In addition, for simplicity, all nanopores are simulated as slit geometry, while the all-atom kerogen model has been used to study hydrocarbon adsorption and kinetics within [183]. Unlocking these effects coupled with the PSD effect on hydrocarbon mixture adsorption and recovery in shale nanoporous media remain as future tasks.

公式章 (下一章) 节 1

## CHAPTER 4 Hydrocarbon Mixture and $CO_2$ Adsorptions in a Nanopore–bulk Multiscale System in Relation to $CO_2$ Enhanced Shale Gas Recovery

(A version of this chapter has been published in Chemical Engineering Journal 415 (2021) 128398 by Yingnan Wang and Zhehui Jin)

### Abstract

Thanks to the continuous depletion of conventional gas reservoirs, shale gas plays an important role to meet the global natural gas demand. The $CO_2$ 'huff-n-puff' process has been proven to be an effective method to enhance shale gas recovery and sequestrate $CO_2$. Unlike conventional reservoirs, shale media can contain a significant amount of nano-scaled pores and their pore volume can be comparable to that of macropores and fractures in which fluids behave as bulk. While previous works studied the mechanisms of the $CO_2$ 'huff-n-puff' process in shale gas exploitation, the volume partitioning effect between nanopores and macropores/fractures was not fully taken into account. In this work, we built nanopore–bulk multiscale models with varying pore size distributions (PSDs) to study the $CO_2$ 'huff-n-puff' process in a constant volume depletion (CVD) setting by using density functional theory (DFT). We found that the volume partitioning effect on adsorption, fluid compositions, and hydrocarbon mixture ($C_1$, $C_2$, and $C_3$) recovery is significant in the $CO_2$ 'huff-n-puff' process. The majority of hydrocarbon mixtures can be released from smaller nanopores during the $CO_2$ 'huff' and 'soak' process, while the average hydrocarbon densities in larger nanopores might increase. During the $CO_2$ 'huff' and 'soak' process, due to a stronger confinement effect in smaller pores, the PSD case with a higher volume ratio of smaller pores releases fewer hydrocarbons, while storing more $CO_2$ per unit pore volume. Overall, the volume partitioning has a significant effect on hydrocarbon adsorption, compositions, and recovery as well as $CO_2$ storage during the $CO_2$ 'huff-n-puff' process in shale gas exploitation and geological $CO_2$ sequestration.

## 4.1. Introduction

Thanks to the continuous depletion of conventional gas reservoirs [166] and the growing global energy demand [190], shale gas has become an important natural gas supply. Due to the presence of a significant amount of nanosized pores [191], shale media is associated with ultra-low permeability and porosity [49-51]. In contrast to the conventional gas reservoirs, in shale media, surface adsorption plays a dominant role in total gas uptake and estimation of the gas-in-place (GIP) [5]. On the other hand, based on field data [52], shale gas production rates generally plummet rapidly which greatly hampers its exploration and development activities. In fact, the average recovery efficiency of shale gas is less than 10%, if only horizontal and hydraulic fracturing methods are implemented [53]. As an enhanced gas recovery (EGR) method, $CO_2$ injection has been proven to be an effective method to drive up shale gas production rate by up to 8 times [52]. Additionally, considering abundant storage capacity and the readily-available underground, as well as surface infrastructures, $CO_2$ injection into shale gas reservoirs, can be a viable option to alleviate carbon emissions through geological $CO_2$ sequestrations [54, 55].

During the $CO_2$-EGR process in shale gas exploitation, $CO_2$ 'huff-n-puff' is one of the most widely used methods [52, 56-58], which can be generally separated into $CO_2$ injection ('huff'), well shut-in ('soak'), and production ('puff') periods [59, 60]. There have been a few experimental measurements on $CO_2$ 'huff-n-puff' on shale gas recovery [61-64]. Holmes *et al.* [61] implemented experiments about $CO_2$ uptake in powered idealized shales of both organic and inorganic components. Their results indicated shale sorption has a positive linear correlation with increasing total organic carbon and pore capacity and suggested understanding other characteristics of additional pore size, like varying composition, maturity, and pore size distribution, is of great importance. Liu *et al.* [62, 63] used the low-field nuclear magnetic resonance (NMR) spectroscopy to quantitatively identify the adsorbed, pore-medium-confined, and free $C_1$ during pressure drawdown and the $CO_2$ 'huff-n-puff' process under simplified laboratory conditions at 35 °C. They found that the desorption efficiency of adsorbed $C_1$ is enhanced by ~26% due to $CO_2$ injection. On the other hand, numerical simulations have been widely used to investigate the $CO_2$ 'huff-n-puff' process for shale gas recovery and $CO_2$ sequestration [73, 74, 192]. Xu *et al.* [73] studied the performance of $CO_2$ 'huff-n-puff' in a triple-porosity dule-permeability shale

model by considering gas adsorption/desorption, competitive adsorption, and binary gas diffusion. They found that the supercritical $CO_2$ 'huff-n-puff' can increase shale gas recovery by 15%. Their simulation results also revealed that gas production rate and ultimate recovery would be higher for a higher total organic carbon (TOC) content. Kim *et al*. [74] assessed the performance of $CO_2$ 'huff-n-puff' in three different shale formations by multi-component numerical simulations. They reported that the $CO_2$ 'huff-n-puff' enhances $C_1$ production by 6% in the Barnett shale, while it is less effective in the other two shale models due to different shale rock properties. Although these numerical simulations are helpful to understand the effect of $CO_2$ injection on shale gas recovery and geological $CO_2$ sequestration, the underlying mechanisms governing these phenomena occurring in nanosized pores, like the composition change, the interplay between bulk and nanopores, mixtures competitive adsorption/desorption during $CO_2$ injection/sequestration, *etc*., are largely ambiguous.

In this context, molecular simulations and theoretical modeling have also been applied to study $CO_2$ 'huff-n-puff' performance in shale gas recovery and geological $CO_2$ sequestration from molecular perspectives [5, 65-72]. Yuan *et al*. [66] studied the enhanced recovery, adsorption energy, and configuration of $C_1$-$CO_2$ mixtures in carbon nanotubes (CNT) by molecular dynamics (MD) simulations. They found that the pre-adsorbed $C_1$ can be displaced by $CO_2$ injection in CNT and the recovery of $C_1$ is enhanced by more than 15%. Zhou *et al*. [69, 70] studied pure and hydrocarbon mixture recovery during $CO_2$ 'huff-n-puff' in kerogen nanopores by GCMC simulations. They explicitly investigated the effect of moisture content, pore size, and injection cycles. They found that during pressure drawdown, while $C_1$ in the adsorption layer and the middle of the pores can be recovered, $C_3$ can only be recovered in the middle of the pores. On the other hand, the injected $CO_2$ can recover hydrocarbons in the adsorption layer. Zhang *et al*. [71] studied the recovery mechanisms of $C_1$-$C_2$-$C_3$ mixtures in organic and inorganic nanopores during the $CO_2$ 'huff-n-puff' process. They revealed that $CO_2$ 'huff' and ‘soak’ is more efficient in organic nanopores in terms of recovery, which is more obvious for the heavier component ($C_3$). Due to $CO_2$ injection, $CO_2$ is stored in nanopores by displacing hydrocarbons and dominating the first adsorption layer in both organic and inorganic nanopores. Bakhshian *et al.* [72] developed a coupled adsorption and deformation model

based on lattice density functional theory (DFT) and finite-element formulation. They found a faster, and a higher amount of adsorption in duct pores compared with that of a slit pore and demonstrated a sharp rise in adsorption isotherm and swelling strain near the bulk critical point of $CO_2$. While these molecular simulations and theoretical studied $CO_2$-EGR and $CO_2$ sequestration from molecular perspectives, they generally assume that the bulk phase volume is much larger than that of nanopores so that the fluid injection into and release from the nanopores do not alter the fluid compositions in bulk.

However, in shale reservoirs, the pore volume in nanopores can be comparable to that of macropores/fractures [8, 75], and the volume partitioning among nanopores and macropores/fractures (bulk) plays an important role in fluid properties and phase behaviors [48, 78-81]. Due to the comparable pore volume, adsorbed/released fluids in/from nanopores could influence bulk fluid properties, which in turn could further affect fluid density distributions in nanopores through chemical equilibrium [70, 71, 76, 77]. A few works incorporated such a nanopore–bulk multiscale system to study the properties of pure and hydrocarbon mixtures [48, 78, 80-84]. They generally show that hydrocarbon mixture phase behaviors in the nanopore–bulk multiscale system are different from those in the systems with infinitely large bulk reservoirs. Thus, to simulate the hydrocarbons recovery process in shale reservoirs, a constant volume depletion (CVD) method can be implemented. In our previous work [79], we studied the effect of volume partitioning on hydrocarbon mixture adsorption in three different shale samples in a CVD setting by using engineering density functional theory (DFT). We found that due to the volume partitioning, the bulk fluid composition keeps changing during the pressure drawdown process and the released hydrocarbon properties are dependent on pore size distribution (PSD). However, to the best of our knowledge, the effect of volume partitioning on $CO_2$-EGR and $CO_2$ sequestration during the $CO_2$ 'huff-n-puff' process has not been revealed yet.

Thus, in this work, we explicitly study the effect of volume partitioning on hydrocarbon mixtures and $CO_2$ adsorption in shale nanoporous media during the $CO_2$ 'huff-n-puff' process. Kerogen is the main constituent of organic matters in shale, which greatly contributes to the total GIP [68, 193-195]. For simplicity, in this work, we use carbon slit nanopores [77, 140, 156, 157] to represent kerogen nanopores, which have shown a good agreement with experimental measurements on gas adsorption in kerogen nanoporous

media [14, 196, 197]. Note that the "nanopores" used in this work include micropores (< 2 nm) and mesopores (2–50 nm) [198]. Three different PSD cases based on characterizations of shale sub-formations are considered in a CVD setting, in which nanopore volume is comparable to that in the bulk region. By using perturbed-chain-statistical-associating-fluid-theory-based DFT (PC-SAFT DFT) [199-201], which has shown an excellent agreement with experimental measurements and molecular simulations in terms of fluid adsorption characteristics [200-210], hydrocarbon mixtures and $CO_2$ adsorption, their density distributions, and average densities in nanopores can be explicitly calculated. On the other hand, in contrast to molecular simulations, PC-SAFT DFT can significantly reduce the calculation time [203-206, 211]. During the primary pressure drawdown and $CO_2$ 'puff' processes, hydrocarbon mixtures and $CO_2$ are depleted from the nanopore–bulk multiscale system by the CVD method, while during $CO_2$ 'huff' and 'soak' process, $CO_2$ is injected without any fluid recovery from the entire system. Our work should provide a fundamental understanding about the effect of volume partitioning on hydrocarbon mixtures and $CO_2$ adsorption characteristics and important insights into shale gas exploitations and geological $CO_2$ sequestrations during the $CO_2$ 'huff-n-puff' process.

## 4.2. Model and Methodology

### 4.2.1. Nanopore–Bulk Multiscale System

The nanopore–bulk multiscale system consists of two distinct parts: nanopores and the bulk region [79]. The bulk region may refer to hydraulic/natural fractures as well as macropores in the shale matrix. It is reported that in large pores (≥ 50 nm), fluid properties are similar to those in bulk [125, 170]. Thus, similar to our previous work [79], we assume that hydrocarbon mixtures and $CO_2$ in pores larger than 50 nm behave as bulk. On the other hand, pores of size smaller than 50 nm are treated as nanopores in which fluid–surface interactions are explicitly considered. Based on the PSDs from Eagle Ford [167], Horn River [182], and Middle Bakken [181] shale sub-formation characterizations, four distinct nanopores are used to represent micropores and mesopores in shale: 2 nm (≤2 nm), 5 nm (2~10 nm), 15 nm (10~20 nm), and 30 nm (20~50 nm) [79]. The pore volume fractions in each nanopore and the bulk region are presented in **Table 4-1**. In our model, the pressure $P$ is dictated by the fluid pressure in the bulk region. While the chemical potential of each component in nanopores is the same as that in bulk at equilibrium, we

do not consider the interfaces between nanopores and the bulk region. It has been shown that the mechanical equilibrium between nanopores and bulk is always automatically satisfied by the equality of chemical potentials [186].

**Table 4-1** Volume ratios and absolute volume in the nanopore–bulk multiscale systems of PSDs from the Eagle Ford (EF) [167], Middle Bakken (MB) [181], and Horn River (HR) [182] shale sub-formations.

| | | Nanopores | | | | Bulk |
|---|---|---|---|---|---|---|
| | | 2 nm | 5 nm | 15 nm | 30 nm | |
| Volume ratio (%) | EF | 11.50 | 27.50 | 12.00 | 18.00 | 31.00 |
| | MB | 2.87 | 15.00 | 33.38 | 34.53 | 14.22 |
| | HR | 0.48 | 2.59 | 4.61 | 20.73 | 71.59 |
| Absolute volume ($m^3$) | EF | 0.1150 | 0.2750 | 0.1200 | 0.1800 | 0.3100 |
| | MB | 0.0287 | 0.1500 | 0.3338 | 0.3453 | 0.1422 |
| | HR | 0.0048 | 0.0259 | 0.0461 | 0.2073 | 0.7159 |

### 4.2.2. Material Balance

In this work, material balance calculation is necessary for 1) primary pressure drop; 2) $CO_2$ 'huff' and 'soak'; 3) $CO_2$ 'puff' processes. During the CVD process, the bulk region volume is expanded to lower the bulk pressure, while the fluids in the excess bulk volume are removed from the entire system [81]. The system temperature is fixed at 333.15 K with an initial pressure $P_0 = 500$ bar, which is representative of the typical temperature and pressure of shale gas reservoirs [55, 212, 213]. $C_1$-$C_2$-$C_3$ mixtures are used to represent hydrocarbon mixtures and the initial bulk compositions for three different PSD cases are listed in **Table 4-2**. The initial mole fraction of component $k$ in the entire system, $X_k^{init}$, at $P_0$ is given as

$$X_k^{init}\left(P_0\right) = \frac{m_k^{init}\left(P_0\right)}{\sum_{k=C_1,C_2,C_3} m_k^{init}\left(P_0\right)}, k = C_1, C_2, C_3, \tag{4-1}$$

with

$$m_k^{init}\left(P_0\right) = \rho_{k,b}^{init}\left(P_0\right)V_b + \sum_W \rho_{ave,k,W}^{init}\left(P_0\right)V_{p,W}, k = C_1, C_2, C_3, \tag{4-2}$$

where $V_{p,W}$ is the pore volume of the nanopore of $W$, $V_b$ is the bulk volume. In this work, we set the entire system volume identical for all three PSD cases as 1 $m^3$. The pore and bulk volume as well as their volume ratios are listed in **Table 4-1**. $\rho_{k,b}^{init}\left(P_0\right)$ and $\rho_{ave,k,W}^{init}\left(P_0\right)$ are molar density of component $k$ in bulk and average molar density of component $k$ in nanopore of $W$ at $P_0$, respectively, $m_k^{init}\left(P_0\right)$ is the total mole number of component $k$ at $P_0$. While $\rho_{k,b}^{init}\left(P_0\right)$ is obtained from the PC-SAFT equation of state (EOS) at $P_0$, $\rho_{ave,k,W}^{init}\left(P_0\right)$ is obtained from the PC-SAFT DFT.

**Table 4-2** Initial bulk mole fractions for $C_1$-$C_2$-$C_3$ mixtures in different PSDs.

| | $C_1$ | $C_2$ | $C_3$ | Sum |
|---|---|---|---|---|
| Eagle Ford | 0.85 | 0.15 | 0.05 | 1 |
| Middle Bakken | 0.85 | 0.15 | 0.05 | 1 |
| Horn River | 0.85 | 0.15 | 0.05 | 1 |

During the CVD process, $V_{p,W}$ does not change but $V_b$ expands as $P$ decreases, and the fluids in the excess bulk volume are then removed. The material balance is applied to calculate the expanded bulk volume $V_{k,b}^o\left(P\right)$ based on component $k$ before fluid removal at given $P$ and the removed fluid $m_k^{re}\left(P\right)$ of component $k$ in the excess bulk volume,

$$V_{k,b}^o\left(P\right)=\frac{m_k^o\left(P\right)-\sum_W \rho_{ave,k,W}\left(P\right)V_{p,W}}{X_{k,b}\left(P\right)\rho_b\left(P\right)},\ k=C_1,C_2,C_3, \tag{4-3}$$

$$m_k^{re}\left(P\right)=\left[V_b^o\left(P\right)-V_b\right]\rho_{k,b}\left(P\right),\ k=C_1,C_2,C_3, \tag{4-4}$$

where $m_k^o\left(P\right)$ is the total mole number of component $k$ at $P$ before removal; $\rho_{ave,k,W}\left(P\right)$ and $\rho_b\left(P\right)$ are the average molar density of component $k$ in nanopore of $W$ and molar density of component $k$ in bulk at $P$, respectively; $X_{k,b}\left(P\right)$ refers to the mole fraction of component $k$ in bulk at $P$. An iterative method is used to find the bulk mole fraction $\left\{X_{k,b}\left(P\right)\right\}$, which satisfies that $V_{k,b}^o\left(P\right)$ converge at the actual expanded

bulk volume $V_b^o(P)$. Thus, the remaining fluids in the entire system $m_k^n(P)$ of component $k$ at $P$ are given as

$$m_k^n(P) = m_k^o(P) - m_k^{re}(P), k = C_1, C_2, C_3. \quad (4\text{-}5)$$

Then, $m_k^n(P)$ serves as $m_k^o$ at the subsequent pressure condition. In each step, we lower $P$ by 2 bar in all PSD cases until $P_1$ = 100 bar, which can be a typical $CO_2$ injection pressure in the fields [52, 57, 192, 214, 215].

Then, the $CO_2$ 'huff' and 'soak' process during which bulk fluids and those in nanopores reach chemical equilibrium after $CO_2$ injection is initiated by injecting an equal amount of $CO_2$ in each PSD case as listed in **Table 4-3**. We note that in this process, both bulk and nanopore volumes remain unchanged and no fluids are released from the entire system. Due to $CO_2$ injection, the bulk pressure is elevated to a higher pressure $P_2$, while the bulk composition is altered. To find the equilibrium bulk composition and pressure, the materials balance equations are solved, which are given as,

$$\begin{cases} m_k(P_2) = m_k(P_1) = \rho_{k,b}(P_2)V_b + \sum_W \rho_{ave,k,W}(P_2)V_{p,W}, \ k = C_1, C_2, C_3 \\ m_{co_2}(P_2) = m_{co_2}^{inj}(P_1) = \rho_{co_2,b}(P_2)V_b + \sum_W \rho_{ave,co_2,W}(P_2)V_{p,W} \\ \sum_{k=C_1,C_2,C_3} X_{k,b}(P_2) + X_{CO_2,b}(P_2) = 1 \end{cases} \quad (4\text{-}6)$$

where $m_k(P_1)$ and $m_k(P_2)$ are the total mole number of component $k$ in the entire system at $P_1$ and $P_2$, respectively; $m_{CO_2}^{inj}(P_1)$ is the total mole number of injected $CO_2$ at $P_1$; $m_{CO_2}(P_2)$ is the total mole number of $CO_2$ in the entire system at $P_2$. The bulk composition and pressure are obtained by solving Eq. (4-6) iteratively. The equilibrium bulk pressures and compositions in each PSD case are listed in **Table 4-4**.

**Table 4-3** Injected $CO_2$ amount and its molar ratio in the total system at $P_1$ = 100 bar in each PSD.

| | Injected $CO_2$ | |
|---|---|---|
| | Absolute amount (mol) | Molar ratio in system |
| Eagle Ford | 2379.58 | 27.1% |
| Middle Bakken | 2379.58 | 30.0% |
| Horn River | 2379.58 | 33.9% |

During the $CO_2$ 'puff' process, the pressure continues to decrease from $P_2$. The bulk volume expands and fluids are released from the entire system during the $CO_2$ 'puff' process as pressure drops. The material balance of hydrocarbon mixtures and $CO_2$ in the entire system during the $CO_2$ 'puff' process is given as,

$$\begin{cases} V_{k,b}^{o}(P) = \dfrac{m_k^o(P) - \sum_W \rho_{ave,k,W}(P) V_{p,W}}{X_{k,b}(P)\rho_b(P)} \\ m_k^{re}(P) = \left[V_b^o(P) - V_b\right]\rho_{k,b}(P) \\ m_k^n(P) = m_k^o(P) - m_k^{re}(P) \end{cases} , k = C_1, C_2, C_3, CO_2 . \quad (4\text{-}7)$$

The bulk pressure decreases by 2 bar in each step. Though $P_2$ in each PSD case is slightly different as shown in **Table 4-4**, the end pressure of all PSDs is set as $P_3 = 50$ bar [70, 71, 216, 217].

**Table 4-4** Bulk pressure, composition, and densities of hydrocarbons and $CO_2$ in various PSD cases before and after $CO_2$ 'huff' and 'soak' processes. Note that the $\Delta P_{b,\ after}$ is defined as $\Delta P_{b,after} = \dfrac{\left|\bar{P}_{b,after} - P_{b,after}\right|}{\bar{P}_{b,after}} \times 100\%$, where $P_{b,after}$ and $\bar{P}_{b,after}$ are bulk pressure for each PSD and the average bulk pressure for all three PSDs after $CO_2$ 'huff' and 'soak', respectively. $\Delta\rho_b / \rho_b^{bef} = \left(\rho_b^{aft} - \rho_b^{bef}\right) / \rho_b^{bef}$ represents the relative increases of bulk density, where $\rho_b^{aft}$, $\rho_b^{bef}$ are bulk densities of each component before and after $CO_2$ 'huff' and 'soak', respectively.

| | PSD cases | Bulk pressure $P_b$ (bar) | $\Delta P_{b,after}$ (%) | Bulk composition | | | | Bulk density $\rho_b$ (kmol/m$^3$) | | | | $\Delta\rho_b/\rho_b^{bef}$ | | |
|---|---|---|---|---|---|---|---|---|---|---|---|---|---|---|
| | | | | $C_1$ | $C_2$ | $C_3$ | $CO_2$ | $C_1$ | $C_2$ | $C_3$ | $CO_2$ | $C_1$ | $C_2$ | $C_3$ |
| Before $CO_2$ 'huff' and 'soak' | EF | 100 | N/A | 0.825 | 0.139 | 0.036 | 0 | 3.55 | 0.60 | 0.15 | 0 | N/A | N/A | N/A |
| | MB | 100 | N/A | 0.809 | 0.148 | 0.043 | 0 | 3.52 | 0.64 | 0.19 | 0 | N/A | N/A | N/A |
| | HR | 100 | N/A | 0.801 | 0.151 | 0.048 | 0 | 3.50 | 0.66 | 0.21 | 0 | N/A | N/A | N/A |
| After $CO_2$ 'huff' and 'soak' | EF | 146.7 | 1.1 | 0.588 | 0.118 | 0.037 | 0.257 | 3.99 | 0.80 | 0.25 | 1.74 | 0.12 | 0.33 | 0.64 |
| | MB | 144.8 | 0.2 | 0.557 | 0.114 | 0.039 | 0.290 | 3.77 | 0.77 | 0.26 | 1.96 | 0.07 | 0.20 | 0.42 |
| | HR | 143.7 | 0.9 | 0.526 | 0.102 | 0.035 | 0.337 | 3.56 | 0.69 | 0.24 | 2.27 | 0.02 | 0.05 | 0.13 |

### 4.2.3. The Perturbed-chain-statistical-associating-fluid-theory-based Density Functional Theory (PC-SAFT DFT)

The perturbed-chain-statistical-associating-fluid-theory-based density functional theory (PC-SAFT DFT) [199, 200] is used to consider the chemical equilibrium between hydrocarbon fluids in bulk region and nanopores. Based on Wertheim's first-order thermodynamic perturbation theory [218-221], fluid molecules in the framework of PC-SAFT DFT are treated as coarse-grained representations of real ones, where non-spherical molecules are assumed to be chains of tangentially bonded spherical segments with the van der Waals interaction [199]. In this work, segments in each chain are treated identically [199, 222]. The temperatures in nanopores and the bulk region are the same. The PC-SAFT DFT calculations are applied to the fluids in nanopores only, for a given pressure and temperature condition. The equilibrium hydrocarbon mixture and $CO_2$ densities in the bulk region and their density distributions in nanopores are determined by mass conservation and chemical equilibrium between the fluids in nanopores and those in bulk.

Within the framework of DFT, for a given nanopore, the grand potential $\Omega\left[\left\{\rho_k(\mathbf{r})\right\}\right]$, which is functional of density distribution $\left\{\rho_k(\mathbf{r})\right\}$, is the thermodynamic function of choice and related to the Helmholtz free-energy functional $F\left[\left\{\rho_k(\mathbf{r})\right\}\right]$ via the Lagrange transformation [146],

$$\Omega\left[\left\{\rho_k(\mathbf{r})\right\}\right] = F\left[\left\{\rho_k(\mathbf{r})\right\}\right] + \sum_k \int \rho_k(\mathbf{r})\left[\Psi_k(\mathbf{r}) - \mu_k\right] d\mathbf{r}, \tag{4-8}$$

where $d\mathbf{r}$ is differential volume, and $\Psi_k(\mathbf{r})$ is the solid surface external potential of the component $k$ at the positional vector $\mathbf{r}$; $\mu_k$ is the chemical potential of component $k$ in bulk [147]. $\rho_k(\mathbf{r})$ is the number density distribution of component $k$ at positional vector $\mathbf{r}$,

given as $\rho_k(\mathbf{r}) = m_k \rho_k^{seg}(\mathbf{r})$, in which $m_k$ is the segment number of component $k$ and $\rho_k^{seg}(\mathbf{r})$ is the local averaged number density of all segments of component $k$ [199, 200, 207].

The Helmholtz free-energy $F\left[\{\rho_k(\mathbf{r})\}\right]$ is further decomposed into two parts [200]: ideal-gas term $F^{id}\left[\{\rho_k(\mathbf{r})\}\right]$ and the excess term arising from the intermolecular interactions and molecular configurations $F^{ex}\left[\{\rho_k(\mathbf{r})\}\right]$,

$$F\left[\{\rho_k(\mathbf{r})\}\right] = F^{id}\left[\{\rho_k(\mathbf{r})\}\right] + F^{ex}\left[\{\rho_k(\mathbf{r})\}\right]. \tag{4-9}$$

The ideal-gas term is given as [147],

$$\beta F^{id}\left[\{\rho_k(\mathbf{r})\}\right] = \sum_k \int \rho_k(\mathbf{r})\left[\ln\left(\rho_k(\mathbf{r})\Lambda_k^3\right) - 1\right] d\mathbf{r} \ , \tag{4-10}$$

where $\beta = 1/(k_B T)$; $\Lambda_k$ is the de Broglie wavelength of component $k$. $k_B$ and $T$ represent the Boltzmann constant and the absolute temperature, respectively.

In Eq. (2-16), molecules are modeled as chains of freely-joined spherical segments. The total excess Helmholtz free-energy $F^{ex}\left[\{\rho_k(\mathbf{r})\}\right]$ is given as [199, 200],

$$F^{ex}\left[\{\rho_k(\mathbf{r})\}\right] = F^{ex,hs}\left[\{\rho_k(\mathbf{r})\}\right] + F^{ex,hc}\left[\{\rho_k(\mathbf{r})\}\right] + F^{ex,disp}\left[\{\rho_k(\mathbf{r})\}\right] + F^{ex,assoc}\left[\{\rho_k(\mathbf{r})\}\right], \tag{4-11}$$

where $F^{ex,hs}\left[\{\rho_k(\mathbf{r})\}\right]$ and $F^{ex,hc}\left[\{\rho_k(\mathbf{r})\}\right]$ represent the excess Helmholtz free energy arising from the hard-sphere and the connectivity of segments in the hard-chain, respectively. The dispersion term $F^{ex,disp}\left[\{\rho_k(\mathbf{r})\}\right]$ accounts for the attractive van der Waals interactions of chain molecules. The association term $F^{ex,assoc}\left[\{\rho_k(\mathbf{r})\}\right]$ describes excess Helmholtz energy due to the formation of hydrogen bonds. Details about the excess Helmholtz free-energy term $F^{ex}\left[\{\rho_k(\mathbf{r})\}\right]$ are shown in **Appendix C.1**. In this work, the $C_1$, $C_2$, $C_3$, and $CO_2$ are considered to be without a charge so the association term is omitted [116]. The parameters for hydrocarbons and $CO_2$ are from PC-SAFT EOS [223] which are listed in **Table C-1**.

At equilibrium, the grand potential functional reaches the minimum concerning density profile $\rho_k(\mathbf{r})$ [140],

$$\frac{\delta\Omega\left[\left\{\rho_k(\mathbf{r})\right\}\right]}{\delta\rho_k(\mathbf{r})}=0, \tag{4-12}$$

where the symbol $\delta$ represents the functional derivative. The equilibrium density distributions of species are obtained by the minimization of the grand potential functional [151],

$$\rho_k(\mathbf{r})=\exp\left[\beta\mu_k-\beta\Psi_k(\mathbf{r})-\frac{\delta\beta F^{ex}\left[\left\{\rho_k(\mathbf{r})\right\}\right]}{\delta\rho_k(\mathbf{r})}\right]. \tag{4-13}$$

The density distribution in Eq. (2-17) is solved by the Picard iteration method [152]. The bulk density is used as the initialization for the calculation of the first pressure condition. The initial guess for other pressure conditions is from the density distributions at the preceding pressure [140].

For simplicity, we use carbon-slit pores which are described by two planar structureless graphite surfaces to represent nanopores in the system [77, 140, 156, 157]. Such carbon nanopore structures have been applied to the study of gas adsorption in shale and shown excellent agreement with GCMC simulation results and experimental data [10]. In a carbon-slit pore, the density distributions only vary in the $z$ direction perpendicular to the solid surfaces, *i.e.*, $\rho_k(\mathbf{r})=\rho_k(z)$. The 10-4-3 Steele potential [158] is used to describe the fluid–surface interactions $\varphi_{sk}$,

$$\varphi_{sk}(z)=2\pi m_k\rho_s\varepsilon_{sk}\sigma_{sk}^2\Delta\left[\frac{2}{5}\left(\frac{\sigma_{sk}}{z}\right)^{10}-\left(\frac{\sigma_{sk}}{z}\right)^4-\frac{\sigma_{sk}^4}{3\Delta(0.61\Delta+z)^3}\right], \tag{4-14}$$

where $z$ represents the position in a perpendicular direction relative to the pore surface. $m_k$ is the segment number of component $k$. $\rho_s=114$ nm$^{-3}$ is the density of graphite and $\Delta=0.335$ nm represents the interlayer spacing of graphite; $\varepsilon_{sk}$ and $\sigma_{sk}$ are potential expansion parameters and follow the simple mixing rule: $\varepsilon_{sk}=\sqrt{\varepsilon_s\varepsilon_k}$ , and $\sigma_{sk}=\left(\sigma_s+d_k(T)\right)/2$ . The energy and size parameters of the graphite surface are $\sigma_s=0.3345$ nm, $\varepsilon_s/k_B=28$ K [78, 224]. $\varepsilon_k$ is the fluid energy of a segment of composition $k$, and $d_k(T)$ is the temperature-dependent effective segment diameter of

composition $k$, which is defined as $d_k(T)=\sigma_k\left(1-0.12\exp\left(-3\left(\varepsilon_k/k_bT\right)\right)\right)$ [199]. The fluid energy $\varepsilon_k$ and the segment diameter $\sigma_k$ parameters are from PC-SAFT EOS [223] and are listed in **Table C-1**. In slit-nanopores, the external potential $\Psi_k(\mathbf{r})$ for component *k* in Eq. (2-17) is given as,

$$\Psi_k(z)=\varphi_{sk}(z)+\varphi_{sk}(W-z). \tag{4-15}$$

The average density of component *k* in nanopores $\rho_{ave,k}$ is calculated as,

$$\rho_{ave,k}=\frac{\int_0^{W_{ef}}\rho_k(z)\,dz}{W_{ef}}, \tag{4-16}$$

where $W_{ef}=W-\sigma_s$ is the effective pore size; $W$ is the pore size as used in Eqs. (4-2) and (3-18) [187].

### 4.2.4. Grand Canonical Monte Carlo (GCMC) Simulation

GCMC simulation has been widely used as one of the most powerful tools to study hydrocarbons and $CO_2$ adsorption under confinement [65, 225-228]. To calibrate our PC-SAFT DFT calculations, we compared density profiles and average densities in nanopores of hydrocarbon and $CO_2$ mixtures from PC-SAFT DFT with those from GCMC simulations. The details of GCMC simulation and comparison with PC-SAFT DFT are shown in **Appendix C.3** and **C.4,** respectively.

## 4.3. Results and Discussions

In this section, we use three simplified PSDs from Eagle Ford (EF) [167], Middle Bakken (MB) [181], and Horn River (HR) [182] shale sub-formations to study the effect of volume partitioning on hydrocarbons and $CO_2$ mixture adsorption during $CO_2$ 'huff-n-puff' process. The initial mole fractions in the bulk region are set the same in each PSD case as shown in **Table 4-2**.

In **Figure 4-1**, we present the average molar densities of hydrocarbons and $CO_2$ during $CO_2$ 'huff-n-puff' process in $W=2$ nm pores. For comparison, we also depict the average molar densities in a direct pressure drawdown from $P_0$ to $P_3$. During the primary pressure drawdown from $P_0$ to $P_1$, $C_1$ is released from the pores, while $C_3$ adsorption in nanopores increases. As $P$ drops, the PSD case with a higher volume ratio of smaller

pores (*i.e.*, EF) releases less $C_1$ and $C_2$ from 2-nm pores, while adsorbing less $C_3$. As $CO_2$ is injected, the bulk pressure increases with slight differences among the three PSD cases as shown in **Table 4-4**. During the $CO_2$ 'huff' and 'soak' process, the decrease in all hydrocarbon densities is smaller in the EF case. In addition, with the same amount of injected $CO_2$, the $CO_2$ average density in the 2-nm pores in the EF case is the lowest. During the $CO_2$ 'puff' process, $C_1$ is continuously released from pores, while $C_3$ adsorption in nanopores increases, then decreases at low pressures. The $CO_2$ average density decreases in all PSD cases during the $CO_2$ 'puff' process, while $CO_2$ adsorption in the EF case decreases less.

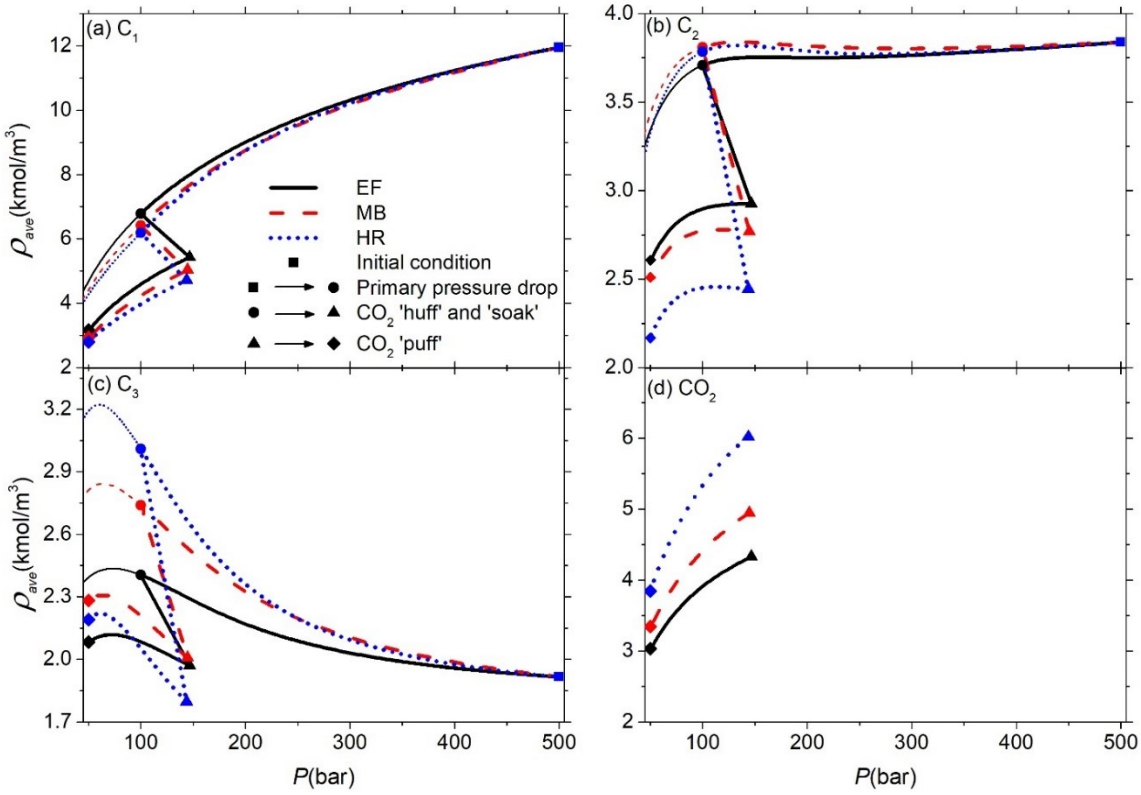


**Figure 4-1** The average molar densities in $W$ = 2 nm pores of (a) $C_1$; (b) $C_2$; (c) $C_3$; and (d) $CO_2$ in various PSD cases at $T$ = 333.15 K. The black solid lines represent average density from Eagle Ford. Red dashed lines are from Middle Bakken and blue dotted lines are from Horn River. Thick and thin lines represent $CO_2$ 'huff-n-puff' and direct pressure drawdown processes, respectively. Squares represent the initial condition. The route from squares to circles represents the primary pressure drop; the route from circles to triangles represents the $CO_2$ 'huff' and 'soak' processes; the route from triangles to rhombs represents the $CO_2$ 'puff' process.

In **Figure 4-2**, we present molar density profiles of hydrocarbons and $CO_2$ in 2-nm pores. During the primary pressure drawdown, $C_1$ densities in the adsorption layer

and the middle of the pores decrease, while the opposite is true for $C_3$ due to strong fluid–surface interactions, as in our previous work [79]. During the $CO_2$ 'huff' and 'soak', $C_1$, $C_2$, and $C_3$ are released from both adsorption layers and the middle of pores. In the EF case, hydrocarbon release from the 2-nm pores due to the $CO_2$ 'huff' and 'soak' is less significant than those in the MB and HR cases, especially for $C_3$. Due to the stronger competitive adsorption in the vicinity of the pore surface, the volume partitioning shows a more obvious effect on adsorption layers. On the other hand, $CO_2$ densities in the adsorption layers and the middle of the pores in the EF case are the smallest in all PSD cases. Apart from the PSD effect, it is worthy to note that the total organic carbon might be another important factor that could influence the $CO_2$ adsorption under nanoconfinement [61]. During the $CO_2$ 'puff' process, $C_1$, $C_2$, and $CO_2$ densities decrease, while $C_3$ density increases. Compared with other PSD cases, the EF case releases more $C_1$, $C_2$, and $CO_2$, while adsorbs less $C_3$, which is opposite to that during the primary pressure drop.

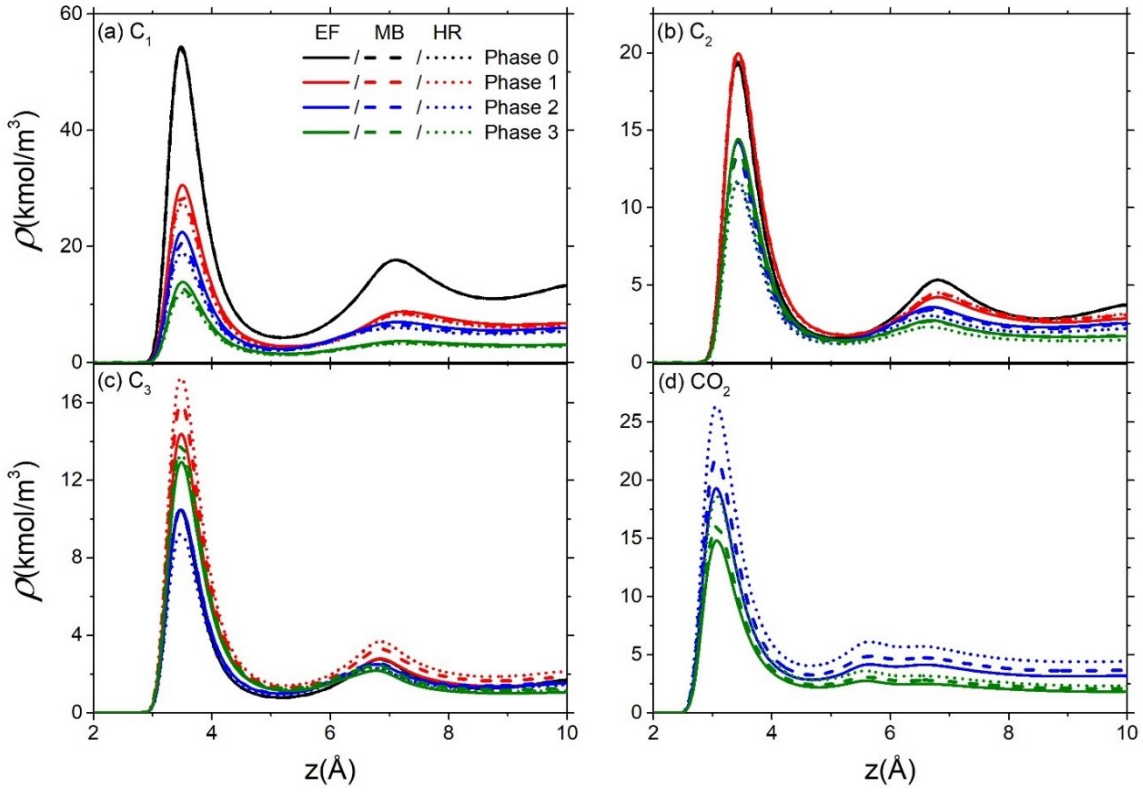


**Figure 4-2** The molar density profiles in $W = 2$ nm pores of (a) $C_1$; (b) $C_2$; (c) $C_3$; and (d) $CO_2$ in various PSD cases at $T = 333.15$ K. Black lines represent molar density profiles at initial condition ( $P_0$ ). Red, bulk, and green lines represent molar density profiles at

pressures of end of the primary pressure drop ($P_1$), $CO_2$ 'huff' and 'soak' ($P_2$), and $CO_2$ 'puff' ($P_3$), respectively. Solid, dashed, dotted lines represent mole density profiles from Eagle Ford, Middle Bakken, and Horn River, respectively.

The average molar densities of each component in $W = 15$ nm pores are shown in **Figure 4-3**. The average densities for $W = 5$ nm and $W = 30$ nm pores as well as in the bulk region are shown in **Appendix C.5**. During the primary pressure drop, all hydrocarbon densities decrease as $P$ drops. During the $CO_2$ 'huff' and 'soak' processes, hydrocarbon densities increase in the EF and MB cases as $CO_2$ is injected, while the opposite is true for the HR case. For $CO_2$, similar to **Figure 4-1**, its average molar density in the EF case is higher. During the $CO_2$ 'puff' process, all components are released from the pores as pressure drops.

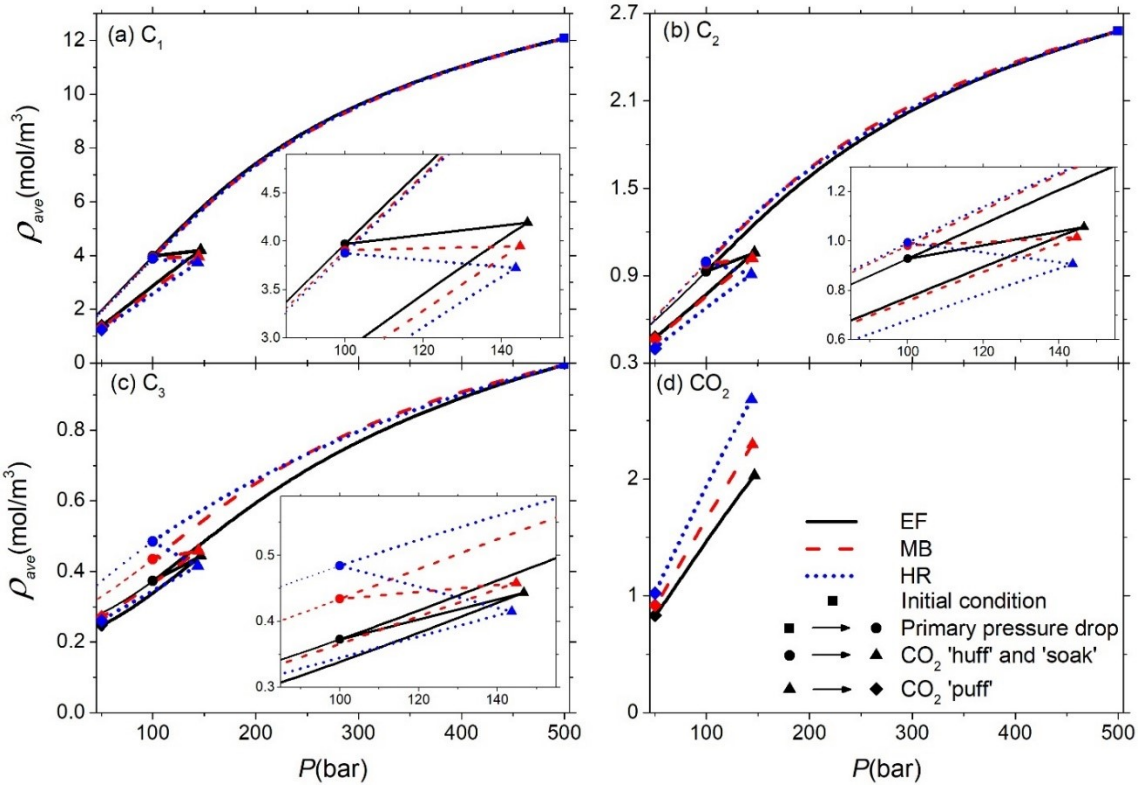


**Figure 4-3** The average molar densities in $W = 15$ nm pores of (a) $C_1$; (b) $C_2$; (c) $C_3$; and (d) $CO_2$ in various PSD cases at $T = 333.15$ K. The black solid lines represent average density from Eagle Ford. Red dashed lines are from Middle Bakken and blue dotted lines are from Horn River. Thick and thin lines represent scenarios with/without $CO_2$ 'huff-n-puff', respectively. Squares represent the initial condition. The route from squares to circles represents the primary pressure drop; the route from circles to triangles represents the $CO_2$ 'huff' and 'soak' processes, and the route from triangles to rhombs represents the $CO_2$ 'puff' process. The $CO_2$ 'huff' and 'soak' processes are amplified in inset figures.

In **Figure 4-4**, we present the molar density profiles for each component in $W = 15$ nm pores. The molar density profiles for $W = 5$ nm and $W = 30$ nm pores are shown in **Appendix C.6**. During the primary pressure drop, $C_1$ is released from adsorption layers and the middle of pores, while $C_2$ and $C_3$ are mostly released from the middle of pores. The change in the $C_2$ adsorption layers is negligible, while the $C_3$ adsorption layer becomes more prominent. The $CO_2$ 'huff' and 'soak' process has an opposite effect on hydrocarbons densities in the adsorption layers and the middle of pores: they are released from adsorption layers, while their densities in the middle of pores increase.

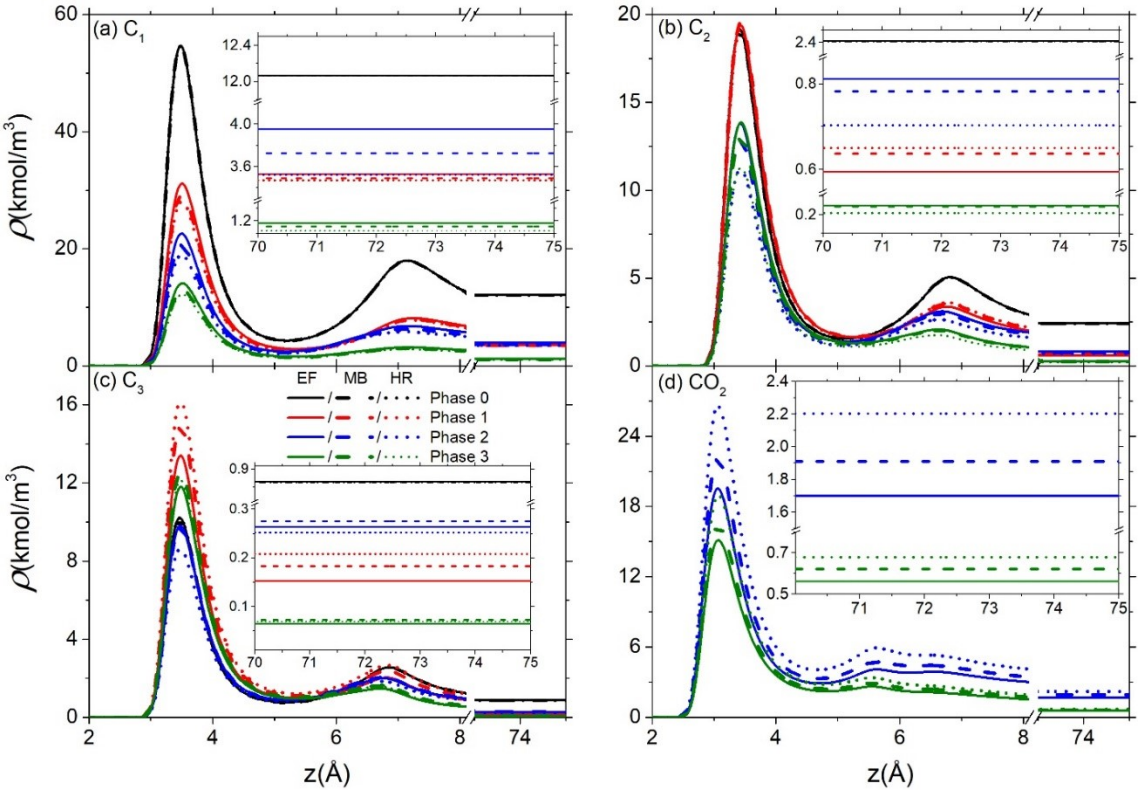


**Figure 4-4** The molar density profiles in $W = 15$ nm pores of (a) $C_1$; (b) $C_2$; (c) $C_3$; and (d) $CO_2$ in various PSD cases at $T = 333.15$ K. Black lines represent molar density profiles at initial condition ($P_0$). Red, bulk, and green lines represent mole density profiles at pressures of the end of the primary pressure drop ($P_1$), $CO_2$ 'huff' and 'soak' ($P_2$), and $CO_2$ 'puff' ($P_3$), respectively. Solid, dashed, dotted lines represent mole density profiles from Eagle Ford, Middle Bakken, and Horn River, respectively. The densities of the middle of pores are amplified and shown as inserted figures.

The effect of volume partitioning on the compositions of each component in $W = 2$ nm and $W = 15$ nm is shown in **Figure 4-5**. The compositions of each component in $W$

= 5 nm and $W$ = 30 nm pores are shown in **Appendix C.7**. During the $CO_2$ 'huff' and 'soak' process, PSD strongly affects the equilibrium compositions in nanopores. In the EF case, the compositions of hydrocarbons in pores reduce less. During the $CO_2$ 'puff' process, in $W$ = 2 nm pores, though $C_1$, $C_2$, and $CO_2$ are released from pores, the $C_1$ and $CO_2$ compositions decrease, while the $C_2$ composition increases. On the other hand, the $C_3$ composition in 2-nm pores increases. In $W$ = 15 nm pores, $C_1$ composition decreases, while $C_2$ and $C_3$ compositions increase. However, the $CO_2$ composition increases in $W$ = 15 nm pores.

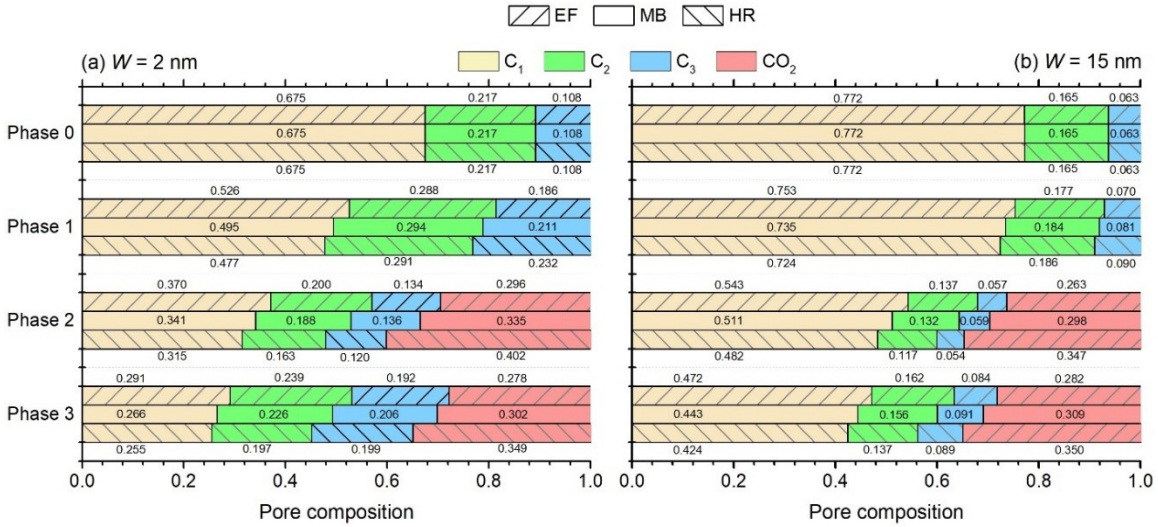


**Figure 4-5** Compositions of each component in (a) $W$ = 2 nm; (b) $W$ = 15 nm pores in various PSD cases at $T$ = 333.15 K. Phase 0 represents the initial condition; Phase 1 represents the primary pressure drop; Phase 2 represents the $CO_2$ 'huff' and 'soak' process, and Phase 3 represents the $CO_2$ 'puff' process. The pore compositions shown for Phase 1, 2, 3 are the composition at the pressure of the end of each phase.

The bulk pressure, composition, and densities of hydrocarbon components and $CO_2$ in various PSD cases before and after $CO_2$ 'huff' and 'soak' processes are listed in **Table 4-4**. Though the same amount of $CO_2$ is injected in each PSD case, more $CO_2$ is adsorbed into nanopores in the EF case. Thus, in the EF case, the $CO_2$ equilibrium bulk composition is smaller, while the hydrocarbon component compositions are higher. On the other hand, $P_2$ in different PSD cases are similar. Meanwhile, the bulk density increases due to $CO_2$ injection, while increasing more in the EF case. Bulk compositions in different PSD cases are also presented in **Figure 4-6**. During the $CO_2$ 'huff' and 'soak' process, PSD strongly affects the equilibrium bulk compositions. As the volume ratio of the bulk region decreases, more $CO_2$ is absorbed into nanopores, and more hydrocarbons

($C_1$, $C_2$, and $C_3$) are released from the nanopores to the bulk region. As a result, in the EF case, the hydrocarbon bulk composition is higher. In turn, their average molar densities in nanopores increase. During the $CO_2$ 'puff' process, both $C_2$ and $CO_2$ bulk compositions increase as $P$ drops, while the opposite is true for $C_1$ and $C_3$.

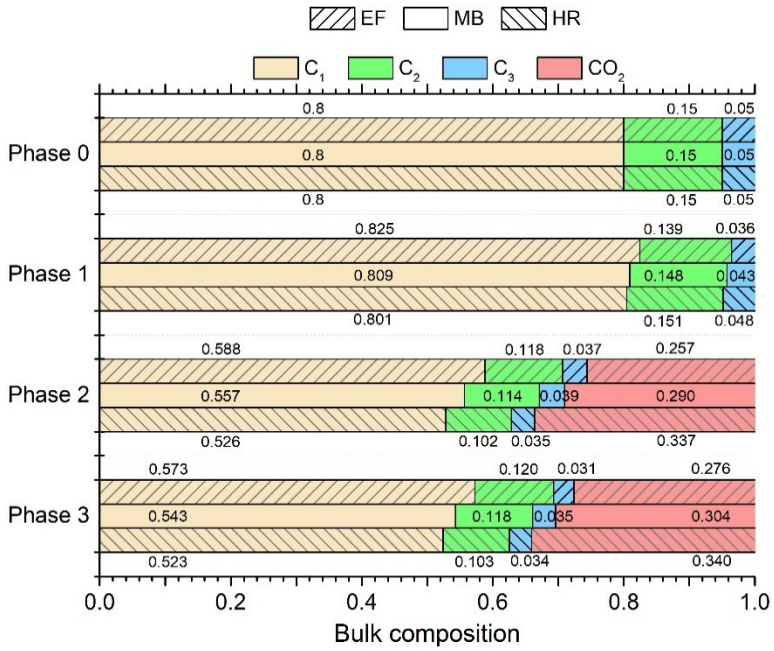


**Figure 4-6** Bulk compositions of each component in various PSD cases. Phase 0 represents the initial condition at $T$ = 333.15 K; Phase 1 represents the primary pressure drop; Phase 2 represents the $CO_2$ 'huff' and 'soak' process, and Phase 3 represents the $CO_2$ 'puff' process. The bulk compositions shown for Phase 1, 2, 3 are the composition at the pressure of the end of each phase.

To investigate hydrocarbons recovery from nanopores and the bulk region in different phases, we calculate the hydrocarbon-releasing factor, which is given as,

$$\text{Hydrocarbon-releasing factor} = \frac{\rho_k^{beg} - \rho_k^{end}}{\rho_k^{\text{int}}}, k = C_1, C_2, C_3, \tag{4-17}$$

where $\rho_k^{beg}$, $\rho_k^{end}$ represent bulk or pore molar density of component $k$ at the beginning and end of a phase, respectively. $\rho_k^{\text{int}}$ represents bulk or pore molar density of component $k$ at the initial condition (*i.e.*, Phase 0). In **Figure 4-7**, we present hydrocarbon-releasing factors in nanopores ($W$ = 2 nm and $W$ = 15 nm) and the bulk region in various PSD cases. The hydrocarbon-releasing factors in $W$ = 5 nm and $W$ = 30 nm pores are shown in **Appendix C.8**. During the primary pressure drop, the EF case has a lower $C_1$-releasing factor, while higher $C_2$- and $C_3$-releasing factors in both pores and the bulk region.

During the $CO_2$ 'huff' and 'soak' process, the EF case has a lower releasing factor for all components in both pores and the bulk region. The recovery of hydrocarbon mixtures for the $CO_2$ 'huff' and 'soak' process is mainly from small pores. In the $CO_2$ 'puff' process, the EF case has higher releasing factors for all components in pores and higher $C_1$- and $C_2$-releasing factors in the bulk, while the MB shows a slightly higher $C_3$-releasing factor in the bulk.

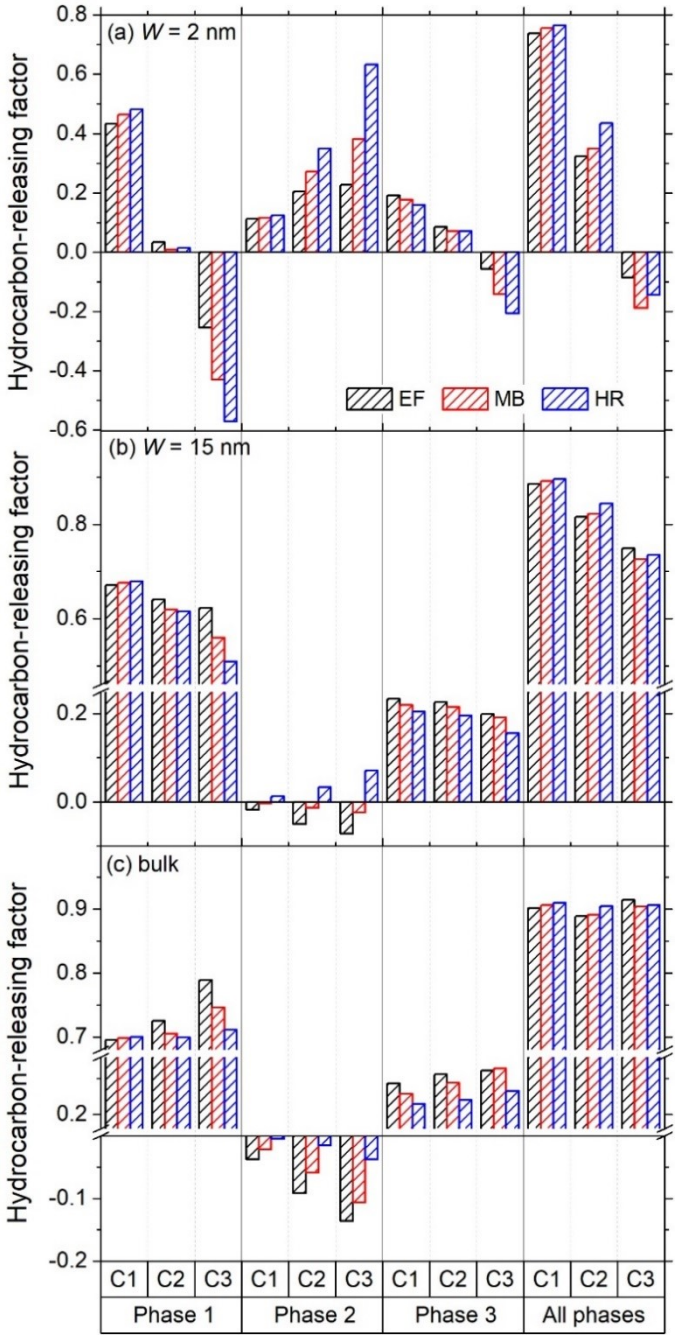


**Figure 4-7** The hydrocarbon-releasing factors in (a) $W$ = 2 nm; (b) $W$ = 15 nm; (c) the

bulk region in various PSD cases at $T$ = 333.15 K. Phase 1 represents the primary pressure drop; Phase 2 represents the $CO_2$ 'huff' and 'soak' process, and Phase 3 represents the $CO_2$ 'puff' process; All phases represent the whole process from the initial condition to the abandoned pressure in the $CO_2$ 'huff-n-puff'.

In **Figure 4-8**, hydrocarbon components recoveries from the entire nanopore–bulk multiscale system in different phases and various PSD cases with $CO_2$ 'huff-n-puff' process are shown, which are defined as,

$$\text{Recovery} = \frac{N_k^{beg} - N_k^{end}}{N_k^{\text{int}}}, k = C_1, C_2, C_3, \tag{4-18}$$

where $N_k^{beg}$ and $N_k^{end}$ represent the molar number of component $k$ at the beginning and end of each phase, respectively. $N_k^{\text{int}}$ represents the molar number of component $k$ at the initial condition. As there is no production during the $CO_2$ 'huff' and 'soak' process, the recovery is zero in Phase 2. To show the $CO_2$ 'huff-n-puff' enhancement effect, hydrocarbon recovery in each pore, the bulk region as well as the entire nanopore–bulk multiscale system with/without $CO_2$ 'huff-n-puff' processes are listed in **Table 4-5**. The $CO_2$ 'huff-n-puff' process enhances the total hydrocarbon recovery by more than 5%, while the enhancement in the heavier component recovery in small pores (2-nm pores) can be between 16.4% to 52.3% in different PSD cases. Due to the volume partitioning, the EF case has the highest enhanced hydrocarbon recovery due to the $CO_2$ 'huff-n-puff' process.

**Table 4-5** Hydrocarbon recoveries in each pore, the bulk region, and the entire nanopore–bulk multiscale system with/without the $CO_2$ 'huff-n-puff' process. Note that w/ and w/o represent with and without, respectively.

| | PSD cases | Recovery | | | | | | | | | | | | | | | | | |
|---|---|---|---|---|---|---|---|---|---|---|---|---|---|---|---|---|---|---|---|
| | | 2nm | | | 5nm | | | 15nm | | | 30nm | | | Bulk | | | System | | |
| | | $C_1$ | $C_2$ | $C_3$ | $C_1$ | $C_2$ | $C_3$ | $C_1$ | $C_2$ | $C_3$ | $C_1$ | $C_2$ | $C_3$ | $C_1$ | $C_2$ | $C_3$ | $C_1$ | $C_2$ | $C_3$ |
| W/ $CO_2$ injection | EF | 0.737 | 0.323 | -0.085 | 0.847 | 0.671 | 0.485 | 0.887 | 0.816 | 0.749 | 0.896 | 0.857 | 0.833 | 0.902 | 0.889 | 0.915 | 0.864 | 0.715 | 0.538 |
| | MB | 0.756 | 0.349 | -0.189 | 0.856 | 0.684 | 0.440 | 0.893 | 0.822 | 0.726 | 0.901 | 0.860 | 0.817 | 0.906 | 0.891 | 0.904 | 0.888 | 0.799 | 0.669 |
| | HR | 0.765 | 0.434 | -0.144 | 0.861 | 0.724 | 0.459 | 0.897 | 0.844 | 0.735 | 0.905 | 0.878 | 0.822 | 0.910 | 0.904 | 0.906 | 0.906 | 0.886 | 0.846 |
| W/O $CO_2$ injection | EF | 0.608 | 0.129 | -0.249 | 0.776 | 0.580 | 0.402 | 0.837 | 0.771 | 0.715 | 0.851 | 0.824 | 0.814 | 0.861 | 0.867 | 0.910 | 0.802 | 0.639 | 0.469 |
| | MB | 0.630 | 0.105 | -0.468 | 0.783 | 0.569 | 0.308 | 0.841 | 0.762 | 0.667 | 0.854 | 0.816 | 0.780 | 0.863 | 0.859 | 0.889 | 0.834 | 0.731 | 0.596 |
| | HR | 0.641 | 0.134 | -0.667 | 0.786 | 0.583 | 0.221 | 0.842 | 0.768 | 0.622 | 0.855 | 0.820 | 0.749 | 0.863 | 0.860 | 0.871 | 0.857 | 0.831 | 0.784 |
| Enhanced Recovery | EF | 12.9% | 19.3% | 16.4% | 7.1% | 9.1% | 8.3% | 5.0% | 4.5% | 3.5% | 4.5% | 3.3% | 2.0% | 4.1% | 2.2% | 0.5% | 6.2% | 7.6% | 6.9% |
| | MB | 12.6% | 24.4% | 27.9% | 7.3% | 11.5% | 13.2% | 5.2% | 6.0% | 5.9% | 4.7% | 4.4% | 3.6% | 4.4% | 3.2% | 1.5% | 5.4% | 6.9% | 7.3% |
| | HR | 12.3% | 30.0% | 52.3% | 7.5% | 14.1% | 23.8% | 5.5% | 7.6% | 11.2% | 5.0% | 5.8% | 7.3% | 4.6% | 4.4% | 3.5% | 4.9% | 5.4% | 6.2% |

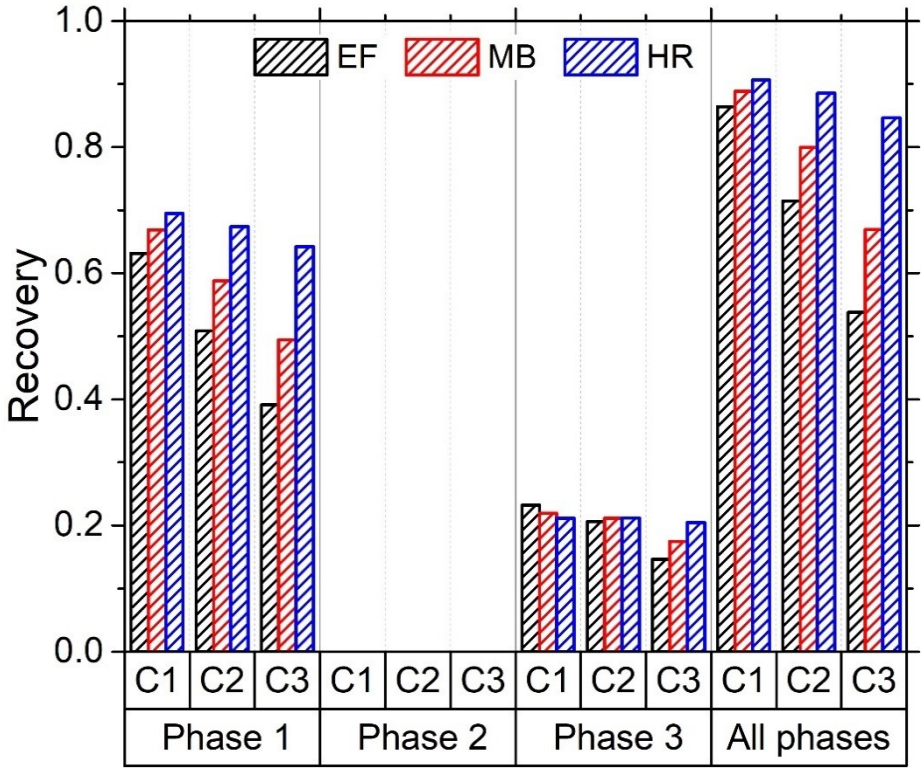


**Figure 4-8** The recovery of hydrocarbon components in the nanopore–bulk multiscale system in different phases in various PSD cases with $CO_2$ 'huff-n-puff' process at $T$ = 333.15 K. Phase 1 represents the primary pressure drop; Phase 2 represents the $CO_2$ 'huff' and 'soak' process, and Phase 3 represents the $CO_2$ 'puff' process; All phases represent the whole process from the initial condition to the abandoned pressure in the $CO_2$ 'huff-n-puff'.

The $CO_2$ sequestration ratio in nanopores, bulk, and the total nanopore–bulk multiscale system in various PSD cases are shown in **Figure 4-9**, which is defined as,

$$CO_2 \text{ sequestration ratio} = \frac{N_{CO_2}^{sequestered}}{N_{CO_2}^{after\_soak}}, \tag{4-19}$$

where $N_{CO_2}^{sequestered}$ represents the molar number of $CO_2$ remaining in nanopores, bulk, or the total nanopore–bulk multiscale system at the abandoned pressure, and $N_{CO_2}^{after\_soak}$ represents the initial molar number of $CO_2$ in nanopores, bulk, or the total nanopore–bulk multiscale system after $CO_2$ 'huff' and 'soak' process. A stronger confinement effect in smaller pores allows for enhancing $CO_2$ storage. A higher volume ratio of smaller pores case can store more $CO_2$ in nanopores and the bulk region. As a result, the PSD with a higher volume ratio of smaller pores has a higher total $CO_2$ sequestration ratio.

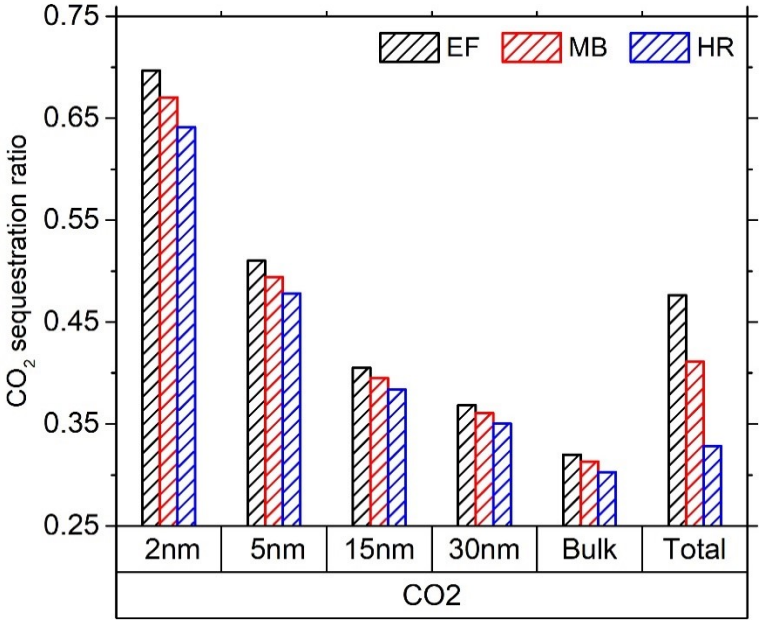


**Figure 4-9** The $CO_2$ sequestration ratio in nanopores, bulk, and the total nanopore-bulk multiscale system in various PSDs.

### 4.4. Conclusions

In this work, we use the PC-SAFT DFT to study the $CO_2$ 'huff-n-puff' process in a nanopore–bulk multiscale system by a CVD process, in which mass balance and volume partitioning are explicitly considered. During the $CO_2$ 'huff' and 'soak' process, a large number of hydrocarbons can be released from small nanopores, especially for the heavier components. On the other hand, in the larger nanopores ($W \geq 15$ nm), the average density of hydrocarbons might increase. For hydrocarbon density distributions, the $CO_2$ injection has mixed influences on the adsorption layers and the middle of pores: hydrocarbons are released from the adsorption layers, while their densities in the middle of pores increase. Compared with the case without the $CO_2$ 'huff-n-puff' process, the $CO_2$ 'huff-n-puff' process prompts hydrocarbon release from nanopores, especially for the heavier components in the smaller pores.

The volume partitioning effects on nanopore adsorption and compositions are significant in the $CO_2$ 'huff-n-puff' process. During the $CO_2$ 'huff' and 'soak' process, a PSD case with a higher volume ratio of smaller pores (*i.e.*, the Eagle Ford case) releases fewer hydrocarbons ($C_1$, $C_2$, $C_3$). The volume partitioning also shows a more obvious effect on altering the density of adsorption layers than that in the middle of pores, especially in the larger pores. In addition, it also shows a strong influence on the

equilibrium bulk composition. Hydrocarbon recovery is also strongly affected by volume partitioning. For small pores, the recovery of $C_2$ and $C_3$ mainly stems from the $CO_2$ 'huff' and 'soak' period, while, in larger pores, the hydrocarbon recovery is mainly from pressure drops. In the nanopore–bulk multiscale system, the hydrocarbon recovery due to $CO_2$ injection is mainly from the smaller pores. The smaller pores with a stronger confinement effect can adsorb more $CO_2$ per unit pore volume. As a result, a PSD case with a higher volume ratio of smaller pores can store more $CO_2$.

Collectively, the volume partitioning shows strong influences on hydrocarbon adsorption and recovery as well as $CO_2$ sequestration in nanopores during $CO_2$ 'huff-n-puff' process. Our work should provide a fundamental understanding about the effect of volume partitioning on hydrocarbon mixture adsorption characteristics and important insights into the optimization of enhanced shale gas recovery and $CO_2$ sequestration. On the other hand, moisture exists in shale media which can affect hydrocarbon and $CO_2$ adsorption [55]. Besides, kerogen in shale can contain various heteroatoms [69, 183, 194]. Unlocking these effects coupled with volume partitioning in the nanopore–bulk multiscale system on hydrocarbon and $CO_2$ adsorption will be explicitly studied in our future works.

公式章 (下一章) 节 1

# CHAPTER 5 Effect of Energetical and Geometrical Heterogeneity of Kerogen on BET Surface Area Characterization and Methane Adsorption

(A version of this chapter has been published in Energy Fuels 2022 by Yingnan Wang, Wanying Pang, and Zhehui Jin. DOI: 10.1021/acs.energyfuels.2c01603.)

## Abstract

Surface area is an important parameter for methane ($CH_4$) adsorption estimation in shale nanoporous media. Kerogen, as the main constituent of shale organic matters, has exceptionally high surface areas due to extensive nanoscale pores. The Brunauer–Emmett–Teller (BET) method has been extensively used to characterize the surface area of various porous materials. However, its applicability for the surface area characterization of kerogen mesopores has not been investigated yet. In this work, the effect of geometrical and energetical heterogeneity on $N_2$ adsorption isotherms and the subsequent BET surface area ($S_{BET}$) characterization is studied by using the grand canonical Monte Carlo (GCMC) simulations. We find that $N_2$ adsorption sites are mainly within the "basin" and "valley" regions on kerogen surfaces, while in the "ridge" regions its adsorption rarely takes place at 77 K from 0.005 bar to 0.05 bar. On the other hand, surface chemistry shows a significant effect on external potential and $N_2$ adsorption amount. In addition, while $S_{BET}$ agrees well with geometric surface area ($S_{geo}$) in graphite mesopores, in kerogen and pseudo-kerogen mesopores, $S_{BET}$ is generally lower than $S_{geo}$. Interestingly, $S_{BET}$ correlates well with $CH_4$ excess adsorption in kerogen mesopores at 333.15 K and 300 bar, outperforming $S_{geo}$. This work provides some crucially important fundamental understanding about the $S_{BET}$ characterization of kerogen mesopores which can guide $CH_4$ adsorption capacity prediction in kerogen nanoporous media and shale GIP estimation.

## 5.1. Introduction

As a transition fuel, natural gas plays an ever-increasingly important role to meet the global energy demand, while reaching net-zero carbon emission by 2050 [229]. The U.S. Energy Information Administration (EIA) predicts that the global natural gas demand is projected to grow 22% in the next three decades [1]. On the other hand, due to the continuous depletion of conventional natural gas reservoirs, shale gas has become an important natural gas source. For example, in the United States, ~ 80% of total dry natural gas production is from shale formations in 2020 [1]. Unlike conventional reservoirs, surface adsorption plays a dominant role in shale gas due to the presence of a significant amount of nanosized pores in shale media [2-4]. Shale rocks are heterogeneous complex structural and mineralogical systems consisting of inorganic matters (calcites, quartz, pyrites, clays, *etc.*) and organic matters [5, 6]. Kerogen is the main constituent of organic matter, which generates hydrocarbons via chemical decomposition [7]. It is also the main methane storage site as methane adsorption capacity in shale rocks has shown a positive correlation with the total organic carbon (TOC) content [6, 8, 9]. Therefore, the accurate characterization of surface area in kerogen nanoporous media becomes utterly important in the prediction of shale gas-in-place (GIP). [5, 230, 231]

The Brunauer–Emmett–Teller (BET) theory has been widely used to obtain surface area by characterizing $N_2$ adsorption isotherm at 77 K in various porous media, the so-called BET surface area ( $S_{BET}$ ), including activated carbon [85], metal organic frameworks (MOFs) [86-88], silica [89-91], and zeolite [92], *etc*. It is also one of the standard methods to obtain a surface area in shale rocks [5] and isolated kerogen [232, 233]. BET theory assumes that the multilayer adsorption of ideal gas takes place on a perfectly-smooth ideal homogeneous surface [7]. For micropores, Rouquerol *et al.* [234] introduced two consistency criteria for the selected pressure range: 1) the constant $C$ ( $k_0$ in this work) in the BET equation should be positive; 2) the value of $n\left(P_0 - P\right)$ should increase with $P / P_0$. To ensure the validity of the selected pressure range, they further introduced two additional conditions: 3) the pressure value corresponding to the monolayer capacity in the adsorption isotherms should be in the selected fitting range; 4) $P / P_0$ calculated from

the fitted BET equation at $n = n_m$ should not be apart from the experimental one. In addition, it is commonly believed that the characterized surface area in shale and kerogen mainly refers to that in mesopores and macropores, assuming that 77 K $N_2$ cannot penetrate into micropores [5, 7]. On the other hand, in contrast to the basic assumptions in BET theory, kerogen surface may not be perfectly smooth [6] (*i.e.*, geometrical heterogeneity), and it carries energetical heterogeneity [95] with a number of heteroatoms such as N, S, and O.

There have been a number of previous studies on the effect of energetical and geometrical heterogeneity on $S_{BET}$ in porous media [86, 96-104]. Gómez-Gualdrón *et al.* [86] compared $S_{BET}$ in micro- and mesoporous MOFs with the $N_2$-accessible surface area (NASA), the so-called geometric surface area ( $S_{geo}$ ). They found that there are discrepancies between $S_{BET}$ and $S_{geo}$ , while the BET calculation can significantly overestimate the true monolayer loading in MOFs, which is consistent with the findings of Tian and Wu [105], Gelb and Gubbins [106], and Coasne *et al.* [91]. Walton and Snurr [235] and Bae *et al.* [92] independently validated the applicability of $S_{BET}$ in microporous MOFs by interpreting $N_2$ adsorption isotherms. They compared $S_{BET}$ with accessible surface area for MOFs and found that the two types of surface areas agree well with each other with < 10 % deviation in micropores. While these studies have provided important insights into the effect of energetical and geometrical heterogeneity on $S_{BET}$ , a careful analysis of their effect on kerogen $S_{BET}$ is still lacking. In addition, whether $S_{BET}$ can be a good indicator for methane ($CH_4$) adsorption capacity in kerogen nanopores remains unanswered.

Therefore, in this work, we conduct simulations of 77 K $N_2$ adsorption in 13 kerogen slit mesopores, and their respective pseudo-kerogen models to study the effect of kerogen geometrical and energetical heterogeneity on $S_{BET}$ characterization. Mesopores (pore width larger than 2 nm) are chosen because 1) the previous work [105] has shown that, in carbon micropores, $S_{BET}$ is larger than $S_{geo}$ due to the strong surface correlation; 2) it

is generally conceived that 77 K $N_2$ cannot penetrate shale and kerogen micropores[5]. The slit geometry is used for simplicity, while it is one of the most common pore geometries in shale rocks [7]. We carefully analyze the effect of geometrical and energetical heterogeneity on $N_2$ adsorption isotherms and the subsequent $S_{BET}$ characterization. For comparison, we also simulate 77 K $N_2$ adsorption in perfectly-smooth graphite mesopores to obtain their $S_{BET}$. We found that $N_2$ adsorption sites are mainly within the "basin" and "valley" regions on kerogen surfaces, while in "ridge" regions its adsorption rarely occurs. On the other hand, surface chemistry shows a significant effect on external potential and $N_2$ adsorption amount. Additionally, while $S_{BET}$ agrees well with $S_{geo}$ in graphite mesopores, $S_{BET}$ is generally lower than $S_{geo}$ in kerogen and pseudo-kerogen mesopores. The deviation becomes more significant as surface roughness becomes more significant and the fraction of the "ridge" surface increases. Interestingly, $S_{BET}$ correlates well with methane ($CH_4$) excess adsorption in kerogen mesopores, while it outperforms $S_{geo}$. It is probably because both $N_2$–kerogen and $CH_4$–kerogen interactions are mainly van der Waals type, while their adsorption sites largely overlap. This work provides some crucially important fundamental understanding about $S_{BET}$ characterization in kerogen mesopores which can guide $CH_4$ adsorption capacity prediction in kerogen nanoporous media and shale GIP estimation. The framework of this work for surface area characterization might be extended to other organic-rich rocks, like coal, considering the importance of the surface area and $CH_4$ adsorption in these rocks [236].

### 5.2. Model and Methodology

In this section, we first illustrate the procedures to create kerogen matrices (as kerogen substrates) and construct slit pores. The kerogen slit pore and surface are characterized in terms of geometrical surface area ($S_{geo}$), average pore size ($W_{ave}$), and effective pore volume ($V_p$). Geometrical heterogeneity is defined as the corrugation of the surface altitude/topology (*i.e.*, the surface is not perfectly smooth). To study the effect of geometrical heterogeneity, we create a number of kerogen matrices with varying surface roughness. The effect of energetical heterogeneity is investigated by replacing

kerogen heteroatoms (N, S, and O) with C atoms. Besides, details about $N_2$ and $CH_4$ adsorption simulations (*i.e.*, grand canonical Monte Carlo simulations) are provided. In addition, we also describe the procedures to obtain $S_{BET}$ of kerogen mesopores.

### 5.2.1. Kerogen Matrix and Slit Pore Construction

Classical molecular dynamics (MD) simulations are employed to build kerogen matrices with the GROMCS simulation package [237, 238]. The Type II-C mature kerogen macromolecule unit ($C_{242}H_{219}O_{13}N_5S_2$, as shown in **Figure D-1 (a)**) adopted from Ungerer *et al.* [239] is used to construct kerogen matrices, which has good agreement with experimental data in terms of elemental analysis, functional group distributions, *etc*. The consistent valence force field (CVFF) [2-4] is used to describe kerogen macromolecules. The force field parameters of kerogen are listed in **Table D-1**. A number of simulation studies [6, 240] using dummy particles to build rough kerogen surfaces have been reported. In this work, two different methods are used to build kerogen matrices with relatively smooth and rough surfaces.

To obtain a relatively-smooth kerogen matrix, 20 kerogen macromolecules are compressed by two rigid smooth graphene sheets as shown in **Figure D-1 (a)**, which are generated by an all-atom model in the VMD package [241] with a dimension of 5.44 nm × 5.51 nm in the *x*-*y* plane. Only the repulsive forces between the graphene sheet and kerogen macromolecules are considered. To compress these kerogen macromolecules, an external pressure of 7000 bar (*i.e.*, an external acceleration of −0.9 nm/ps$^2$ to each C atom on graphene) is added to the upper graphene sheet in the *z*-direction, while the bottom graphene sheet is fixed. Meanwhile, an annealing simulation with the temperature gradually declining from 900 K to 333.15 K is conducted for 2.5 ns, and then another 1.5 ns of simulation at 333.15 K is conducted to reach equilibrium. The final relatively-smooth kerogen matrix (denoted as **krg1**) thickness is ~3.5 nm with a density of 1.37 g/cm$^3$ (the process of density calculation is described in **Appendix D.3**).

To make rough kerogen matrices, we initially attempted to use a rigid upper smooth graphene sheet and a rigid bottom rough graphene sheet with varying degrees of roughness to compress kerogen macromolecules under the same procedures as for **krg1**. However, we find that the roughness of final kerogen matrices always falls into a very narrow range which can hardly represent a wide range of kerogen surface roughness.

Therefore, we use an alternative method to generate relatively-rough kerogen matrices by compressing kerogen macromolecules with a rigid upper smooth graphene sheet and a rigid bottom rough pseudo-kerogen sheet, which is conducted in a two-step simulation process.

In the first step, to build the rough pseudo-kerogen sheet, 20 kerogen macromolecules are compressed by two rigid smooth graphene sheets as shown in **Figure D-1 (b)**. Similarly, these two graphene sheets are generated by the all-atom model in the VMD package with a dimension of 5.44 nm × 5.51 nm in the *x*-*y* plane, while only the repulsive forces between the graphene sheet and kerogen macromolecules are considered. To generate pseudo-kerogen sheets with varying roughness, an external pressure ranging from 50 to 10000 bar is added to the upper graphene sheet in the *z*-direction to compress kerogen macromolecules with the same initial configurations. Then, the same annealing processes used for a relatively-smooth kerogen matrix are applied.

In the second step, relatively-rough kerogen matrices are obtained by compressing 20 kerogen macromolecules by a rigid upper smooth graphene sheet and a rigid bottom rough pseudo-kerogen sheet generated in the first step as shown in **Figure D-1 (b)**. An external pressure of 7000 bar is added to the upper graphene sheet in the *z*-direction, while the bottom rough pseudo-kerogen sheet is fixed. The same annealing simulation processes are conducted to allow kerogen matrices to reach equilibrium and 12 relatively-rough kerogen matrices are obtained. These 12 rough kerogen matrices are denoted as **krg2** to **krg12** whose thickness is from ~ 3.8 nm to ~ 4.5 nm. Their densities are from 1.20 to 1.37 g/cm$^3$, which are listed in **Table D-2**. Compared with the experimental density data for kerogen Type II-C, [239, 242] the deviation of density is < 10 %.

Though high external pressure (*i.e.*, 7000 bar) is used to compress kerogen macromolecules, a number of internal cavities (the so-called dead pores) inevitably exist within the kerogen matrices. To avoid their effect, all dead pores within kerogen matrices are blocked by dummy particles [6, 240]. As shown in **Figure 5-1**, kerogen slit pores are constructed by two parallel kerogen matrices. The upper kerogen matrix is obtained by rotating the lower one 180° along the *y*-direction to ensure that the inner surfaces of kerogen slit pores have the same surface morphology. Then, the upper kerogen matrix is shifted upwards in the *z*-direction to form kerogen slit mesopores. The shifting distance is

case-dependent, determined by the average pore size criterion, which is explained in the following subsection.

For the smooth graphite mesopore, the graphite surface consists of three layers of graphene sheets generated by the all-atom model in the VMD package[241] with a dimension of 5.44 nm × 5.51 nm in the *x*-*y* plane, and the interlayer spacing is set at 0.335 nm. To build the smooth graphite slit mesopore, two parallel smooth graphite surfaces are separated by 5.35 nm as shown in **Figure 5-1**, which is the distance between the center of C atoms in the innermost layers of two graphite surfaces and defined as pore size $W$.

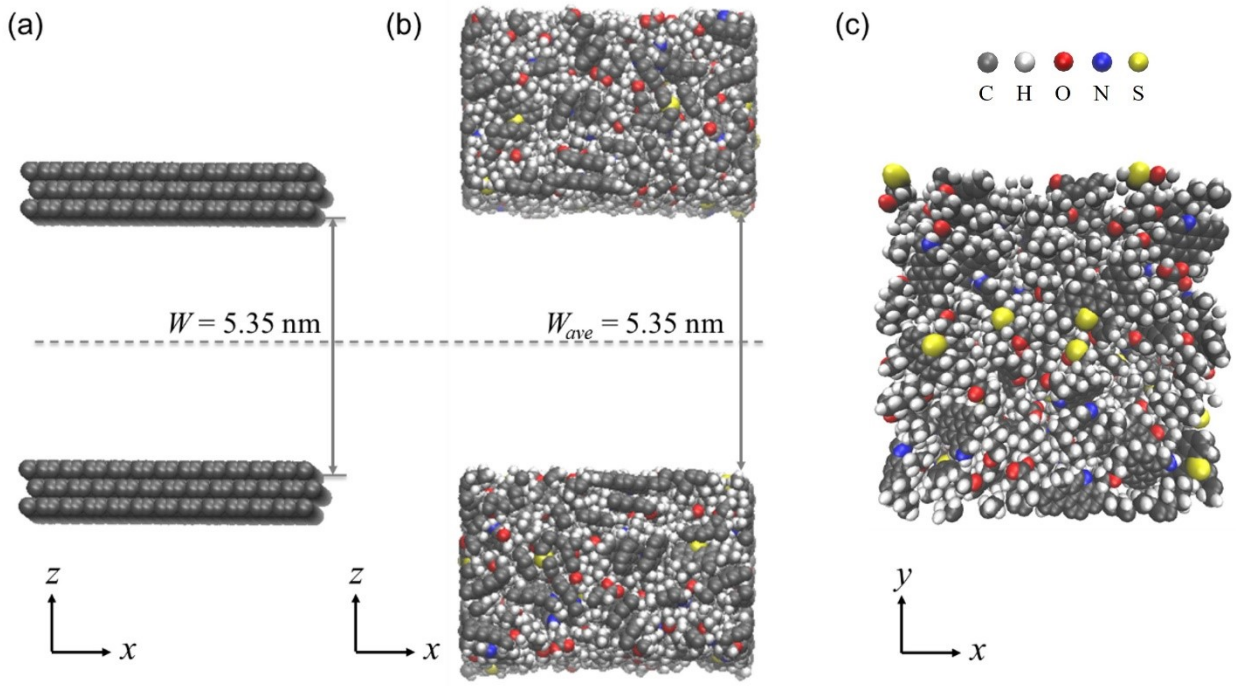


**Figure 5-1** Schematic illustration of slit pore models with $W = 5.35$ nm: (a) graphite model, (b) kerogen model, and (c) surface morphology of **krg1**.

### 5.2.2. Kerogen Surface and Slit Pore Characterization

The geometric surface area $S_{geo}$ (also known as accessible surface area) is defined as surface area calculated by rolling a probe molecule over the surface [105, 243]. In this work, a single-site $N_2$ molecule is used as the probe molecule to measure $S_{geo}$ of kerogen slit pores. The probe molecule is randomly inserted around each atom of the kerogen surface. The $S_{geo}$ is calculated by the fraction of probe molecules that did not overlap with other atoms or dummy particles.

To describe the kerogen surface characterizations, surface roughness ( $RO$ ) is an essential macroscopic parameter. In this work, $RO$ is defined as,

$$RO = \frac{S_{geo}}{S_{xy}}, \tag{5-1}$$

where $S_{geo}$ and $S_{xy}$ are geometric surface area and cross-sectional area of the *x*-*y* plane, respectively. $RO$ and other geometric parameters of the 13 kerogen models used in this work are listed in **Table 5-1**.

**Table 5-1** Geometric parameters and BET surface areas of graphite, kerogen, and pseudo-kerogen surfaces.

| Case # | X-Axis (Å) | Y-Axis (Å) | $W_{ave}$ (nm) | $S_{xy}$ ($nm^2$) | $S_{geo}$ ($nm^2$) | $S_{BET}$ ($nm^2$) | *RO* |
|---|---|---|---|---|---|---|---|
| graphite | 54.35 | 55.05 | 5.35 | 29.92 | 30.22 | 29.96 | 1.01 |
| krg1 | 51.58 | 51.05 | 5.35 | 26.33 | 35.07 | 31.07 | 1.33 |
| krg2 | 51.57 | 51.02 | 5.35 | 26.31 | 39.04 | 35.13 | 1.48 |
| krg3 | 51.56 | 51.10 | 5.35 | 26.35 | 39.28 | 36.72 | 1.49 |
| krg4 | 51.56 | 51.09 | 5.35 | 26.34 | 41.51 | 38.48 | 1.58 |
| krg5 | 50.34 | 51.05 | 5.35 | 25.70 | 43.54 | 31.06 | 1.69 |
| krg6 | 51.57 | 51.02 | 5.35 | 26.31 | 44.80 | 42.52 | 1.70 |
| krg7 | 51.33 | 52.05 | 5.35 | 26.72 | 47.90 | 42.50 | 1.79 |
| krg8 | 50.69 | 51.08 | 5.35 | 25.89 | 48.94 | 42.52 | 1.89 |
| krg9 | 51.55 | 51.08 | 5.35 | 26.33 | 51.89 | 42.52 | 1.97 |
| krg10 | 50.69 | 51.08 | 5.35 | 25.89 | 51.30 | 44.90 | 1.98 |
| krg11 | 52.57 | 52.05 | 5.35 | 27.36 | 55.70 | 45.90 | 2.04 |
| krg12 | 50.34 | 51.05 | 5.35 | 25.70 | 54.84 | 44.88 | 2.13 |
| krg13 | 51.53 | 51.08 | 5.35 | 26.32 | 60.75 | 50.47 | 2.31 |
| krg1* | 51.58 | 51.05 | 5.35 | 26.33 | 35.48 | 26.82 | 1.35 |
| krg2* | 51.57 | 51.02 | 5.35 | 26.31 | 39.64 | 26.82 | 1.51 |
| krg3* | 51.56 | 51.10 | 5.35 | 26.35 | 40.53 | 29.89 | 1.54 |
| krg4* | 51.56 | 51.09 | 5.35 | 26.34 | 42.12 | 29.89 | 1.60 |
| krg5* | 50.34 | 51.05 | 5.35 | 25.70 | 45.77 | 31.03 | 1.78 |
| krg6* | 51.57 | 51.02 | 5.35 | 26.31 | 46.11 | 32.27 | 1.75 |
| krg7* | 51.33 | 52.05 | 5.35 | 26.72 | 47.07 | 33.61 | 1.76 |
| krg8* | 50.69 | 51.08 | 5.35 | 25.89 | 49.48 | 32.27 | 1.91 |
| krg9* | 51.55 | 51.08 | 5.35 | 26.33 | 50.28 | 35.06 | 1.91 |
| krg10* | 50.69 | 51.08 | 5.35 | 25.89 | 51.80 | 33.61 | 2.00 |
| krg11* | 52.57 | 52.05 | 5.35 | 27.36 | 53.43 | 32.14 | 1.95 |
| krg12* | 50.34 | 51.05 | 5.35 | 25.70 | 55.14 | 35.06 | 2.15 |
| krg13* | 51.53 | 51.08 | 5.35 | 26.32 | 57.93 | 36.65 | 2.20 |
| krg1** | 51.58 | 51.05 | 5.35 | 26.33 | 35.07 | 28.83 | 1.33 |
| krg2** | 51.57 | 51.02 | 5.35 | 26.31 | 39.04 | 31.03 | 1.48 |
| krg3** | 51.56 | 51.10 | 5.35 | 26.35 | 39.28 | 32.27 | 1.49 |
| krg4** | 51.56 | 51.09 | 5.35 | 26.34 | 41.51 | 33.61 | 1.58 |
| krg5** | 50.34 | 51.05 | 5.35 | 25.70 | 43.54 | 26.05 | 1.69 |
| krg6** | 51.57 | 51.02 | 5.35 | 26.31 | 44.80 | 35.08 | 1.70 |
| krg7** | 51.33 | 52.05 | 5.35 | 26.72 | 47.90 | 36.65 | 1.79 |
| krg8** | 50.69 | 51.08 | 5.35 | 25.89 | 48.94 | 35.06 | 1.89 |
| krg9** | 51.55 | 51.08 | 5.35 | 26.33 | 51.89 | 38.43 | 1.97 |
| krg10** | 50.69 | 51.08 | 5.35 | 25.89 | 51.30 | 38.46 | 1.98 |
| krg11** | 52.57 | 52.05 | 5.35 | 27.36 | 55.70 | 36.65 | 2.04 |
| krg12** | 50.34 | 51.05 | 5.35 | 25.70 | 54.84 | 38.39 | 2.13 |
| krg13** | 51.53 | 51.08 | 5.35 | 26.32 | 60.75 | 42.43 | 2.31 |
| krg1*** | 51.58 | 51.05 | 5.35 | 26.33 | 35.48 | 29.91 | 1.35 |
| krg2*** | 51.57 | 51.02 | 5.35 | 26.31 | 39.64 | 31.06 | 1.51 |
| krg3*** | 51.56 | 51.10 | 5.35 | 26.35 | 40.53 | 35.11 | 1.54 |
| krg4*** | 51.56 | 51.09 | 5.35 | 26.34 | 42.12 | 36.72 | 1.60 |
| krg5*** | 50.34 | 51.05 | 5.35 | 25.70 | 45.77 | 36.72 | 1.78 |
| krg6*** | 51.57 | 51.02 | 5.35 | 26.31 | 46.11 | 38.46 | 1.75 |
| krg7*** | 51.33 | 52.05 | 5.35 | 26.72 | 47.07 | 40.38 | 1.76 |
| krg8*** | 50.69 | 51.08 | 5.35 | 25.89 | 49.48 | 38.46 | 1.91 |
| krg9*** | 51.55 | 51.08 | 5.35 | 26.33 | 50.28 | 40.40 | 1.91 |
| krg10*** | 50.69 | 51.08 | 5.35 | 25.89 | 51.80 | 40.40 | 2.00 |
| krg11*** | 52.57 | 52.05 | 5.35 | 27.36 | 53.43 | 38.44 | 1.95 |
| krg12*** | 50.34 | 51.05 | 5.35 | 25.70 | 55.14 | 42.48 | 2.15 |
| krg13*** | 51.53 | 51.08 | 5.35 | 26.32 | 57.93 | 44.83 | 2.20 |

For kerogen slit pores, the geometric insertion method[106, 244] is used to calculate the average pore size $W_{ave}$. For a random position, the largest insertion sphere which

includes the given position and is tangent with the kerogen surface is defined as the pore size for the given position. Thus, the average pore size $W_{ave}$ for a given kerogen slit pore can be determined by

$$W_{ave} = \int D_{ins} f\left(D_{ins}\right) dD_{ins}, \tag{5-2}$$

where $D_{ins}$ represents the diameter of the largest insertion sphere and $f\left(D_{ins}\right)$ is the fraction of a given $D_{ins}$. In this work, the average pore sizes of 13 kerogen models and their respective pseudo-kerogen models are all set as $W_{ave} = 5.35$ nm.

In this work, $CH_4$ excess adsorption in kerogen mesopores is calculated. The details of the process can be found in **Appendix D.4**.

To investigate the energetical heterogeneity effect, three types of artificial pseudo-kerogen-carbon models are designed and listed in **Table 5-2**. In the first artificial model (denoted as **krg***), we replace all kerogen heteroatoms (N, S, and O) with C atoms as in the graphite model with LJ size and energy parameters as $\sigma = 0.34$ nm and $\varepsilon / k_b = 28$ K. We note that three different types of C atoms are present in the kerogen model (see **Table D-1**). In the second artificial model (denoted as **krg****), we tune the LJ energy parameters $\varepsilon$ of kerogen heteroatoms (N, S, and O) as $\varepsilon$ for C atom in graphite while keeping their respective LJ size diameters $\sigma$ intact. For the third artificial model (denoted as **krg*****), the LJ size parameters $\sigma$ of kerogen heteroatoms (N, S, and O) are revised to $\sigma$ for C atom in graphite while keeping their respective LJ energy diameters $\varepsilon$ intact. By building these pseudo-kerogen carbon models, we qualitatively investigate the effect of energetical heterogeneity.

**Table 5-2** Illustration of each type of kerogen model.

| Types | Designs | Purposes |
|---|---|---|
| krg | original kerogen models | benchmark |
| krg* | replace heteratoms by active carbons (C) | investigate surface chemistry effect |
| krg** | revise heteratoms' energy parameters by ε (C) | investigate energy-parameter effect |
| krg*** | revise heteratoms' size parameters by σ (C) | investigate size-parameter effect |

### 5.2.3. Gas Adsorption Simulation

Grand canonical Monte Carlo (GCMC) simulations are applied to describe gas ($N_2$ and $CH_4$) adsorption in kerogen and smooth graphite mesopores in this work. The details of the process can be found in **Appendix D.5**.

### 5.2.4. Brunauer−Emmett−Teller (BET) Theory

The BET theory [245] has been widely used to estimate the surface area in porous materials by interpreting $N_2$ adsorption isotherms [90, 105]. In the BET theory, there are several key assumptions: (i) the surface is assumed to be flat and homogenous; (ii) The interactions among adsorbate molecules in the same layer are ignored; (iii) The adsorption layer becomes infinitely thick at the saturation pressure; (iv) The heat of adsorption for the first layer is greater than the second (and higher) layer where the heat of adsorption is the same as the heat of liquefaction. With all these assumptions, the BET equation is given as, [245]

$$\frac{P/P_0}{n\left(1-P/P_0\right)} = \frac{1}{n_m k_0} + \frac{k_0 - 1}{n_m k_0}\left(\frac{P}{P_0}\right), \tag{5-3}$$

where $P$ and $P_0$ are bulk pressure and saturation pressure of the adsorbate, respectively; $n$ represents the total adsorption amount at pressure $P$; $n_m$ is the effective monolayer capacity; $k_0$ is a parameter proportional to the exponential of the reduced surface adsorption energy. Both $n_m$ and $k_0$ can be obtained from the linear regression of the $N_2$ adsorption isotherms in BET plots.

The surface area in the BET theory is calculated by

$$S_{BET} = n_m a^2, \tag{5-4}$$

where $a^2$ represents the cross-sectional area of each $N_2$ molecule. $a^2 = 0.162$ nm$^2$ is used for the BET theory and obtained by assuming that the monolayer $N_2$ density is equal to the $N_2$ bulk density at 77 K [246]. To ensure the BET fitting plot is in a reasonable pressure region, the consistency criteria suggested in Rouquerol *et al.* [234] for the BET theory are applied in this work. The resultant pressure range for BET plots is 0.005~0.05 bar for $N_2$ adsorption in all kerogen and graphite models. We note that in this pressure range, $N_2$ adsorption in kerogen and graphite mesopores is mainly dominated by surface adsorption, while its free gas density is negligible.

## 5.3. Results and Discussions

In this section, we conduct $N_2$ adsorption simulations in 13 kerogen slit mesopores and their respective pseudo-kerogen models to investigate the effect of energetical and geometrical heterogeneity on $S_{BET}$ characterization. The effect of geometrical and energetical heterogeneity on $N_2$ adsorption isotherms at 77 K as well as the subsequent $S_{BET}$ characterization is carefully analyzed. The applicability of the BET method in kerogen mesopores is investigated by comparing $S_{BET}$ with $S_{geo}$. We also correlate $S_{BET}$ and $S_{geo}$ with the $CH_4$ adsorption amount at 333.15 K and 300 bar to assess their applicability.

### 5.3.1. The Effect of Geometrical Heterogeneity on $N_2$ Adsorption

The $N_2$ adsorption per cross-sectional area of the *x*-*y* plane $\Gamma_{N_2}/S_{xy}$ and geometric surface area $\Gamma_{N_2}/S_{geo}$ at various relative pressure in 13 kerogen and graphite models are presented in **Figure 5-2**. For clarity, only five kerogen models (*i.e.*, **krg1**, **krg5**, **krg7**, **krg9**, and **krg12**) and graphite models are shown, while $N_2$ adsorption in other kerogen models is shown in **Figure D-2**. $RO$ for each model is also labeled in the figure legend. Both $\Gamma_{N_2}/S_{xy}$ and $\Gamma_{N_2}/S_{geo}$ increase with $P$ as expected, while no clear trend is observed as $RO$ increases. To further analyze the surface roughness effect, $N_2$ adsorption at a given pressure $P$ = 0.05 bar for all kerogen and graphite models is depicted in **Figure 5-3**. Ideally, $S_{geo}$ should have a perfect linear correlation with *RO* considering its definition. However, due to the slight difference in the cross-sectional area of the *x*-*y* plane of each kerogen surface, the correlation is not perfectly linear though $S_{geo}$ still has an excellent linear correlation with *RO* as shown in **Figure 5-3 (a)**. On the other hand, $\Gamma_{N_2}/S_{xy}$ generally increases with $RO$ due to more adsorption sites. However, some kerogen cases with similar $RO$ have notably different $N_2$ adsorption amounts, where the deviation can be as much as 25%. These outliers indicate that purely using $RO$ to describe $N_2$ adsorption may not be viable. $\Gamma_{N_2}/S_{geo}$ has a more random relationship

with $RO$, which further indicates that other factors can significantly affect the $N_2$ adsorption in kerogen mesopores.

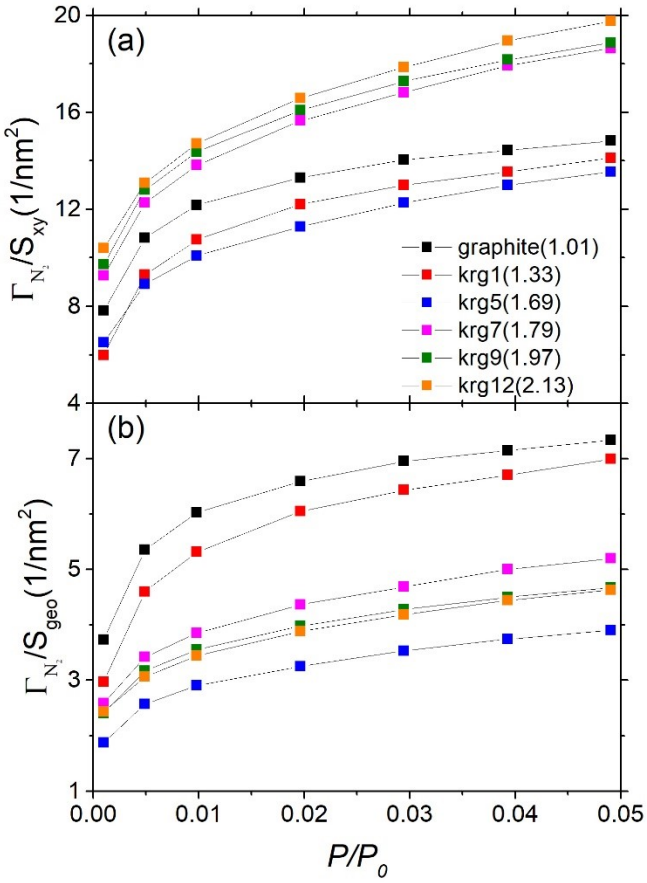


**Figure 5-2** $N_2$ adsorption (a) per cross-sectional area of the *x*-*y* plane $S_{xy}$; (b) per geometric surface area $S_{geo}$ in the graphite and select kerogen models. The numbers in parentheses represent the surface roughness of each model.

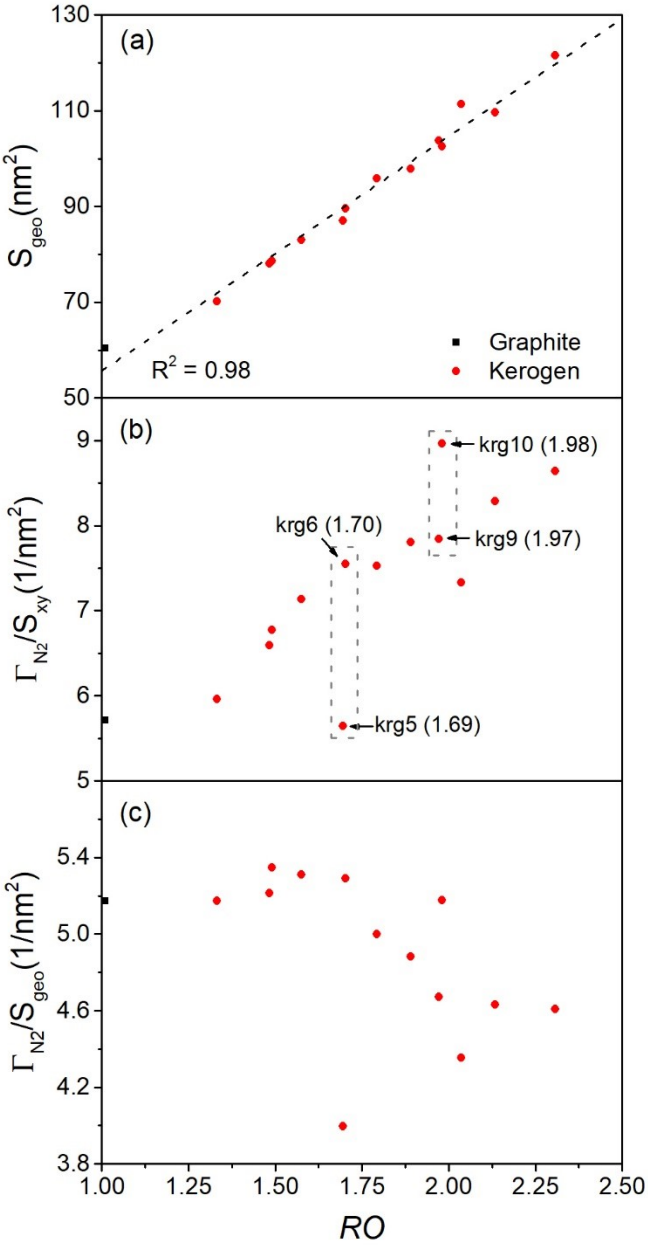


**Figure 5-3** (a) Geometric surface area; (b) The $N_2$ adsorption per cross-sectional area of the *x*-*y* plane $\Gamma_{N_2}/S_{xy}$ ; (c) $N_2$ adsorption per geometric surface area $\Gamma_{N_2}/S_{geo}$ versus $RO$. The adsorption amount is obtained at 0.05 bar. The black square and red circles represent $N_2$ adsorption in graphite and kerogen slit pore, respectively.

The topology of kerogen can be an important factor for $N_2$ adsorption. To better understand the effect of geometrical heterogeneity on $N_2$ adsorption, in **Figure 5-4**, we present the two-dimensional (2-D) $N_2$ density contour plots, their adsorption sites, and corresponding external potential, using **krg1** at 0.05 bar as a representative. The total $N_2$ adsorption is used to depict the surface adsorption, as $N_2$ density in the middle of the

mesopores is negligible (see **Figure D-3**). As shown in **Figure 5-4 (a)**, the $N_2$ adsorption in the *x*-*y* plane exhibits heterogeneous density distribution. In **Figures 5-4 (b)**, surface amplitude and $N_2$ adsorption are used to analyze the geometrical heterogeneity effect. The $N_2$ high-density adsorption sites are defined in **Appendix D.8**. Besides, the kerogen surface can be divided into "basin", "valley", and "ridge" regions according to their topology. The "ridge" regions are zoned by contour lines according to the local altitude, which can be case-dependent and their criteria are listed in **Table 5-3**. The high-density adsorption sites mainly fall in the "basin" and "valley" regions, while the "ridge" regions can hardly contain these sites. This phenomenon is consistent with other kerogen models as shown in **Figure D-4**. The external potential of the kerogen topology is used to explain the $N_2$ adsorption preferences on the kerogen surface as shown in **Figure 5-4 (c)**. To calculate the external potential, the system space is divided into $100 \times 100 \times 100$ bins. The external potential is calculated by the LJ interaction between the $N_2$ molecule and kerogen surface atoms at the center of each bin as long as it is in the kerogen pore space and not overlapped with the kerogen surface. To show external potential in 2-D (the *x*-*y* plane), the external potentials with the same *x* and *y* coordinates are summed along the *z*-direction. The "basin" and "valley" regions typically have more negative external potentials, *i.e.*, stronger attraction to $N_2$ molecules leading to a higher adsorption amount. On the other hand, the "ridge" regions have higher external potentials. The kerogen topology (geometrical heterogeneity) can directly affect external potential, which can further influence the $N_2$ adsorption.

**Table 5-3 "**Ridge" criteria, "ridge" surface area, and $N_2$ adsorption per geometric surface area in kerogen and pseudo-kerogen cases with different topologies.

| Case # | Ridge criteria in *z* - direction (Å) | $S_{rdg}/S_{geo}$ | $\Gamma_{N2}/S_{geo}$ (1/nm$^2$) |
|---|---|---|---|
| krg1 | 37.30 | 0.29 | 5.575 |
| krg2 | 35.80 | 0.34 | 5.591 |
| krg3 | 37.78 | 0.34 | 5.914 |
| krg4 | 35.19 | 0.29 | 5.821 |
| krg5 | 38.51 | 0.68 | 4.417 |
| krg6 | 35.47 | 0.40 | 5.889 |
| krg7 | 40.30 | 0.39 | 5.588 |
| krg8 | 36.29 | 0.46 | 5.378 |
| krg9 | 38.10 | 0.60 | 5.189 |
| krg10 | 36.23 | 0.42 | 5.616 |
| krg11 | 34.75 | 0.60 | 4.814 |
| krg12 | 39.60 | 0.60 | 5.088 |
| krg13 | 35.60 | 0.51 | 5.060 |
| krg1* | 37.24 | 0.30 | 4.435 |
| krg2* | 38.46 | 0.43 | 3.904 |
| krg3* | 43.38 | 0.12 | 4.420 |
| krg4* | 38.34 | 0.23 | 4.301 |
| krg5* | 39.65 | 0.39 | 4.171 |
| krg6* | 39.78 | 0.26 | 4.202 |
| krg7* | 40.20 | 0.31 | 4.218 |
| krg8* | 39.70 | 0.38 | 3.905 |
| krg9* | 38.35 | 0.48 | 4.131 |
| krg10* | 39.10 | 0.57 | 3.927 |
| krg11* | 37.69 | 0.57 | 3.506 |
| krg12* | 39.70 | 0.50 | 3.794 |
| krg13* | 37.39 | 0.61 | 3.758 |

319

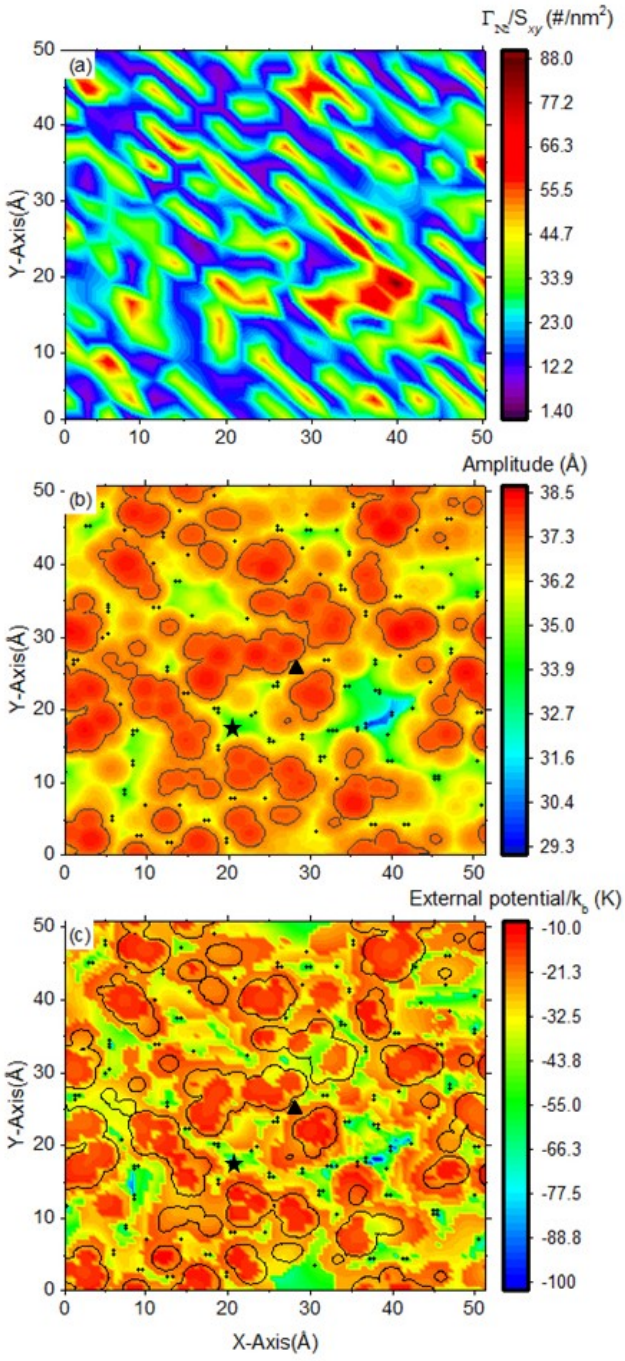


**Figure 5-4** $N_2$ adsorption on kerogen surface (**krg1**) at 0.05 bar: (a) 2-D density contour plot; (b) amplitude contour plot; (c) external potential contour plot. Black dots represent the high-density sites of $N_2$ adsorption on the kerogen surface. In panels (b) and (c), the triangle and star symbols are representatives of adsorption sites in the "valley" and "basin" areas, respectively. The "ridge" areas are enclosed by the black solid contour lines.

### 5.3.2. The Effect of Energetical Heterogeneity on $N_2$ Adsorption

Apart from the geometrical heterogeneity effect, the surface energetical heterogeneity can be another important factor affecting $N_2$ adsorption in kerogen slit

mesopores. To investigate the surface chemistry effect, $N_2$ adsorption simulations in kerogen and their respective three types of pseudo-kerogen models (as listed in **Table 5-2**) are conducted and analyzed.

To reveal the energetical heterogeneity effect on $N_2$ adsorption, **krg10** and its pseudo models are selected as a representative. Instead of the **krg1** model, **krg10** and its pseudo models, which have relatively rough surfaces, are selected to show the general application of our results. In **Figure 5-5**, $N_2$ adsorption amounts in **krg10**, **krg10***, **krg10****, and **krg10***** at various pressure conditions are depicted. $N_2$ adsorption amounts in these pseudo-kerogen models are lower than that in **krg10**. The difference between **krg10** and **krg10**** highlights the energy-parameter effect, while that between **krg10** and **krg10***** indicates the size-parameter effect. To further analyze the surface chemistry effect, the 2-D $N_2$ density contour plots in **krg10**, **krg10***, **krg10****, and **krg10***** at 0.05 bar are shown in **Figure 5-6**. Each density contour consists of 20 × 20 bins of local $N_2$ density. Comparing (a) and (c) can reveal the effect of energy parameters, while comparing (a) and (d) can display the effect of size parameters. With the same surface topology, $N_2$ density contour plots in **krg10** and **krg10**** are generally similar, but there are more high-density sites in **krg10** than **krg10****, as energy parameters in **krg10**** are less attractive. A similar phenomenon is also observed when comparing **krg10*** and **krg10***. However, when comparing **krg10** and **krg10***** as well as comparing **krg10*** and **krg10**** (note that they have the same energy parameters but different size parameters), there are noticeable differences in 2-D $N_2$ density contour plots. It is because altering the size-parameters can effectively change the geometrical heterogeneity which plays a significant role in $N_2$ adsorption as we discussed above. The adsorption sites might be "relocated" with different surface topologies. Some "lost" adsorption sites can be compensated to some degree elsewhere as shown in **Figure D-5**, which can explain the $N_2$ adsorption amount order (*i.e.*, **krg10** > **krg10***** > **krg10**** > **krg10***) as shown in **Figure 5-5**. The density distribution comparisons in the *z*-direction have been conducted and shown in **Figure D-6**.

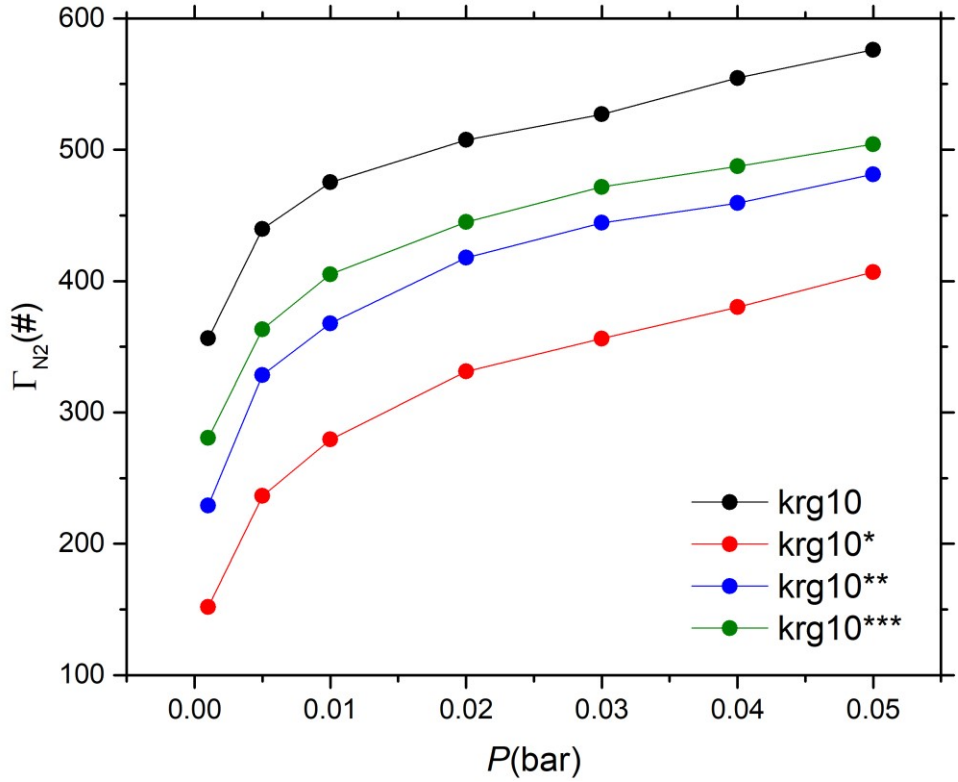


**Figure 5-5** $N_2$ adsorption amounts in krg10, krg10*, krg10**, and krg10*** at various pressures.

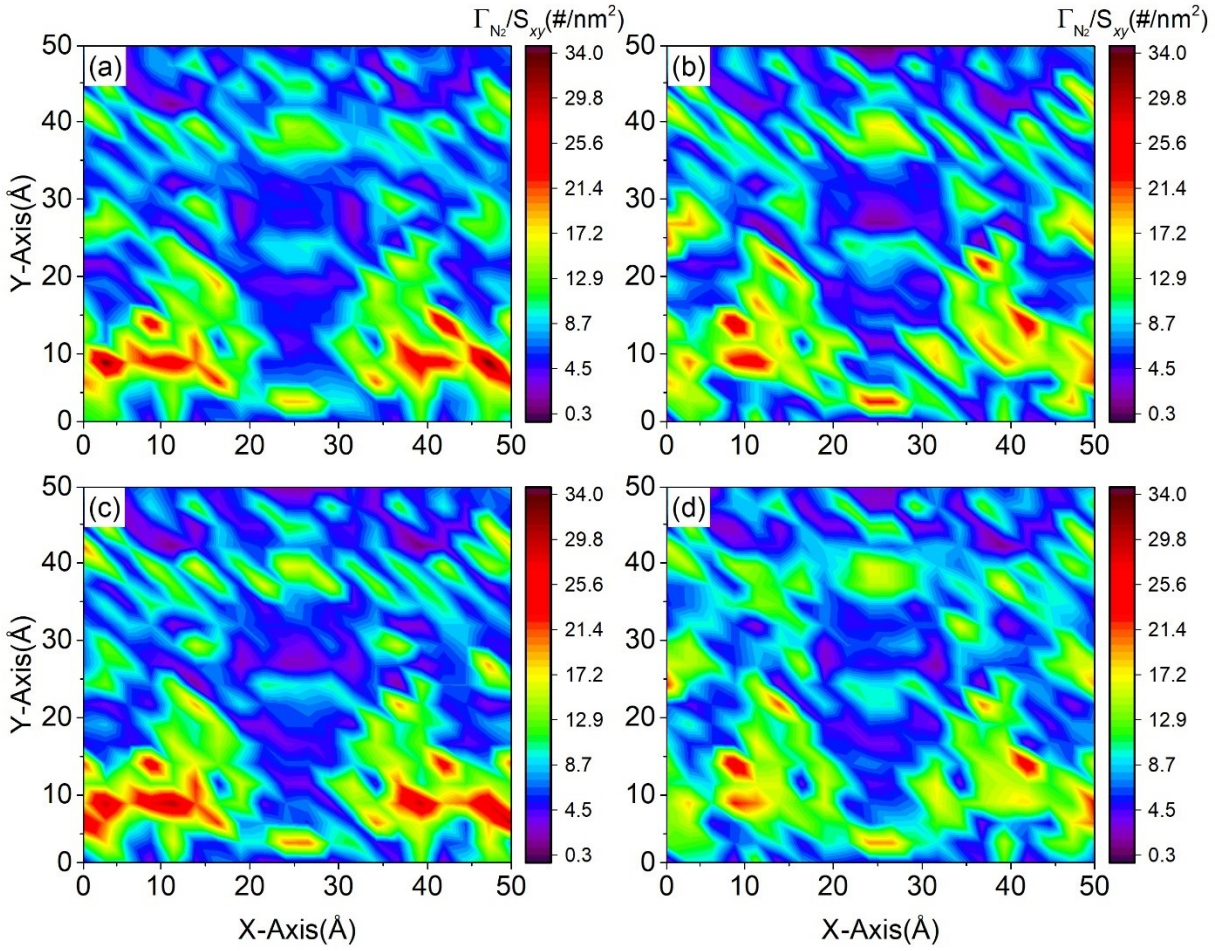


**Figure 5-6** 2-D $N_2$ density contour plots in (a) krg10; (b) krg10*; (c) krg10**; (d) krg10*** at 0.05 bar.

In **Figure 5-7**, we present the surface topology and external potential contour plots of **krg10**, **krg10***, **krg10****, and **krg10*****. In addition, we display the high-density sites at 0.05 bar. For **krg10**, the high-density sites are defined in the same manner as in **Figure 5-4**. On the other hand, for **krg10***, **krg10****, and **krg10*****, we use the same cut-off density value as in **krg10** to qualify as the high-density sites. As a result, there are 200, 129, 156, and 193 high-density sites in **krg10**, **krg10***, **krg10****, and **krg10*****,** respectively. Most of these high-density sites are outside of the "ridge" regions. The fewer high-density sites in **krg10***, **krg10****, and **krg10***** than **krg10** can explain the lower $N_2$ adsorption amounts in these models as shown in **Figure 5-5**. While the number of high-density sites in **krg10**** is much smaller than **krg10***, we note that some high-density sites in **krg10**** are in $N_2$ strongly-accumulating areas (*i.e.*, the dark red areas in 2-D density contour plots in **Figure 5-6 (c)**). Collectively, both size and energy

parameters show significant impacts on $N_2$ adsorption. In addition, we also present the external potential contour plots in **Figure 5-7**. The external potentials are more negative in **Figure 5-7 (a2)** than in **Figure 5-7 (c2)** as we discussed above. On the other hand, comparing **Figure 5-7 (a2)** and **Figure 5-7 (d2)** indicates that altering the size-parameters can affect external potential contour plots, in part due to altered surface topology as shown in **Figure 5-7 (a1)** and **Figure 5-7 (d1)**. It further endorses the importance of surface topology on $N_2$ adsorption. $N_2$ adsorption amounts in all kerogen cases and their respective artificial models at 0.05 bar are shown in **Figure D-7**.

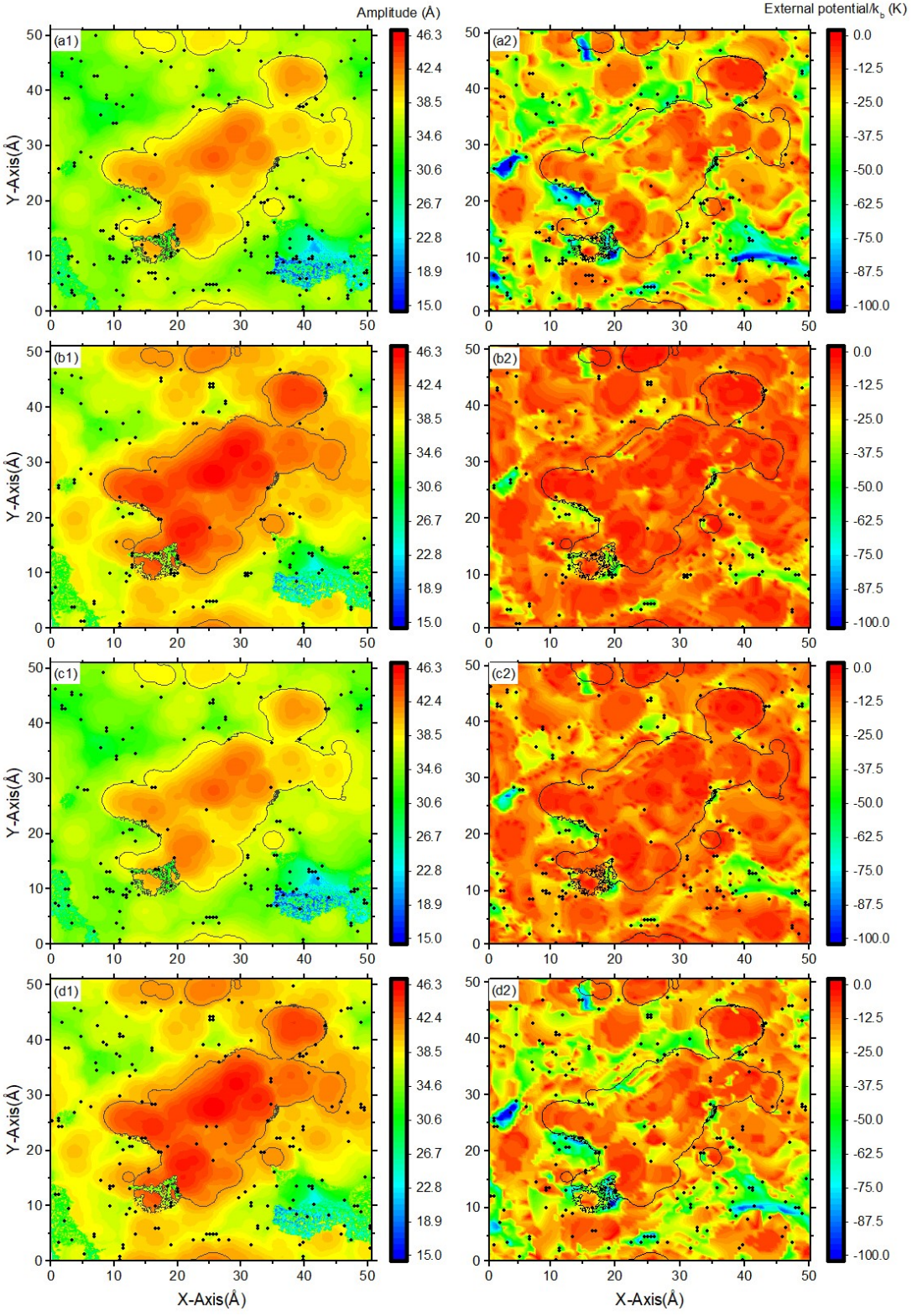


**Figure 5-7** (a1) Amplitude contour plot; (a2) external potential contour plot of **krg10**; (b1) amplitude contour plot; (b2) external potential contour plot of **krg10***; (c1) amplitude contour plot; (c2) external potential contour plot of **krg10****; (d1) amplitude

contour plot; (d2) external potential contour plot of **krg10*****. $N_2$ high-density sites at 0.05 bar are displayed as black dots. The "ridge" areas are enclosed by contour lines.

To further analyze the geometrical and energetical heterogeneity effect on $N_2$ adsorption, the relationship between the $N_2$ adsorption amount per accessible surface area $\Gamma_{N_2} / S_{geo}$ at 0.05 bar and the fraction of the "ridge" regions in the accessible surface $S_{rdg} / S_{geo}$ are presented in **Figure 5-8**. In addition, $N_2$ adsorption in graphite mesopores is also depicted. For all types of kerogen models, $\Gamma_{N_2} / S_{geo}$ and $S_{rdg} / S_{geo}$ have a linear correlation with a negative slope and $R^2 \sim 0.8$. In **Figure 5-8 (a)**, the *y*-intercept of the extrapolated trendline is close to the graphite case (deviation ~ 10 %). On the other hand, with the same surface topologies ((a) versus (c); (b) versus (d)), the slope of their trendlines are similar.

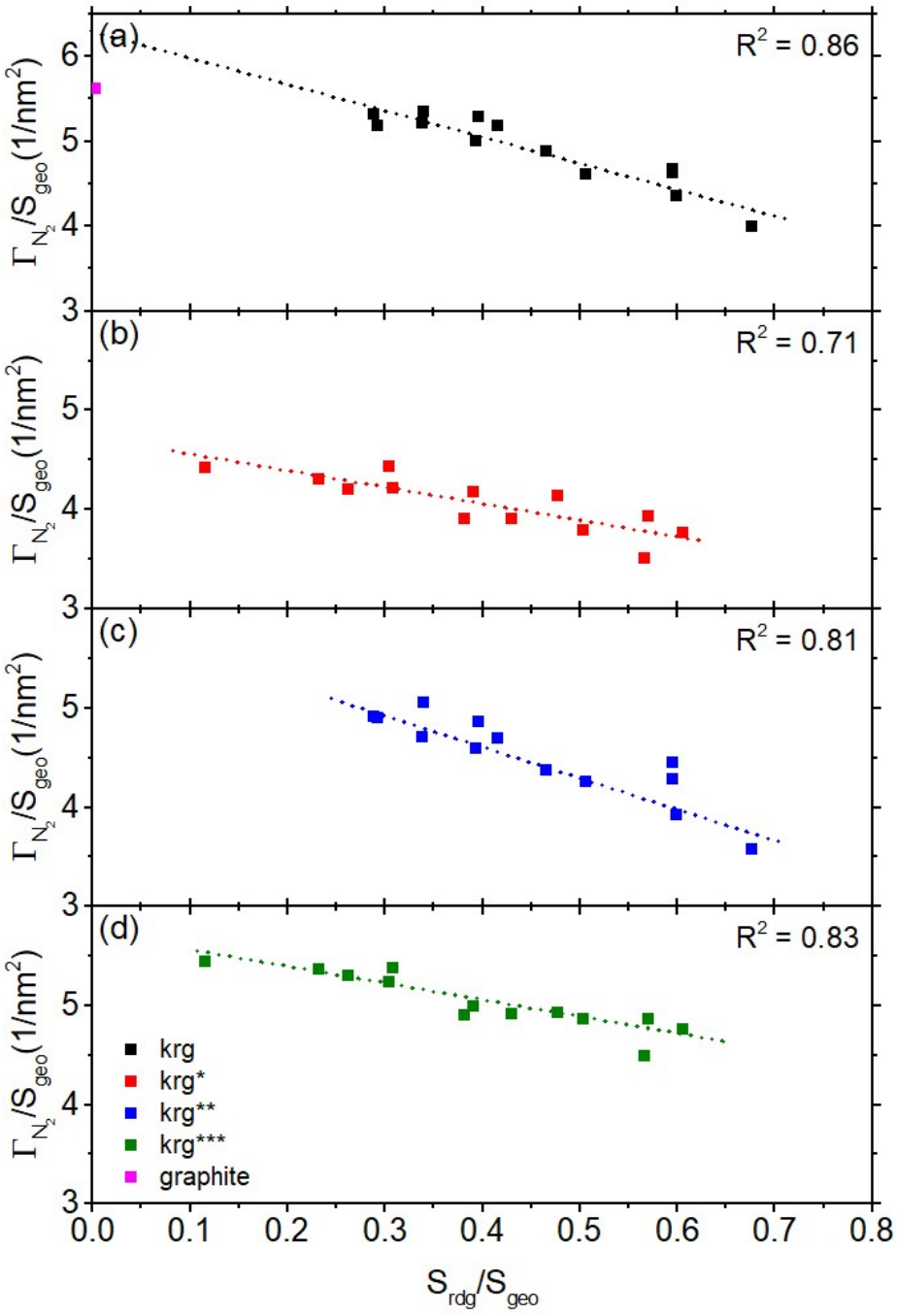


**Figure 5-8** The relationship between the "ridge" area and $N_2$ adsorption amount in kerogen mesopores at 0.05 bar. The dashed lines are trendlines of each type of model.

The predicted $S_{BET}$ for kerogen slit mesopores are then compared against $S_{geo}$ as shown in **Figure 5-9**. $S_{BET}$ is obtained based on the BET plots as shown in **Figure D-8**, and $S_{BET}$ of the graphite, kerogen models, and their artificial models are listed in **Table**

404 **5-1**. $S_{BET}$ agrees well with $S_{geo}$ in graphite mesopores, which is consistent with reported
405 results[86], while $S_{BET}$ is lower than $S_{geo}$ in **krg**, **krg***, **krg****, and **krg*****. As $RO$ and
406 $S_{rdg}/S_{geo}$ increase, the deviation generally becomes more significant. We note that $S_{BET}$
407 is a direct result of $N_2$ adsorption in kerogen mesopores. Therefore, $S_{BET}$ reflects the $N_2$
408 adsorption sites to some degree. To satisfy the consistency criteria[234] for the BET theory,
409 a low-pressure range is used for the BET fitting. As a result, the "ridge effect", *i.e.*, the
410 "ridge" regions having a low tendency to adsorb $N_2$, could have a significant influence on
411 $N_2$ adsorption. Thus, the presence of "ridge" regions is one main reason that $S_{BET}$ is
412 generally lower than $S_{geo}$ in kerogen mesopores. Walton *et al.* [235] found that $S_{BET}$
413 matches well with $S_{geo}$ by using $N_2$ adsorption in MOFs. Tian and Wu [105] investigated
414 the BET performances for 1200 hypothetical MOFs by using $N_2$ adsorption. They stated
415 that the BET method may either underestimate or overestimate $S_{geo}$ depending on the
416 surface energy and pore size, which is in line with the findings of Coasne *et al.* [89] and
417 Gómez-Gualdrón *et al.* [86]. Gómez-Gualdrón *et al.* [86] believe the overestimation of $S_{BET}$
418 might be because of the significantly overestimated monolayer loading in MOFs in BET
419 calculations. Furthermore, Coasne *et al.* [89] hypothesized that the negative curvature might
420 be the reason for the BET method underestimating the surface area of a fully-disordered
421 Vycor-like porous matrix, which is very similar to the "ridge" effect discussed in this
422 work. While we find that $S_{BET}$ is systematically lower than $S_{geo}$ in kerogen mesopores,
423 the following questions still arise: a) Which surface area performs better in terms of $CH_4$
424 adsorption estimation, $S_{BET}$ or $S_{geo}$? b) Are the $N_2$ adsorption sites generally similar to
425 $CH_4$ adsorption sites?

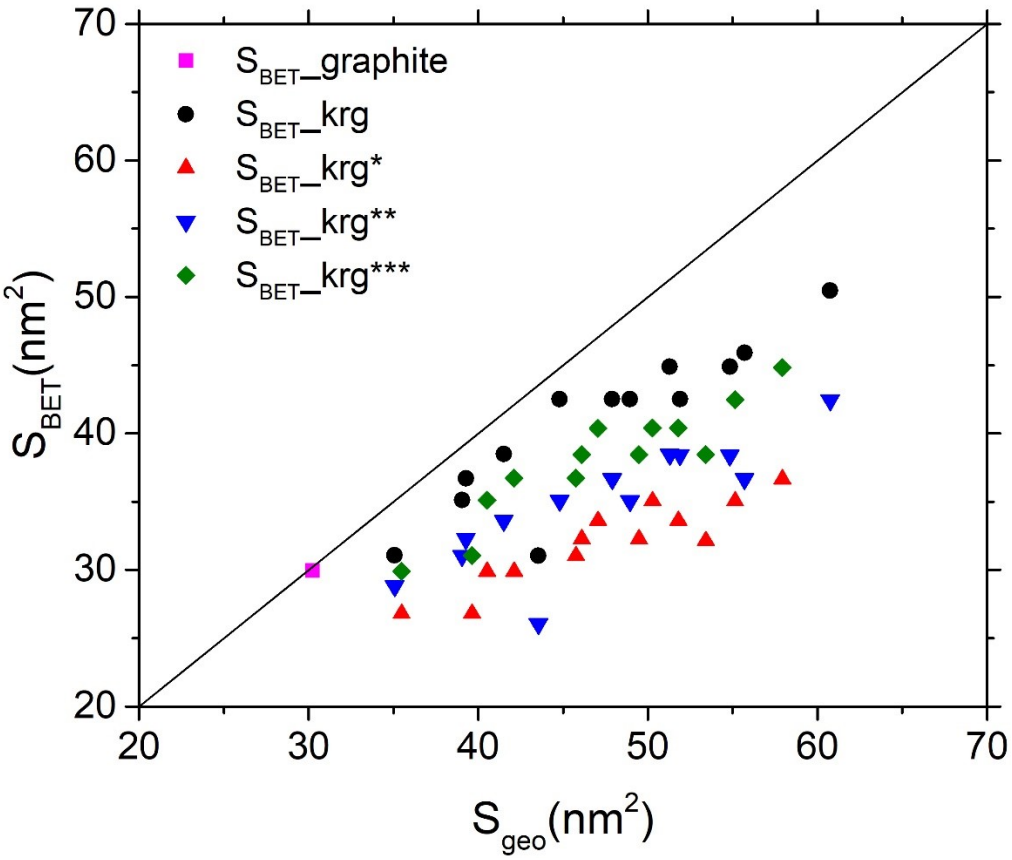


**Figure 5-9** Comparisons between the BET surface area $S_{BET}$ and geometric surface area $S_{geo}$ for graphite, kerogen, and pseudo-kerogen models with different roughness and fraction of "ridge" area.

### 5.3.3. $CH_4$ Adsorption Estimation

In experimental measurements, $CH_4$ excess adsorption can be obtained via volumetric and gravimetric methods[7], while it can be converted to absolute adsorption. Very recently, Zeng *et al.*[247] used NMR measurements to obtain the $CH_4$ total adsorption amount in shale samples. In this subsection, we first study $CH_4$ adsorption characteristics in kerogen mesopores and assess the applicability of $S_{BET}$ in terms of $CH_4$ excess adsorption and total adsorption.

In **Figure 5-10 (a)**, we present a one-dimensional (1-D) $CH_4$ density profile in the *z*-direction at 300 bar and 333.15 K in **krg1** as a representative. $CH_4$ shows a strong adsorption layer in the vicinity of the kerogen surface, while its density in the middle of the pore regresses to its bulk value. Therefore, the main contribution to the $CH_4$ excess adsorption is from the $CH_4$ adsorption sites on the kerogen surface. The $CH_4$ high-excess-

density sites ($CH_4$ excess density is defined as the local density minus its bulk density) on the kerogen surface are presented in **Figure 5-10 (b)**. Similar to $N_2$ high-density sites, $CH_4$ high-excess-density sites are mainly located outside of the "ridge" areas. In other words, surface topology plays an important role in $CH_4$ excess adsorption in kerogen mesopores.

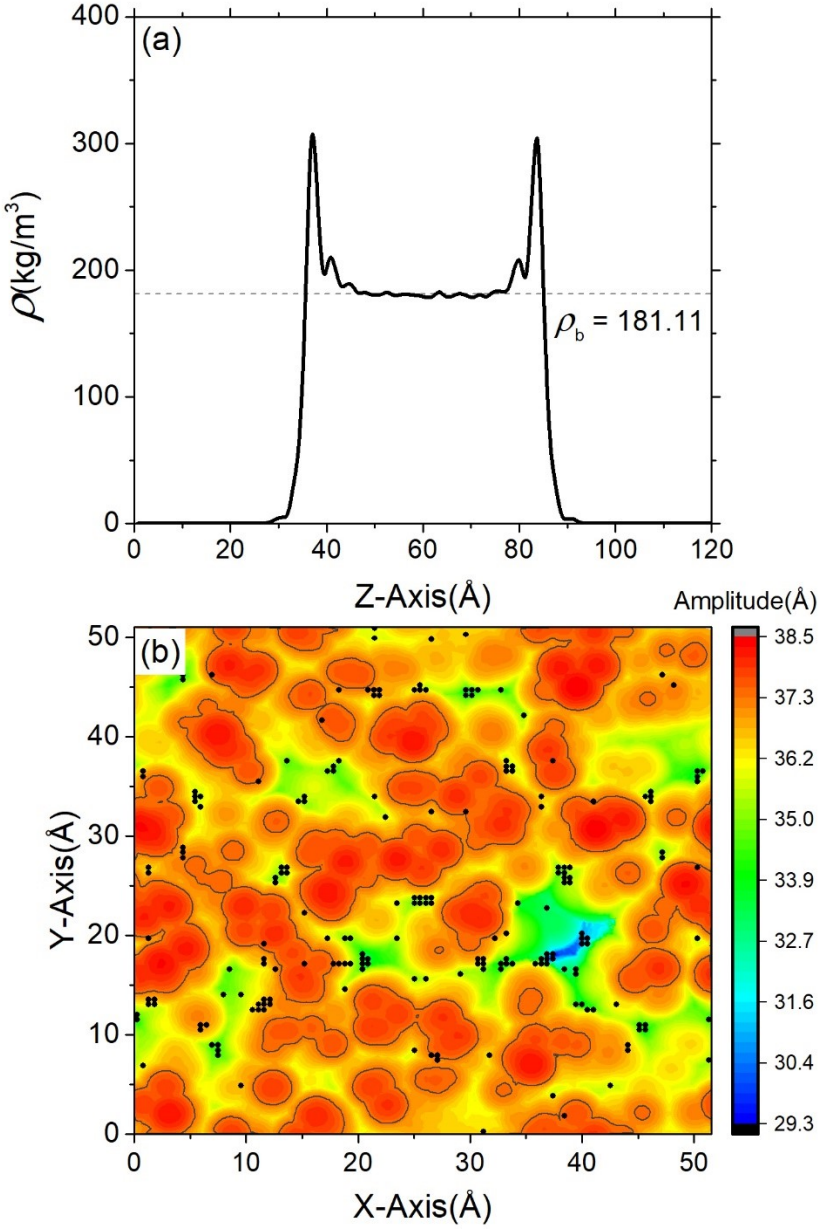


**Figure 5-10** $CH_4$ adsorption in **krg1** at 300 bar and 333.15 K: (a) 1-D density profile in the *z*-direction; (b) amplitude contour plot and $CH_4$ high-excess-density sites.

To show the qualification of being an indicator of $CH_4$ excess adsorption, in **Figure 5-11**, we present the correlations between $CH_4$ excess adsorption and $S_{BET}$ as

well as $S_{geo}$ in various kerogen models at 300 bar and 333.15 K. We note that **krg6**, **krg7**, **krg8**, and **krg9** have very similar $S_{BET}$ values as shown in **Figure 5-11 (a)**. Due to similar $RO$ (1.70~1.97), they have similar $N_2$ adsorption amount versus pressure relationships, leading to almost the same intercepts and slopes in the BET plots. It also illustrates that the BET method might be problematic in surface area estimation for heterogeneous slit mesopores to some degree. Overall, the $CH_4$ excess adsorption has a better linear correlation with $S_{BET}$ than $S_{geo}$. It is probably because both $N_2$–kerogen and $CH_4$–kerogen interactions are mainly van der Waals type, while their adsorption sites largely overlap (outside of the "ridge" areas). The linear relationship between $CH_4$ excess adsorption and $S_{BET}$ has been observed in the literature.[248] It indicates that $S_{BET}$ is still a reasonably good choice to estimate $CH_4$ excess adsorption in kerogen mesopores, even though its basic assumptions may not fit well with the characteristics of kerogen (energetical and geometrical heterogeneity). In addition, $S_{BET}$ also shows a better linear correlation with $CH_4$ total adsorption than $S_{geo}$ as depicted in **Figure D-9** due to the similar effective pore volume of these kerogen models as listed in **Table D-2**.

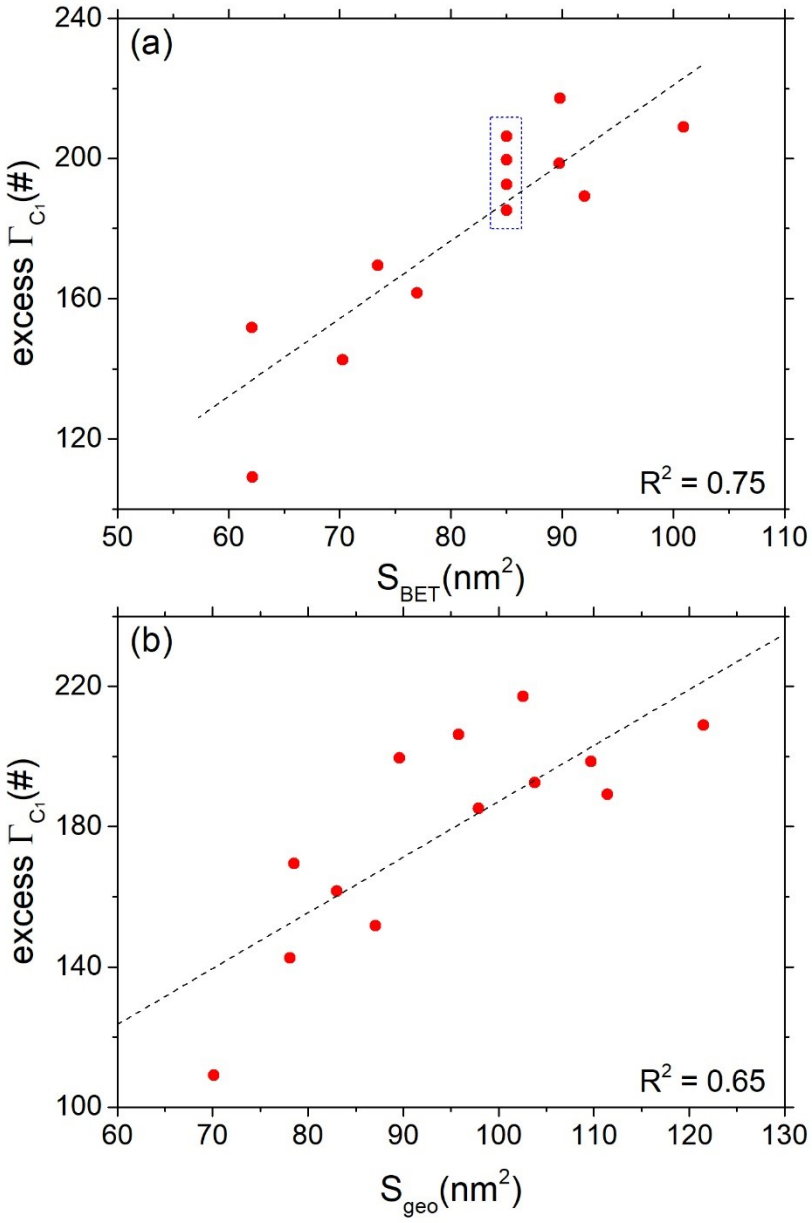


**Figure 5-11** $CH_4$ excess adsorption versus (a) $S_{BET}$; (b) $S_{geo}$ at 300 bar.

While our study can provide some crucially important fundamental understanding about $S_{BET}$ characterization and $CH_4$ adsorption prediction in kerogen mesopores, we note a few important suggestions to further expand our findings. First, the $N_2$ model used for $S_{BET}$ characterization is based on the single-site LJ fluid, which has been widely used in $N_2$ adsorption simulations[249-251]. While Arora *et al.*[251] claimed that the quadrupole moment of $N_2$ has a negligible effect on $N_2$ adsorption in graphite slit pores at 303 K, whether $N_2$–kerogen interaction is mainly dominated by the van der Waals interaction

still needs to be tested. Second, the lack of experimental measurements with well-characterized kerogen surface properties to verify $N_2$–kerogen interaction is utterly needed. In addition, considering the complicated *in-situ* conditions, the effect of kerogen maturity and moisture on $S_{BET}$ characterization should be addressed in future studies.

### 5.4. Conclusions

In this work, we conduct simulations of $N_2$ adsorption at 77 K in 13 kerogen slit mesopores and their respective pseudo-kerogen models to study the effect of kerogen geometrical and energetical heterogeneity on $S_{BET}$ characterization. The effect of surface roughness, topology, and chemistry on $N_2$ adsorption and the subsequent $S_{BET}$ characterization are carefully investigated. For comparison, we also simulate 77 K $N_2$ adsorption in perfectly-smooth graphite mesopores to obtain $S_{BET}$. We found that $N_2$ adsorption sites are mainly within the "basin" and "valley" regions on the kerogen surface, while in "ridge" regions its adsorption rarely takes place. On the other hand, surface chemistry shows a significant effect on external potential and $N_2$ adsorption amount. $S_{BET}$ is generally lower than $S_{geo}$ in kerogen and pseudo-kerogen mesopores. The deviation becomes more significant as $RO$ and $S_{rdg}/S_{geo}$ increase. In contrast, $S_{BET}$ agrees well with $S_{geo}$ in graphite mesopores. On the other hand, $CH_4$ high-excess-adsorption sites are also mainly outside of the "ridge" regions. As a result, $S_{BET}$ correlates well with $CH_4$ excess adsorption in kerogen mesopores, outperforming $S_{geo}$. The good performance of $S_{BET}$ in terms of $CH_4$ adsorption estimation is probably because the van der Waals type interactions are used to describe $N_2$–kerogen and $CH_4$–kerogen interactions. This work provides some crucially important fundamental understanding about $S_{BET}$ characterization in kerogen mesopores which can guide $CH_4$ adsorption capacity prediction in kerogen nanoporous media and shale GIP estimation. The framework of this work for surface area characterization might be extended to other organic-rich rocks, like coal, considering the importance of the surface area and $CH_4$ adsorption in these rocks.公式章 (下一章) 节 1

# CHAPTER 6 Conclusions and Recommendations for Future Work

## 6.1. Key Conclusions

Due to the strong fluid–surface interaction in nanopores, gas adsorption plays a significant role in the properties and behaviors of confined fluids in shale nanoporous media. The objectives of this thesis fall in two main target areas as stated in CHAPTER 1,

I. Gas adsorption and phase behaviors in shale organic nanoporous media

II. Surface area characterization of shale organic media

In the first main target area, we have investigated the gas adsorption and phase behaviors in shale organic nanoporous media by using a single-pore model (CHAPTER 2), a multi-scale nanopore–bulk model (CHAPTER 3), and the effect of $CO_2$ injection in a multi-scale nanopore–bulk model (CHAPTER 4). We have studied pure hydrocarbon adsorption and phase behaviors in shale organic nanopores a single-pore model by using engineering DFT and investigated the validity of the Kelvin equation and the EOS–$P_{cap}$ method in kerogen (using graphite to represent in this section) small nanopores. Besides, the effect of PSD/volume partitioning on gas adsorption, properties of confined hydrocarbon mixtures, and their recovery employing PSDs from various shale sub-formations was characterized by engineering DFT in a multi-scale bulk–nanopore model. Additionally, we also investigated the effect of $CO_2$ injection during the $CO_2$ 'huff-n-puff' process on gas adsorption, recovery, and $CO_2$ geological sequestration in a multi-scale bulk–nanopore model by a CVD process, in which mass balance and volume partitioning are explicitly considered. This section provides important insights into the prediction of phase behaviors of confined fluids which are at the heart of many engineering applications, such as shale/tight oil production. It also provides a fundamental understanding about the effect of PSD/volume partitioning on hydrocarbon mixture adsorption characteristics in nanopores in shale porous media and the optimization of enhanced shale gas recovery and $CO_2$ sequestration.

In the second main target area, we have investigated surface area characterization of shale organic media (CHAPTER 5). The effect of geometrical and energetical heterogeneity on $N_2$ adsorption isotherms and the subsequent BET surface area ($S_{BET}$) characterization has been studied. The effect of surface roughness, topology, and

chemistry on $N_2$ adsorption and $S_{BET}$ characterization are carefully investigated. Besides, we have also investigated the applicability of the BET method for the surface area characterization of kerogen mesopores and the correlation between $S_{BET}$ and methane adsorption. This section provides some crucially important fundamental understanding about $S_{BET}$ characterization in kerogen mesopores which can guide $CH_4$ adsorption capacity prediction in kerogen nanoporous media and shale GIP estimation. The framework of this work for surface area characterization might be extended to other organic-rich rocks, like coal, considering the importance of the surface area and $CH_4$ adsorption in these rocks.

In summary, by using theoretical modeling/ molecular simulations, this work studied gas adsorption, phase behaviors, and surface area characterization in shale organic nanoporous media. The pore size effect, the PSD effect, and the effect of $CO_2$ injection coupled with the PSD effect on gas adsorption, phase behaviors, and gas recovery have been investigated. On the other hand, we also investigated surface area characterizations of kerogen. The effect of geometrical and energetical heterogeneity and the applicability of the BET method for the surface area characterization of kerogen mesopores have been investigated. This thesis provides some crucially important insights into the optimization of shale gas recovery, geological $CO_2$ sequestration, $CH_4$ adsorption capacity prediction, and shale gas-in-place (GIP) estimation in kerogen nanoporous media.

### 6.2. Recommendations for Future Work

Based on the results of this thesis and the conclusions, here are some recommendations for future research:

For the first part of this thesis, regarding the adsorption and phase behaviors of nanoconfined fluids, we have investigated the effect of nanoconfinement, the effect of pore size distribution, and the effect of $CO_2$ injection on adsorption and phase behaviors of hydrocarbon in nanopores. In our models, for simplicity, all nanopores are simulated as slit geometry, while various pore types can exist in shale reservoirs. On the other hand, moisture exists in shale media which can affect hydrocarbon and $CO_2$ adsorption [55]. Unlocking these effects coupled with volume partitioning in the nanopore–bulk

multiscale system on hydrocarbon and $CO_2$ adsorption should provide a fundamental understanding about the effect of volume partitioning on hydrocarbon mixtures adsorption characteristics and important insights into the optimization of enhanced shale gas recovery and $CO_2$ sequestration.

For the second part of this thesis, regarding the surface area characterization of kerogen, we have investigated the advantages and limitations of different surface area measurements and the effect of energetical and geometrical heterogeneity of kerogen on the BET surface area characterization. In our models, while our study can provide some crucially important fundamental understanding about surface area characterization and $CH_4$ adsorption prediction in kerogen mesopores, we note a few important suggestions to further expand our findings. First, the $N_2$ model used for surface area characterization is based on the single-site LJ fluid. While the quadrupole moment of $N_2$ is always considered to have a negligible effect on $N_2$ adsorption in graphite slit pores, whether $N_2$–kerogen interaction is mainly dominated by the Van der Waals interaction still needs to be tested. Moreover, the lack of experimental measurements with well-characterized kerogen surface properties to verify $N_2$–kerogen interaction is utterly needed. In addition, considering the complicated *in-situ* conditions, the effect of kerogen maturity and moisture on surface area characterization should be addressed in future studies.

公式章 1 节 1

# REFERENCES


1. Nalley, S.; LaRose, A., Annual Energy Outlook 2021. *Energy Information Administration, Washington, DC* **2021**.
2. Ho, T. A.; Wang, Y.; Ilgen, A.; Criscenti, L. J.; Tenney, C. M., Supercritical CO2-induced atomistic lubrication for water flow in a rough hydrophilic nanochannel. *Nanoscale* **2018,** 10, (42), 19957-19963.
3. Chong, L.; Sanguinito, S.; Goodman, A. L.; Myshakin, E. M., Molecular characterization of carbon dioxide, methane, and water adsorption in micropore space of kerogen matrix. *Fuel* **2021,** 283, 119254.
4. Michalec, L.; Lísal, M., Molecular simulation of shale gas adsorption onto overmature type II model kerogen with control microporosity. *Molecular Physics* **2017,** 115, (9-12), 1086-1103.
5. Psarras, P.; Holmes, R.; Vishal, V.; Wilcox, J., Methane and CO2 Adsorption Capacities of Kerogen in the Eagle Ford Shale from Molecular Simulation. *Accounts of Chemical Research* **2017,** 50, (8), 1818-1828.
6. Tesson, S.; Firoozabadi, A., Methane Adsorption and Self-Diffusion in Shale Kerogen and Slit Nanopores by Molecular Simulations. *The Journal of Physical Chemistry C* **2018,** 122, (41), 23528-23542.
7. Pang, W.; Wang, Y.; Jin, Z., Comprehensive Review about Methane Adsorption in Shale Nanoporous Media. *Energy & Fuels* **2021,** 35, (10), 8456-8493.
8. Ross, D. J. K.; Marc Bustin, R., The importance of shale composition and pore structure upon gas storage potential of shale gas reservoirs. *Marine and Petroleum Geology* **2009,** 26, (6), 916-927.
9. Clayton, C., PETROLEUM GEOLOGY | Chemical and Physical Properties. In *Encyclopedia of Geology*, Selley, R. C.; Cocks, L. R. M.; Plimer, I. R., Eds. Elsevier: Oxford, 2005; pp 248-260.
10. Jin, Z.; Firoozabadi, A., Thermodynamic Modeling of Phase Behavior in Shale Media. *SPE Journal* **2016,** 21, (1).
11. Jin, Z.; Firoozabadi, A., Phase behavior and flow in shale nanopores from molecular simulations. *Fluid Phase Equilibria* **2016,** 430, 156-168.
12. Didar, B. R.; Akkutlu, I. Y., Pore-size Dependence of Fluid Phase Behavior and Properties in Organic-Rich Shale Reservoirs. In *SPE International Symposium on Oilfield Chemistry*, Society of Petroleum Engineers: The Woodlands, Texas, USA, 2013; p 19.
13. Elliott, J. A. W., On the complete Kelvin equation. *Chemical Engineering Education* **2001,** 35, (4), 274-278.
14. Jin, Z.; Firoozabadi, A., Thermodynamic Modeling of Phase Behavior in Shale Media. *SPE Journal* **2016,** 21, (1), 190-207.
15. Jatukaran, A.; Zhong, J.; Persad, A. H.; Xu, Y.; Mostowfi, F.; Sinton, D., Direct Visualization of Evaporation in a Two-Dimensional Nanoporous Model for Unconventional Natural Gas. *ACS Applied Nano Materials* **2018,** 1, (3), 1332-1338.
16. Ravikovitch, P. I.; Domhnaill, S. C. O.; Neimark, A. V.; Schueth, F.; Unger, K. K., Capillary Hysteresis in Nanopores: Theoretical and Experimental Studies of Nitrogen Adsorption on MCM-41. *Langmuir* **1995,** 11, (12), 4765-4772.
17. Kruk, M.; Jaroniec, M.; Sayari, A., Application of Large Pore MCM-41 Molecular Sieves To Improve Pore Size Analysis Using Nitrogen Adsorption Measurements. *Langmuir* **1997,** 13, (23), 6267-6273.
18. Miyahara, M.; Kanda, H.; Yoshioka, T.; Okazaki, M., Modeling Capillary Condensation in Cylindrical Nanopores: A Molecular Dynamics Study. *Langmuir* **2000,** 16, (9), 4293-4299.
19. Walton, J. P. R. B.; Quirke, N., Capillary Condensation: A Molecular Simulation Study. *Molecular Simulation* **1989,** 2, (4-6), 361-391.
20. Lastoskie, C.; Gubbins, K. E.; Quirke, N., Pore size distribution analysis of microporous carbons: a density functional theory approach. *The Journal of Physical Chemistry* **1993,** 97, (18), 4786-4796.

21. Takei, T.; Chikazawa, M.; Kanazawa, T., Validity of the Kelvin equation in estimation of small pore size by nitrogen adsorption. *Colloid and Polymer Science* **1997,** 275, (12), 1156-1161.
22. Zandavi, S. H.; Ward, C. A., Nucleation and growth of condensate in nanoporous materials. *Physical Chemistry Chemical Physics* **2015,** 17, (15), 9828-9834.
23. Zhong, J.; Riordon, J.; Zandavi, S. H.; Xu, Y.; Persad, A. H.; Mostowfi, F.; Sinton, D., Capillary Condensation in 8 nm Deep Channels. *The Journal of Physical Chemistry Letters* **2018,** 9, (3), 497-503.
24. Yang, Q.; Jin, B.; Banerjee, D.; Nasrabadi, H., Direct visualization and molecular simulation of dewpoint pressure of a confined fluid in sub-10 nm slit pores. *Fuel* **2019,** 235, 1216-1223.
25. Fisher, L. R.; Israelachvili, J. N., Direct experimental verification of the Kelvin equation for capillary condensation. *Nature* **1979,** 277, 548-549.
26. Zhang, K.; Jia, N.; Li, S.; Liu, L., Thermodynamic phase behaviour and miscibility of confined fluids in nanopores. *Chemical Engineering Journal* **2018,** 351, 1115-1128.
27. Sandoval, D.; Yan, W.; Michelsen, M. L.; Stenby, E. H., Phase Envelope Calculations for Reservoir Fluids in the Presence of Capillary Pressure. In *SPE Annual Technical Conference and Exhibition*, Society of Petroleum Engineers: Houston, Texas, USA, 2015; p 15.
28. Ma, Y.; Jin, L.; Jamili, A., Modifying van der Waals Equation of State to Consider Influence of Confinement on Phase Behavior. In *SPE Annual Technical Conference and Exhibition*, Society of Petroleum Engineers: New Orleans, Louisiana, USA, 2013; p 12.
29. Zuo, J. Y.; Guo, X.; Liu, Y.; Pan, S.; Canas, J.; Mullins, O. C., Impact of Capillary Pressure and Nanopore Confinement on Phase Behaviors of Shale Gas and Oil. *Energy & Fuels* **2018,** 32, (4), 4705-4714.
30. Zhang, Y.; Lashgari, H. R.; Di, Y.; Sepehrnoori, K., Capillary Pressure Effect on Hydrocarbon Phase Behavior in Unconventional Reservoirs. In *SPE Low Perm Symposium*, Society of Petroleum Engineers: Denver, Colorado, USA, 2016; p 13.
31. Liu, Y.; Jin, Z.; Li, H. A., Comparison of Peng-Robinson Equation of State With Capillary Pressure Model With Engineering Density-Functional Theory in Describing the Phase Behavior of Confined Hydrocarbons. *SPE Journal* **2018,** 23, (5), 1784-1797.
32. Dong, X.; Liu, H.; Hou, J.; Wu, K.; Chen, Z., Phase Equilibria of Confined Fluids in Nanopores of Tight and Shale Rocks Considering the Effect of Capillary Pressure and Adsorption Film. *Industrial & Engineering Chemistry Research* **2016,** 55, (3), 798-811.
33. Stimpson, B. C.; Barrufet, M. A., Thermodynamic Modeling of Pure Components Including the Effects of Capillarity. *Journal of Chemical & Engineering Data* **2016,** 61, (8), 2844-2850.
34. Rezaveisi, M.; Sepehrnoori, K.; Pope, G. A.; Johns, R. T., Compositional Simulation Including Effect of Capillary Pressure on Phase Behavior. In *SPE Annual Technical Conference and Exhibition*, Society of Petroleum Engineers: Houston, Texas, USA, 2015; p 37.
35. Sandoval, D. R.; Yan, W.; Michelsen, M. L.; Stenby, E. H., Influence of Adsorption and Capillary Pressure on Phase Equilibria inside Shale Reservoirs. *Energy & Fuels* **2018,** 32, (3), 2819-2833.
36. Liu, Y.; Li, H. A.; Okuno, R., Phase Behavior of Fluid Mixtures in a Partially Confined Space. In *SPE Annual Technical Conference and Exhibition*, Society of Petroleum Engineers: Dubai, UAE, 2016; p 26.
37. Gelb, L. D.; Gubbins, K. E.; Radhakrishnan, R.; Sliwinska-Bartkowiak, M., Phase separation in confined systems. *Reports on Progress in Physics* **1999,** 62, (12), 1573-1659.
38. Evans, R., Fluids adsorbed in narrow pores: phase equilibria and structure. *Journal of Physics: Condensed Matter* **1990,** 2, (46), 8989.
39. Jin, Z., Bubble/dew point and hysteresis of hydrocarbons in nanopores from molecular perspective. *Fluid Phase Equilibria* **2018,** 458, 177-185.
40. Singh, S.; Sinha, A.; Deo, G.; K. Singh, J., Vapor−Liquid Phase Coexistence, Critical Properties, and Surface Tension of Confined Alkanes. *Journal of Physical Chemistry C* **2009,** 113, (17), 7170-7180.

41. Neimark, A. V.; Vishnyakov, A., Gauge cell method for simulation studies of phase transitions in confined systems. *Physical Review E* **2000,** 62, (4), 4611-4622.
42. Jin, B.; Nasrabadi, H., Phase behavior of multi-component hydrocarbon systems in nano-pores using gauge-GCMC molecular simulation. *Fluid Phase Equilibria* **2016,** 425, 324-334.
43. Pitakbunkate, T.; Balbuena, P. B.; Moridis, G. J.; Blasingame, T. A., Effect of Confinement on Pressure/Volume/Temperature Properties of Hydrocarbons in Shale Reservoirs. *SPE Journal* **2016,** 21, (2), 621-634.
44. Bui, K.; Akkutlu, I. Y., Hydrocarbons Recovery From Model-Kerogen Nanopores. *SPE Journal* **2017,** 22, (03), 854-862.
45. Freeman, C.; Moridis, G. J.; Michael, G. E.; Blasingame, T. A., Measurement, Modeling, and Diagnostics of Flowing Gas Composition Changes in Shale Gas Wells. In *SPE Latin America and Caribbean Petroleum Engineering Conference*, Society of Petroleum Engineers: Mexico City, Mexico, 2012; p 25.
46. Luo, S.; Lutkenhaus, J. L.; Nasrabadi, H., Multi-Scale Fluid Phase Behavior Simulation in Shale Reservoirs by a Pore-Size-Dependent Equation of State. In *SPE Annual Technical Conference and Exhibition*, Society of Petroleum Engineers: San Antonio, Texas, USA, 2017.
47. Luo, S.; Lutkenhaus, J. L.; Nasrabadi, H., Effect of Nano-Scale Pore Size Distribution on Fluid Phase Behavior of Gas IOR in Shale Reservoirs. In *SPE Improved Oil Recovery Conference*, Society of Petroleum Engineers: Tulsa, Oklahoma, USA, 2018.
48. Jin, B.; Bi, R.; Nasrabadi, H., Molecular simulation of the pore size distribution effect on phase behavior of methane confined in nanopores. *Fluid Phase Equilibria* **2017,** 452, 94-102.
49. Alharthy, N. S.; Nguyen, T.; Teklu, T.; Kazemi, H.; Graves, R., Multiphase Compositional Modeling in Small-Scale Pores of Unconventional Shale Reservoirs. In *SPE Annual Technical Conference and Exhibition*, Society of Petroleum Engineers: New Orleans, Louisiana, USA, 2013; p 20.
50. Arogundade, O.; Sohrabi, M., A Review of Recent Developments and Challenges in Shale Gas Recovery. In *SPE Saudi Arabia Section Technical Symposium and Exhibition*, Society of Petroleum Engineers: Al-Khobar, Saudi Arabia, 2012; p 31.
51. Jin, L.; Ma, Y.; Jamili, A., Investigating The Effect of Pore Proximity on Phase Behavior And Fluid Properties in Shale Formations. In *SPE Annual Technical Conference and Exhibition*, Society of Petroleum Engineers: New Orleans, Louisiana, USA, 2013; p 16.
52. Louk, K.; Ripepi, N.; Luxbacher, K.; Gilliland, E.; Tang, X.; Keles, C.; Schlosser, C.; Diminick, E.; Keim, S.; Amante, J.; Michael, K., Monitoring CO2 storage and enhanced gas recovery in unconventional shale reservoirs: Results from the Morgan County, Tennessee injection test. *Journal of Natural Gas Science and Engineering* **2017,** 45, 11-25.
53. Sandrea, R., Evaluating production potential of mature US oil, gas shale plays. *Oil and Gas Journal* **2012,** 110, (12), 58-67.
54. Bui, M.; Adjiman, C. S.; Bardow, A.; Anthony, E. J.; Boston, A.; Brown, S.; Fennell, P. S.; Fuss, S.; Galindo, A.; Hackett, L. A.; Hallett, J. P.; Herzog, H. J.; Jackson, G.; Kemper, J.; Krevor, S.; Maitland, G. C.; Matuszewski, M.; Metcalfe, I. S.; Petit, C.; Puxty, G.; Reimer, J.; Reiner, D. M.; Rubin, E. S.; Scott, S. A.; Shah, N.; Smit, B.; Trusler, J. P. M.; Webley, P.; Wilcox, J.; Mac Dowell, N., Carbon capture and storage (CCS): the way forward. *Energy & Environmental Science* **2018,** 11, (5), 1062-1176.
55. Zhou, J.; Jin, Z.; Luo, K. H., The role of brine in gas adsorption and dissolution in kerogen nanopores for enhanced gas recovery and CO2 sequestration. *Chemical Engineering Journal* **2020,** 399, 125704.
56. Iddphonce, R.; Wang, J.; Zhao, L., Review of CO2 injection techniques for enhanced shale gas recovery: Prospect and challenges. *Journal of Natural Gas Science and Engineering* **2020,** 77, 103240.
57. Mohagheghian, E.; Hassanzadeh, H.; Chen, Z., CO2 sequestration coupled with enhanced gas recovery in shale gas reservoirs. *Journal of CO2 Utilization* **2019,** 34, 646-655.

58. Berawala, D. S.; Østebø Andersen, P., Evaluation of Multicomponent Adsorption Kinetics for CO2 Enhanced Gas Recovery from Tight Shales. In *SPE Europec featured at 81st EAGE Conference and Exhibition*, Society of Petroleum Engineers: London, England, UK, 2019; p 26.
59. Eshkalak, M. O.; Al-shalabi, E. W.; Sanaei, A.; Aybar, U.; Sepehrnoori, K., Enhanced Gas Recovery by CO2 Sequestration versus Re-fracturing Treatment in Unconventional Shale Gas Reservoirs. In *Abu Dhabi International Petroleum Exhibition and Conference*, Society of Petroleum Engineers: Abu Dhabi, UAE, 2014; p 18.
60. Sheng, J. J., Critical review of field EOR projects in shale and tight reservoirs. *Journal of Petroleum Science and Engineering* **2017,** 159, 654-665.
61. Holmes, R.; Aljamaan, H.; Vishal, V.; Wilcox, J.; Kovscek, A. R., Idealized Shale Sorption Isotherm Measurements To Determine Pore Capacity, Pore Size Distribution, and Surface Area. *Energy & Fuels* **2019,** 33, (2), 665-676.
62. Liu, J.; Yao, Y.; Liu, D.; Elsworth, D., Experimental evaluation of CO2 enhanced recovery of adsorbed-gas from shale. *International Journal of Coal Geology* **2017,** 179, 211-218.
63. Liu, J.; Xie, L.; Yao, Y.; Gan, Q.; Zhao, P.; Du, L., Preliminary Study of Influence Factors and Estimation Model of the Enhanced Gas Recovery Stimulated by Carbon Dioxide Utilization in Shale. *ACS Sustainable Chemistry & Engineering* **2019,** 7, (24), 20114-20125.
64. Li, L.; Li, C.; Kang, T., Adsorption/Desorption Behavior of CH4 on Shale during the CO2 Huff-and-Puff Process. *Energy & Fuels* **2019,** 33, (6), 5147-5152.
65. Sui, H.; Yao, J., Effect of surface chemistry for CH4/CO2 adsorption in kerogen: A molecular simulation study. *Journal of Natural Gas Science and Engineering* **2016,** 31, 738-746.
66. Yuan, Q.; Zhu, X.; Lin, K.; Zhao, Y.-P., Molecular dynamics simulations of the enhanced recovery of confined methane with carbon dioxide. *Physical Chemistry Chemical Physics* **2015,** 17, (47), 31887-31893.
67. Zeng, K.; Jiang, P.; Lun, Z.; Xu, R., Molecular Simulation of Carbon Dioxide and Methane Adsorption in Shale Organic Nanopores. *Energy & Fuels* **2019,** 33, (3), 1785-1796.
68. Huang, L.; Ning, Z.; Wang, Q.; Qi, R.; Zeng, Y.; Qin, H.; Ye, H.; Zhang, W., Molecular simulation of adsorption behaviors of methane, carbon dioxide and their mixtures on kerogen: Effect of kerogen maturity and moisture content. *Fuel* **2018,** 211, 159-172.
69. Zhou, J.; Jin, Z.; Luo, K. H., Effects of Moisture Contents on Shale Gas Recovery and CO2 Sequestration. *Langmuir* **2019,** 35, (26), 8716-8725.
70. Zhou, J.; Jin, Z.; Luo, K. H., Insights into recovery of multi-component shale gas by CO2 injection: A molecular perspective. *Fuel* **2020,** 267, 117247.
71. Zhang, M.; Zhan, S.; Jin, Z., Recovery mechanisms of hydrocarbon mixtures in organic and inorganic nanopores during pressure drawdown and CO2 injection from molecular perspectives. *Chemical Engineering Journal* **2020,** 382, 122808.
72. Bakhshian, S.; Hosseini, S. A., Prediction of CO2 adsorption-induced deformation in shale nanopores. *Fuel* **2019,** 241, 767-776.
73. Xu, R.; Zeng, K.; Zhang, C.; Jiang, P., Assessing the feasibility and CO2 storage capacity of CO2 enhanced shale gas recovery using Triple-Porosity reservoir model. *Applied Thermal Engineering* **2017,** 115, 1306-1314.
74. Kim, T. H.; Cho, J.; Lee, K. S., Evaluation of CO2 injection in shale gas reservoirs with multi-component transport and geomechanical effects. *Applied Energy* **2017,** 190, 1195-1206.
75. T, L.; Ko, R., Origin and characterization of Eagle Ford pore networks in the south Texas Upper Cretaceous shelf. *AAPG Bulletin* **2017,** 101, (3), 387-418.
76. Zhong, J.; Zhao, Y.; Lu, C.; Xu, Y.; Jin, Z.; Mostowfi, F.; Sinton, D., Nanoscale Phase Measurement for the Shale Challenge: Multicomponent Fluids in Multiscale Volumes. *Langmuir* **2018,** 34, (34), 9927-9935.

77. Zhao, Y.; wang, y.; Zhong, J.; Xu, Y.; Sinton, D.; Jin, Z., Bubble Point Pressures of Hydrocarbon Mixtures in Multiscale Volumes from Density Functional Theory. *Langmuir* **2018,** 34, (46), 14058-14068.
78. Zhao, Y.; Jin, Z., Hydrocarbon-Phase Behaviors in Shale Nanopore/Fracture Model: Multiscale, Multicomponent, and Multiphase. *SPE Journal* **2019,** 24, (06), 2526-2540.
79. Wang, Y.; Jin, Z., Effect of pore size distribution on hydrocarbon mixtures adsorption in shale nanoporous media from engineering density functional theory. *Fuel* **2019,** 254, 115650.
80. Luo, S.; Lutkenhaus, J. L.; Nasrabadi, H., Effect of Nanoscale Pore-Size Distribution on Fluid Phase Behavior of Gas-Improved Oil Recovery in Shale Reservoirs. *SPE Journal* **2020,** 25, (03), 1406-1415.
81. Wang, L.; Yin, X.; Neeves, K. B.; Ozkan, E., Effect of Pore-Size Distribution on Phase Transition of Hydrocarbon Mixtures in Nanoporous Media. *SPE Journal* **2016,** 21, (6), 1981-1995.
82. Luo, S.; Lutkenhaus, J. L.; Nasrabadi, H., Multi-Scale Fluid Phase Behavior Simulation in Shale Reservoirs by a Pore-Size-Dependent Equation of State. In *SPE Annual Technical Conference and Exhibition*, Society of Petroleum Engineers: San Antonio, Texas, USA, 2017; p 22.
83. Luo, S.; Lutkenhaus, J. L.; Nasrabadi, H., Experimental study of pore size distribution effect on phase transitions of hydrocarbons in nanoporous media. *Fluid Phase Equilibria* **2019,** 487, 8-15.
84. Wang, L.; Neeves, K.; Yin, X.; Ozkan, E., Experimental Study and Modeling of the Effect of Pore Size Distribution on Hydrocarbon Phase Behavior in Nanopores. In *SPE Annual Technical Conference and Exhibition*, Society of Petroleum Engineers: Amsterdam, The Netherlands, 2014; p 15.
85. Moore, J. D.; Palmer, J. C.; Liu, Y.-C.; Roussel, T. J.; Brennan, J. K.; Gubbins, K. E., Adsorption and diffusion of argon confined in ordered and disordered microporous carbons. *Applied Surface Science* **2010,** 256, (17), 5131-5136.
86. Gómez-Gualdrón, D. A.; Moghadam, P. Z.; Hupp, J. T.; Farha, O. K.; Snurr, R. Q., Application of Consistency Criteria To Calculate BET Areas of Micro- And Mesoporous Metal–Organic Frameworks. *Journal of the American Chemical Society* **2016,** 138, (1), 215-224.
87. Senkovska, I.; Kaskel, S., Ultrahigh porosity in mesoporous MOFs: promises and limitations. *Chemical Communications* **2014,** 50, (54), 7089-7098.
88. Yuan, D.; Getman, R. B.; Wei, Z.; Snurr, R. Q.; Zhou, H.-C., Stepwise adsorption in a mesoporous metal–organic framework: experimental and computational analysis. *Chemical Communications* **2012,** 48, (27), 3297-3299.
89. Coasne, B.; Gubbins, K. E.; Pellenq, R. J.-M., A Grand Canonical Monte Carlo Study of Adsorption and Capillary Phenomena in Nanopores of Various Morphologies and Topologies: Testing the BET and BJH Characterization Methods. *Particle & Particle Systems Characterization* **2004,** 21, (2), 149-160.
90. Coasne, B.; Di Renzo, F.; Galarneau, A.; Pellenq, R. J. M., Adsorption of Simple Fluid on Silica Surface and Nanopore: Effect of Surface Chemistry and Pore Shape. *Langmuir* **2008,** 24, (14), 7285-7293.
91. Coasne, B.; Grosman, A.; Ortega, C.; Pellenq, R. J. M., Physisorption in nanopores of various sizes and shapes : A Grand Canonical Monte Carlo simulation study. In *Studies in Surface Science and Catalysis*, Rodriguez-Reinoso, F.; McEnaney, B.; Rouquerol, J.; Unger, K., Eds. Elsevier: 2002; Vol. 144, pp 35-42.
92. Bae, Y.-S.; Yazaydın, A. Ö.; Snurr, R. Q., Evaluation of the BET Method for Determining Surface Areas of MOFs and Zeolites that Contain Ultra-Micropores. *Langmuir* **2010,** 26, (8), 5475-5483.
93. Wei, M.; Xiong, Y.; Zhang, L.; Li, J., The effect of sample particle size on the determination of pore structure parameters in shales. *International Journal of Coal Geology* **2016,** 163, 177-185.
94. Yuan, Y.; Rezaee, R.; Al-Khdheeawi, E. A.; Hu, S.-Y.; Verrall, M.; Zou, J.; Liu, K., Impact of Composition on Pore Structure Properties in Shale: Implications for Micro-/Mesopore Volume and Surface Area Prediction. *Energy & Fuels* **2019,** 33, (10), 9619-9628.
95. Bousige, C.; Ghimbeu, C. M.; Vix-Guterl, C.; Pomerantz, A. E.; Suleimenova, A.; Vaughan, G.; Garbarino, G.; Feygenson, M.; Wildgruber, C.; Ulm, F.-J.; Pellenq, R. J. M.; Coasne, B., Realistic molecular model of kerogen's nanostructure. *Nature Materials* **2016,** 15, (5), 576-582.

96. Sing, K., The use of nitrogen adsorption for the characterisation of porous materials. *Colloids and Surfaces A: Physicochemical and Engineering Aspects* **2001,** 187-188, 3-9.
97. Do, D. D.; Do, H. D., Modeling of Adsorption on Nongraphitized Carbon Surface: GCMC Simulation Studies and Comparison with Experimental Data. *The Journal of Physical Chemistry B* **2006,** 110, (35), 17531-17538.
98. Seaton, N. A.; Friedman, S. P.; MacElroy, J. M. D.; Murphy, B. J., The Molecular Sieving Mechanism in Carbon Molecular Sieves: A Molecular Dynamics and Critical Path Analysis. *Langmuir* **1997,** 13, (5), 1199-1204.
99. Lucena, S. M. P.; Paiva, C. A. S.; Silvino, P. F. G.; Azevedo, D. C. S.; Cavalcante, C. L., The effect of heterogeneity in the randomly etched graphite model for carbon pore size characterization. *Carbon* **2010,** 48, (9), 2554-2565.
100. Wongkoblap, A.; Do, D. D., The effects of energy sites on adsorption of Lennard–Jones fluids and phase transition in carbon slit pore of finite length a computer simulation study. *Journal of Colloid and Interface Science* **2006,** 297, (1), 1-9.
101. Shi, K.; Santiso, E. E.; Gubbins, K. E., Bottom-Up Approach to the Coarse-Grained Surface Model: Effective Solid–Fluid Potentials for Adsorption on Heterogeneous Surfaces. *Langmuir* **2019,** 35, (17), 5975-5986.
102. Shi, K.; Santiso, E. E.; Gubbins, K. E., Conformal Sites Theory for Adsorbed Films on Energetically Heterogeneous Surfaces. *Langmuir* **2020,** 36, (7), 1822-1838.
103. Jagiello, J.; Olivier, J. P., 2D-NLDFT adsorption models for carbon slit-shaped pores with surface energetical heterogeneity and geometrical corrugation. *Carbon* **2013,** 55, 70-80.
104. Jagiello, J.; Olivier, J. P., Carbon slit pore model incorporating surface energetical heterogeneity and geometrical corrugation. *Adsorption* **2013,** 19, (2), 777-783.
105. Tian, Y.; Wu, J., A comprehensive analysis of the BET area for nanoporous materials. *AIChE Journal* **2018,** 64, (1), 286-293.
106. Gelb, L. D.; Gubbins, K. E., Characterization of Porous Glasses: Simulation Models, Adsorption Isotherms, and the Brunauer−Emmett−Teller Analysis Method. *Langmuir* **1998,** 14, (8), 2097-2111.
107. Falk, K.; Coasne, B.; Pellenq, R.; Ulm, F.-J.; Bocquet, L., Subcontinuum mass transport of condensed hydrocarbons in nanoporous media. *Nature Communications* **2015,** 6, 6949.
108. Debe, M. K., Electrocatalyst approaches and challenges for automotive fuel cells. *Nature* **2012,** 486, 43.
109. Cervilla, A.; Corma, A.; Fornes, V.; Llopis, E.; Palanca, P.; Rey, F.; Ribera, A., Intercalation of [MoVIO2(O2CC(S)Ph2)2]2- in a Zn(II)-Al(III) Layered Double Hydroxide Host: A Strategy for the Heterogeneous Catalysis of the Air Oxidation of Thiols. *Journal of the American Chemical Society* **1994,** 116, (4), 1595-1596.
110. Scherer, G. W., Theory of Drying. *Journal of the American Ceramic Society* **1990,** 73, (1), 3-14.
111. Vorhauer, N.; Wang, Y. J.; Kharaghani, A.; Tsotsas, E.; Prat, M., Drying with Formation of Capillary Rings in a Model Porous Medium. *Transport in Porous Media* **2015,** 110, (2), 197-223.
112. Lee, J.; Laoui, T.; Karnik, R., Nanofluidic transport governed by the liquid/vapour interface. *Nature Nanotechnology* **2014,** 9, 317-324.
113. Stevens, B.; Feingold, G., Untangling aerosol effects on clouds and precipitation in a buffered system. *Nature* **2009,** 461, (7264), 607.
114. Li, X.; Hede, T.; Tu, Y.; Leck, C.; Ågren, H., Surface-Active cis-Pinonic Acid in Atmospheric Droplets: A Molecular Dynamics Study. *The Journal of Physical Chemistry Letters* **2010,** 1, (4), 769-773.
115. Kovács, T.; Meldrum, F. C.; Christenson, H. K., Crystal Nucleation without Supersaturation. *The Journal of Physical Chemistry Letters* **2012,** 3, (12), 1602-1606.

116. Liu, J.; Wang, L.; Xi, S.; Asthagiri, D.; Chapman, W. G., Adsorption and Phase Behavior of Pure/Mixed Alkanes in Nanoslit Graphite Pores: An iSAFT Application. *Langmuir* **2017,** 33, (42), 11189-11202.
117. Fisher, L. R.; Gamble, R. A.; Middlehurst, J., The Kelvin equation and the capillary condensation of water. *Nature* **1981,** 290, 575-576.
118. Shardt, N.; Elliott, J. A. W., Isobaric Vapor–Liquid Phase Diagrams for Multicomponent Systems with Nanoscale Radii of Curvature. *The Journal of Physical Chemistry B* **2018,** 122, (8), 2434-2447.
119. Melrose, J. C., Model calculations for capillary condensation. *AIChE Journal* **1966,** 12, (5), 986-994.
120. Nojabaei, B.; Johns, R. T.; Chu, L., Effect of Capillary Pressure on Fluid Density and Phase Behavior in Tight Rocks and Shales. *SPE Reservoir Evaluation & Engineering* **2012,** 16, (3), 281-289.
121. Dullien, F. A. L.; Brenner, H., *Porous Media: Fluid Transport and Pore Structure*. Elsevier Science: 2012.
122. Wongkoblap, A.; Do, D. D.; Birkett, G.; Nicholson, D., A critical assessment of capillary condensation and evaporation equations: A computer simulation study. *Journal of Colloid and Interface Science* **2011,** 356, (2), 672-680.
123. Stokes, R. J.; Evans, D. F., *Fundamentals of interfacial engineering*. Wiley-VCH: New York, 1997.
124. Whalen, J. W., *Physical chemistry of surfaces, fourth edition (Adamson, Arthur W.)*. American Chemical Society: 1983; Vol. 60, p A322.
125. Zhong, J.; Zandavi, S. H.; Li, H.; Bao, B.; Persad, A. H.; Mostowfi, F.; Sinton, D., Condensation in One-Dimensional Dead-End Nanochannels. *ACS Nano* **2017,** 11, (1), 304-313.
126. Tsukahara, T.; Maeda, T.; Hibara, A.; Mawatari, K.; Kitamori, T., Direct measurements of the saturated vapor pressure of water confined in extended nanospaces using capillary evaporation phenomena. *RSC Advances* **2012,** 2, (8), 3184-3186.
127. Parsa, E.; Yin, X.; Ozkan, E., Direct Observation of the Impact of Nanopore Confinement on Petroleum Gas Condensation. In *SPE Annual Technical Conference and Exhibition*, Society of Petroleum Engineers: Houston, Texas, USA, 2015; p 7.
128. Fisher, L. R.; Israelachvili, J. N., Experimental studies on the applicability of the Kelvin equation to highly curved concave menisci. *Journal of Colloid and Interface Science* **1981,** 80, (2), 528-541.
129. Kohonen, M. M.; Christenson, H. K., Capillary Condensation of Water between Rinsed Mica Surfaces. *Langmuir* **2000,** 16, (18), 7285-7288.
130. Fisher, L. R.; Israelachvili, J. N., Direct experimental verification of the Kelvin equation for capillary condensation. *Nature* **1979,** 277, (5697), 548-549.
131. Alam, M. A.; Clarke, A. P.; Duffy, J. A., Capillary Condensation and Desorption of Binary Mixtures of N2−Ar Confined in a Mesoporous Medium. *Langmuir* **2000,** 16, (20), 7551-7553.
132. Factorovich, M. H.; Molinero, V.; Scherlis, D. A., Vapor Pressure of Water Nanodroplets. *Journal of the American Chemical Society* **2014,** 136, (12), 4508-4514.
133. Barrett, E. P.; Joyner, L. G.; Halenda, P. P., The Determination of Pore Volume and Area Distributions in Porous Substances. I. Computations from Nitrogen Isotherms. *Journal of the American Chemical Society* **1951,** 73, (1), 373-380.
134. Broekhoff, J. C. P.; de Boer, J. H., Studies on pore systems in catalysts: IX. Calculation of pore distributions from the adsorption branch of nitrogen sorption isotherms in the case of open cylindrical pores A. Fundamental equations. *Journal of Catalysis* **1967,** 9, (1), 8-14.
135. Broekhoff, J. C. P.; De Boer, J. H., Studies on pore systems in catalysts: XI. Pore distribution calculations from the adsorption branch of a nitrogen adsorption isotherm in the case of “ink-bottle” type pores. *Journal of Catalysis* **1968,** 10, (2), 153-165.

136. Nelson, A. K.; Kalyuzhnyi, Y. V.; Patsahan, T.; McCabe, C., Liquid-vapor phase equilibrium of a simple liquid confined in a random porous media: Second-order Barker-Henderson perturbation theory and scaled particle theory. *Journal of Molecular Liquids* **2020,** 300, 112348.
137. Dong, W.; Chen, X., Scaled particle theory for bulk and confined fluids: A review. *Science China Physics, Mechanics & Astronomy* **2018,** 61, (7), 70501.
138. Qiao, C. Z.; Zhao, S. L.; Liu, H. L.; Dong, W., Augmented Scaled Particle Theory. *The Journal of Physical Chemistry B* **2020,** 124, (7), 1207-1217.
139. Tan, S. P.; Piri, M., Equation-of-state modeling of confined-fluid phase equilibria in nanopores. *Fluid Phase Equilibria* **2015,** 393, 48-63.
140. Li, Z.; Jin, Z.; Firoozabadi, A., Phase Behavior and Adsorption of Pure Substances and Mixtures and Characterization in Nanopore Structures by Density Functional Theory. *SPE Journal* **2014,** 19, (6), 1096-1109.
141. Peng, D.-Y.; Robinson, D. B., A New Two-Constant Equation of State. *Industrial & Engineering Chemistry Fundamentals* **1976,** 15, (1), 59-64.
142. Young, T., III. An essay on the cohesion of fluids. *Philosophical Transactions of the Royal Society of London* **1805,** 95, 65-87.
143. Firoozabadi, A., *Thermodynamics and applications of hydrocarbon energy production*. McGraw Hill Professional: 2015.
144. Ward, C. A.; Balakrishnan, A.; Hooper, F. C., On the Thermodynamics of Nucleation in Weak Gas-Liquid Solutions. *Journal of Basic Engineering* **1970,** 92, (4), 695-701.
145. Thomson, W., LX. On the equilibrium of vapour at a curved surface of liquid. *The London, Edinburgh, and Dublin Philosophical Magazine and Journal of Science* **1871,** 42, (282), 448-452.
146. Evans, R., The nature of the liquid-vapour interface and other topics in the statistical mechanics of non-uniform, classical fluids. *Advances in Physics* **1979,** 28, (2), 143-200.
147. Li, Z.; Firoozabadi, A., Interfacial tension of nonassociating pure substances and binary mixtures by density functional theory combined with Peng–Robinson equation of state. *The Journal of Chemical Physics* **2009,** 130, (15), 154108.
148. Rosenfeld, Y., Free-energy model for the inhomogeneous hard-sphere fluid mixture and density-functional theory of freezing. *Physical Review Letters* **1989,** 63, (9), 980-983.
149. Ebner, C.; Saam, W. F., New Phase-Transition Phenomena in Thin Argon Films. *Physical Review Letters* **1977,** 38, (25), 1486-1489.
150. Ebner, C.; Saam, W. F.; Stroud, D., Density-functional theory of simple classical fluids. I. Surfaces. *Physical Review A* **1976,** 14, (6), 2264-2273.
151. Yu, Y.-X.; Wu, J., Structures of hard-sphere fluids from a modified fundamental-measure theory. *The Journal of Chemical Physics* **2002,** 117, (22), 10156-10164.
152. Yu, Y.-X.; Wu, J., Density functional theory for inhomogeneous mixtures of polymeric fluids. *The Journal of Chemical Physics* **2002,** 117, (5), 2368-2376.
153. Mathias, P. M.; Naheiri, T.; Oh, E. M., A density correction for the Peng—Robinson equation of state. *Fluid Phase Equilibria* **1989,** 47, (1), 77-87.
154. Hoyos, B., Generalized liquid volume shifts for the Peng-Robinson equation of state for C1 to C8 hydrocarbons. *Latin American applied research* **2004,** 34, 83-89.
155. Jhaveri, B. S.; Youngren, G. K., Three-Parameter Modification of the Peng-Robinson Equation of State To Improve Volumetric Predictions. *SPE-13118-PA* **1988,** 3, (03), 1033-1040.
156. Adesida, A. G.; Akkutlu, I.; Resasco, D. E.; Rai, C. S., Characterization of Barnett Shale Kerogen Pore Size Distribution using DFT Analysis and Grand Canonical Monte Carlo Simulations. In *SPE Annual Technical Conference and Exhibition*, Society of Petroleum Engineers: Denver, Colorado, USA, 2011.
157. Kuila, U.; Prasad, M., Understanding Pore-Structure And Permeability In Shales. In *SPE Annual Technical Conference and Exhibition*, Society of Petroleum Engineers: Denver, Colorado, USA, 2011.

158. Steele, W. A., The physical interaction of gases with crystalline solids: I. Gas-solid energies and properties of isolated adsorbed atoms. *Surface Science* **1973,** 36, (1), 317-352.
159. Johnson, R. E.; Dettre, R. H.; Brandreth, D. A., Dynamic contact angles and contact angle hysteresis. *Journal of Colloid and Interface Science* **1977,** 62, (2), 205-212.
160. Puibasset, J., Counting metastable states within the adsorption/desorption hysteresis loop: A molecular simulation study of confinement in heterogeneous pores. *The Journal of Chemical Physics* **2010,** 133, (10), 104701.
161. Luo, S.; Lutkenhaus, J. L.; Nasrabadi, H., Confinement-Induced Supercriticality and Phase Equilibria of Hydrocarbons in Nanopores. *Langmuir* **2016,** 32, (44), 11506-11513.
162. Goodstein, D. L.; Hamilton, J. J.; Lysek, M. J.; Vidali, G., Phase diagrams of multilayer adsorbed methane. *Surface Science* **1984,** 148, (1), 187-199.
163. Inaba, A.; Morrison, J. A., The wetting transition and adsorption/desorption hysteresis for the CH4/graphite system. *Chemical Physics Letters* **1986,** 124, (4), 361-364.
164. Morishige, K.; Shikimi, M., Adsorption hysteresis and pore critical temperature in a single cylindrical pore. *The Journal of Chemical Physics* **1998,** 108, (18), 7821-7824.
165. Yu, W.; Sepehrnoori, K., *Shale Gas and Tight Oil Reservoir Simulation*. 1st ed.; Elsevier: 2019; p 430.
166. Gasparik, M.; Ghanizadeh, A.; Bertier, P.; Gensterblum, Y.; Bouw, S.; Krooss, B., High-Pressure Methane Sorption Isotherms of Black Shales from The Netherlands. *Energy & Fuels* **2012,** 26, (8), 4995-5004.
167. Ko, L.; Loucks, R.; Ruppel, S.; Zhang, T.; Peng, S., Origin and characterization of Eagle Ford pore networks in the south Texas Upper Cretaceous shelf. *AAPG Bulletin* **2017,** 101, (3), 387-418.
168. Thommes, M.; Köhn, R.; Fröba, M., Sorption and pore condensation behavior of pure fluids in mesoporous MCM-48 silica, MCM-41 silica, SBA-15 silica and controlled-pore glass at temperatures above and below the bulk triple point. *Applied Surface Science* **2002,** 196, (1–4), 239-249.
169. Kittaka, S.; Morimura, M.; Ishimaru, S.; Morino, A.; Ueda, K., Effect of Confinement on the Fluid Properties of Ammonia in Mesopores of MCM-41 and SBA-15. *Langmuir* **2009,** 25, (3), 1718-1724.
170. Alfi, M.; Nasrabadi, H.; Banerjee, D., Experimental investigation of confinement effect on phase behavior of hexane, heptane and octane using lab-on-a-chip technology. *Fluid Phase Equilibria* **2016,** 423, 25-33.
171. Luo, S.; Lutkenhaus, J. L.; Nasrabadi, H., Experimental Study of Confinement Effect on Hydrocarbon Phase Behavior in Nano-Scale Porous Media Using Differential Scanning Calorimetry. In *SPE Annual Technical Conference and Exhibition*, Society of Petroleum Engineers: Houston, Texas, USA, 2015.
172. Cho, H.; Caputo, D.; Bartl, M. H.; Deo, M., Measurements of hydrocarbon bubble points in synthesized mesoporous siliceous monoliths. *Chemical Engineering Science* **2018,** 177, 481-490.
173. Luo, S.; Lutkenhaus, J. L.; Nasrabadi, H., Use of differential scanning calorimetry to study phase behavior of hydrocarbon mixtures in nano-scale porous media. *Journal of Petroleum Science and Engineering* **2018,** 163, 731-738.
174. Luo, S.; Nasrabadi, H.; Lutkenhaus, J. L., Effect of confinement on the bubble points of hydrocarbons in nanoporous media. *AIChE Journal* **2016,** 62, (5), 1772-1780.
175. Do, D. D.; Do, H. D., Pore Characterization of Carbonaceous Materials by DFT and GCMC Simulations: A Review. *Adsorption Science & Technology* **2003,** 21, (5), 389-423.
176. Bymaster, A.; Chapman, W. G., An iSAFT Density Functional Theory for Associating Polyatomic Molecules. *The Journal of Physical Chemistry B* **2010,** 114, (38), 12298-12307.
177. Travalloni, L.; Castier, M.; Tavares, F. W., Phase equilibrium of fluids confined in porous media from an extended Peng–Robinson equation of state. *Fluid Phase Equilibria* **2014,** 362, 335-341.

178. Travalloni, L.; Castier, M.; Tavares, F. W.; Sandler, S. I., Thermodynamic modeling of confined fluids using an extension of the generalized van der Waals theory. *Chemical Engineering Science* **2010,** 65, (10), 3088-3099.
179. Vishnyakov, A.; Neimark, A. V., Multicomponent gauge cell method. *The Journal of Chemical Physics* **2009,** 130, (22), 224103.
180. Zhao, Y.; wang, y.; Zhong, J.; Xu, Y.; Sinton, D.; Jin, Z., Bubble Point Pressures of Hydrocarbon Mixtures in Multiscale Volumes from Density Functional Theory. *Langmuir* **2018,** Accepted.
181. Liu, K.; Ostadhassan, M.; Zhou, J.; Gentzis, T.; Rezaee, R., Nanoscale pore structure characterization of the Bakken shale in the USA. *Fuel* **2017,** 209, 567-578.
182. Mark E. Curtis, C. H. S., Raymond J. Ambrose, and Chandra S. Rai, Microstructural investigation of gas shales in two and three dimensions using nanometer-scale resolution imagingMicrostructure of Gas Shales. *AAPG Bulletin* **2012,** 96, (4), 665-677.
183. Lee, T.; Bocquet, L.; Coasne, B., Activated desorption at heterogeneous interfaces and long-time kinetics of hydrocarbon recovery from nanoporous media. *Nature Communications* **2016,** 7, 11890.
184. Akkutlu, I. Y.; Baek, S.; Olorode, O. M.; Wei, P.; Tongyi, Z.; Shuang, A., Shale Resource Assessment in Presence of Nanopore Confinement. In *SPE/AAPG/SEG Unconventional Resources Technology Conference*, Unconventional Resources Technology Conference: Austin, Texas, USA, 2017; p 21.
185. Sing, K. S. W., Reporting physisorption data for gas/solid systems with special reference to the determination of surface area and porosity (Recommendations 1984). In *Pure and Applied Chemistry*, 1985; Vol. 57, p 603.
186. Panagiotopoulos, A. Z., Adsorption and capillary condensation of fluids in cylindrical pores by Monte Carlo simulation in the Gibbs ensemble. *Molecular Physics* **1987,** 62, (3), 701-719.
187. Olivier, J. P., Modeling physical adsorption on porous and nonporous solids using density functional theory. *Journal of Porous Materials* **1995,** 2, (1), 9-17.
188. Tang, X.; Zhang, J.; Wang, X.; Yu, B.; Ding, W.; Xiong, J.; Yang, Y.; Wang, L.; Yang, C., Shale characteristics in the southeastern Ordos Basin, China: Implications for hydrocarbon accumulation conditions and the potential of continental shales. *International Journal of Coal Geology* **2014,** 128-129, 32-46.
189. Wu, H.; He, Y.; Qiao, R., Recovery of Multicomponent Shale Gas from Single Nanopores. *Energy & Fuels* **2017,** 31, (8), 7932-7940.
190. *IEA (2019), World Energy Outlook 2019, IEA, Paris* https://www.iea.org/reports/world-energy-outlook-2019.
191. Chalmers, G. R.; Bustin, R. M.; Power, I. M., Characterization of gas shale pore systems by porosimetry, pycnometry, surface area, and field emission scanning electron microscopy/transmission electron microscopy image analyses: Examples from the Barnett, Woodford, Haynesville, Marcellus, and Doig units. *AAPG Bulletin* **2012,** 96, (6), 1099-1119.
192. Wu, M.; Ding, M.; Yao, J.; Li, C.; Li, X.; Zhu, J., Development of a multi-continuum quadruple porosity model to estimate CO2 storage capacity and CO2 enhanced shale gas recovery. *Journal of Petroleum Science and Engineering* **2019,** 178, 964-974.
193. Wu, Y.; Fan, T.; Jiang, S.; Yang, X.; Ding, H.; Meng, M.; Wei, D., Methane Adsorption Capacities of the Lower Paleozoic Marine Shales in the Yangtze Platform, South China. *Energy & Fuels* **2015,** 29, (7), 4160-4167.
194. Zhang, T.; Ellis, G. S.; Ruppel, S. C.; Milliken, K.; Yang, R., Effect of organic-matter type and thermal maturity on methane adsorption in shale-gas systems. *Organic Geochemistry* **2012,** 47, 120-131.
195. Hao, F.; Zou, H.; Lu, Y., Mechanisms of shale gas storage: Implications for shale gas exploration in China. *AAPG Bulletin* **2013,** 97, (8), 1325-1346.

196. Mosher, K.; He, J.; Liu, Y.; Rupp, E.; Wilcox, J., Molecular simulation of methane adsorption in micro- and mesoporous carbons with applications to coal and gas shale systems. *International Journal of Coal Geology* **2013,** 109-110, 36-44.
197. Liu, Y.; Wilcox, J., Molecular simulation of CO2 adsorption in micro- and mesoporous carbons with surface heterogeneity. *International Journal of Coal Geology* **2012,** 104, 83-95.
198. Rouquerol, J.; Avnir, D.; Fairbridge, C.; Everett, D.; Haynes, J.; Pernicone, N.; Ramsay, J.; Sing, K.; Unger, K., Recommendations for the characterization of porous solids (Technical Report). *Pure and applied chemistry* **1994,** 66, (8), 1739.
199. Gross, J., A density functional theory for vapor-liquid interfaces using the PCP-SAFT equation of state. *The Journal of Chemical Physics* **2009,** 131, (20), 204705.
200. Tripathi, S.; Chapman, W. G., Microstructure of inhomogeneous polyatomic mixtures from a density functional formalism for atomic mixtures. *The Journal of Chemical Physics* **2005,** 122, (9), 094506.
201. Tripathi, S.; Chapman, W. G., Microstructure and Thermodynamics of Inhomogeneous Polymer Blends and Solutions. *Physical Review Letters* **2005,** 94, (8), 087801.
202. Klink, C.; Gross, J., A Density Functional Theory for Vapor–Liquid Interfaces of Mixtures Using the Perturbed-Chain Polar Statistical Associating Fluid Theory Equation of State. *Industrial & Engineering Chemistry Research* **2014,** 53, (14), 6169-6178.
203. Jain, S.; Dominik, A.; Chapman, W. G., Modified interfacial statistical associating fluid theory: A perturbation density functional theory for inhomogeneous complex fluids. *The Journal of Chemical Physics* **2007,** 127, (24), 244904.
204. Liu, J.; Xi, S.; Chapman, W. G., Competitive Sorption of CO2 with Gas Mixtures in Nanoporous Shale for Enhanced Gas Recovery from Density Functional Theory. *Langmuir* **2019,** 35, (24), 8144-8158.
205. Camacho Vergara, E. L.; Kontogeorgis, G. M.; Liang, X., Gas Adsorption and Interfacial Tension with Classical Density Functional Theory. *Industrial & Engineering Chemistry Research* **2019,** 58, (14), 5650-5664.
206. Shen, G.; Ji, X.; Öberg, S.; Lu, X., A hybrid perturbed-chain SAFT density functional theory for representing fluid behavior in nanopores: Mixtures. *The Journal of Chemical Physics* **2013,** 139, (19), 194705.
207. Sauer, E.; Gross, J., Classical Density Functional Theory for Liquid–Fluid Interfaces and Confined Systems: A Functional for the Perturbed-Chain Polar Statistical Associating Fluid Theory Equation of State. *Industrial & Engineering Chemistry Research* **2017,** 56, (14), 4119-4135.
208. Sauer, E.; Terzis, A.; Theiss, M.; Weigand, B.; Gross, J., Prediction of Contact Angles and Density Profiles of Sessile Droplets Using Classical Density Functional Theory Based on the PCP-SAFT Equation of State. *Langmuir* **2018,** 34, (42), 12519-12531.
209. Xu, X.; Cristancho, D. E.; Costeux, S.; Wang, Z.-G., Density-functional theory for polymer-carbon dioxide mixtures: A perturbed-chain SAFT approach. *The Journal of Chemical Physics* **2012,** 137, (5), 054902.
210. Shen, G.; Lu, X.; Ji, X., Modeling of molecular gas adsorption isotherms on porous materials with hybrid PC-SAFT–DFT. *Fluid Phase Equilibria* **2014,** 382, 116-126.
211. Emborsky, C. P.; Feng, Z.; Cox, K. R.; Chapman, W. G., Recent advances in classical density functional theory for associating and polyatomic molecules. *Fluid Phase Equilibria* **2011,** 306, (1), 15-30.
212. Chen, L.; Zuo, L.; Jiang, Z.; Jiang, S.; Liu, K.; Tan, J.; Zhang, L., Mechanisms of shale gas adsorption: Evidence from thermodynamics and kinetics study of methane adsorption on shale. *Chemical Engineering Journal* **2019,** 361, 559-570.
213. Rexer, T. F. T.; Benham, M. J.; Aplin, A. C.; Thomas, K. M., Methane Adsorption on Shale under Simulated Geological Temperature and Pressure Conditions. *Energy & Fuels* **2013,** 27, (6), 3099-3109.

214. Whittaker, S.; Rostron, B.; Hawkes, C.; Gardner, C.; White, D.; Johnson, J.; Chalaturnyk, R.; Seeburger, D., A decade of CO2 injection into depleting oil fields: Monitoring and research activities of the IEA GHG Weyburn-Midale CO2 Monitoring and Storage Project. *Energy Procedia* **2011,** 4, 6069-6076.
215. Fathi, E.; Akkutlu, I. Y., Multi-component gas transport and adsorption effects during CO2 injection and enhanced shale gas recovery. *International Journal of Coal Geology* **2014,** 123, 52-61.
216. Bi, R.; Luo, S.; Lutkenhaus, J.; Nasrabadi, H., Compositional Simulation of Cyclic Gas Injection in Liquid-Rich Shale Reservoirs Using Existing Simulators with a Framework for Incorporating Nanopores. In *SPE Improved Oil Recovery Conference*, Society of Petroleum Engineers: Tulsa, Oklahoma, USA, 2020; p 21.
217. Luo, S.; Lutkenhaus, J. L.; Nasrabadi, H., Effect of Nano-Scale Pore Size Distribution on Fluid Phase Behavior of Gas IOR in Shale Reservoirs. In *SPE Improved Oil Recovery Conference*, Society of Petroleum Engineers: Tulsa, Oklahoma, USA, 2018; p 14.
218. Wertheim, M. S., Fluids with highly directional attractive forces. I. Statistical thermodynamics. *Journal of Statistical Physics* **1984,** 35, (1), 19-34.
219. Wertheim, M. S., Fluids with highly directional attractive forces. II. Thermodynamic perturbation theory and integral equations. *Journal of Statistical Physics* **1984,** 35, 35.
220. Wertheim, M. S., Fluids with highly directional attractive forces. III. Multiple attraction sites. *Journal of Statistical Physics* **1986,** 42, (3), 459-476.
221. Wertheim, M. S., Fluids with highly directional attractive forces. IV. Equilibrium polymerization. *Journal of Statistical Physics* **1986,** 42, (3), 477-492.
222. Dominik, A.; Tripathi, S.; Chapman, W. G., Bulk and Interfacial Properties of Polymers from Interfacial SAFT Density Functional Theory. *Industrial & Engineering Chemistry Research* **2006,** 45, (20), 6785-6792.
223. Gross, J.; Sadowski, G., Perturbed-Chain SAFT: An Equation of State Based on a Perturbation Theory for Chain Molecules. *Industrial & Engineering Chemistry Research* **2001,** 40, (4), 1244-1260.
224. Wang, Y.; Shardt, N.; Lu, C.; Li, H.; Elliott, J. A. W.; Jin, Z., Validity of the Kelvin equation and the equation-of-state-with-capillary-pressure model for the phase behavior of a pure component under nanoconfinement. *Chemical Engineering Science* **2020,** 226, 115839.
225. Kurniawan, Y.; Bhatia, S. K.; Rudolph, V., Simulation of binary mixture adsorption of methane and CO2 at supercritical conditions in carbons. *AIChE Journal* **2006,** 52, (3), 957-967.
226. Pitakbunkate, T.; Blasingame, T. A.; Moridis, G. J.; Balbuena, P. B., Phase Behavior of Methane–Ethane Mixtures in Nanopores. *Industrial & Engineering Chemistry Research* **2017,** 56, (40), 11634-11643.
227. Sharma, A.; Luxami, V.; Paul, K., Purine-benzimidazole hybrids: Synthesis, single crystal determination and in vitro evaluation of antitumor activities. *European Journal of Medicinal Chemistry* **2015,** 93, 414-422.
228. Wang, S.; Feng, Q.; Javadpour, F.; Hu, Q.; Wu, K., Competitive adsorption of methane and ethane in montmorillonite nanopores of shale at supercritical conditions: A grand canonical Monte Carlo simulation study. *Chemical Engineering Journal* **2019,** 355, 76-90.
229. In *Draft CMA decision proposed by the President*, Glasgow Climate Change Conference, Glasgow, 2021; Glasgow, 2021.
230. Wang, Y.; Jin, Z., Hydrocarbon mixture and CO2 adsorptions in A nanopore-bulk multiscale system in relation to CO2 enhanced shale gas recovery. *Chemical Engineering Journal* **2021,** 415, 128398.
231. Kim, J.; Kim, D.; Lee, W.; Lee, Y.; Kim, H., Impact of total organic carbon and specific surface area on the adsorption capacity in Horn River shale. *Journal of Petroleum Science and Engineering* **2017,** 149, 331-339.
232. Liu, K.; Ostadhassan, M.; Zou, J.; Gentzis, T.; Rezaee, R.; Bubach, B.; Carvajal-Ortiz, H., Nanopore structures of isolated kerogen and bulk shale in Bakken Formation. *Fuel* **2018,** 226, 441-453.

233. Zhao, H.; Wu, T.; Firoozabadi, A., High pressure sorption of various hydrocarbons and carbon dioxide in Kimmeridge Blackstone and isolated kerogen. *Fuel* **2018,** 224, 412-423.
234. Rouquerol, J.; Llewellyn, P.; Rouquerol, F., Is the BET equation applicable to microporous adsorbents. *Stud. Surf. Sci. Catal* **2007,** 160, (07), 49-56.
235. Walton, K. S.; Snurr, R. Q., Applicability of the BET Method for Determining Surface Areas of Microporous Metal−Organic Frameworks. *Journal of the American Chemical Society* **2007,** 129, (27), 8552-8556.
236. Li, Y.; Wang, Z.; Tang, S.; Elsworth, D., Re-evaluating adsorbed and free methane content in coal and its ad- and desorption processes analysis. *Chemical Engineering Journal* **2022,** 428, 131946.
237. Berendsen, H. J. C.; van der Spoel, D.; van Drunen, R., GROMACS: A message-passing parallel molecular dynamics implementation. *Computer Physics Communications* **1995,** 91, (1), 43-56.
238. Van Der Spoel, D.; Lindahl, E.; Hess, B.; Groenhof, G.; Mark, A. E.; Berendsen, H. J. C., GROMACS: Fast, flexible, and free. *Journal of Computational Chemistry* **2005,** 26, (16), 1701-1718.
239. Ungerer, P.; Collell, J.; Yiannourakou, M., Molecular Modeling of the Volumetric and Thermodynamic Properties of Kerogen: Influence of Organic Type and Maturity. *Energy & Fuels* **2015,** 29, (1), 91-105.
240. Zhou, B.; Xu, R.; Jiang, P., Novel molecular simulation process design of adsorption in realistic shale kerogen spherical pores. *Fuel* **2016,** 180, 718-726.
241. Humphrey, W.; Dalke, A.; Schulten, K., VMD: visual molecular dynamics. *Journal of molecular graphics* **1996,** 14, (1), 33-38.
242. Okiongbo, K. S.; Aplin, A. C.; Larter, S. R., Changes in Type II Kerogen Density as a Function of Maturity: Evidence from the Kimmeridge Clay Formation. *Energy & Fuels* **2005,** 19, (6), 2495-2499.
243. Düren, T.; Millange, F.; Férey, G.; Walton, K. S.; Snurr, R. Q., Calculating Geometric Surface Areas as a Characterization Tool for Metal−Organic Frameworks. *The Journal of Physical Chemistry C* **2007,** 111, (42), 15350-15356.
244. Gelb, L. D.; Gubbins, K. E., Pore Size Distributions in Porous Glasses: A Computer Simulation Study. *Langmuir* **1999,** 15, (2), 305-308.
245. Brunauer, S.; Emmett, P. H.; Teller, E., Adsorption of Gases in Multimolecular Layers. *Journal of the American Chemical Society* **1938,** 60, (2), 309-319.
246. Sing, K. S. W., 7 - Assessment of Surface Area by Gas Adsorption. In *Adsorption by Powders and Porous Solids (Second Edition)*, Rouquerol, F.; Rouquerol, J.; Sing, K. S. W.; Llewellyn, P.; Maurin, G., Eds. Academic Press: Oxford, 2014; pp 237-268.
247. Zeng, K.; Lu, T.; Jiang, P.; Zhou, B.; Xu, R., Methane adsorption capacity measurement in shale matrix nanopores at high pressure by low-field NMR and molecular simulation. *Chemical Engineering Journal* **2022,** 430, 133151.
248. Ji, L.; Zhang, T.; Milliken, K. L.; Qu, J.; Zhang, X., Experimental investigation of main controls to methane adsorption in clay-rich rocks. *Applied Geochemistry* **2012,** 27, (12), 2533-2545.
249. Neimark, A. V.; Ravikovitch, P. I.; Grün, M.; Schüth, F.; Unger, K. K., Pore Size Analysis of MCM-41 Type Adsorbents by Means of Nitrogen and Argon Adsorption. *Journal of Colloid and Interface Science* **1998,** 207, (1), 159-169.
250. Yin, Y. F.; Mays, T.; McEnaney, B., Adsorption of Nitrogen in Carbon Nanotube Arrays. *Langmuir* **1999,** 15, (25), 8714-8718.
251. Arora, G.; Wagner, N. J.; Sandler, S. I., Adsorption and Diffusion of Molecular Nitrogen in Single Wall Carbon Nanotubes. *Langmuir* **2004,** 20, (15), 6268-6277.
252. Neimark, A. V.; Ravikovitch, P. I.; Vishnyakov, A., Bridging scales from molecular simulations to classical thermodynamics: density functional theory of capillary condensation in nanopores. *Journal of Physics: Condensed Matter* **2003,** 15, (3), 347-365.

253. Ravikovitch, P. I.; Neimark, A. V., Density Functional Theory of Adsorption in Spherical Cavities and Pore Size Characterization of Templated Nanoporous Silicas with Cubic and Three-Dimensional Hexagonal Structures. *Langmuir* **2002,** 18, (5), 1550-1560.
254. Gor, G. Y.; Neimark, A. V., Adsorption-Induced Deformation of Mesoporous Solids: Macroscopic Approach and Density Functional Theory. *Langmuir* **2011,** 27, (11), 6926-6931.
255. Myint, P. C.; McClelland, M. A.; Nichols, A. L., Application of the Peng–Robinson Equation of State to Energetic Materials RDX and TNT: Pure Components, Liquid Mixtures, and Solid Mixtures. *Industrial & Engineering Chemistry Research* **2016,** 55, (7), 2252-2266.
256. Elliott, J. R.; Lira, C. T., *Introductory Chemical Engineering Thermodynamics*. Pearson Education: 2012.
257. Roth, R.; Evans, R.; Lang, A.; Kahl, G., Fundamental measure theory for hard-sphere mixtures revisited: the White Bear version. *Journal of Physics: Condensed Matter* **2002,** 14, (46), 12063-12078.
258. Wertheim, M. S., Fluids with highly directional attractive forces. I. Statistical thermodynamics. *Journal of Statistical Physics* **1984,** 35, 19.
259. Kierlik, E.; Rosinberg, M. L., A perturbation density functional theory for polyatomic fluids. II. Flexible molecules. *The Journal of Chemical Physics* **1993,** 99, (5), 3950-3965.
260. Martin, M. G., MCCCS Towhee: a tool for Monte Carlo molecular simulation. *Molecular Simulation* **2013,** 39, (14-15), 1212-1222.
261. Martin, M. G.; Siepmann, J. I., Transferable Potentials for Phase Equilibria. 1. United-Atom Description of n-Alkanes. *The Journal of Physical Chemistry B* **1998,** 102, (14), 2569-2577.
262. Lorentz, H. A., Ueber die Anwendung des Satzes vom Virial in der kinetischen Theorie der Gase. *Annalen der Physik* **1881,** 248, (1), 127-136.
263. Yeh, I.-C.; Berkowitz, M. L., Ewald summation for systems with slab geometry. *The Journal of Chemical Physics* **1999,** 111, (7), 3155-3162.
264. Shelley, J. C., Boundary condition effects in simulations of water confined between planar walls. *Molecular Physics* **1996,** 88, (2), 385-398.
265. Alejandre, J.; Tildesley, D. J.; Chapela, G. A., Molecular dynamics simulation of the orthobaric densities and surface tension of water. *The Journal of Chemical Physics* **1995,** 102, (11), 4574-4583.
266. Widom, B., Some Topics in the Theory of Fluids. *The Journal of Chemical Physics* **1963,** 39, (11), 2808-2812.
267. Tian, Y.; Yan, C.; Jin, Z., Characterization of Methane Excess and Absolute Adsorption in Various Clay Nanopores from Molecular Simulation. *Scientific Reports* **2017,** 7, (1), 12040.
268. Siderius, D. W.; Gelb, L. D., Extension of the Steele 10-4-3 potential for adsorption calculations in cylindrical, spherical, and other pore geometries. *The Journal of Chemical Physics* **2011,** 135, (8), 084703.
269. Li, J.; Rao, Q.; Xia, Y.; Hoepfner, M.; Deo, M. D., Confinement-Mediated Phase Behavior of Hydrocarbon Fluids: Insights from Monte Carlo Simulations. *Langmuir* **2020,** 36, (26), 7277-7288.
270. Linstrom, P. J.; Mallard, W. G., The NIST Chemistry WebBook: A Chemical Data Resource on the Internet. *Journal of Chemical & Engineering Data* **2001,** 46, (5), 1059-1063.

公 式 章 1 节 1

## Appendix A

### A.1. The Radius of Mean Curvature

**Table A-1** Mean radii for different geometries and phase transition types. Note that the contact angles in all geometries are assumed to be zero.

| Geometries | Phase transition types | Mean curvature | Mean radii |
|---|---|---|---|
| Cylindrical pores | Condensation | $\frac{1}{r_m}=\frac{1}{2}\left(\frac{1}{r}+0\right)$ | $r_m=2r$ |
| | Evaporation | $\frac{1}{r_m}=\frac{1}{2}\left(\frac{1}{r}+\frac{1}{r}\right)$ | $r_m=r$ |
| Slit pores | Condensation<br>Evaporation | $\frac{1}{r_m}=\frac{1}{2}\left(\frac{1}{W/2}+0\right)$ | $r_m=W$ |
| Rectangular nanochannels | Condensation<br>Evaporation | $\frac{1}{r_m}=\frac{1}{2}\left(\frac{1}{W/2}+\frac{1}{D/2}\right)\approx\frac{1}{2}\left(\frac{1}{W/2}+0\right)$ | $r_m\approx W$ |
| Droplets | Condensation<br>Evaporation | $\frac{1}{r_m}=\frac{1}{2}\left(\frac{1}{r}+\frac{1}{r}\right)$ | $r_m=r$ |
| Bridge between crossed cylinders | Condensation<br>Evaporation | $\frac{1}{r_m}=\frac{1}{2}\left(\frac{1}{r_1}+\frac{1}{r_2}\right)\approx\frac{1}{2}\left(\frac{1}{r_1}+0\right)$ | $r_m\approx 2r_1$ |

Note: $r_m$ represents the radius of the mean curvature, *i.e.*, mean radius; $r$ represents the radius of cylindrical pores or droplets; $W$ is the pore width of slit pores or nanochannels; and $r_1$, $r_2$ are the principal radii of curvature. (as shown in **Figure A-1**)

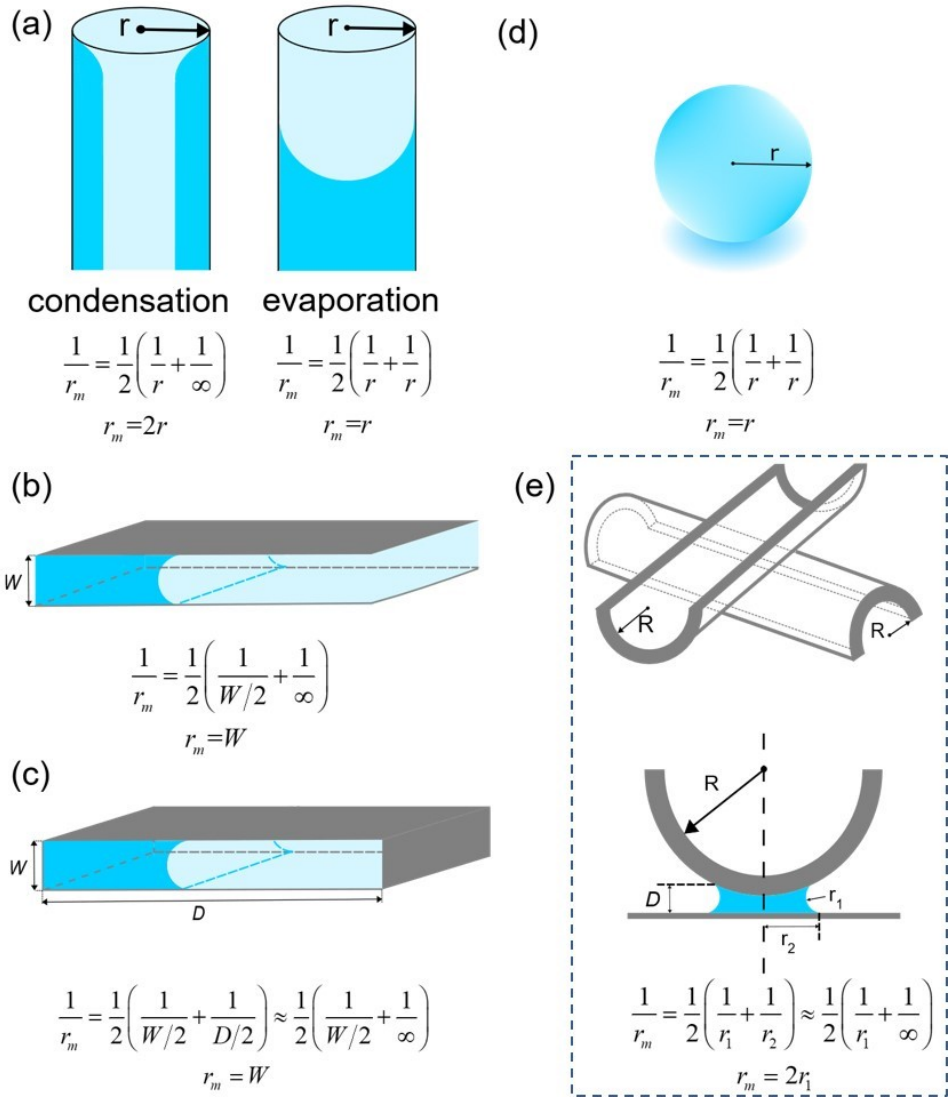


**Figure A-1** Schematics of mean radii and radii of curvature of the liquid–vapor interface in various geometries: (a) fluid in cylindrical pores showing the different mean radii of condensation and evaporation; (b) fluid in a slit pore; (c) fluid in a rectangular nanochannel; (d) spherical droplet; (e) liquid bridge between crossed cylinders which is often approximated as a liquid bridge between a sphere and a flat plate (Note: $R >> r_2 >> r_1$).

## A.2. Literature Details of Data Points Shown in Figure 1-1 Summarizing Examinations of the Kelvin Equation

Table A-2 Literature of data points shown in Figure 1-1.
KE—Kelvin equation; SKE—simplified Kelvin equation; CKE—complete Kelvin equation;
w/ film—Kelvin equations with adsorption film thickness correction; w/o film—Kelvin equations without adsorption film thickness correction;
GCMC—grand canonical Monte Carlo simulation; MD—molecular dynamics simulation; NLDFT—non-local density functional theory; LDFT—local density functional theory.

**(a)** Literature comparing Kelvin equations with experimental measurements.

| No. in Fig. 1 | Authors | Samples | Methods | *T* (K) | *P* (bar) | Adsorption layer | KE types | Geometries | Substrate materials | Phase transition types | Contact[#1] angle (degree) | Mean[#2] radii (nm) | ΔP% | | KE valid $r_m$ (nm) |
|---|---|---|---|---|---|---|---|---|---|---|---|---|---|---|---|
| | | | | | | | | | | | | | w/ film | w/o film | |
| 1 | Zandavi *et al.* [22#3] | Heptane | MCM-41, SBA-15 | 298 | 0–0.06 | Not included | CKE | Cylindrical pores | Silica | Evaporation | 0 | 1.3, 3.3 | N/A | 0%–8.1% | 1.3, 3.35 |
| | | Octane | | | | | | | | | 0 | | | | |
| | | Toluene | | | | | | | | | 0 | | | | |
| | | Water | | | | | | | | | 0 | | | | |
| 2 | Takei *et al.* [21 #4] | Nitrogen | Silica–glass chip | 77 | 0–1 | Included | SKE | Cylindrical pores | Silica | Condensation | 0 | 3–6 | 0.4%–10.4% | N/A | >3.2 |
| 3 | Yang *et al.* [24] | n-Butane | Lab-on-a-chip, GCMC | 298.35 | 2–2.5 | Not included | CKE | Rectangular nanochannels | Silica | Condensation | 0 | 4, 10, 50 | N/A | 0.5%–9% | >4 |

| | | | | | | | | | | | | | | | |
|---|---|---|---|---|---|---|---|---|---|---|---|---|---|---|---|
| 4 | Zhong *et al.* [23] | Propane | Silicon–glass chip | 286.15–339.15 | 6–23 | Not included | CKE | Rectangular nanochannels | Silica | Condensation | 0 | 8 | N/A | <1% | 8 |
| 5 | Fisher *et al.* [25, 128#**5**] | Cyclohexane | Mica–glass chip | 294.15 | 0.08–0.11 | Included | CKE | Bridge between crossed cylinders | Mica | Condensation | 6 | 8–40 | 1%–9% | N/A | >8 |
| 6 | Kruk *et al.* [17 #**6**] | Nitrogen | MCM–41 | 77 | 0–1 | Included | SKE | Cylindrical pores | Silica | Condensation | 0 | 2–6.5 | N/A | 27%–87% | Invalid in $r_m < 6.5$ |
| | | | | | | | | | | Evaporation | 0 | 1–3.25 | 18%–42.8 | 27.5%–79.8% | Invalid in $r_m < 3.25$ |
| 7 | Jatukaran *et al.* [15] | Propane | Visualized nanofluidic chip | 287.2–317.5 | 6–14 | Not included | SKE | Slit pores | Silica | Evaporation | 0 | 9 | N/A | 10.4% | Invalid in $r_m = 9$ |
| 8 | Kohonen *et al.* [129 #7] | Water | Rinsed mica surfaces | 298.15 | 0.88–1 | Not Included | CKE | Bridge between crossed cylinders | Mica | Condensation | 0 | 10–100 | N/A | <3% | >10 |
| 9 | Shardt *et al.* [118 #**8**] | Nitrogen | Vycor glass | 89–91 | 3 | Not Included | CKE | Cylindrical pores | Silica | Condensation | 0 | 4 | N/A | <1% | 4 |

| | | | | | | | | | | | | | | | |
|---|---|---|---|---|---|---|---|---|---|---|---|---|---|---|---|
| | | Argon | Vycor glass | 101–103 | 3 | Not Included | CKE | Cylindrical pores | Silica | Condensation | 0 | 4 | N/A | <1% | 4 |
| | | | | | | | | | | Evaporation | 0 | 2 | N/A | <1% | 2 |
| 10 | Parsa *et al*.[127] **#9** | Propane | Transparent nano-fluidic | 292–293.5 | 7.4–8.5 | Not included | SKE | Rectangular nanochannels | Silica | Condensation | 0 | 30, 50, 500 | N/A | <1% | >30 |
| | | | | | | | | | | Evaporation | 0 | | | | |
| 11 | Zhong *et al*.[125] | Propane | Silicon–glass chip | 314–347.9 | 14–34 | Not included | CKE | Rectangular nanochannels | Silica | Condensation | 0 | 70 | N/A | <1% | 70 |
| 12 | Tsukahara*et al*.[126]**#10** | Water | Silicon–glass chip | 295.15 | 0.026–0.02645 | Not included | SKE | Rectangular nanochannels | Silica | Evaporation | 10 | 103, 262, 514 | N/A | <1% | >103 |

**(b)** Literature comparing Kelvin equations with simulations or theoretical calculations.

| No. in Fig. 1 | Authors | Samples | Methods | $T$ (K) | $P$ (bar) | Adsorption layer | KE types | Geometries | Substrate materials | Phase transition types | Contact angle (degree) | Mean radii (nm) | ΔP% | | KE valid $r_m$ (nm) |
|---|---|---|---|---|---|---|---|---|---|---|---|---|---|---|---|
| | | | | | | | | | | | | | w/ film | w/o film | |
| 3 | Yang *et al.* [24] | n-Butane | Lab–on–a–chip, GCMC | 298.35 | 2–2.5 | Not included | CKE | Rectangular nanochannels | Silica | Condensation | 0 | 4, 10, 50 | N/A | 0.5%–9% | >4 |
| 13 | Factorovich*et al.* [132] **#11** | Water | GCMD | 278–318 | 0–33 | N/A | SKE | Droplets | N/A | Condensation | N/A | 0.35–2 | N/A | 5%–76% | >0.6 |
| | | | | | | | | | | Evaporation | | | | 3%-50% | |
| 14 | Walton *et al.* [19] | Nitrogen | GCMC | 76.1 | 0–1 | Not included | SKE | Slit pores | Graphite | Condensation | 0 | 2–10 | N/A | 0.7%–96% | >5 |
| 15 | Ravikovitch*et al.* [16] **#12** | Nitrogen | NLDFT | 77.35 | 0–1 | Not included | SKE | Cylindrical pores | Silica | Evaporation | 0 | 0.7–4 | N/A | 10%–96% | Invalid in $r_m < 4$ |
| 16 | Lastoskie *et al.* [20] | Nitrogen | NLDFT, LDFT | 77 | 0–1 | Included | SKE | Slit pores | Graphite | Condensation | 0 | 0.8–5, | 1%-100% | 27.5%–100% | 21.4 |
| 17 | Miyahara *et al.* [18] | Nitrogen | MD, proposed | 120.3 | 0–1 | Included | SKE | Cylindrical pores | Silica | Condensation | 0 | 2–4 | 10% | 40%–88.5% | >5 |

Notes:

#1. The details of contact angles used in Kelvin equations, experiments, theoretical calculations, and simulations are given in **Table A-2 (c)**.

#2. Mean radius is defined as $\frac{1}{r_m}=\frac{1}{2}\left(\frac{1}{r_1}+\frac{1}{r_2}\right)$. It has different relationships with pore diameter or pore width according to varying geometries. Mean radii used in **Table A-2** are calculated as shown in **Table A-1**.

**(c)** Details of contact angles used in Kelvin equations, experiments, theoretical calculations, and simulations.

| No. in Fig. 1 | Authors | Samples | Substrate Materials | Contact angles used in KE | Methods for contact angles in KE | Contact angles in experiments, theoretical calculations, or simulations | |
|---|---|---|---|---|---|---|---|
| | | | | | | Experiments | Simulations or theoretical calculations |
| 1 | Zandavi *et al.* [22] *#3* | Heptane | Silica | 0 | Assumed according to experimental measurements | Assumed. Note: the contact angles decrease with vapor pressure in measurements and are assumed to be zero at wetting pressure. The contact angle in radii calculations is assumed as zero. | N/A |
| | | Octane | | | | | |
| | | Toluene | | | | | |
| | | Water | | | | | |
| 2 | Takei *et al.* [21] *#4* | Nitrogen | Silica | 0 | Assumed | Assumed | N/A |
| 3 | Yang *et al.* [24] | n-Butane | Silica | 0 | Assumed | Assumed | Assumed |
| 4 | Zhong *et al.* [23] | Propane | Silica | 0 | Measured and extrapolated | Measured. Note: the contact angle of the condensation interface is temperature-dependent in highly confined systems. In their cases, they assumed the contact angle to be zero at $T > 284.5\ K$. | N/A |
| 5 | Fisher *et al.* [25, 128] *#5* | Cyclohexane | Mica | 6 | Assumed | Assumed | N/A |

| | | | | | | | |
|---|---|---|---|---|---|---|---|
| 6 | Kruk *et al.* [17] ***#6*** | Nitrogen | Silica | 0 | Assumed | Assumed | N/A |
| 7 | Jatukaran *et al.* [15] | Propane | Silica | 0 | Assumed according to experimental measurements | Assumed. Note: the assumed contact angle is according to their previous experiments. | N/A |
| 8 | Kohonen *et al.* [129] ***#7*** | Water | Mica | 0 | Assumed | Assumed | N/A |
| 9 | Shardt *et al*. [118] ***#8*** | Nitrogen<br>Argon | Silica | 0 | Assumed | Assumed | N/A |
| 10 | Parsa *et al*. [127]***#9*** | Propane | Silica | 0 | Assumed | Assumed | N/A |
| 11 | Zhong *et al*. [125] | Propane | Silica | 0 | Assumed according to experimental measurements | Assumed. Note: the assumed contact angle is according to their previous experiments. | N/A |
| 12 | Tsukahara *et al.* [126]***#10*** | Water | Silica | 10 | Assumed | Assumed | N/A |
| 13 | Factorovich *et al.* [132]***#11*** | Water | N/A | N/A | N/A | N/A | N/A |
| 14 | Walton *et al.* [19] | Nitrogen | Graphite | 0 | Assumed | N/A | Assumed. Note: at $T > T_w$, *i.e.*, the wetting temperature, the liquid in |

| | | | | | | | |
|---|---|---|---|---|---|---|---|
| | | | | | | | nanopores is considered to be completely wetted |
| 15 | Ravikovitch *et al.* [16#12] | Nitrogen | Silica | 0 | Assumed | N/A | Assumed |
| 16 | Lastoskie *et al.* [20] | Nitrogen | Graphite | 0 | Assumed | N/A | Assumed. Note: the graphitic pores are considered to be completely wetting pores |
| 17 | Miyahara *et al.* [18] | Nitrogen | Silica | 0 | Assumed | N/A | Assumed |

#3. Zandavi *et al.* considered contact angle changes with pressure while they also assumed that contact angle reduced to zero when evaporation occurs. $\theta = 0°$ is used for their pore radius predictions. According to the Kelvin equation, deviations between predicted and real pore radii are converted into deviations of vapor phase pressures in our calculations. In their original paper, the radii of cylindrical pores are expressed as $r_m = \frac{2\gamma}{P_0\left(x_w^V - \frac{V_m^V}{V_m^L}\ln(x_w^V) - 1\right)}$, where $x_w^V = \frac{P^V}{P_0}$ is vapor phase pressure radio, $V_m^V = RT / P_0$ is vapor molar volume. $P^V$ can be obtained by iteration for various pore radii. The $P^V$ corresponding to the measured pore radii can be inferred from the measured $x_w^V$, while the $P^V$ of predicted pore radii can be calculated by iteration. Saturation pressure and molar volume of vapor and liquid phases from the NIST Chemistry WebBook were used in our calculations.

#4. Takei *et al.* showed the relationship of pore size to a ratio of $\gamma V_m^L$ in the pore to $\gamma V_m^L$ of the bulk liquid. The deviations in $\gamma V_m^L$ are also converted into deviations of vapor phase pressures in our calculations. According to the SKE, the vapor phase pressure

$P^V = P_0 \exp\left[-\frac{2\gamma V_m^L}{\left(r_p - t_{ad}\right)RT}\right]$ can be calculated according to different $\gamma V_m^L$, where $r_p$ is cylindrical pore size and $t_{ad}$ is adsorption film thickness. The $P^V$ calculated by experimental $\gamma V_m^L$ of the pore and $\gamma V_m^L$ of the bulk are corresponding to the true vapor phase pressure in pores and predicted SKE, respectively.

#5. Fisher *et al*. used a mica substrate and considered the contact angle to be a very small value of 6°.

#6. Kruk *et al.* considered SKE, SKE with adsorption film thickness, and SKE with a correction of radius. We only chose the data corresponding to the SKE and SKE with adsorption film thickness (*i.e.*, data with corrected radius is not included).

#7. Kohonen *et al.* assumed that the contact angle of water on mica is very small. Thus, the meniscus radius of curvature is given by half of the surface separation at the meniscus.

#8. Shardt *et al.* calculated temperature deviations at given vapor phase pressures for nitrogen/argon binary mixtures. We only choose data for pure nitrogen and pure argon. Temperature deviations are converted into pressure differences. In their paper, they showed measured results from the literature and their predicted saturation temperatures of pure nitrogen and argon at the given pressure. By using a similar method to that mentioned above, the vapor phase pressures can be calculated by iteration according to the measured and predicted saturation temperatures. The deviation between these two $P^V$ is depicted in Fig. 1.

#9. The result obtained from the 500-nm chip in Parsa *et al.* stands as an exception where the condensation pressure is higher than the bulk vapor pressure.

#10. Tsukahara *et al*. used a finite contact angle of 10° between water and silica. Considering the effect of contact angle 10° in the Young–Laplace equation is still not significant ($\cos\left(10^\circ\right) = 0.985$); this work is still included in literature comparisons.

#11. Factorovich *et al*. studied spherical water droplets and no substrate was used. They considered the curvature effect on surface tension with the Tolman equation. Only Tolman length $\delta = 0$ for Kelvin equation prediction was used to compare with experimental results, in which the surface tension is a constant, independent of pore size at a given temperature.

#12. Ravikovitch *et al.* did not provide details of the Kelvin equation used in Ref. [16]. In their other papers [252-254], the contact angle between nitrogen and silica is assumed to be zero. Thus, we assume that the contact angle used in Ref [16] is zero.

### A.3. Chemical Potential from the PR-EOS

The Peng–Robinson equation of state [141] for a pure component is given as,

$$P = \frac{RT}{V_m - b} - \frac{a}{V_m(V_m + b) + b(V_m - b)}, \tag{A-1}$$

where $R$ is the gas constant, $V_m$ is molar volume, and $a$, $b$ are constant parameters given as,

$$\begin{cases} a = \dfrac{0.45724 R^2 T_c^2}{P_c}\left[1 + c(1 - \sqrt{T_r})\right]^2 \\ b = \dfrac{0.0778 R T_c}{P_c} \end{cases}, \tag{A-2}$$

in which $T_c$ and $P_c$ are critical temperature and pressure, respectively; $T_r = T / T_c$ represents reduced temperature; and *R* is the gas constant. The parameter $c$ is given as,

$$c = \begin{cases} 0.37464 + 1.54226\omega - 0.26992\omega^2, & \omega < 0.5 \\ 0.3796 + 1.485\omega - 0.1644\omega^2 + 0.01667\omega^3, & \omega > 0.5 \end{cases}, \tag{A-3}$$

where $\omega$ is the acentric factor. Using compressibility factor $Z = PV_m / RT$, Eq. (A-1) can be transformed to,

$$Z^3 - (1 - B)Z^2 + (A - 3B^2 - 2B)Z - (AB - B^2 - B^3) = 0, \tag{A-4}$$

with

$$\begin{cases} A = \dfrac{aP}{R^2 T^2} \\ B = \dfrac{bP}{RT} \end{cases}. \tag{A-5}$$

The chemical potential of a pure component can be divided into two parts: ideal chemical potential $\mu^{id}$ and excess chemical potential $\mu^{ex}$, *i.e.*,

$$\mu(P,T) = \mu^{id}(P,T) + \mu^{ex}(P,T) \tag{A-6}$$

The ideal chemical potential $\mu^{id}$ can be obtained from,

$$\mu^{id}(P,T) = k_B T \ln\left(\rho_b \lambda_{th}{}^3\right), \tag{A-7}$$

where $k_B$ is the Boltzmann constant, and $\lambda_{th} = h/\sqrt{2\pi m k_B T}$ represents thermal de Broglie wavelength, in which $h$ is the Planck constant and $m$ is the mass of a fluid particle.

The excess chemical potential $\mu^{ex}$ can be expressed as [255, 256],

$$\mu^{ex}(P,T) = RT \ln \varphi(T,P), \tag{A-8}$$

where $\varphi$ is fugacity coefficient defined as

$$\ln \varphi(P,T) = -\ln(Z-B) + \frac{B}{Z-B} - \frac{AZ}{Z^2+2BZ-B^2} - \frac{A}{2\sqrt{2}B} \ln \frac{Z+(1+\sqrt{2})B}{Z+(1-\sqrt{2})B}. \tag{A-9}$$

More details of derivations of Eq. (A-9) can be found in Refs.[255, 256].

At equilibrium, the chemical potentials of the liquid and vapor phases should be equal,

$$\mu^V(P^V,T) = \mu^L(P^L,T). \tag{A-10}$$

To be consistent with DFT calculations, the volume shift parameter (VSP) [155] is only used for density correction (as shown in the main text), while no VSP is used for chemical potential calculations.

### A.4. PR–EOS Parameters for Propane

**Table A-3** PR–EOS parameters, cross molecular diameters and attraction–energy parameters [140].

| | $T_c$ (K) | $P_c$ (bar) | $M_w$ (g/mol) | $\omega$ | $VSP$ | $\sigma$(Å) | $\varepsilon^{pe}/k_B$ (K) |
|---|---|---|---|---|---|---|---|
| $C_3$ | 369.83 | 42.48 | 44.1 | 0.153 | −0.0869 | 3.548 | 1866 |

### A.5. Excess Helmholtz Free Energy Functional in Engineering DFT

The excess Helmholtz free energy functional includes two parts: one part is obtained by extending the PR–EOS with a weighted density approximation (WDA) [148] to inhomogeneous conditions to account for the physical interactions,

$$F_{ph}^{ex}[\rho(\mathbf{r})] = \int d\mathbf{r}\, \phi_{ph}[\rho(\mathbf{r})], \tag{A-11}$$

where $\phi_{ph}\left[\rho(\mathbf{r})\right]$ is the reduced excess Helmholtz energy density functional. We use $n_0(\mathbf{r})$ and $n_3(\mathbf{r})$ functions in Rosenfeld's fundamental measure theory [148] to mathematically represent the "geometrical properties" of molecules and account for interactions in inhomogeneous conditions,

$$\begin{cases} n_0(\mathbf{r}) = \dfrac{1}{\pi\sigma^2}\int d\mathbf{r}'\rho(\mathbf{r}')\delta\left(\dfrac{\sigma}{2}-|\mathbf{r}-\mathbf{r}'|\right) \\ n_3(\mathbf{r}) = \int d\mathbf{r}'\rho(\mathbf{r}')\theta\left(\dfrac{\sigma}{2}-|\mathbf{r}-\mathbf{r}'|\right) \end{cases}, \tag{A-12}$$

where $\delta(\mathbf{r})$ is the Dirac delta function and $\theta(\mathbf{r})$ is the Heaviside step function, and $\sigma$ is the "effective diameter" of the fluid. As a result, the reduced excess Helmholtz $\phi_{ph}\left[\rho(\mathbf{r})\right]$ extended by WDA is expressed as,

$$\begin{aligned} \phi_{ph}\left[\rho(\mathbf{r})\right] &= \phi_{ph}\left[n_\alpha(\mathbf{r})\right] \\ &= -n_0\ln(1-4n_3) - \frac{{n_0}^2 a}{8\sqrt{2}n_3 k_B T}\ln\left[\frac{1+4\left(1+\sqrt{2}\right)n_3}{1+4\left(1-\sqrt{2}\right)n_3}\right], \end{aligned} \tag{A-13}$$

where $a$ represents the energy parameter of the fluid.

The other part of the excess Helmholtz free energy $F_{pe}^{ex}\left[\rho(\mathbf{r})\right]$ accounts for the long–range intermolecular attractions by using a quadratic density expansion (QDE) [149, 150].

$$\beta F_{pe}^{ex} = -\frac{1}{4}\iint d\mathbf{r}d\mathbf{r}'\beta u^{pe}\left(|\mathbf{r}-\mathbf{r}'|\right)\left[\rho(\mathbf{r})-\rho(\mathbf{r}')\right]^2, \tag{A-14}$$

in which the pair potential $u^{pe}(r)$ is modeled by the attractive part of the Lennard Jones potential,

$$u^{pe}(r) = \begin{cases} 0, & r < \sigma \\ -\varepsilon^{pe}\left(\dfrac{\sigma}{r}\right)^6, & r \geq \sigma \end{cases}, \tag{A-15}$$

where $\varepsilon^{pe}$ and $\sigma$ are the potential expansion parameter and cross the molecular diameter of the fluid component.公式章 (下一章) 节 1

## Appendix B

### B.1. Phase Diagrams of Bulk Hydrocarbon Mixtures

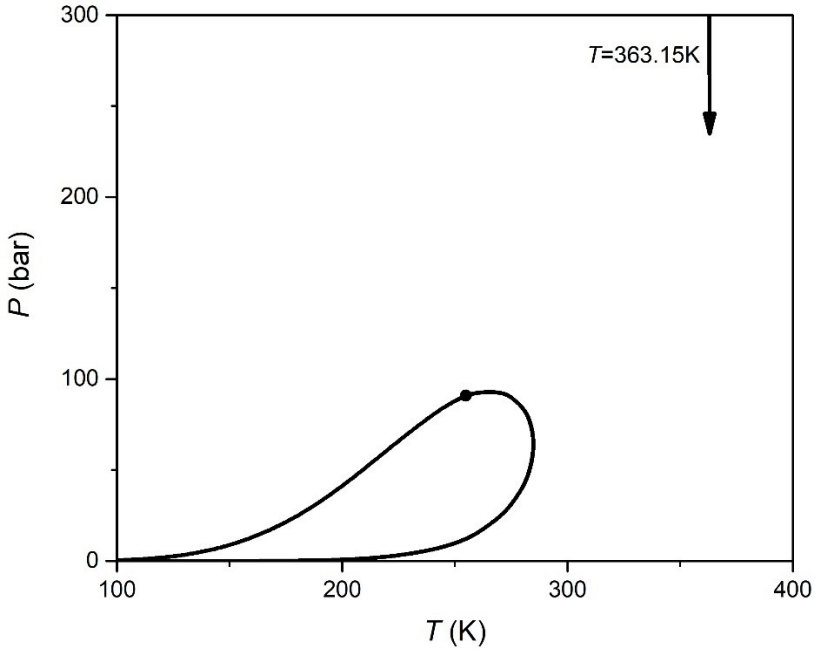


**Figure B-1** Phase diagrams of $C_1$-$C_2$-$C_3$-$nC_4$ quaternary mixture. Mole ratios in quaternary mixture are $C_1$: $C_2$: $C_3$: $nC_4$ = 0.7152: 0.1639: 0.095: 0.0259. The arrow shows our calculations conditions that decreases pressure from 300 bar at $T$ = 363.15 K.

### B.2. Binary Interaction Coefficients, Cross Molecular Diameters, Attraction-energy Parameters, and Other PR-EOS Parameters

**Table B-1** Binary interaction coefficient between two hydrocarbon species[140]

| | $C_1$ | $C_2$ | $C_3$ | $nC_4$ |
|---|---|---|---|---|
| $C_1$ | 0 | — | — | — |
| $C_2$ | 0.034 | 0 | — | — |
| $C_3$ | 0.036 | 0 | 0 | — |
| $nC_4$ | 0.038 | 0 | 0 | 0 |

**Table B-2** PR-EOS parameters, cross molecular diameters and attraction-energy parameters [140].

| | $T_c$ (K) | $P_c$ (bar) | $M_w$ (g/mol) | $\omega$ | $VSP$ | $\sigma_i$(Å) | $\varepsilon_i^{pe}/k_B$ (K) |
|---|---|---|---|---|---|---|---|
| $C_1$ | 190.56 | 45.99 | 16.04 | 0.011 | -0.1533 | 2.77 | 1178 |
| $C_2$ | 305.32 | 48.72 | 30.07 | 0.099 | -0.1094 | 3.179 | 1540 |
| $C_3$ | 369.83 | 42.48 | 44.1 | 0.153 | -0.0869 | 3.548 | 1866 |
| $nC_4$ | 425.12 | 37.96 | 58.12 | 0.199 | -0.0672 | 3.858 | 2236 |

公式章 (下一章) 节 1

## Appendix C

### C.1. The Excess Term of Helmholtz Free Energy in PC-SAFT DFT

In PC-SAFT DFT, the excess Helmholtz free energy $F^{ex}\left[\{\rho_k(\mathbf{r})\}\right]$ includes different types of interaction contributions between two chains [200, 201, 223],

$$F^{ex}\left[\{\rho_k(\mathbf{r})\}\right]=F^{ex,hs}\left[\{\rho_k(\mathbf{r})\}\right]+F^{ex,hc}\left[\{\rho_k(\mathbf{r})\}\right]+F^{ex,disp}\left[\{\rho_k(\mathbf{r})\}\right]+F^{ex,assoc}\left[\{\rho_k(\mathbf{r})\}\right], \tag{C-1}$$

where $F^{ex,hs}\left[\{\rho_k(\mathbf{r})\}\right]$ and $F^{ex,hc}\left[\{\rho_k(\mathbf{r})\}\right]$ represent the excess Helmholtz free energy arising from the hard-sphere and hard-chain interactions, respectively. The dispersion term $F^{ex,disp}\left[\{\rho_k(\mathbf{r})\}\right]$ accounts for the attractive van der Waals interactions of chain molecules. The association term $F^{ex,assoc}\left[\{\rho_k(\mathbf{r})\}\right]$ describes the excess Helmholtz energy due to the formation of hydrogen bonds. In this work, $C_1$, $C_2$, $C_3$, and $CO_2$ carry no charge so the association term can be neglected [116].

#### C.1.1. The Hard-sphere Contribution

The excess Helmholtz free energy due to hard-sphere interactions is described by the modified fundamental measure theory (MFMT) [151, 257],

$$\beta F^{ex,hs}\left[\{\rho_k(\mathbf{r})\}\right]=\int \phi^{hs}\left[n_\alpha(\mathbf{r})\right]d\mathbf{r}, \tag{C-2}$$

where $\phi^{hs}$ is the reduced excess Helmholtz free-energy density due to hard core interactions as a function of Rosenfeld weighted densities $n_\alpha(\mathbf{r})$ [148, 151, 257],

$$\phi^{hs}=-n_0\ln(1-n_3)+\frac{n_1n_2-\mathbf{n_1}\cdot\mathbf{n_2}}{1-n_3}+\left(n_2^3-3n_2\mathbf{n_2}\cdot\mathbf{n_2}\right)\frac{n_3+(1-n_3)^2\ln(1-n_3)}{36\pi n_3^2(1-n_3)^2}, \tag{C-3}$$

where $n_0$, $n_1$, $n_2$, and $n_3$ are scalar weighted densities, $\mathbf{n_1}$ and $\mathbf{n_2}$ are the vector weighted densities. $\mathbf{n_1}\cdot\mathbf{n_2}$, $\mathbf{n_2}\cdot\mathbf{n_2}$ denote a scalar product of the two vectors. In slit geometry, the Rosenfeld weighted densities can be expressed as [199, 207]

$$n_0(z)=\sum_k m_k\frac{1}{d_k(T)}\int_{-d_k(T)/2}^{d_k(T)/2}\rho_k^{seg}(z+\hat{z})d\hat{z}, \tag{C-4}$$

$$n_1(z)=\frac{1}{2}\sum_k m_k\int_{-d_k(T)/2}^{d_k(T)/2}\rho_k^{seg}(z+\hat{z})d\hat{z}, \tag{C-5}$$

$$n_2(z)=\pi\sum_k m_k d_k(T)\int_{-d_k(T)/2}^{d_k(T)/2}\rho_k^{seg}(z+\hat{z})d\hat{z}, \tag{C-6}$$

$$n_3(z)=\pi\sum_k m_k\int_{-d_k(T)/2}^{d_k(T)/2}\rho_k^{seg}(z+\hat{z})\left[\left(\frac{d_k(T)}{2}\right)^2-\hat{z}^2\right]d\hat{z}, \tag{C-7}$$

$$\mathbf{n_1}(z)=-\mathbf{e_z}\sum_k m_k\frac{1}{d_k(T)}\int_{-d_k(T)/2}^{d_k(T)/2}\rho_k^{seg}(z+\hat{z})d\hat{z}, \tag{C-8}$$

$$\mathbf{n}_2(z)=-2\pi\mathbf{e_z}\sum_k m_k\int_{-d_k(T)/2}^{d_k(T)/2}\rho_k^{seg}(z+\hat{z})d\hat{z}, \tag{C-9}$$

where $\mathbf{e_z}$ represents the unit vector that points in the z-direction. $m_k$ is the segment number of component $k$. $\rho_k^{seg}(\mathbf{r})$ is a local average of the segment number density of component $k$ at position $\mathbf{r}$. $d_k(T)$ represents a temperature-dependent effective segment diameter, defined as $d_k(T)=\sigma_k\left(1-0.12\exp\left(-3\left(\varepsilon_k/k_bT\right)\right)\right)$ where $\varepsilon_k$ is the fluid energy of a segment of composition $k$ and $\sigma_k$ is the segment diameter.

### C.1.2. The Hard-chain Contribution

Based on Wertheim's first-order thermodynamic perturbation theory [219-221, 258], the excess Helmholtz free-energy of chain connectivity $F^{ex,hc}\left[\{\rho_k(\mathbf{r})\}\right]$ is given as [199, 207],

$$\begin{aligned}\beta F^{ex,hc}\left[\{\rho_k(\mathbf{r})\}\right]=&\sum_k(m_k-1)\int\rho_k^{seg}(\mathbf{r})\left(\ln\rho_k^{seg}(\mathbf{r})-1\right)d\mathbf{r}\\&-\sum_k(m_k-1)\int\rho_k^{seg}(\mathbf{r})\left(\ln\left[y_{kk}^{dd}\left(\bar{\rho}_k^{seg,hc}(\mathbf{r})\right)\lambda_k^{seg}(\mathbf{r})\right]-1\right)d\mathbf{r}\end{aligned} \tag{C-10},$$

where $y_{kk}^{dd}\left(\bar{\rho}_k^{seg,hc}(\mathbf{r})\right)$ is the cavity correlation function evaluated at contact distance $d_k$ between segments of component $k$. $y_{kk}^{dd}\left(\bar{\rho}_k^{seg,hc}(\mathbf{r})\right)$ is approximated locally as a function of a weighted density $\bar{\rho}_k^{seg,hc}(\mathbf{r})$ [199, 200, 259],

$$y_{kk}^{dd}\left(\bar{\rho}_k^{seg,hc}(\mathbf{r})\right)=\frac{1}{1-\overline{\zeta_3}}+\frac{3d_k\overline{\zeta_2}}{2\left(1-\overline{\zeta_3}\right)^2}+\frac{\left(d_k\overline{\zeta_2}\right)^2}{2\left(1-\overline{\zeta_3}\right)^3}, \tag{C-11}$$

where $\overline{\zeta_2}$ and $\overline{\zeta_3}$ are segment densities,

$$\overline{\zeta_n}(\mathbf{r}) = \frac{\pi}{6}\sum_k \overline{\rho}_k^{seg,hc}(\mathbf{r}) m_k d_k^n,\ n = 2,3. \tag{C-12}$$

$\overline{\rho}_k^{seg,hc}(\mathbf{r})$ and $\lambda_k^{seg}(\mathbf{r})$ are weighted densities around a segment with position **r** of the chain contribution of the excess Helmholtz free-energy. In slit pores, the two weighted densities can be expressed as

$$\overline{\rho}_k^{seg,hc}(z) = \frac{3}{4d_k(T)^3}\int_{-d_k(T)}^{d_k(T)} \rho_k^{seg}(z+\hat{z})\left[d_k(T)^2 - \hat{z}^2\right] d\hat{z}, \tag{C-13}$$

$$\lambda_k^{seg}(z) = \frac{1}{2d_k(T)}\int_{-d_k(T)}^{d_k(T)} \rho_k^{seg}(z+\hat{z}) d\hat{z}. \tag{C-14}$$

### C.1.3. The Dispersive Attraction Contribution

The dispersion term $F^{ex,disp}\left[\{\rho_k(\mathbf{r})\}\right]$ is based on the first-order perturbation theory. The weighted density approximation (WDA) method is applied to extend the homogenous system to an inhomogeneous one. In this work, a reduced dispersion contribution to the Helmholtz free-energy $\tilde{a}^{disp}\left(\overline{\rho}_k(\mathbf{r})\right)$ is used to describe $F^{ex,disp}\left[\{\rho_k(\mathbf{r})\}\right]$ [207],

$$\beta F^{ex,disp}\left[\{\rho_k(\mathbf{r})\}\right] = \int \overline{\rho}(\mathbf{r}) \tilde{a}^{disp}\left(\overline{\rho}_k(\mathbf{r})\right) d\mathbf{r} \tag{C-15}$$

where

$$\overline{x_k} = \frac{\overline{\rho}_k(\mathbf{r})}{\overline{\rho}(\mathbf{r})} \tag{C-16}$$

$\overline{\rho}(\mathbf{r})$ is the weighted density of all components at position **r**

$$\overline{\rho}(\mathbf{r}) = \sum_k \frac{3}{4\pi\psi^3 d_k(T)^3}\int \rho_k^{seg}(\mathbf{r}')\Theta\left[\psi d_k(T) - |\mathbf{r}-\mathbf{r}'|\right] d\mathbf{r}', \tag{C-17}$$

where $\rho_k^{seg}(\mathbf{r}')$ is a local average of the segment number density of component $k$ at position $\mathbf{r}'$. $\Theta$ is the Heaviside function. $\psi$ is a universal model parameter and set as

1.3862 [207]. In Eq (C-15), $\tilde{a}^{disp}\left(\bar{\rho}_k\left(\mathbf{r}\right)\right)$ is the Helmholtz free-energy density at position **r** and defined as

$$\tilde{a}^{disp}\left(\bar{\rho}_k\left(\mathbf{r}\right)\right) = -2\pi\bar{\rho}\left(\mathbf{r}\right)I_1\left(\bar{\eta},\bar{m}\right)\overline{m^2\varepsilon\sigma^3} - \pi\bar{\rho}\left(\mathbf{r}\right)\bar{m}C_1I_2\left(\bar{\eta},\bar{m}\right)\overline{m^2\varepsilon^2\sigma^3}, \tag{C-18}$$

where $\bar{m} = \sum_k \overline{x_k} m_k$ is the mean segment number of mixtures, and the abbreviations $\overline{m^2\varepsilon\sigma^3}$, $\overline{m^2\varepsilon^2\sigma^3}$, and $C_1$ are given as,

$$\overline{m^2\varepsilon^n\sigma^3} = \sum_j\sum_k \overline{x_j}\,\overline{x_k} m_j m_k \left(\frac{\varepsilon_{jk}}{k_bT}\right)^n \sigma_{jk}^3, \tag{C-19}$$

$$C_1 = \left[1 + \bar{m}\frac{8\bar{\eta} - 2\bar{\eta}^2}{\left(1-\bar{\eta}\right)^4} + \left(1-\bar{m}\right)\frac{20\bar{\eta} - 27\bar{\eta}^2 + 12\bar{\eta}^3 - 2\bar{\eta}^4}{\left[\left(1-\bar{\eta}\right)\left(2-\bar{\eta}\right)\right]^2}\right]^{-1}, \tag{C-20}$$

where the density (*i.e.*, the packing fraction) $\bar{\eta}$ and the local mole fraction $\overline{x_k}$ are defined as,

$$\bar{\eta} = \frac{\pi}{6}\sum_k \bar{\rho}_k^{seg}\left(\mathbf{r}\right) m_k d_k^3, \tag{C-21}$$

$$\overline{x_k} = \frac{\bar{\rho}_k\left(\mathbf{r}\right)}{\bar{\rho}\left(\mathbf{r}\right)}. \tag{C-22}$$

More details can be found in references [199-201, 207]. In Eq. (C-18), the integrals $I_1\left(\bar{\eta},\bar{m}\right)$, $I_2\left(\bar{\eta},\bar{m}\right)$ are defined as

$$I_1\left(\bar{\eta},\bar{m}\right) = \sum_{i=0}^{6} a_i\left(m\right)\eta^i, \tag{C-23}$$

$$I_2\left(\bar{\eta},\bar{m}\right) = \sum_{i=0}^{6} b_i\left(m\right)\eta^i, \tag{C-24}$$

where the coefficients $a_i\left(m\right)$ and $b_i\left(m\right)$ could be found in Ref. [223] and also listed in **Table C-2**.

## C.2. Parameters in PC-SAFT EOS and PC-SAFT DFT

**Table C-1** Pure component parameters for non-associating substances in PC-SAFT EOS and DFT [199].

Note that $M_k$ is the molar mass of component $k$, $m_k$ is the segment number of component $k$, $\sigma_k$ is the segment diameter of component $k$, and $\varepsilon_k / k_b$ is the segment energy parameter of component $k$.

| | $M_k$ (g/mol) | $m_k$ | $\sigma_k$ (Å) | $\varepsilon_k/k_b$ (K) |
|---|---|---|---|---|
| $C_1$ | 16.043 | 1.000 | 3.7039 | 150.03 |
| $C_2$ | 30.07 | 1.6069 | 3.5206 | 191.42 |
| $C_3$ | 44.096 | 2.002 | 3.6184 | 208.11 |
| $CO_2$ | 44.01 | 2.0729 | 2.7852 | 169.21 |

**Table C-2** Universal model constants for Eq. (C-23) and (C-24) [199].

| $i$ | $a_{0i}$ | $a_{1i}$ | $a_{2i}$ | $b_{0i}$ | $b_{1i}$ | $b_{2i}$ |
|---|---|---|---|---|---|---|
| 0 | 0.9105631445 | -0.3084016918 | -0.0906148351 | 0.7240946941 | -0.5755498075 | 0.0976883116 |
| 1 | 0.6361281449 | 0.1860531159 | 0.4527842806 | 2.2382791861 | 0.6995095521 | -0.2557574982 |
| 2 | 2.6861347891 | -2.5030047259 | 0.5962700728 | -4.0025849485 | 3.8925673390 | -9.155856153 |
| 3 | -26.547362491 | 21.419793629 | -1.7241829131 | -21.003576815 | -17.215471648 | 20.642075974 |
| 4 | 97.759208784 | -65.25588533 | -4.1302112531 | 26.855641363 | 192.67226447 | -38.804430052 |
| 5 | -159.59154087 | 83.318680481 | 13.77663187 | 206.55133841 | -161.82646165 | 93.626774077 |
| 6 | 91.297774084 | -33.74692293 | -8.6728470368 | -355.60235612 | -165.20769346 | -29.666905585 |

## C.3. Grand Canonical Monte Carlo (GCMC) Simulation Details

In GCMC, hydrocarbons and $CO_2$ adsorption are obtained in the grand canonical ensemble with MCCCS Towhee [260]. At a given temperature, a chemical equilibrium of fluids in nanopores and bulk is achieved in a volume-constant system. The TraPPE united atom model [261] is used to describe the interactions between hydrocarbons and $CO_2$. The pairwise-additive Lennard Jones (LJ) 12-6 potential is used to account for the non-bonded interaction,

$$U\left(r_{ij}\right)=4\varepsilon_{ij}\left[\left(\frac{\sigma_{ij}}{r_{ij}}\right)^{12}-\left(\frac{\sigma_{ij}}{r_{ij}}\right)^{6}\right], \tag{C-25}$$

where $r_{ij}$ is the separation distance between atoms $i$ and $j$. $\sigma_{ij}$ and $\varepsilon_{ij}$ are the LJ size and the LJ well depth, respectively. The Lorentz-Berthelot combining rules [262] are used for the cross interactions between the unlike atoms $i$ and $j$,

$$\sigma_{ij}=\frac{1}{2}\left(\sigma_i+\sigma_j\right), \tag{C-26}$$

$$\varepsilon_{ij}=\left(\varepsilon_i\varepsilon_j\right)^{1/2}. \tag{C-27}$$

A cutoff distance of 1.4 nm is applied for the short-range LJ interaction with an analytical tail correction. The bond lengths in $C_2$ and $C_3$ are fixed at 0.154 nm. The bond bending potential is given as,

$$U_{bend}\left(\theta\right)=\frac{K_\theta}{2}\left(\theta-\theta_{eq}\right)^2 \tag{C-28}$$

where $K_\theta=62500$ K/rad$^2$ and $\theta_{eq}=114^\circ$. The Coulomb potential is used to describe the long-range interaction between $CO_2$ molecules,

$$E_{coul}=\frac{e^2}{4\pi\varepsilon_0}\sum_{i\neq j}\frac{q_iq_j}{r_{ij}} \tag{C-29}$$

where $q_i$ is the charge of atom $i$. The three-dimensional Ewald summation (EW3D) is used to account for the long-range electrostatic interactions and an empty space is inserted between periodic simulation cells in the z-direction as a correction method of EW3D for slab geometry, in which the length of the empty space is sufficient to eliminate the artificial effects [69-71, 263-265]. LJ parameters and charges used for hydrocarbon and $CO_2$ are listed in **Table C-3**.

For the fluid–surface interaction along the z-direction, the 10-4-3 Steele potential [158] is used in the GCMC simulation,

$$\varphi_{sf}(z) = 2\pi\rho_s\varepsilon_{sf}\sigma_{sf}^2\Delta\left[\frac{2}{5}\left(\frac{\sigma_{sf}}{z}\right)^{10} - \left(\frac{\sigma_{sf}}{z}\right)^{4} - \frac{\sigma_{sf}^4}{3\Delta\left(0.61\Delta + z\right)^3}\right] \quad \text{(C-30)}$$

where $z$ represents the position in a perpendicular direction relative to the pore surface. $\rho_s = 114$ nm$^{-3}$ is the density of graphite and $\Delta = 0.335$ nm represents the interlayer spacing of graphite; $\varepsilon_{sf}$ and $\sigma_{sf}$ are potential expansion parameters of surface and fluids, following the simple mixing rule: $\varepsilon_{sf} = \sqrt{\varepsilon_s\varepsilon_f}$, and $\sigma_{sf} = \left(\sigma_s + \sigma_f\right)/2$. Here, we set the energy and size parameters of graphite surface to $\sigma_s = 0.3345$ nm, $\varepsilon_s / k_B = 28$ K [78, 224]. $\varepsilon_f$ is the fluid energy, and $\sigma_f$ is the diameter of fluids atoms, which have the same meaning and values as listed in **Table C-3**.

A periodic rectangular simulation box is set as $L_x$ = 4 nm, and $L_y$ = 4 nm in the *x*- and *y*-directions, respectively. In the z-direction, the pore size and the empty space are set as 5 nm and 10 nm, respectively. All GCMC simulations are performed at $T$ = 333.15 K. The Widom insertion method [266] is used to calculate chemical potentials, where the bulk density is obtained from PC-SAFT EOS. For $C_1$, three types of GCMC moves, *i.e.*, inserting, deletion, and translation, are included. For $C_2$, $C_3$, and $CO_2$, rotational moves are also performed. The GCMC simulation for equilibrium consists of 0.15 million Monte Carlo (MC) cycles per fluid molecule and for sampling, the density profiles consist of 0.5 million MC cycles per fluid molecule.

**Table C-3** LJ parameters and charges in hydrocarbons and $CO_2$ [261].

| | σ (Å) | ε/k$_b$ (K) | q (e) |
|---|---|---|---|
| $CH_4$ | 3.73 | 148.0 | 0.00 |
| –$CH_3$ | 3.75 | 98.0 | 0.00 |
| –$CH_2$– | 3.95 | 46.0 | 0.00 |
| C-$CO_2$ | 2.80 | 27.0 | 0.70 |
| O-$CO_2$ | 3.05 | 79.0 | -0.35 |

## C.4. Calibrations for PC-SAFT DFT Calculation Results

### C.4.1. Pure components calibrations

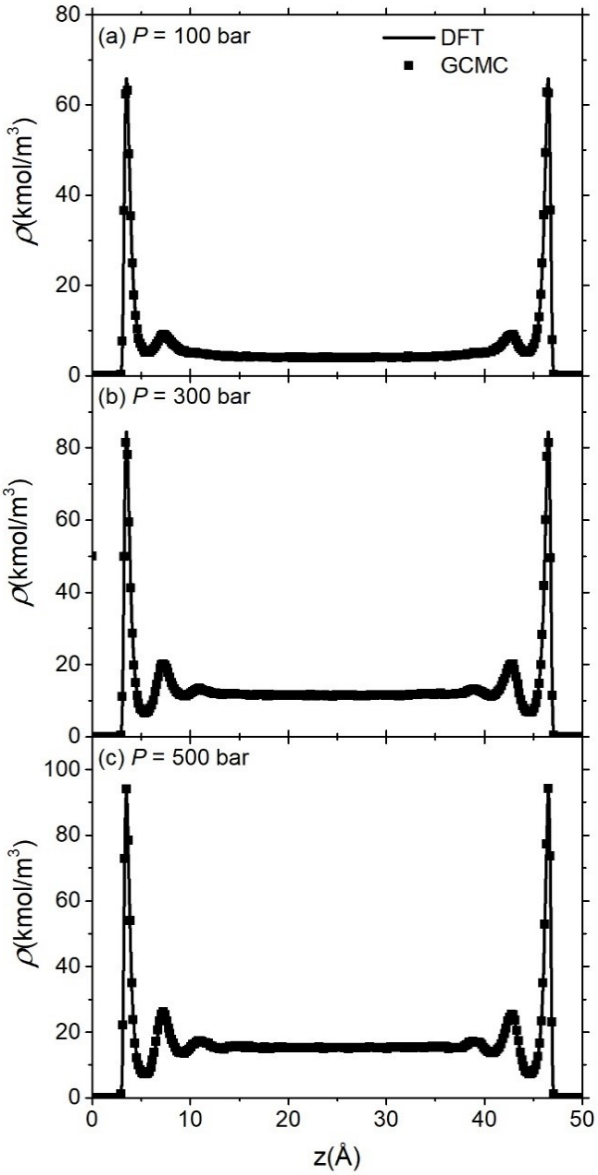


**Figure C-1** Molar density profile of $C_1$ in $W = 5$ nm slit pores at various pressure (a) $P =$ 100 bar, (b) $P = 300$ bar, (c) $P = 500$ bar from PC-SAFT DFT and Grand Canonical Monte Carlo (GCMC) simulation at $T = 333.15$ K.

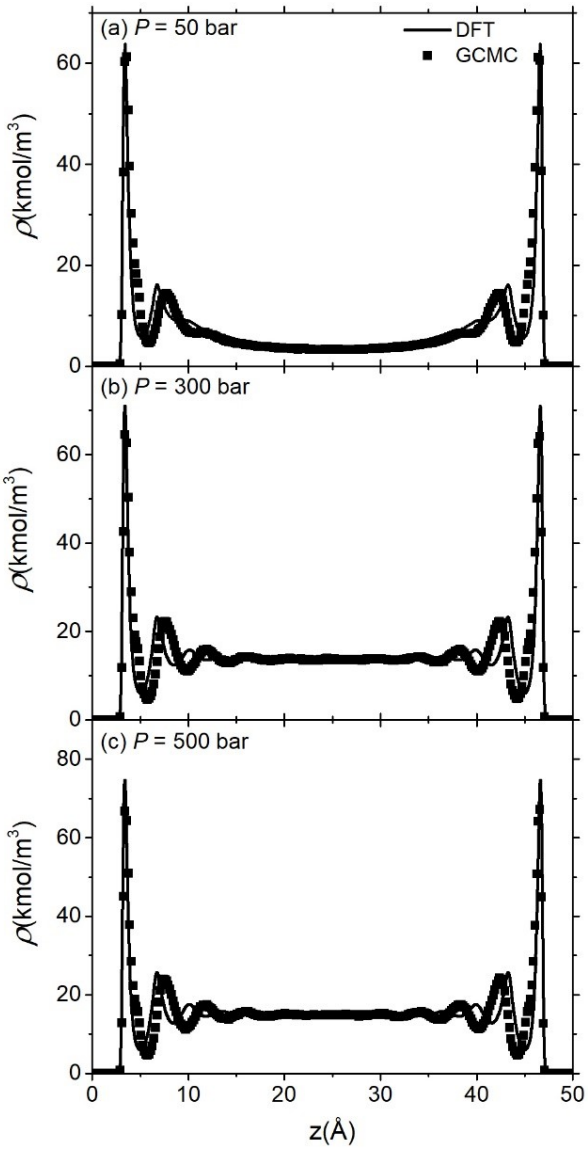


**Figure C-2** Molar density profile of $C_2$ in $W$ = 5 nm slit pores at various pressure (a) $P$ = 50 bar, (b) $P$ = 300 bar, (c) $P$ = 500 bar from PC-SAFT DFT and GCMC at $T$ = 333.15 K.

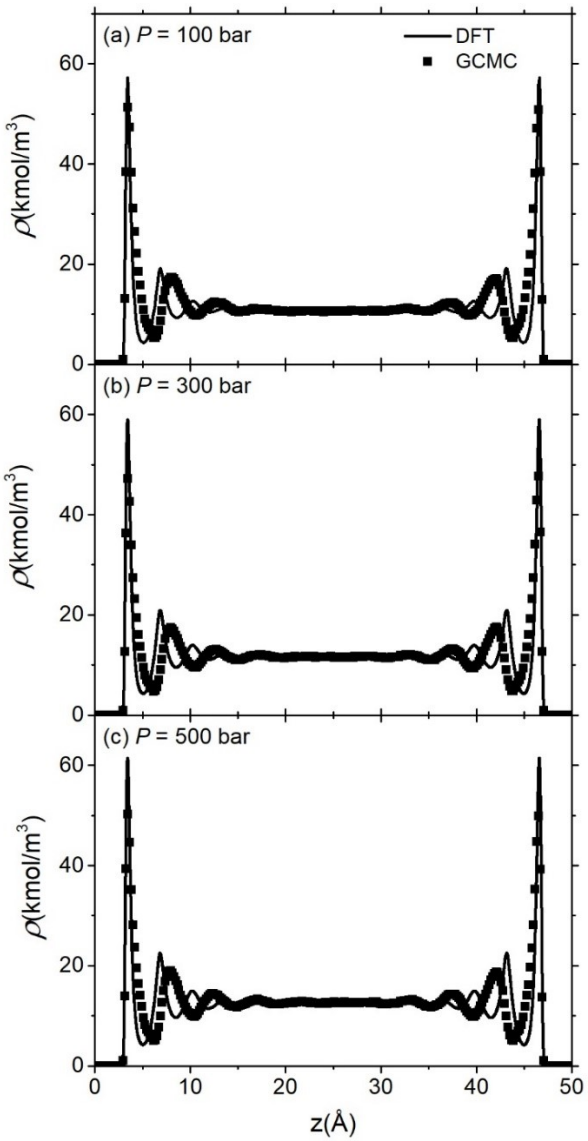


**Figure C-3** Molar density profile of $C_3$ in $W$ = 5 nm slit pores at various pressure (a) $P$ = 100 bar, (b) $P$ = 300 bar, (c) $P$ = 500 bar from PC-SAFT DFT and GCMC at $T$ = 333.15 K.

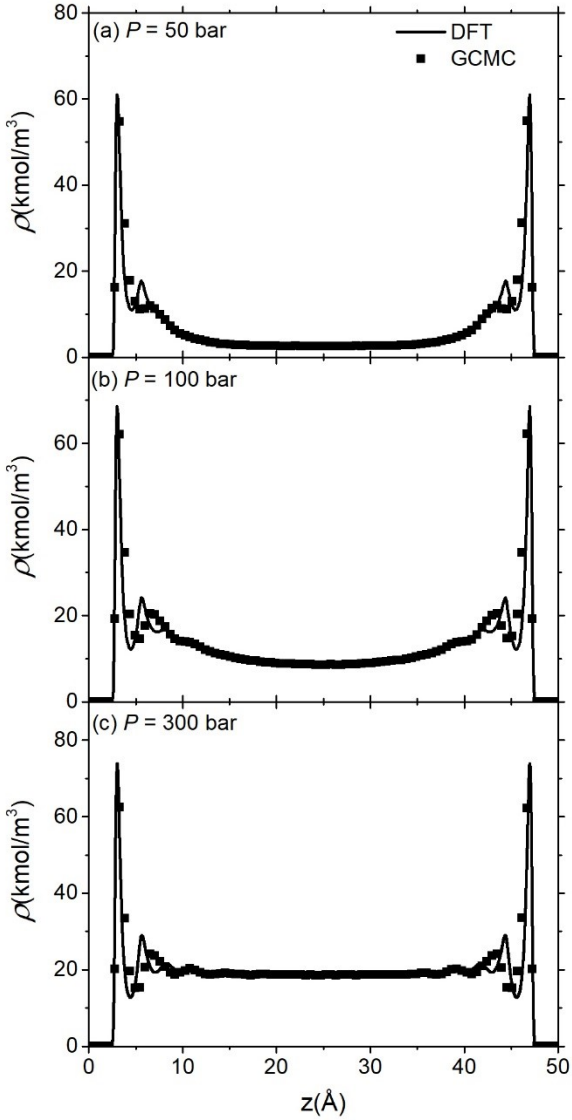


**Figure C-4** Molar density profile of $CO_2$ in $W$ = 5 nm slit pores at various pressure (a) $P$ = 50 bar, (b) $P$ = 100 bar, (c) $P$ = 300 bar from PC-SAFT DFT and GCMC at $T$ = 333.15 K.

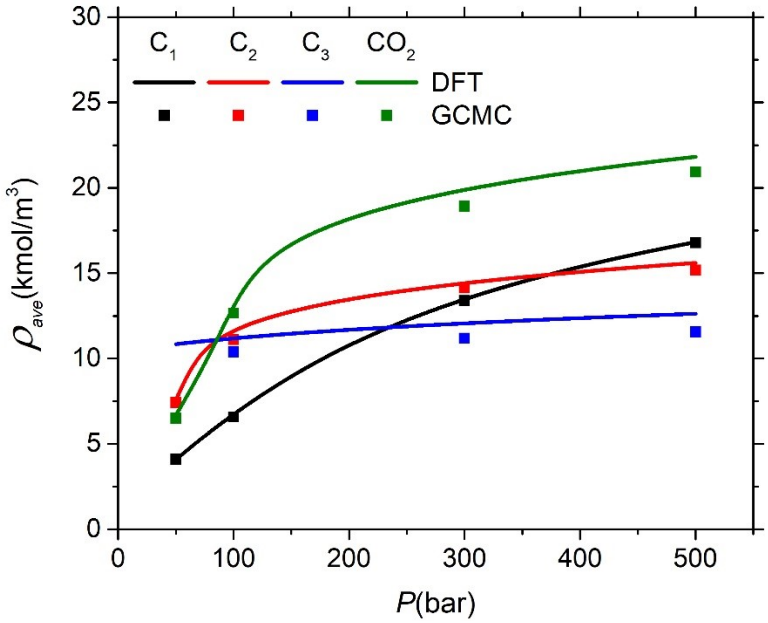


**Figure C-5** Average molar density of pure components in $W$ = 5 nm slit pores at various from PC-SAFT DFT (solid lines) and GCMC (squares) at $T$ = 333.15 K. Black, red, blue, and green colors represent $C_1$, $C_2$, $C_3$, and $CO_2$, respectively.

### C.4.2. Mixtures components calibrations

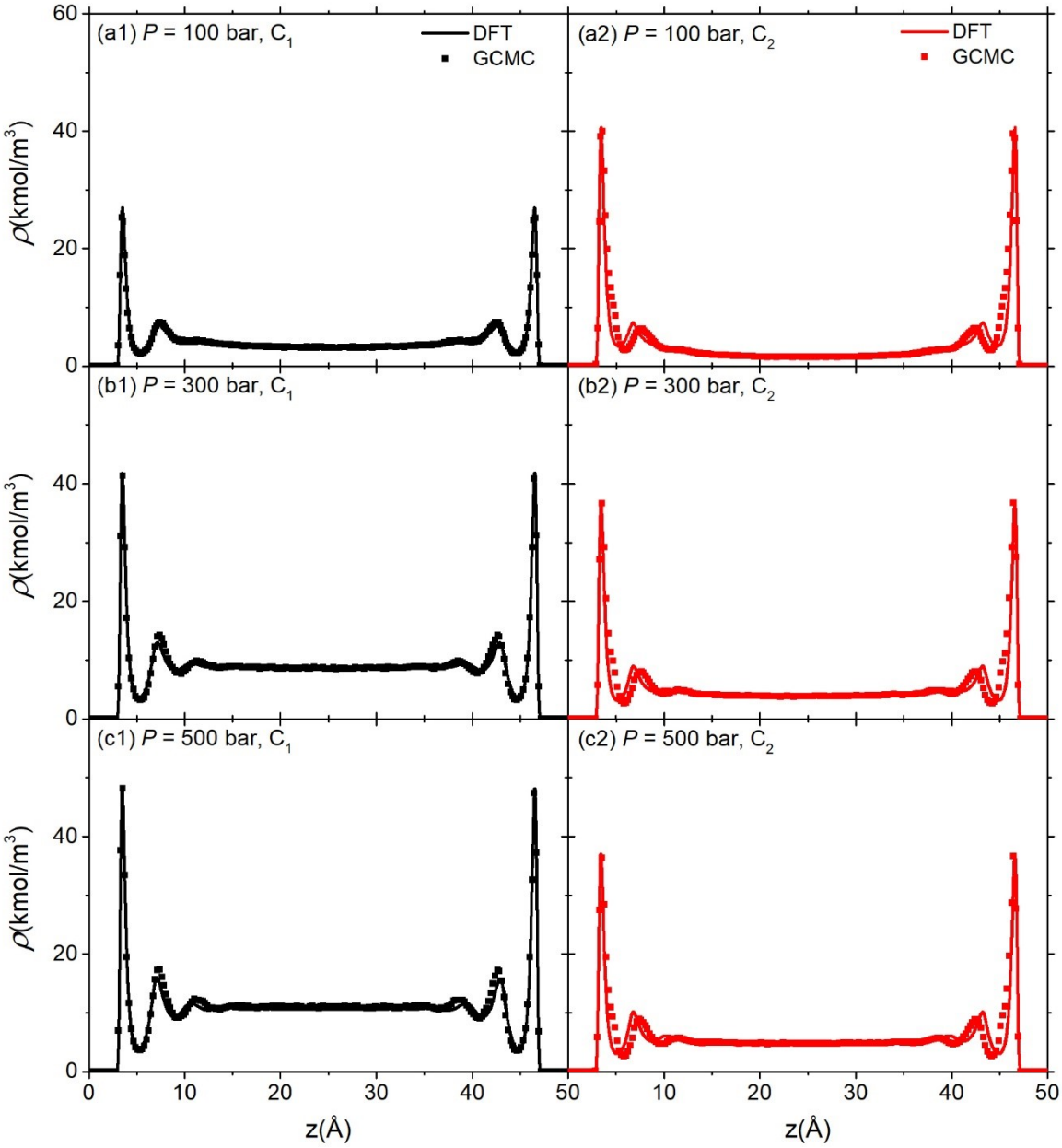


**Figure C-6** Molar density profile of components in $C_1$-$C_2$ hydrocarbon mixtures ($X_{C1}$ = 0.7) in $W$ = 5 nm slit pores at various pressures (a) $P$ = 100 bar, (b) $P$ = 300 bar, (c) $P$ = 500 bar from PC-SAFT DFT and GCMC at $T$ = 333.15 K. Black color represents $C_1$ and red color is $C_2$.

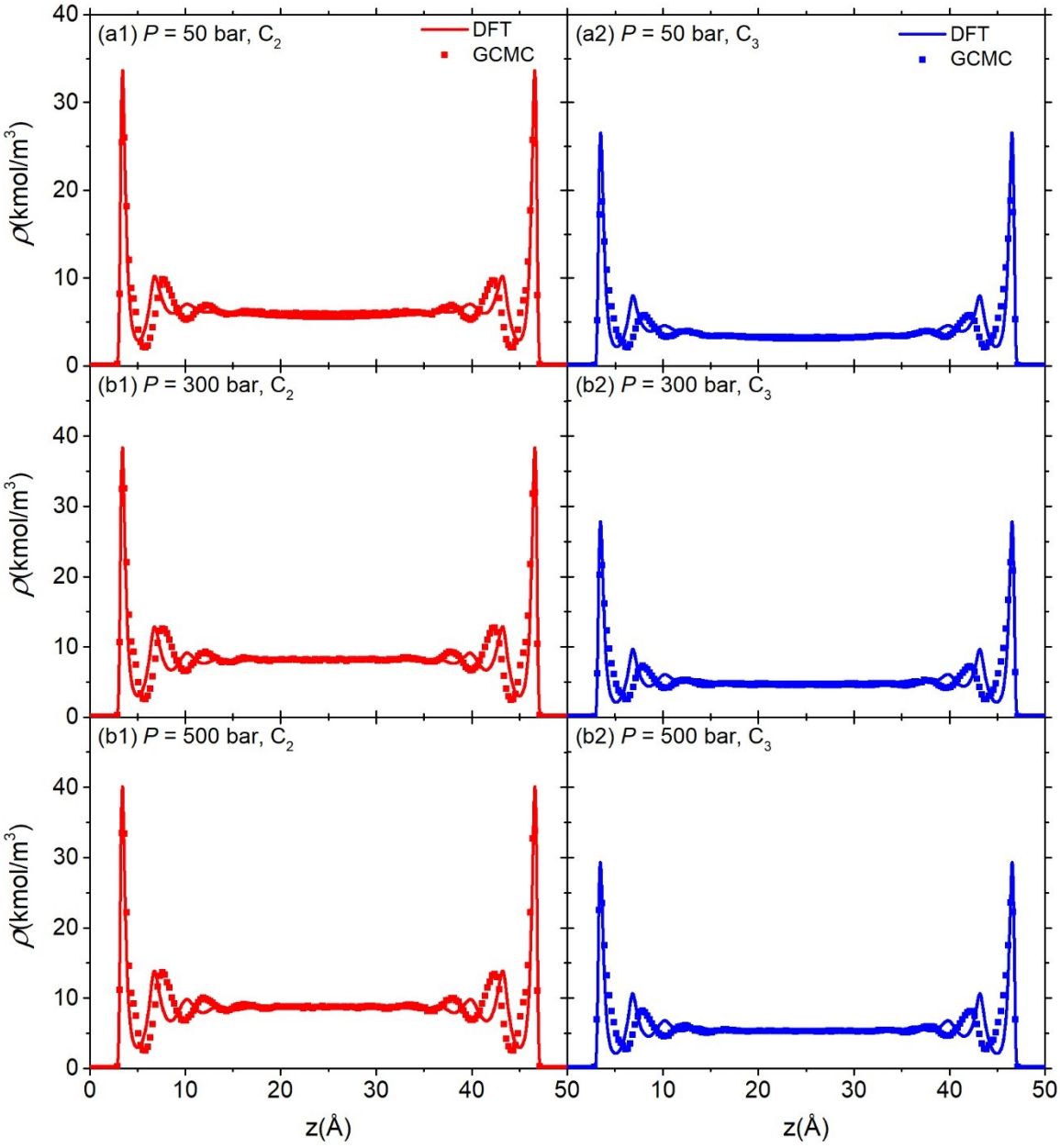


**Figure C-7** Molar density profile of components in $C_2$-$C_3$ hydrocarbon mixtures ($X_{C2}$ = 0.7) in $W$ = 5 nm slit pores at various pressures (a) $P$ = 100 bar, (b) $P$ = 300 bar, (c) $P$ = 500 bar from PC-SAFT DFT and GCMC at $T$ = 333.15 K. Red color represents $C_2$ and blue color is $C_3$.

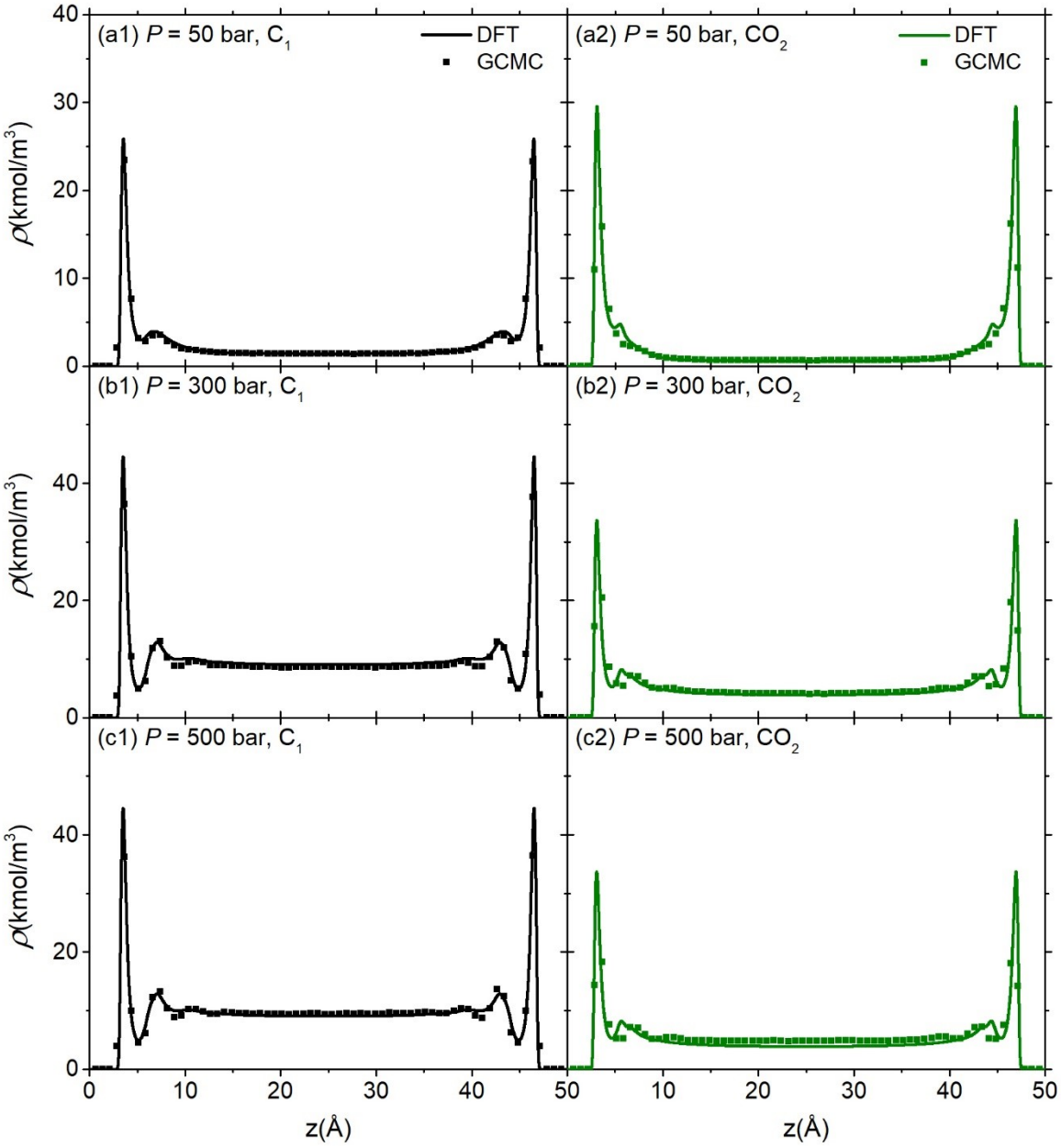


**Figure C-8** Molar density profile of components in $C_1$-$CO_2$ hydrocarbon mixtures ($X_{C1}$ = 0.7) in $W$ = 5 nm slit pores at various pressures (a) $P$ = 50 bar, (b) $P$ = 300 bar, (c) $P$ = 500 bar from PC-SAFT DFT and GCMC at $T$ = 333.15 K. Black color represents $C_1$ and green color is $CO_2$.

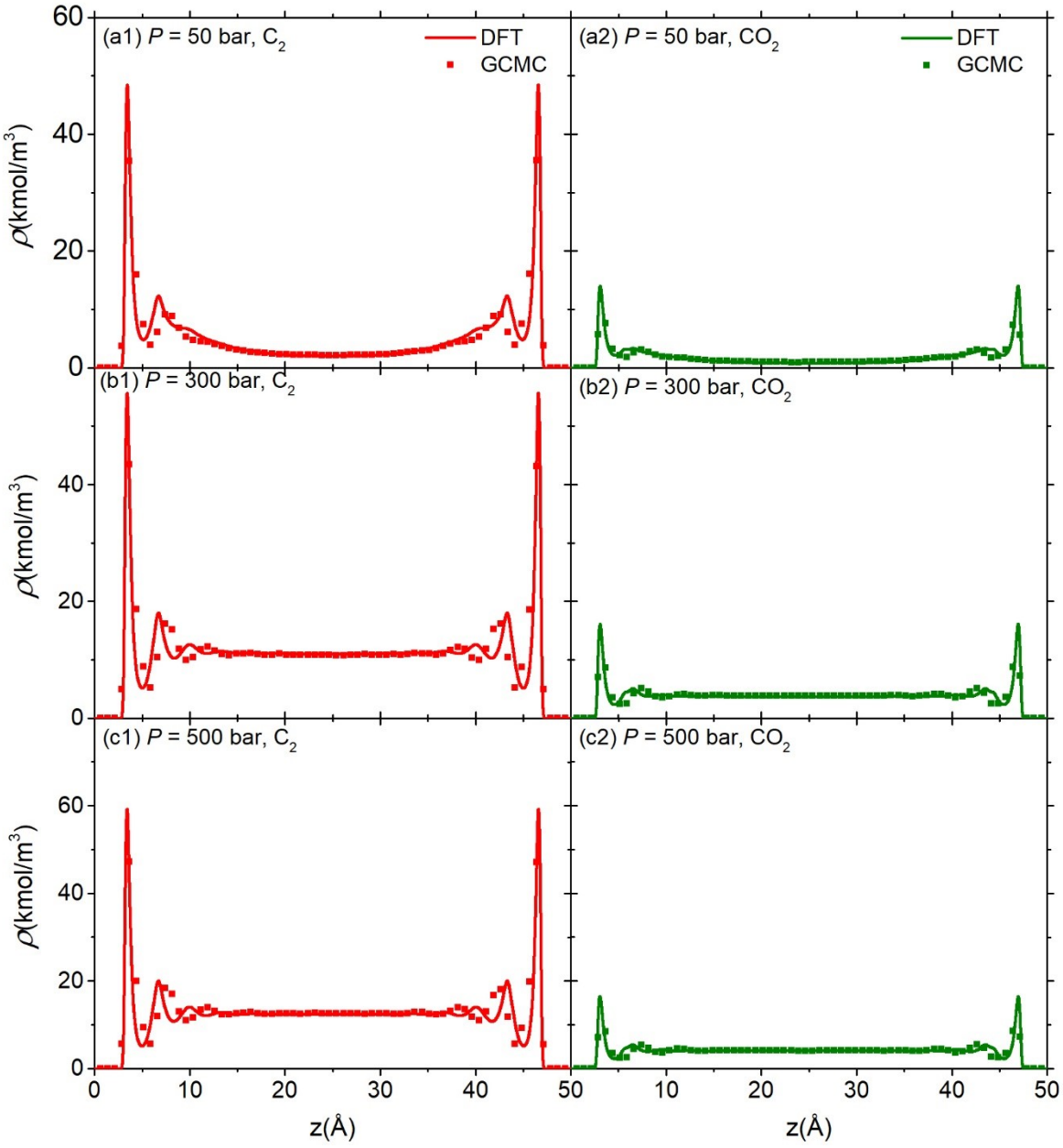


**Figure C-9** Molar density profile of components in $C_2$-$CO_2$ hydrocarbon mixtures ($X_{C2}$ = 0.7) in $W$ = 5 nm slit pores at various pressures (a) $P$ = 50 bar, (b) $P$ = 300 bar, (c) $P$ = 500 bar from PC-SAFT DFT and GCMC at $T$ = 333.15 K. Red color represents $C_2$ and green color is $CO_2$.

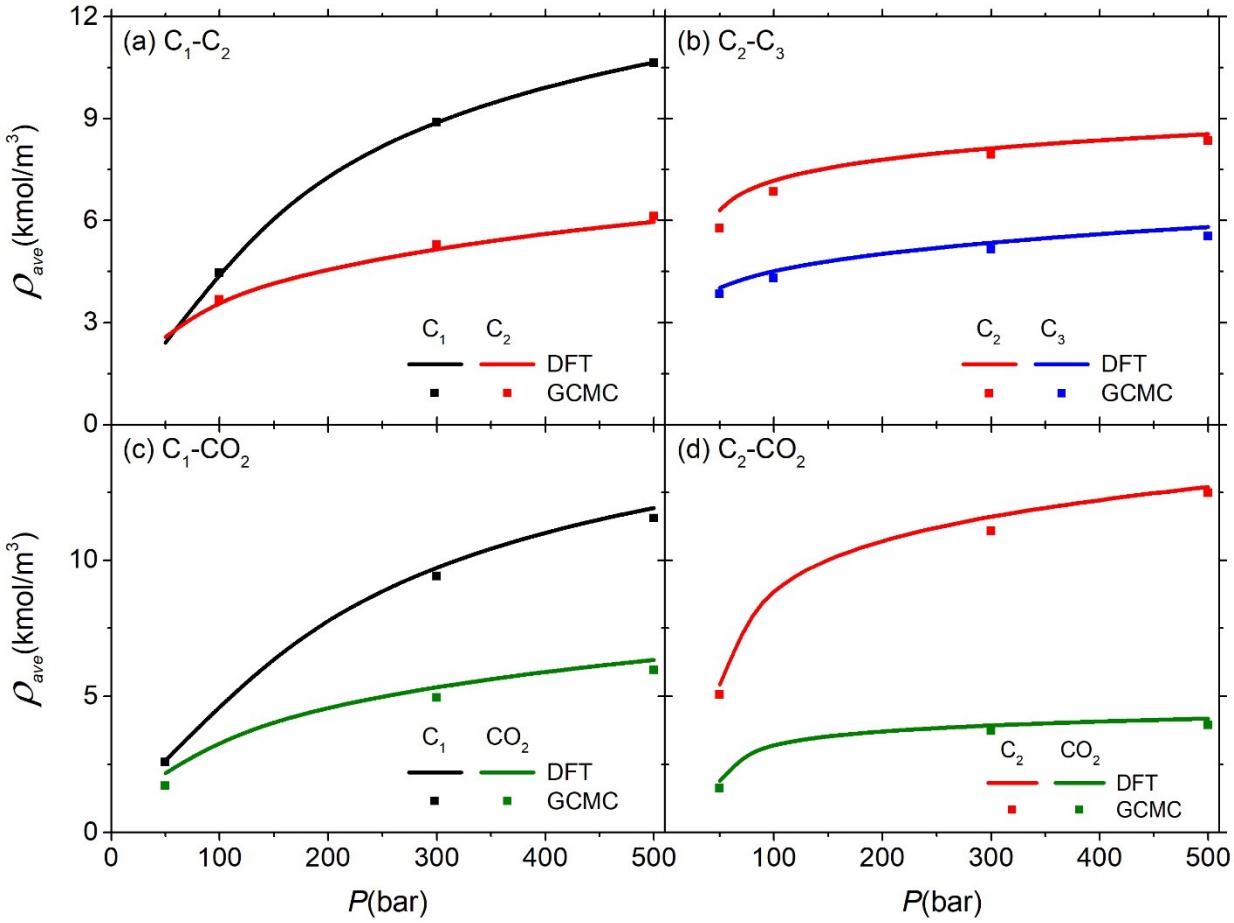


**Figure C-10** Average molar density of mixture components in $W$ = 5 nm slit pores at various pressures from PC-SAFT DFT (solid lines) and GCMC (squares) at $T$ = 333.15 K. Black, red, blue, and green colors represent $C_1$, $C_2$, $C_3$, and $CO_2$, respectively.

## C.5. Average Molar Density of Each Component in W = 5 nm, W = 30 nm Slit Pores and the Bulk.

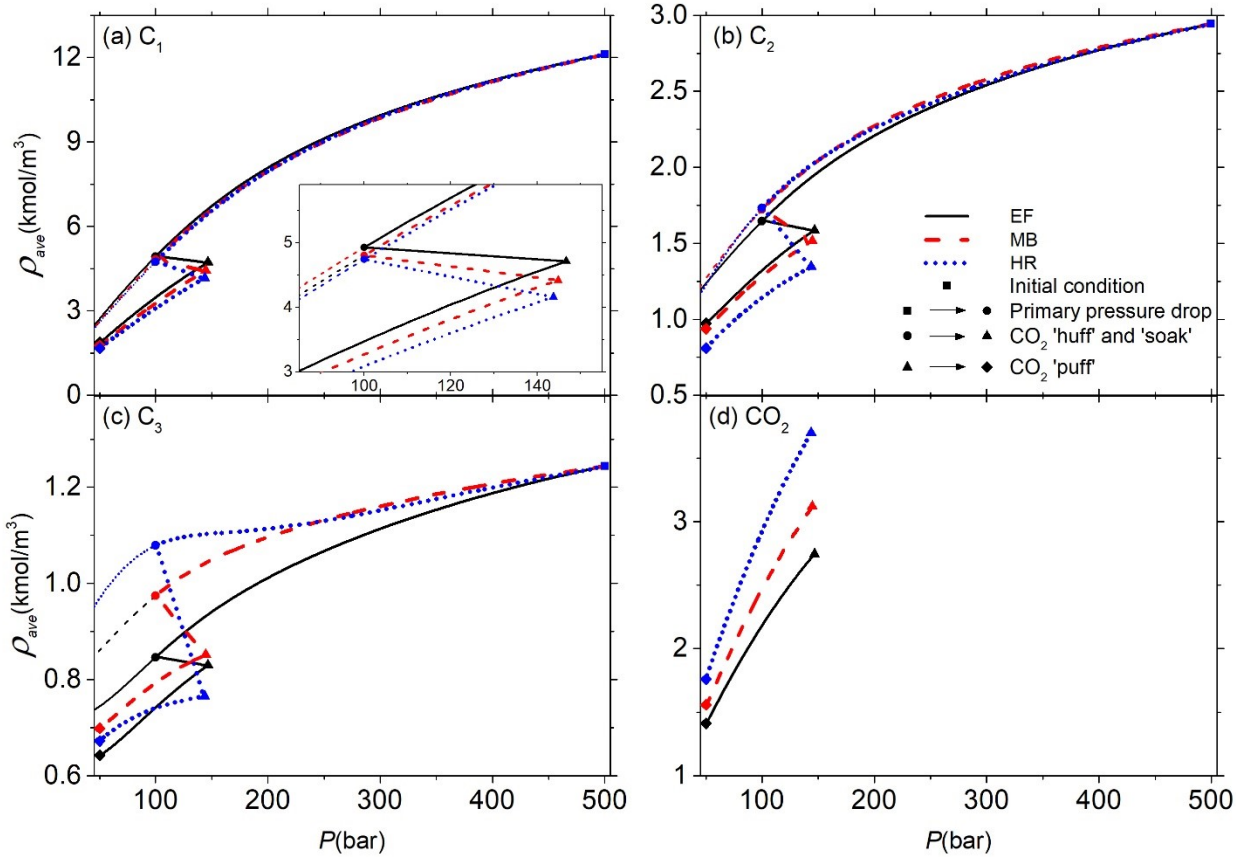


**Figure C-11** The average molar density in $W$ = 5 nm slit pores of (a) $C_1$, (b) $C_2$, (c) $C_3$, and (d) $CO_2$ in various PSD cases at $T$ = 333.15 K. The black solid lines represent average density from Eagle Ford. Red dashed lines are from Middle Bakken and blue dotted lines are from Horn River. Thick and thin lines represent scenarios with/without $CO_2$ 'huff-n-puff', respectively. Squares represent the initial condition. The route from squares to circles represents the primary pressure drop; the route from circles to triangles represents the $CO_2$ 'huff' and 'soak' processes, and the route from triangles to rhombs represents the $CO_2$ 'puff' process. The $CO_2$ 'huff' and 'soak' processes are amplified and shown as inserted figures.

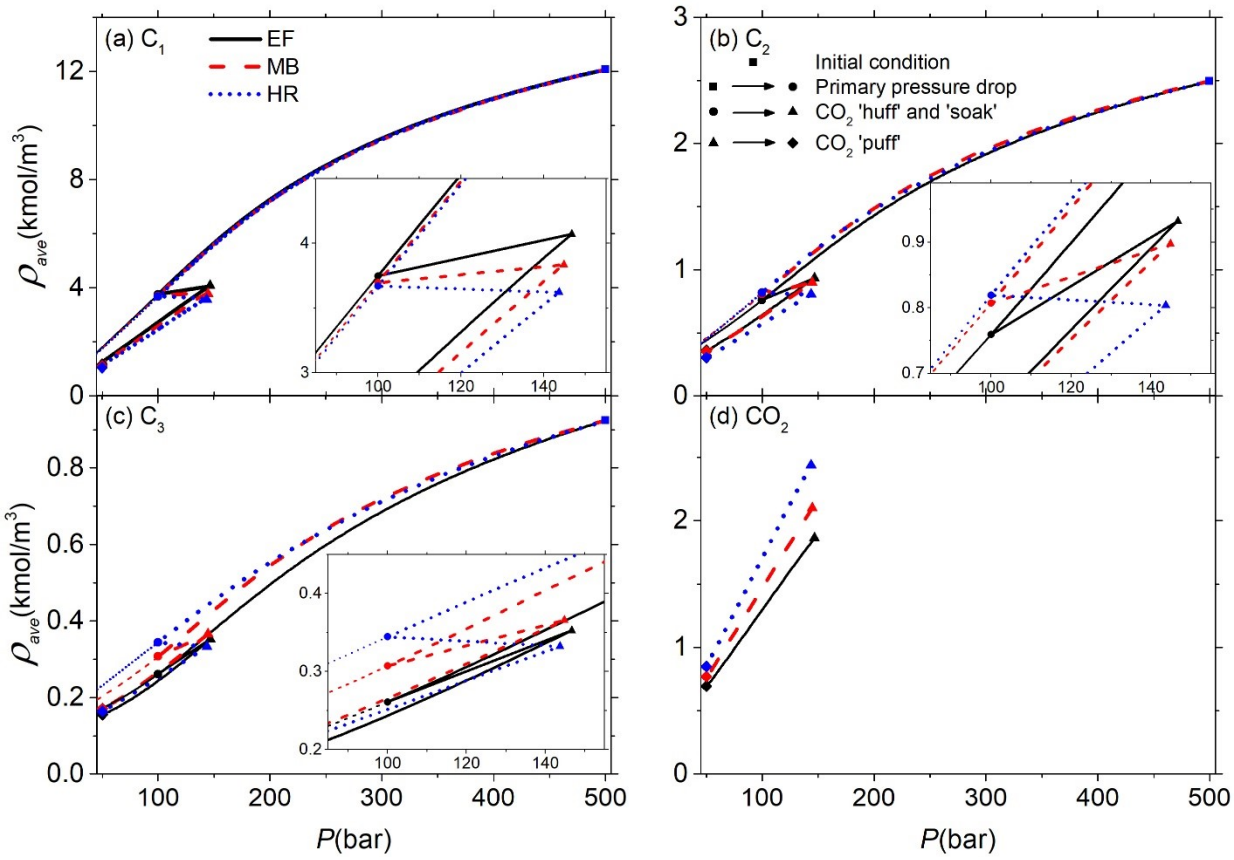


**Figure C-12** The average molar density in $W$ = 30 nm slit pores of (a) $C_1$, (b) $C_2$, (c) $C_3$, and (d) $CO_2$ in various PSD cases at $T$ = 333.15 K. The black solid lines represent average density from Eagle Ford. Red dashed lines are from Middle Bakken and blue dotted lines are from Horn River. Thick and thin lines represent scenarios with/without $CO_2$ 'huff-n-puff', respectively. Squares represent the initial condition. The route from squares to circles represents the primary pressure drop; the route from circles to triangles represents the $CO_2$ 'huff' and 'soak' processes, and the route from triangles to rhombs represents the $CO_2$ 'puff' process. The $CO_2$ 'huff' and 'soak' processes are amplified and shown as inserted figures.

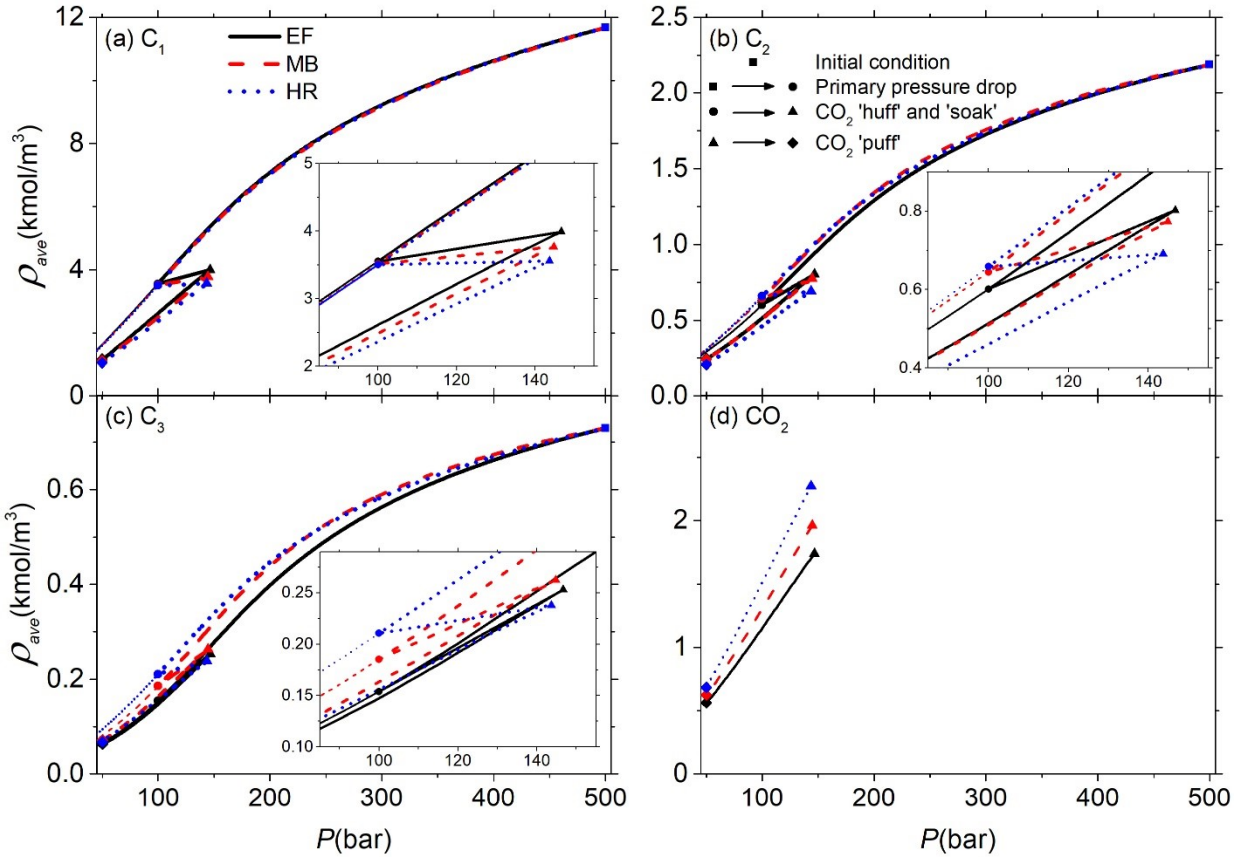


**Figure C-13** The average molar density in the bulk of (a) $C_1$, (b) $C_2$, (c) $C_3$, and (d) $CO_2$ in various PSD cases at $T$ = 333.15 K. The black solid lines represent average density from Eagle Ford. Red dashed lines are from Middle Bakken and blue dotted lines are from Horn River. Thick and thin lines represent scenarios with/without $CO_2$ 'huff-n-puff', respectively. Squares represent the initial condition. The route from squares to circles represents the primary pressure drop; the route from circles to triangles represents the $CO_2$ 'huff' and 'soak' processes, and the route from triangles to rhombs represents the $CO_2$ 'puff' process. The $CO_2$ 'huff' and 'soak' processes are amplified shown as inserted figures.

## C.6. Molar Density Profile of Components in W = 5 nm and W = 30 nm Slit Pores

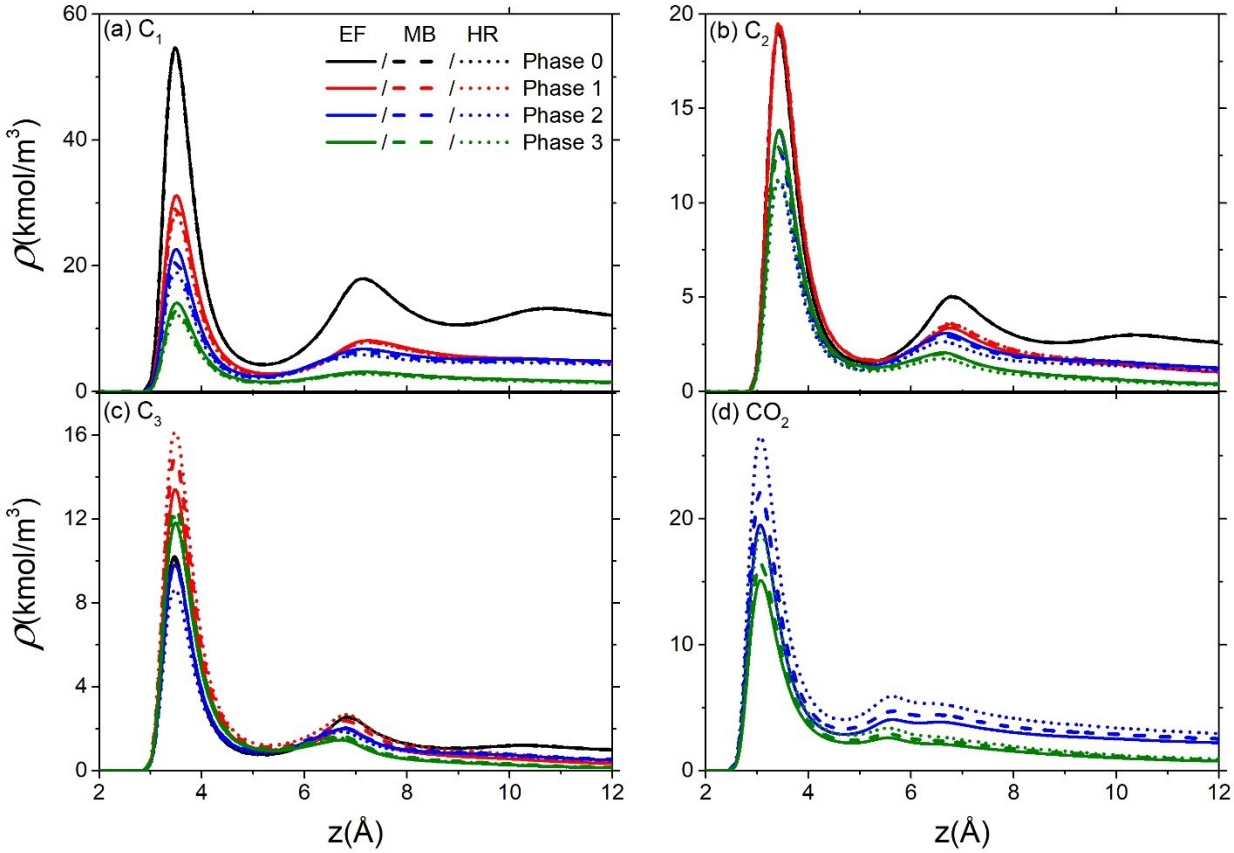


**Figure C-14** The molar density profile in $W$ = 5 nm slit pores of (a) $C_1$, (b) $C_2$, (c) $C_3$, and (d) $CO_2$ at different phases, at $T$ = 333.15 K. Black lines represent mole density profiles at initial condition (Phase 0). Red, bulk, and green lines represent mole density profiles at pressures of the end of the primary pressure drop ( $P_1$ ), $CO_2$ 'soak' ( $P_2$ ), and $CO_2$ 'puff' ( $P_3$ ), respectively. Solid, dashed, dotted lines represent mole density profiles from Eagle Ford, Middle Bakken, and Horn River, respectively.

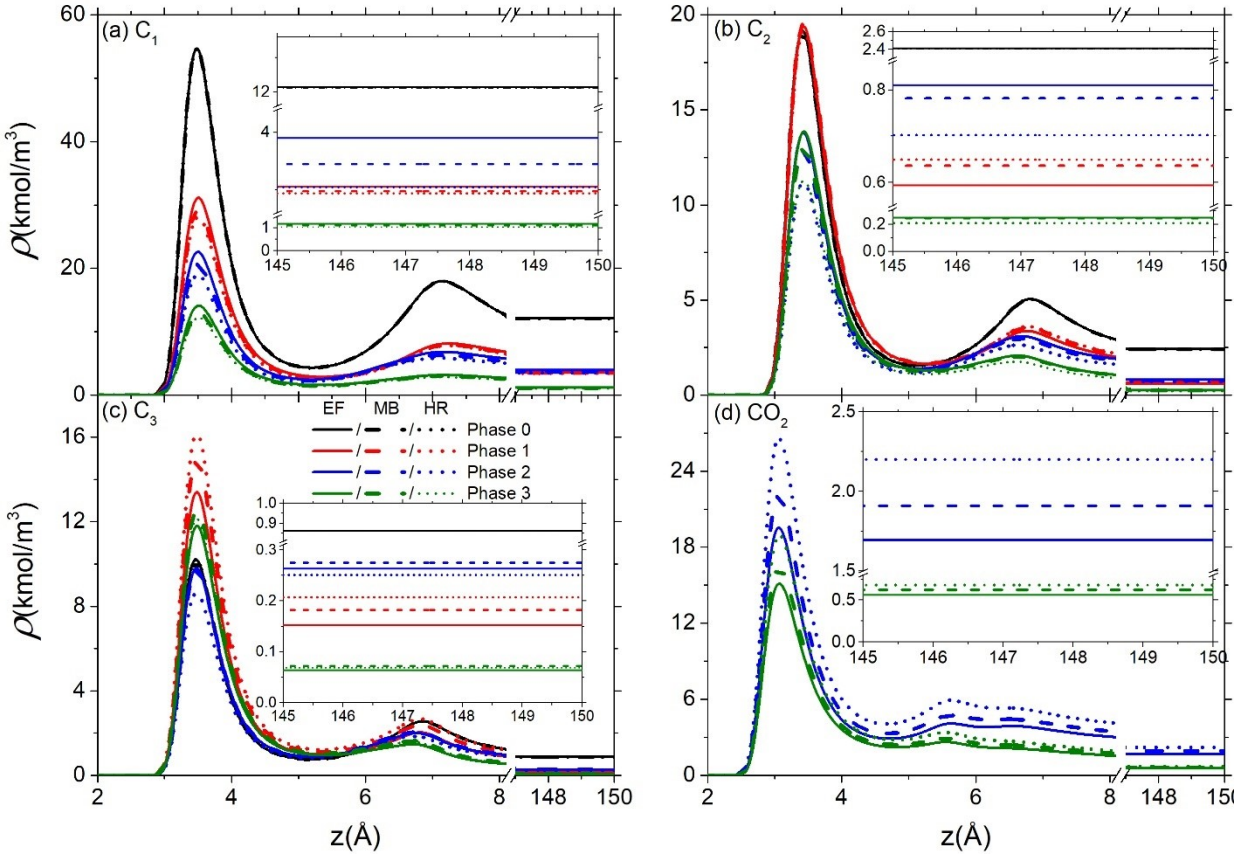


**Figure C-15** The molar density profile in $W$ = 30 nm slit pores of (a) $C_1$, (b) $C_2$, (c) $C_3$, and (d) $CO_2$ at different phases, at $T$ = 333.15 K. Black lines represent mole density profiles at initial condition (Phase 0). Red, bulk, and green lines represent mole density profiles at pressures of the end of the primary pressure drop ( $P_1$ ), $CO_2$ 'soak' ( $P_2$ ), and $CO_2$ 'puff' ( $P_3$ ), respectively. Solid, dashed, dotted lines represent mole density profiles from Eagle Ford, Middle Bakken, and Horn River, respectively.

## C.7. Pore Compositions of Components in W = 5 nm and W = 30 nm Slit Pores

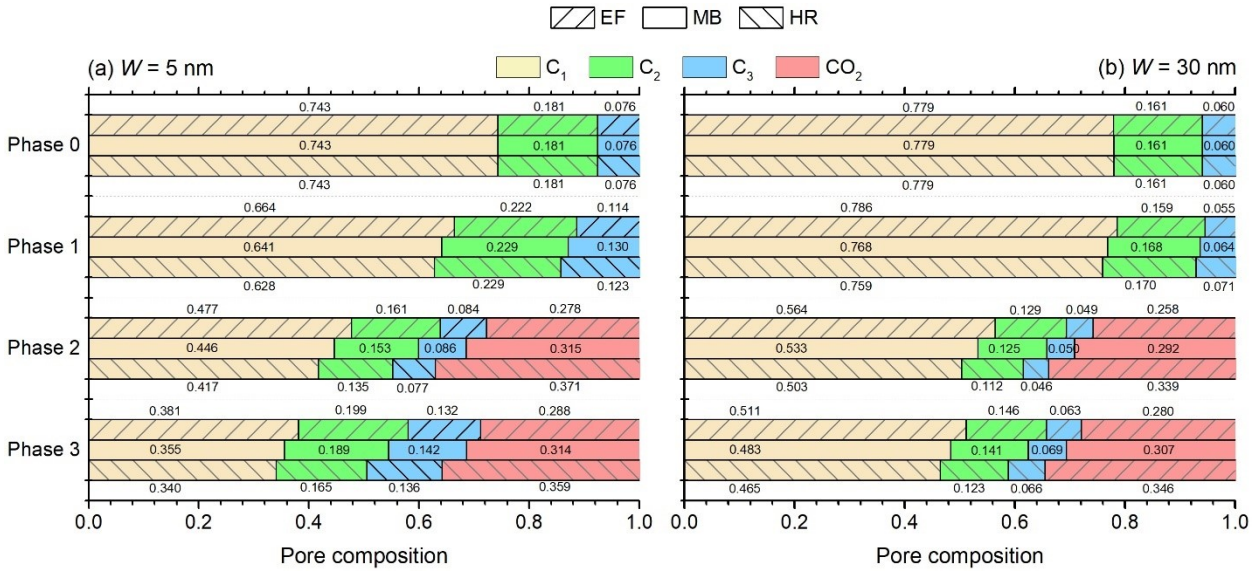


**Figure C-16** Pore compositions of each component in (a) $W$ = 5 nm, (b) $W$ = 30 nm at various $CO_2$ 'huff-n-puff' phases at $T$ = 333.15 K. Phase 0 represents the initial condition; Phase 1 represents the primary pressure drop; Phase 2 represents the $CO_2$ 'huff' and 'soak' processes and Phase 3 represents the $CO_2$ 'puff' process. The pore compositions shown for Phase 1, 2, 3 are the composition at the pressure of the end of each phase.

## C.8. Hydrocarbon-releasing Factor of Hydrocarbon Components in W = 5 nm and W = 30 nm Slit Pores

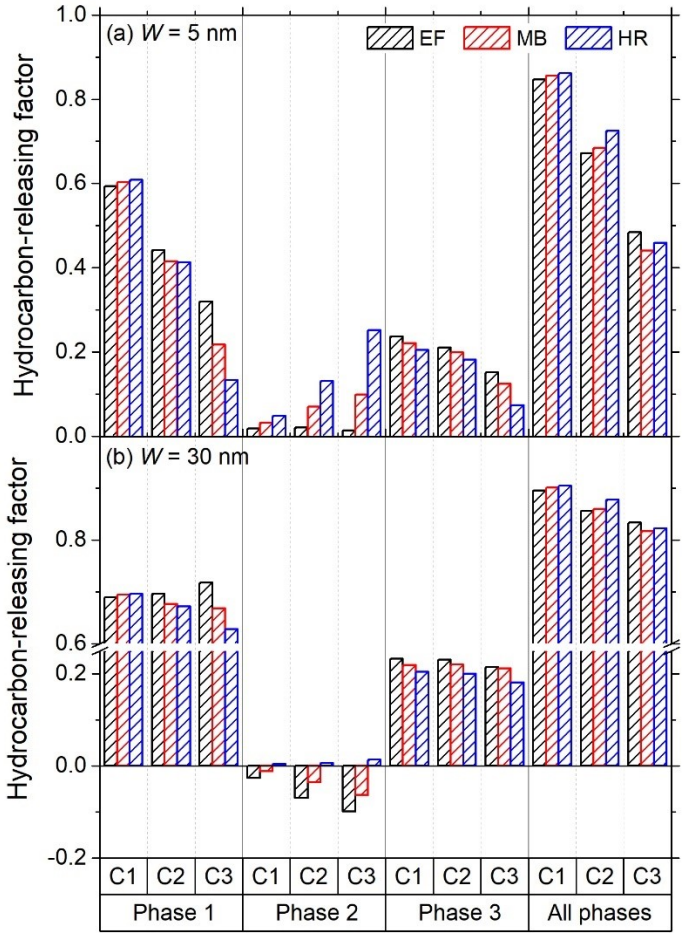


**Figure C-17** The hydrocarbon-releasing factor of hydrocarbon components in $W$ = 5 nm and $W$ = 30 nm slit pores of each phase from various PSD cases at $T$ = 333.15 K. Phase 1 represents the primary pressure drop; Phase 2 represents the $CO_2$ 'huff' and 'soak' processes, and Phase 3 represents the $CO_2$ 'puff' process; All phases represent the whole process from the initial condition to the abandoned pressure.

公式章 (下一章) 节 1

## Appendix D

### D.1. Kerogen Matrix Building Processes

To obtain a relatively-smooth kerogen matrix, 20 kerogen macromolecules are compressed by two rigid smooth graphene sheets as shown in **Figure D-1 (a)**, which are generated by an all-atom model in the VMD package[241] with a dimension of 5.44 nm × 5.51 nm in the *x*-*y* plane. Only the repulsive forces between the graphene sheet and kerogen macromolecules are considered. To compress these kerogen macromolecules, an external pressure of 7000 bar (*i.e.*, an external acceleration of -0.9 nm/ps$^2$ to each C atom on graphene) is added to the upper graphene sheet in the *z*-direction, while the bottom graphene sheet is fixed. Meanwhile, an annealing simulation with the temperature gradually declining from 900 K to 333.15 K is conducted for 2.5 ns, and then another 1.5 ns of simulation at 333.15 K is conducted to reach equilibrium. The final relatively-smooth kerogen matrix (denoted as **krg1**) thickness is ~3.5 nm.

To make rough kerogen matrices, we initially attempted to use a rigid upper smooth graphene sheet and a rigid bottom rough graphene sheet with varying degrees of roughness to compress kerogen macromolecules under the same procedures as for **krg1**. However, we find that the roughness of final kerogen matrices always falls into a very narrow range which can hardly represent a wide range of kerogen surface roughnesses. Therefore, we use an alternative method to generate relatively-rough kerogen matrices by compressing kerogen macromolecules with a rigid upper smooth graphene sheet and a rigid bottom rough pseudo-kerogen sheet, which is conducted in a two-step simulation process.

In the first step, to build the rough pseudo-kerogen sheet, 20 kerogen macromolecules are compressed by two rigid smooth graphene sheets as shown in **Figure D-1 (b)**. Similarly, these two graphene sheets are generated by the all-atom model in the VMD package with a dimension of 5.44 nm × 5.51 nm in the *x*-*y* plane, while only the repulsive forces between the graphene sheet and kerogen macromolecules are considered. To generate pseudo-kerogen sheets with varying roughness, an external pressure ranging from 50 to 10000 bar is added to the upper graphene sheet in the *z*-direction to compress kerogen macromolecules with the same initial configurations. Then, the same annealing processes used for a relatively-smooth kerogen matrix are applied.

In the second step, relatively-rough kerogen matrices are obtained by compressing 20 kerogen macromolecules by a rigid upper smooth graphene sheet and a rigid bottom rough pseudo-kerogen sheet generated in the first step as shown in **Figure D-1 (b)**. An external pressure of 7000 bar is added to the upper graphene sheet in the *z*-direction, while the bottom rough pseudo-kerogen sheet is fixed. The same annealing simulation processes are conducted to allow kerogen matrices to reach equilibrium and 12 relatively-rough kerogen matrices are obtained. These 12 rough kerogen matrices are denoted as **krg2** to **krg12** whose thicknesses are from ~ 3.8 nm to ~ 4.5 nm.

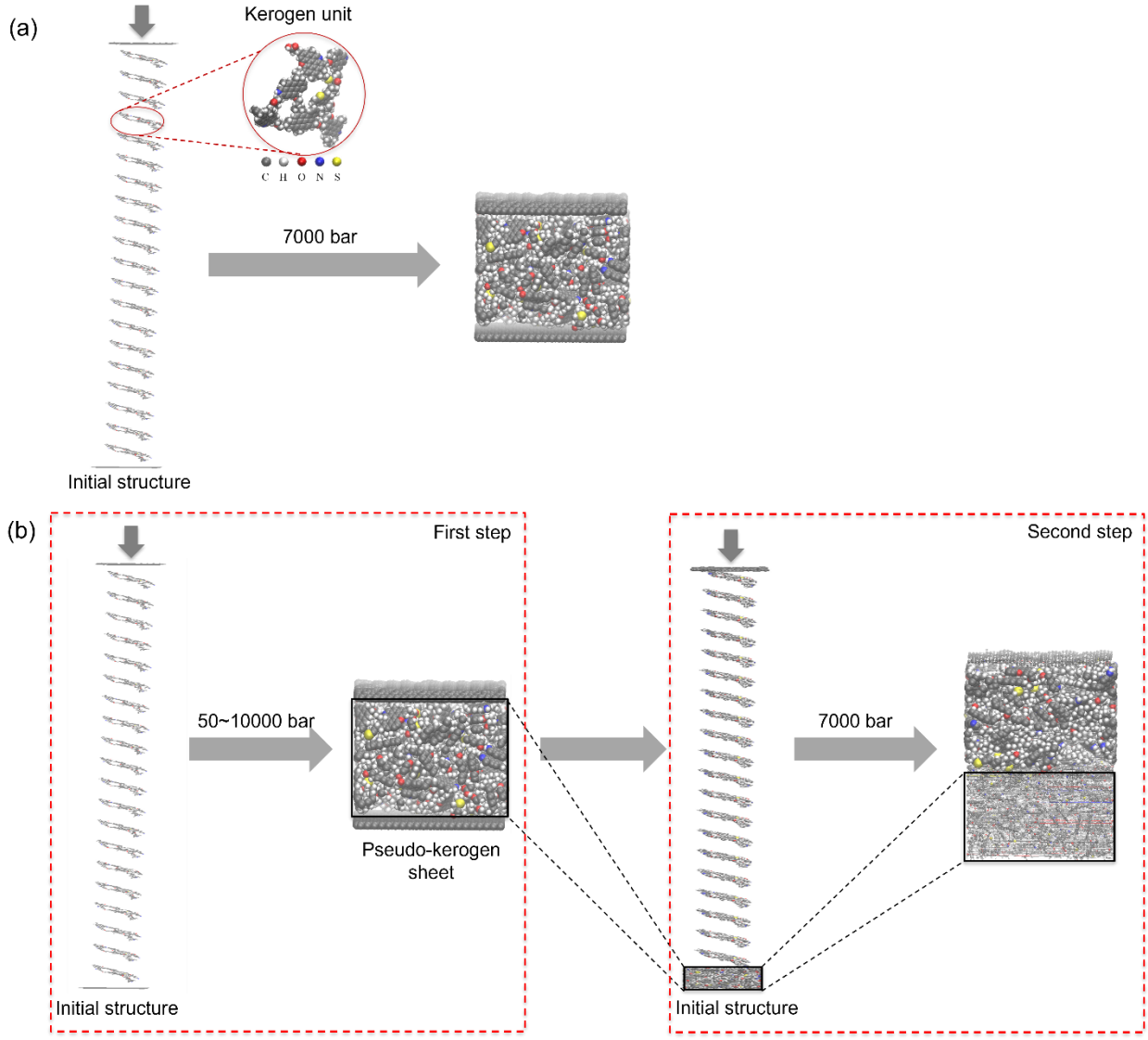


**Figure D-1** Illustration of kerogen matrix building processes: (a) relatively-smooth kerogen matrix; (b) relatively-rough kerogen matrix

## D.2. Force Field Parameters

**Table D-1** LJ parameters of components used in this work.

| Types | | $M_w$(g/mol) | σ(Å) | ε/$k_b$(K) |
|---|---|---|---|---|
| | $N_2$ | 28.013 | 3.615 | 101.50 |
| | $CH_4$ | 16.043 | 3.730 | 148.00 |
| | He | 4.003 | 2.640 | 10.90 |
| Graphite | C | 12.011 | 3.400 | 28.00 |
| | C(c') | 12.011 | 3.617 | 74.51 |
| | C(cs) | 12.011 | 3.617 | 74.51 |
| | C(c5) | 12.011 | 3.617 | 74.51 |
| | C(cp) | 12.011 | 3.617 | 74.51 |
| | C(c=) | 12.011 | 3.617 | 74.51 |
| | C(c1) | 12.011 | 3.875 | 19.64 |
| | C(c2) | 12.011 | 3.875 | 19.64 |
| | C(c3) | 12.011 | 3.875 | 19.64 |
| Kerogen | H(h) | 1.008 | 2.450 | 19.13 |
| | H(ho) | 1.008 | 0.000 | 0.00 |
| | H(hn) | 1.008 | 0.000 | 0.00 |
| | N(np) | 14.007 | 3.501 | 84.08 |
| | O(o) | 15.999 | 2.860 | 114.79 |
| | O(o') | 15.999 | 2.860 | 114.79 |
| | O(oh) | 15.999 | 2.860 | 114.79 |
| | S (s) | 32.064 | 3.368 | 21.64 |
| | S (sp) | 32.064 | 3.368 | 82.57 |

Note: *c'*—$sp^2$ carbon in carbonyl (C=O) group; *cs*—$sp^2$ carbon involved in thiophene; *c5*—$sp^2$ aromatic carbon in five membered ring; *cp*—$sp^2$ aromatic carbon (partial double bonds); *c=*—non-aromatic end doubly bonded carbon; *c1*—$sp^3$ carbon bonded to 1 H, 3 heavy atoms; *c2*—$sp^2$ carbon bonded to 2 H's, 2 heavy atoms; *c3*—$sp^3$ carbon in methyl ($CH_3$) group; *h*—hydrogen bonded to C; *ho*—hydrogen bonded to O; *hn*—hydrogen bonded to N; *np*—$sp^2$ aromatic nitrogen (partial double bonds); *o*—$sp^3$ oxygen in ether or ester groups; *o'*—oxygen in carbonyl (C=O) group; *oh*—oxygen in hydroxyl (OH) group; *s*—sulfur in methionine (C-S-C) group ; *sp*—Sulfur in thiophene.

### D.3. Kerogen Matrices Density Calculations

In a system simulation box, two paralleled kerogen matrices are set at the top and bottom of the box to compose a kerogen slit mesopore. To obtain the density of kerogen matrices, the effective volume of slit mesopores $V_p$ has been calculated first by helium adsorption, whose details are shown in **Appendix D.4**. The volume of the system simulation box $V_{sys}$ is known so that the volume of a kerogen matrix is $V_{krg} = \left(V_{sys} - V_p\right)/2$. The mass of kerogen $m_{krg}$ can be easily obtained by its chemical formula ($C_{242}H_{219}O_{13}N_5S_2$). Thus, the density of a kerogen matrix is calculated by

$$\rho_{krg} = \frac{m_{krg}}{V_{krg}} = \frac{m_{krg}}{\left(V_{sys} - V_p\right)/2}. \tag{D-1}$$

The densities of each kerogen matrix are listed in **Table D-2** below.

**Table D-2** Density, effective volume, and relative volume errors of kerogen models

| Case # | X-Axis (Å) | Y-Axis (Å) | $W_{ave}$ (nm) | $\rho_{krg}$ (g/cm$^3$) | $V_p$ (nm$^3$) | $V_p$_err |
|---|---|---|---|---|---|---|
| krg1 | 51.58 | 51.05 | 5.35 | 1.37 | 152.2 | 2% |
| krg2 | 51.57 | 51.02 | 5.35 | 1.28 | 156.7 | 1% |
| krg3 | 51.56 | 51.10 | 5.35 | 1.20 | 151.5 | 2% |
| krg4 | 51.56 | 51.09 | 5.35 | 1.30 | 158.3 | 2% |
| krg5 | 50.34 | 51.05 | 5.35 | 1.22 | 146.3 | 5% |
| krg6 | 51.57 | 51.02 | 5.35 | 1.36 | 155.4 | 1% |
| krg7 | 51.33 | 52.05 | 5.35 | 1.23 | 146.9 | 5% |
| krg8 | 50.69 | 51.08 | 5.35 | 1.29 | 154.1 | 0% |
| krg9 | 51.55 | 51.08 | 5.35 | 1.30 | 154.4 | 0% |
| krg10 | 50.69 | 51.08 | 5.35 | 1.31 | 156.8 | 1% |
| krg11 | 52.57 | 52.05 | 5.35 | 1.28 | 161.8 | 5% |
| krg12 | 50.34 | 51.05 | 5.35 | 1.28 | 154.8 | 0% |
| krg13 | 51.53 | 51.08 | 5.35 | 1.29 | 160.7 | 4% |

Note: $\rho_{krg}$ refers to the density of the kerogen matrix. $V_{p\_err} = \left|V_p - \bar{V}\right|/\bar{V}$, where $\bar{V}$ is the average of the effective volume of kerogen models.

### D.4. $CH_4$ Excess Adsorption

In this work, $CH_4$ excess adsorption in kerogen mesopores is calculated. To obtain excess adsorption amount as in the volumetric method,[7] the effective pore volume $V_p$ is necessary.[8] Helium adsorption has been widely used to measure $V_p$, assuming that helium surface adsorption is negligible.[194, 248] Then, the total helium uptake is used to calculate $V_p$,

$$V_p = \frac{\langle n_{He} \rangle}{N_A \rho_{b,He}}, \tag{D-2}$$

where $\langle n_{He} \rangle$ is the ensemble-averaged number of helium molecules in a given kerogen slit pore, $\rho_{b,He}$ represents the helium bulk density, and $N_A$ is the Avogadro constant. The helium adsorption simulation is conducted at 333.15 K and pressure ranging from 20 to 100 bar. Helium is described as a single-site Lennard Jones (LJ) fluid[267] with its parameters listed in **Table D-1**.

### D.5. Gas Adsorption Simulation

Grand canonical Monte Carlo (GCMC) simulations are applied to describe gas ($N_2$ and $CH_4$) adsorption in kerogen and smooth graphite mesopores with the MCCCS Towhee simulation package[260]. Both $N_2$ and $CH_4$ molecules are treated as single-site LJ fluids. $N_2$ and $CH_4$ force fields are obtained from Ref. [249] and Ref. [261], respectively. The force field for graphite can be found in Ref. [79, 268, 269]. All these force field parameters are listed in **Table D-1**. The pairwise-additive LJ 12-6 potential is used to account for the fluid–fluid and fluid–surface interactions,

$$U\left(r_{ij}\right) = 4\varepsilon_{ij}\left[\left(\frac{\sigma_{ij}}{r_{ij}}\right)^{12} - \left(\frac{\sigma_{ij}}{r_{ij}}\right)^{6}\right], \tag{D-3}$$

where $r_{ij}$ is the separation distance between atoms $i$ and $j$. $\sigma_{ij}$ and $\varepsilon_{ij}$ are the LJ size and the LJ well depth, respectively. The Lorentz–Berthelot combining rules[262] are used for the cross interactions between the unlike atoms $i$ and $j$,

$$\sigma_{ij} = \frac{1}{2}\left(\sigma_i + \sigma_j\right), \tag{D-4}$$

$$\varepsilon_{ij} = \left(\varepsilon_i \varepsilon_j\right)^{1/2}. \tag{D-5}$$

A cutoff distance of 1.4 nm is applied for the short-range LJ interaction with an analytical tail correction. During gas adsorption simulation, kerogen substrates are considered rigid, which means that the potential energy calculations among kerogen macromolecules are not needed.

A periodic rectangular simulation box is used according to the surface dimensions of each kerogen mesopore, which are ~5 nm, and ~5 nm in the *x*- and *y*-directions, respectively. In the *z*-direction, the box length is ~12 nm including the thickness of kerogen matrices. The three-dimensional periodic boundary conditions (PBCs) are used. GCMC simulations are performed at $T$ = 77 K and $T$ = 333.15 K for $N_2$ and $CH_4$ adsorption, respectively. The Widom insertion method[266] is used to calculate chemical potentials, where the bulk densities are obtained from NIST Chemistry WebBook (SRD69).[270] For $N_2$ and $CH_4$, three types of GCMC moves, *i.e.*, insertion, deletion, and translation, are included. We run 0.15 million Monte Carlo (MC) cycles per fluid molecule for equilibration and 0.5 million MC cycles per fluid molecule for sampling.

### D.6. $N_2$ Adsorption Isotherms

For integrity, $N_2$ adsorption in all cases at all pressure conditions is depicted in **Figure D-2**.

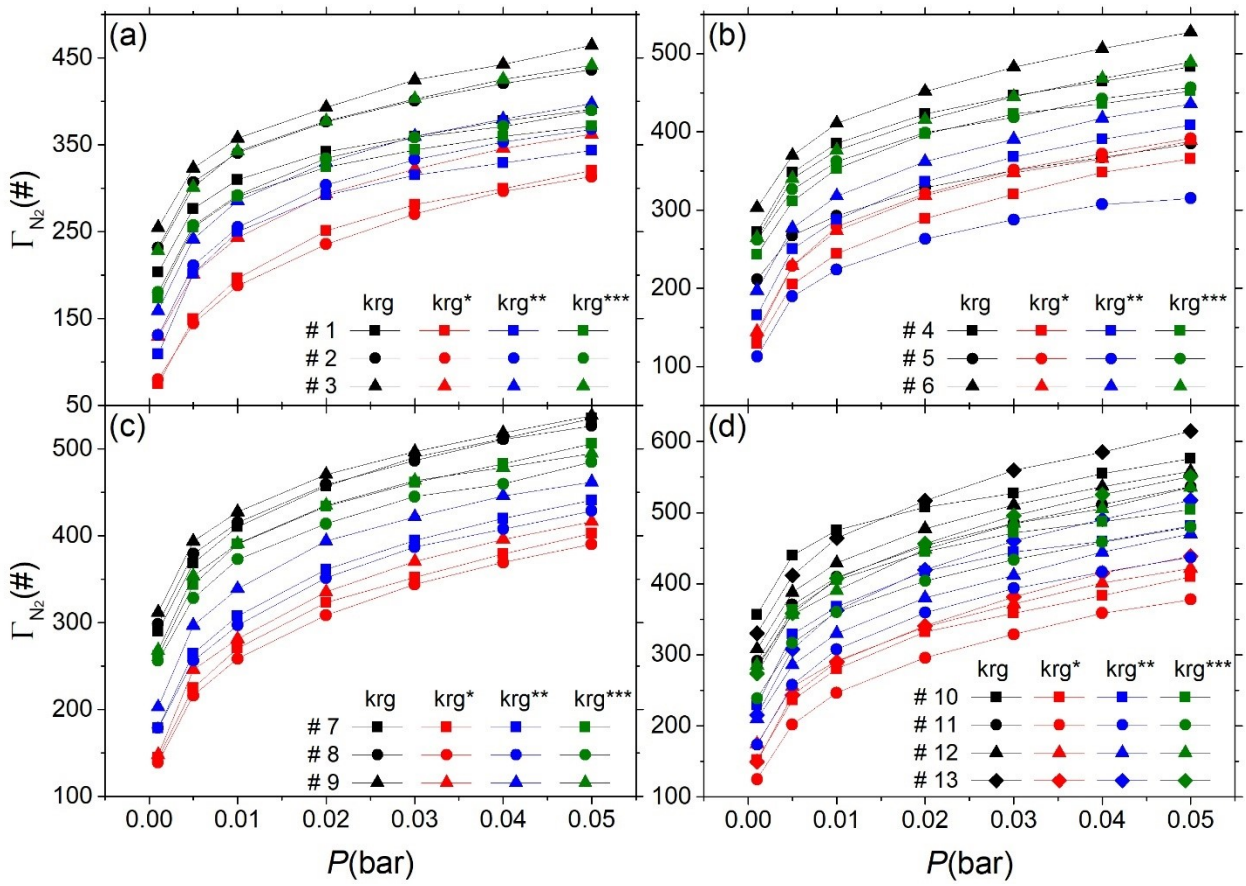


**Figure D-2** $N_2$ adsorption in all kerogen and pseudo-kerogen models at various pressures.

### D.7. $N_2$ Density Profile and Adsorption Layer

As shown in **Figure D-3**, the adsorption layer is defined as the shaded zone where the local density is much higher than the corresponding bulk density. The $N_2$ density in the center of the pore is negligible compared with the density in the adsorption layer which means the difference between total $N_2$ adsorption and $N_2$ surface adsorption can be trivial. That means the total $N_2$ adsorption can be used to depict the surface adsorption behaviors.

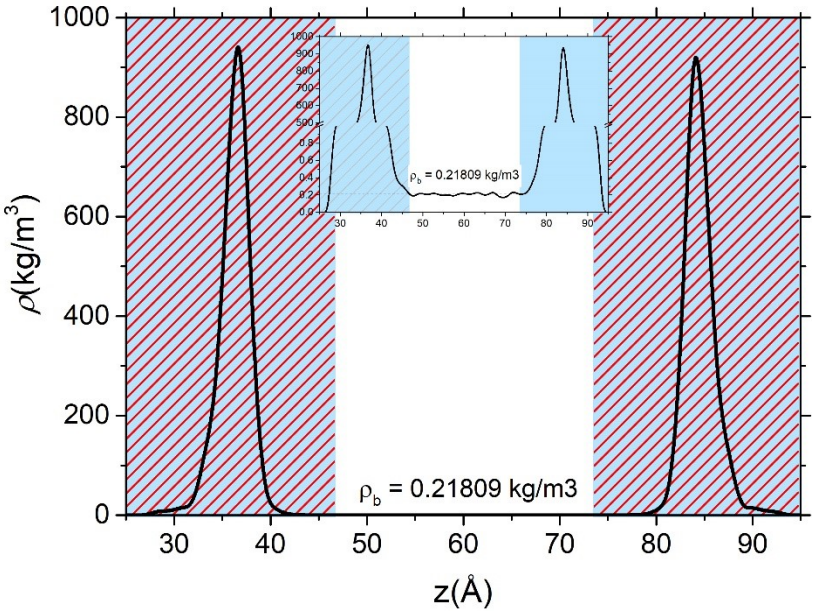


**Figure D-3** $N_2$ adsorption density profile in kerogen slit pore for the krg1 case. The shaded zone is defined as the $N_2$ adsorption layer thickness.

### D.8. $N_2$ High-density Adsorption Sites in Kerogen Slit Mesopores

The kerogen topology is divided into 100 × 100 bins in the *x*-*y* plane. In mesopores, the $N_2$ density in the center of a pore is much less than it is in adsorption layers at such low $T$ and $P$ conditions. To eliminate the pore size effect on average density, the 2-D average density of $N_2$ in the adsorption layer (defined as in **Figure D-3**) in the $(i,j)^{\text{th}}$ bin $\rho_{ave,ad}^{i,j}$ is calculated by,

$$\rho_{ave,ad}^{i,j} = \sum_{ad} N_{N_2}^{i,j} \Big/ H_{ad} \,, \tag{D-6}$$

where $\sum_{ad} N_{N_2}^{i,j}$ is the sum of $N_2$ adsorption in the adsorption layer in the $(i,j)^{\text{th}}$ bin, and $H_{ad}$ is the adsorption layer thickness. The top 200 bins with high $\rho_{ave,ad}^{i,j}$ are defined as high-density $N_2$ adsorption sites on the selected kerogen surface.

### D.9. $N_2$ High-density Sites on Selected Kerogen Surfaces

For integrity, $N_2$ adsorption on more kerogen surfaces is shown below, which shows consistent results with those in the main text.

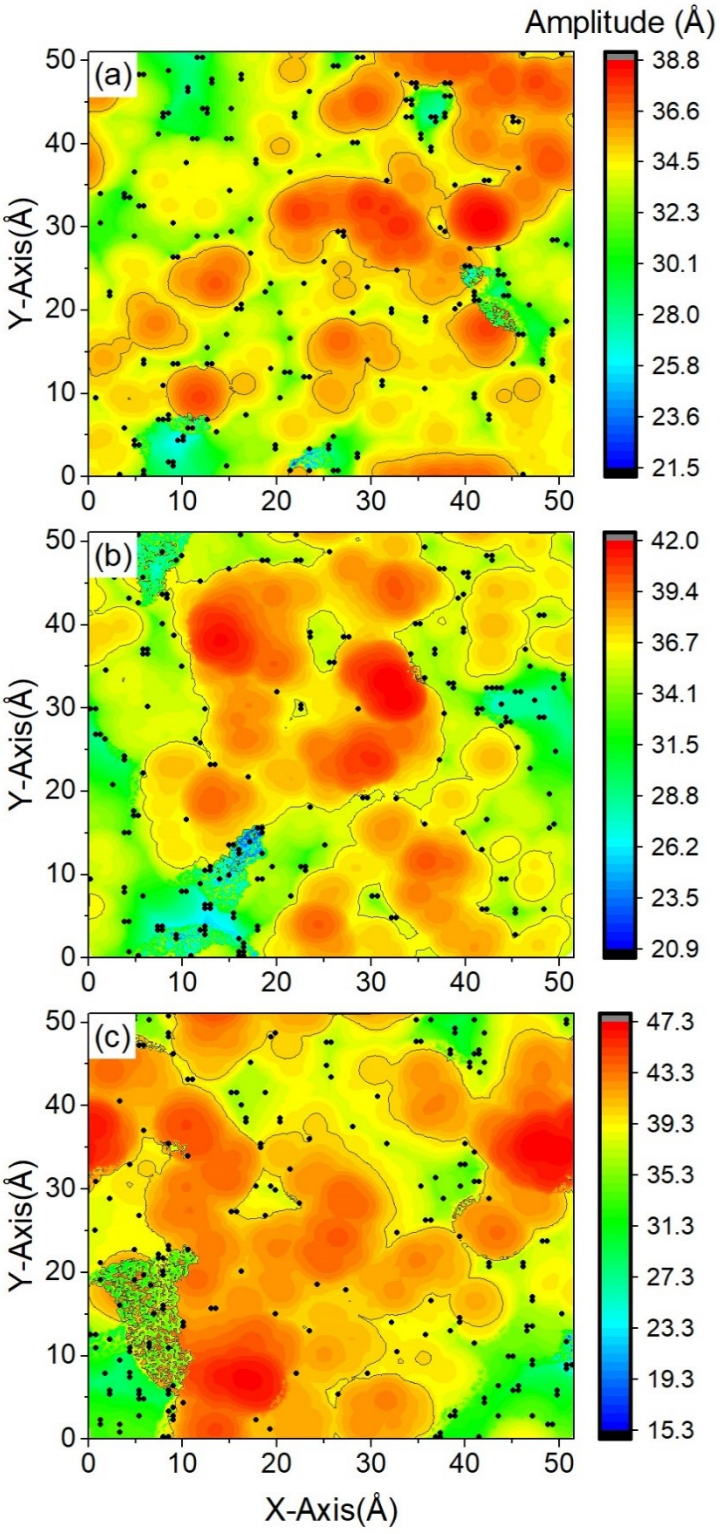


**Figure D-4** $N_2$ high-density sites on kerogen surfaces: panel (a) represents **krg4**; panel (b) represents **krg8**; panel (c) represents **krg12**.

### D.10. $N_2$ Density Difference among Models

In **Figure 5-6**, panels (a) and (c) look very similar to each other, while panels (a) and (d) have a closer adsorption amount according to **Figure 5-5**. It is caused by the "water-downed" phenomenon in the 2-D adsorption contour. To be a more straightforward explanation, the $N_2$ density difference between the **krg10** model and the **krg10**/krg10***** model is depicted below. The contour lines are borders for $\Delta\Gamma_{N_2} / S_{xy} = 0$. In panel (a), most area is negative elucidating a lower $N_2$ adsorption amount

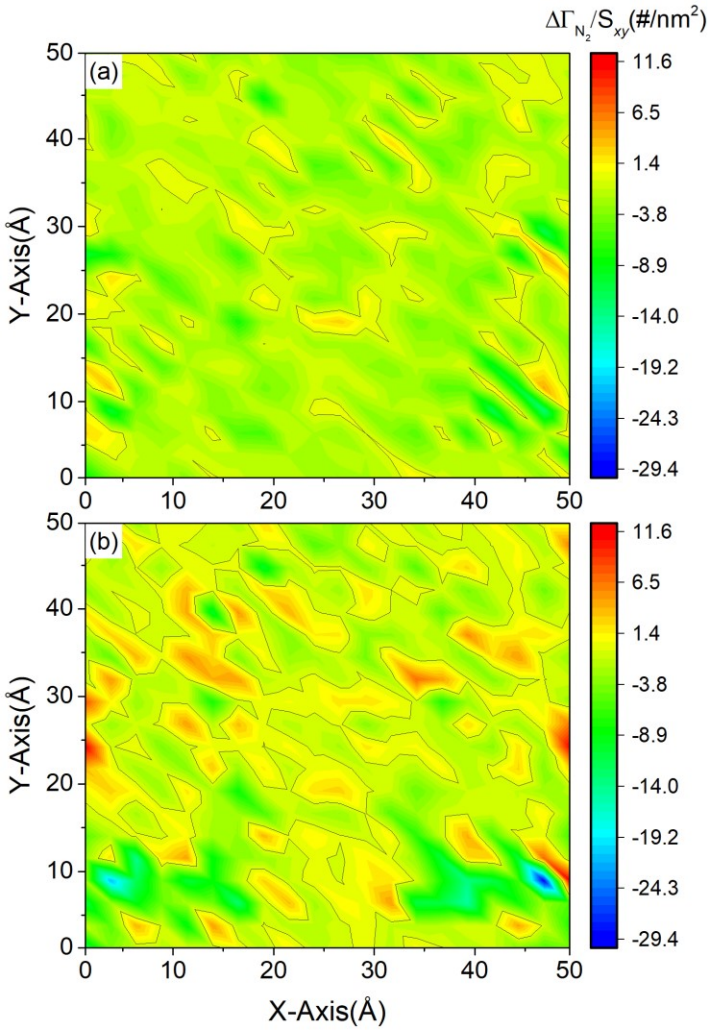


**Figure D-5** $N_2$ density difference between **krg10** and **krg10**/krg10*****: (a) $\Gamma_{N_2}\left(krg10^{**} - krg10\right)$; (b) $\Gamma_{N_2}\left(krg10^{***} - krg10\right)$. The contour lines are the border for $\Delta\Gamma_{N_2} / S_{xy} = 0$.

### D.11. Comparisons of $N_2$ Density Profiles in the *z*-direction

The $N_2$ density profile in the *z*-direction in kerogen and pseudo-kerogen models at 0.05 bar is drawn in **Figure D-6**. Due to the same topology, **krg10** and **krg10****, **krg10*** and **krg10***** have more similar density profiles, respectively. In terms of the $N_2$ density profile in the *z*-direction, the energetical heterogeneity shows less influence than the topology effect.

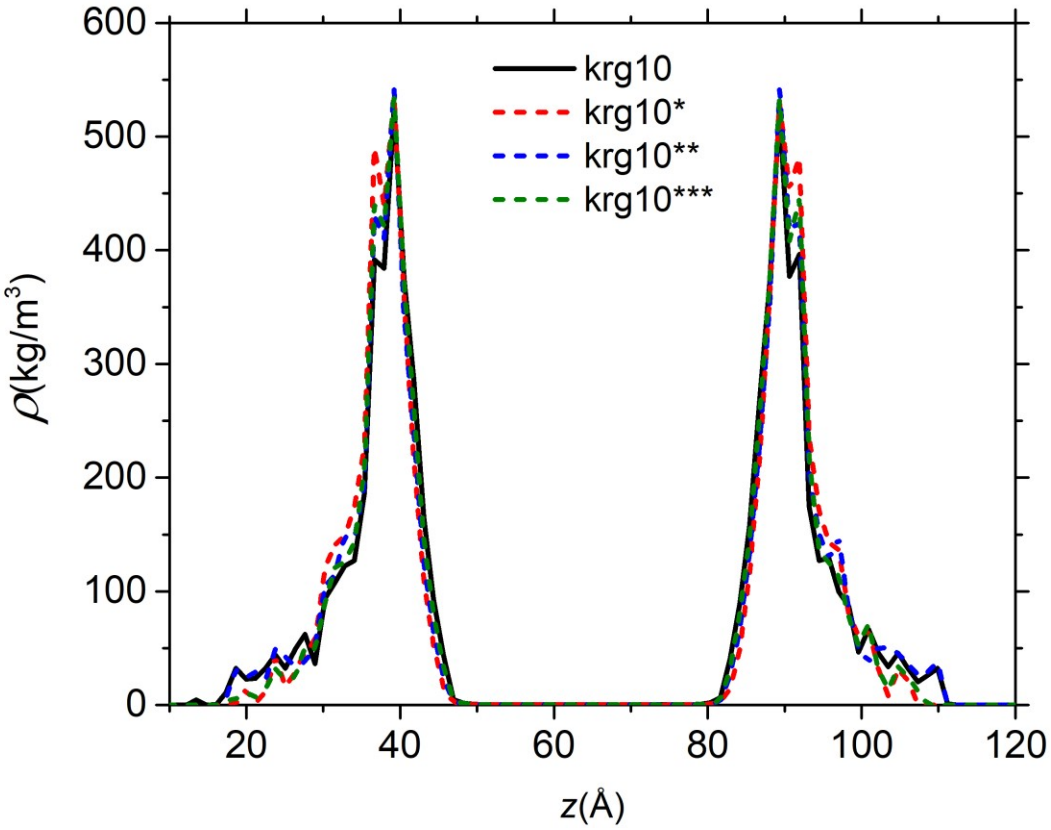


**Figure D-6** $N_2$ density profile in the *z*-direction at 0.05 bar for **krg10**, **krg10***, **krg10****, and **krg10***** models.

### D.12. Comparisons of $N_2$ Adsorption in All Cases

In **Figure D-7**, $N_2$ absorption amounts in **krg**, **krg***, **krg****, and **krg***** at 0.05 bar are presented. As heteroatoms are replaced, $N_2$ adsorption generally decreases in both **krg***, **krg****, and **krg***** except case # 5. The decrease can be up to ~23% in terms of moles, indicating that these heteroatoms can strongly affect $N_2$ adsorption at low pressure at 77 K. The significant adsorption difference indicates that both the size and energy parameters can strongly influence $N_2$ adsorption in kerogen mesopores. For case # 5, the increase of $N_2$ adsorption in **krg5***** models might be related to the high ratio of the "ridge" area in **krg5**.

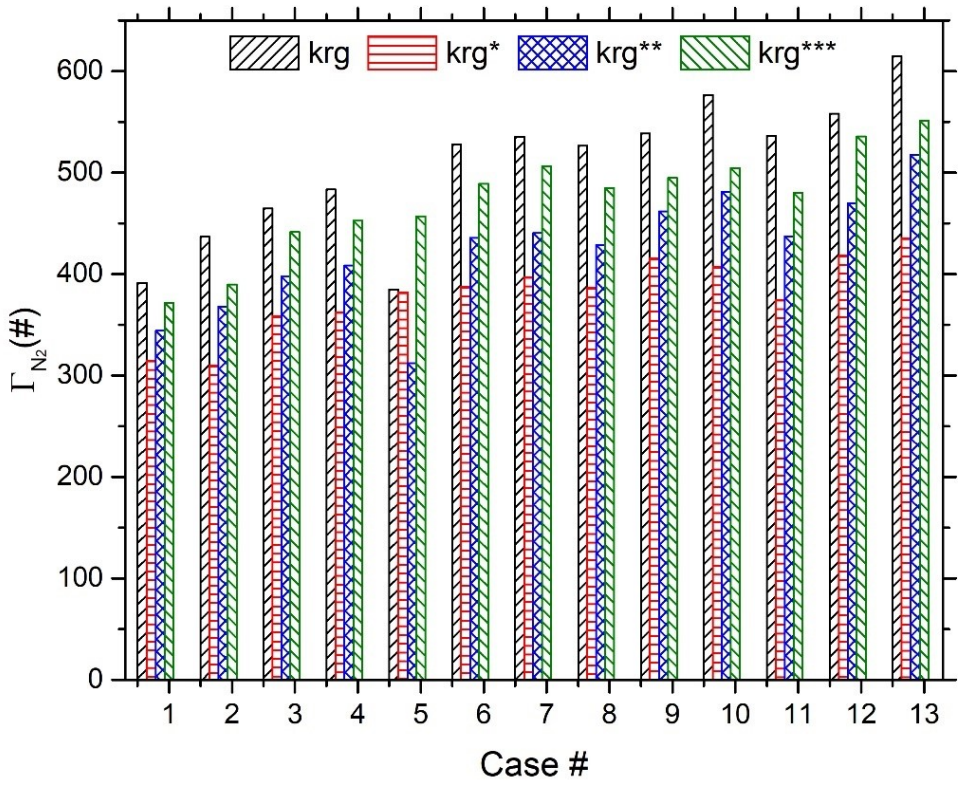


Figure D-7 $N_2$ adsorption amounts in krg, krg*, krg**, and krg*** at 0.05 bar.

**D.13. The BET Plots for Selected Cases**

In this work, we constructed the BET plots for graphite, kerogen, and pseudo-kerogen cases at a pressure range from 0.005 to 0.05 bar. In the BET plots, all linear fitting is determined by $R^2 > 0.99$. In **Figure D-8**, though not including plots for all cases, several selected cases are shown to demonstrate we conducted the BET method correctly.

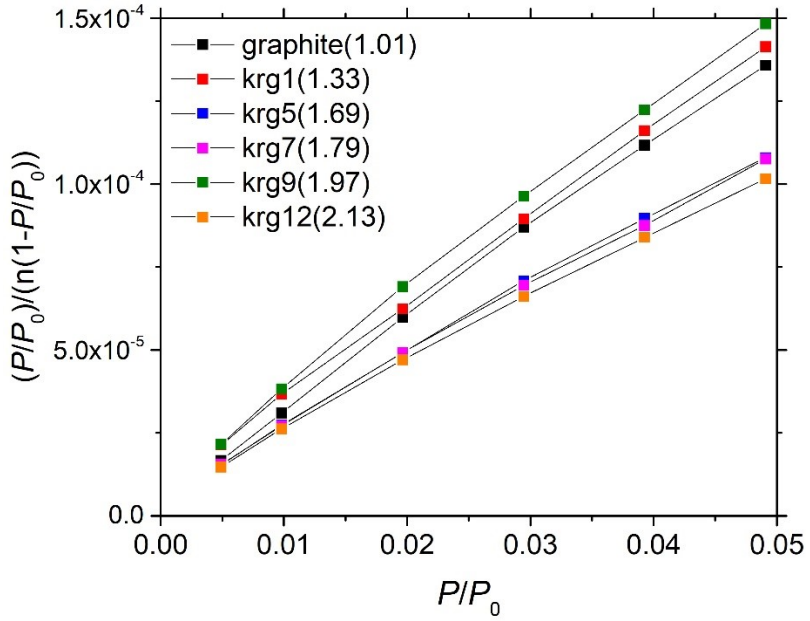


**Figure D-8** BET plots for graphite and kerogen models with various roughnesses.

**D.1. The Relationship between Methane Total Adsorption and Surface Area**

For integrity and interest in $CH_4$ total adsorption, the $CH_4$ net adsorption in kerogen models with various $S_{BET}$ and $S_{geo}$ are depicted in **Figure D-9** where $S_{BET}$ still can be a good choice to estimate the $CH_4$ net adsorption and outperformance of $S_{geo}$. $S_{BET}$ shows a better linear correlation for both $CH_4$ total and excess adsorption, which might be because the effective volume of these kerogen models is similar as listed in **Table D-2**.

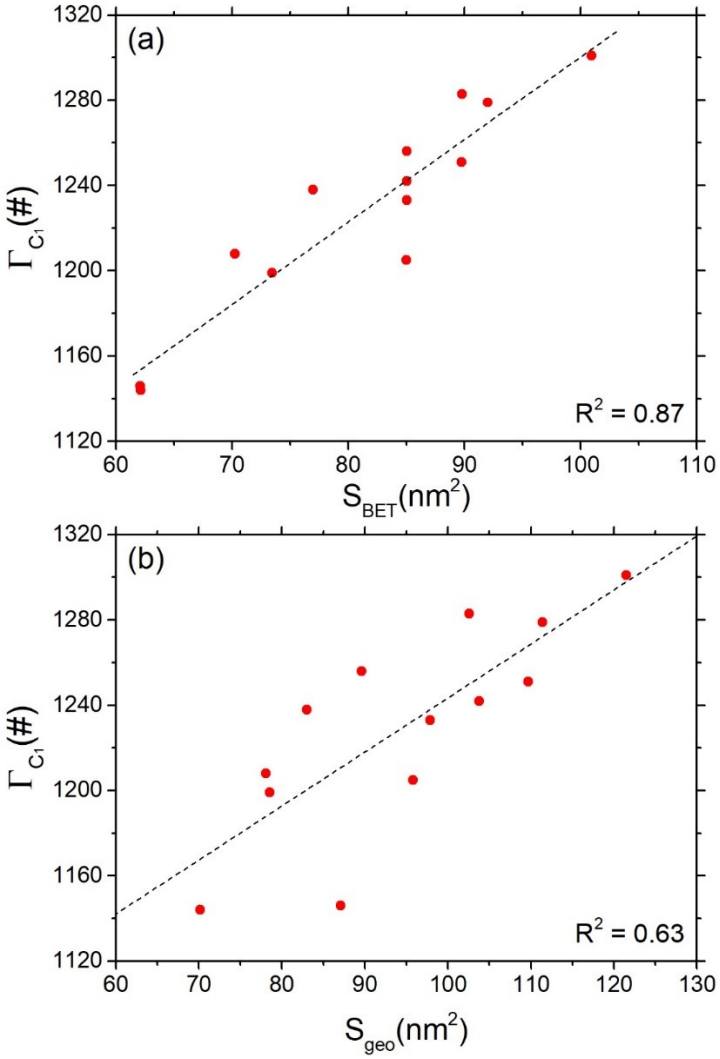


**Figure D-9** Methane total adsorption versus the BET surface area $S_{BET}$ and the geometric surface area $S_{geo}$ at 300 bar.